



UNIVERSITÄT ZU LÜBECK

From the Priority Research Area Infections
Division of Cellular Microbiology
Research Center Borstel-Leibniz Lung Center
Director: Prof. Dr. Ulrich E. Schaible

Influence of Alterations in Iron Metabolism on Anti-mycobacterial Host Defense

Dissertation
for Fulfillment of
Requirements
for the Doctoral Degree
of the University of Lübeck

from the Department of Natural Sciences

Submitted by

Jessica Ebot-Otang Akoh-Arrey
From Yaounde, Cameroon

Lübeck 2023

First referee: Prof. Dr. rer. nat. Ulrich E. Schaible

Second referee: Prof. Dr. med. Christian Sina

Rapporteur: Prof. Dr. rer. nat. Norbert Tautz

Date of oral examination: 29 November 2023

Approved for printing. Lübeck, 19 December 2023

Table of Contents

Table of Contents	iv
Abstract	vii
1 Introduction	1
1.1 Iron Biology	1
1.1.1 Iron acquisition, absorption, and homeostasis	2
1.1.2 Regulation of cellular iron homeostasis via the IRE/IRP network	3
1.1.3 Systemic regulation of iron homeostasis by hepcidin	7
1.1.4 Crosstalk between iron regulation and innate immunity	9
1.2 Tuberculosis	11
1.2.1 Microbiology of <i>M. tuberculosis</i> (Mtb)	12
1.2.2 Epidemiology of TB	12
1.2.3 Pathogenesis and pathophysiology	13
1.2.4 Treatment and vaccine	14
1.2.5 Host response to Mtb and nutritional immunity	15
1.3 The Microbiota	17
1.3.1 The intestinal microbiota	17
1.3.2 The respiratory tract microbiota	18
1.4 Statement of intent and objectives	19
2 Materials	21
2.1 Chemicals and Reagents	21
2.2 Consumables	23
2.3 Buffers, Solutions and Media	24
2.4 Kits	25
2.5 Antibodies	25
2.6 Primers	26
2.7 Equipment	27
2.8 Software	27
2.9 Bacterial Strains	28
2.10 Mice	28
3 Methods	29
3.1 <i>In vitro</i> Experiments	29
3.1.1 Isolation of mouse bone marrow-derived macrophages	29
3.1.2 Isolation of mouse peritoneal macrophages	29
3.1.3 Isolation of mouse alveolar macrophages	30
3.1.4 Treatment of mouse macrophages	30

3.1.5	Culturing of Mtb for <i>in vitro</i> infections	30
3.1.6	Colony-forming unit (CFU) numeration assay	31
3.1.7	Measurement of nitrite production	31
3.2	<i>In vivo</i> Experiments	31
3.2.1	Ethics statement	31
3.2.2	Experimental animals	31
3.2.3	Infection of experimental animals with Mtb	32
3.2.4	Health monitoring	32
3.2.5	Organ removal	33
3.2.6	Colony-forming unit (CFU) enumeration assay	34
3.2.7	Whole blood collection and serum preparation	34
3.3	Histopathological and Immunohistochemical Analyses	34
3.3.1	Tissue processing for histopathology	35
3.3.2	Cryopreservation of tissues	35
3.3.3	Hematoxylin and eosin (H&E) stain	36
3.3.4	Perl's stain	36
3.3.5	Ziehl-Neelsen (ZN) stain	36
3.3.6	Oil Red O stain	37
3.3.7	Immunohistochemistry	37
3.4	Biochemical Analyses	38
3.4.1	Protein concentration measurement	38
3.4.2	Enzyme-linked immunosorbent assay (ELISA)	38
3.4.3	Determination of biochemical iron parameters	38
3.5	Molecular Biology Analyses	38
3.5.1	Total RNA extraction from tissue	38
3.5.2	Quantitative real-time reverse transcription (RT)- polymerase chain reaction (PCR) (qRT-PCR)	39
3.5.3	DNA extraction of tissue	40
3.5.4	Genotyping PCR	41
3.5.5	16S rRNA library preparation	42
3.6	Immunological Analyses	43
3.6.1	Multiplex cytokine assay	43
3.6.2	Measurement of reactive nitrogen species production	43
3.7	Data Analyses	43
3.7.1	Bioinformatic analyses	43
3.7.2	Statistical tests	44
4	Results	45
4.1	Effects of Dietary Iron Manipulation in Mtb Infection <i>in vivo</i>	45
4.1.1	Investigation of host responsiveness to Mtb	45
4.1.2	Histopathological analysis of lung tissue	47
4.1.3	Investigation of indicators of iron status	48
4.1.4	Quantitative evaluation of expression of iron metabolism genes	49
4.1.5	Investigation of mRNA and protein expression levels of inflammatory cytokines	51
4.1.6	Histological analysis for iron deposits in lung tissues	52
4.2	The Role of Iron Regulatory Proteins 1 and 2 in Mtb H37Rv Infection in Macrophages <i>in vitro</i>	54
4.2.1	Assessment of tissue-resident macrophage numbers	54

4.2.2	Investigation of macrophage responsiveness to Mtb	55
4.2.3	Determination of phagocytosis rate of bone marrow-derived macrophages	56
4.2.4	Evaluation of nitric oxide production in macrophages	57
4.2.5	Permissiveness of macrophages to Mtb following iron supplementation and depletion	59
4.3	The Influence of Iron Regulatory Proteins 1 and 2 on Host Responsiveness to Mtb Infection	60
4.3.1	Investigation of host responsiveness to Mtb	61
4.3.2	Clinical and pathological signs of Mtb infection	61
4.3.3	Cytokine and chemokine quantification	64
4.3.4	Determination of iNOS	67
4.3.5	Histopathological analysis of lung and liver tissue	68
4.4	The Role of Iron Regulatory Proteins 1 and 2 on Host Iron Status during Mtb Infection	71
4.4.1	Quantitative evaluation of expression of iron metabolism genes . .	71
4.4.2	Histological analysis for iron deposits in lung, liver and spleen tissues	73
4.4.3	Assessment of red blood cell parameters	76
4.4.4	Evaluation of indicators of iron status	80
4.5	The Influence of Microbiota Composition on Host Phenotypic Variation during Mtb infection	81
4.5.1	Visualization of differences or similarities in caecal microbiota composition	82
4.5.2	16S rRNA taxonomy analysis	86
4.5.3	Investigation of host responsiveness to Mtb following cohousing . .	90
4.5.4	Histopathological analysis of lung tissue	91
4.5.5	Assessment of red blood cell parameters	93
4.5.6	Measurement of immune blood cells	93
4.5.7	Cytokine quantification	94
5	Discussion	97
5.1	The Effects of Altered Iron Regulation On Host Iron Status During Mtb Infection	98
5.2	The Influence of Iron Availability on Mtb Growth in Macrophages and Mice	102
5.3	The Role of Iron in Immunity against Mtb Infection	105
5.4	The Influence of the Gut Microbiota on Host Phenotypic Variation during Mtb Infection	111
5.5	Conclusion and Outlook	115
	Bibliography	119
	Glossary of Symbols and Abbreviations	147
	List of Tables	150
	List of Figures	151
	Appendix	165
	Publications and Presentations	167
	Curriculum vitae	171

Abstract

Tuberculosis (TB) caused by *Mycobacterium tuberculosis* (Mtb) remains a major global health threat. Mtb relies heavily on iron for its growth, metabolism, and virulence. Iron plays an equally crucial role in both the growth and survival of the eukaryotic host and the existing resident organisms within the gut and lung or newly acquired organisms which may further exacerbate TB or pave the way for co-infections. However, the impact of disruptions in iron homeostasis on host iron status during Mtb infection and the contribution of two key regulators of cellular iron metabolism, iron regulatory proteins (IRP) 1 and 2, to TB pathogenesis have not yet been studied. Therefore, this study aimed to investigate the effects of altered iron regulation on host iron status and immune responses before and during experimental Mtb infection.

Wild type (wt) mice were fed an iron-control, iron-low or iron-rich diet before and during Mtb infection. Additionally, wt mice and mice homozygous for IRP1 (*Irp1*^{-/-}) or 2 (*Irp2*^{-/-}) or heterozygous for IRP2 (*Irp2*^{+/-}) were fed standard chow before and after infection with Mtb. Expression of iron metabolism genes, indicators of host iron status, colony-forming units, and cytokine levels were determined at various time points of the infection.

Wt mice fed an iron-rich diet showed higher hepatic hepcidin mRNA expression, higher Mtb loads in lungs, spleens, and livers and more severe pulmonary pathology characterized by larger inflammatory cellular infiltrates compared to controls. Iron-rich diet also led to iron accumulation in alveolar macrophages and elevated serum ferritin levels which was exacerbated during Mtb infection. Similar phenotypes were observed in *Irp2*^{-/-} mice. Furthermore, higher TNF α and IFN γ concentrations were observed in the lungs of Mtb infected *Irp2*^{-/-} mice at days 28 and 63 post Mtb infection (p.i.) as well as in wt mice on an iron-rich diet at days 29 and 120 p.i. IL-1 β , IL-6, KC/GRO, MCP-1 and MIP-2 levels and nitric oxide production were increased in *Irp2*^{-/-} mice compared to *Irp1*^{-/-} and wt mice at day 28 p.i. Therefore, IRP2 downstream effects seem to be relevant for clearing Mtb and mediating host immune responses in the early phase of Mtb infection. Taken together, these results indicate that wt mice on an iron-rich diet and *Irp2*^{-/-} mice developed an iron overload phenotype, which promoted growth of Mtb and inflammation.

To investigate if the observed phenotypes were driven by differences in microbiota composition, a cohousing approach with germ-free wt mice was employed. Examination of the caecal microbiota via 16S rRNA gene sequencing revealed that the genera *Barnesiella* and *Turicibacter* were highly represented in *Irp1*^{-/-} mice, while *Alloprevotella*, *Helicobacter*, and *Flavonifractor* were more abundant in *Irp2*^{+/-} mice when compared to wt mice. Bray-Curtis index of dissimilarity showed comparable caecal microbiota composition between offspring of germ-free wt mice (acceptor mice) cohoused with corresponding wt, *Irp1*^{-/-} and *Irp2*^{+/-} mice. Furthermore, Mtb infection of these acceptor mice revealed lower Mtb loads in the lungs of IRP1-acceptor during the early stages of infection, along with lower serum TNF α and IFN γ and blood monocyte counts. These results suggest an iron availability driven microbiota effect on host response to Mtb infection independent of the iron overload phenotype observed in

Irp2^{-/-} mice, which otherwise rendered these mice more susceptible to Mtb infection. Overall, these results indicate that IRP1 and IRP2 have opposite downstream effects that can influence host responses which control Mtb replication in mice in the early phase of Mtb infection. The data presented in this thesis provides the basis for future studies on the interplay of iron regulatory proteins, Mtb infection, and the ecological dynamics of microbial communities within this context, which could potentially reveal new host-directed therapies to effectively combat TB.

Zusammenfassung

Die durch *Mycobacterium tuberculosis* (Mtb) verursachte Tuberkulose (TB) ist nach wie vor eine große globale Gesundheitsbedrohung. Mtb ist für sein Wachstum, seinen Stoffwechsel und seine Virulenz stark auf Eisen angewiesen. Eisen ist aber auch wichtig für das Wachstum, die Differenzierung und das Überleben sowohl des eukaryotischen Wirts als auch der Mikroorganismen im Darm und in der Lunge als auch für andere Pathogene, als Koinfektionen die TB beeinflussen können. Allerdings sind die Auswirkungen von Störungen der Eisenhomöostase auf den Eisenstatus des Wirts während einer Mtb-Infektion und der Beitrag von zwei Regulatoren des zellulären Eisenstoffwechsels, der Eisenregulierenden Proteine, (IRP) 1 und 2, zur TB Pathogenese noch nicht untersucht worden. Ziel dieser Studie war daher die Untersuchung der Auswirkungen einer veränderten Eisenregulation auf den Eisenstatus des Wirts und die Immunantwort vor und während der experimentellen Mtb-Infektion.

Wildtyp Mäuse (wt) wurden vor und während einer Infektion mit Mtb mit einer eisenfreien, eisenarmen oder eisenreichen Diät gefüttert. Zusätzlich wurden Mäuse, die homozygot für IRP1 (*Irp1*^{-/-}) oder 2 (*Irp2*^{-/-}) oder heterozygot für IRP2 (*Irp2*^{+/-}) vor und nach der Infektion mit Mtb mit Standardfutter ernährt. Die Expression von Eisenstoffwechselgenen, Indikatoren für den Eisenstatus des Wirts, Mtb mengen und Zytokinspiegel wurden zu verschiedenen Zeitpunkten der Infektion bestimmt.

Wt Mäuse, die mit einer eisenreichen Diät gefüttert wurden, zeigten eine höhere hepatische Hpcidin-mRNA-Expression, höhere Mtb-Zahlen in Lunge, Milz und Leber sowie eine schwerere Lungenpathologie, die durch größere entzündliche zelluläre Infiltrate im Vergleich zu den Kontrollen charakterisiert war. Die eisenhaltige Ernährung führte auch zu einer Eisenakkumulation in alveolären Makrophagen und erhöhten Serumferritinwerten was sich während einer Mtb-Infektion noch verschlimmerte. Ähnliche Phänotypen wurden bei *Irp2*^{-/-} Mäuse beobachtet. Höhere TNF α and IFN γ -Konzentrationen in der Lunge von Mtb infizierten *Irp2*^{-/-} Mäuse an den Tagen 28 und 63 nach der Mtb-Infektion (p.i.) sowie bei wt-Mäusen mit eisenreicher Ernährung an den Tagen 29 und 120 p.i. gemessen. Höhere Konzentrationen an IL-1 β , IL-6, KC/GRO, MCP-1- und MIP-2-Spiegel sowie Stickoxid waren bei *Irp2*^{-/-} Mäuse im Vergleich zu *Irp1*^{-/-} und wt-Mäuse am Tag 28 p.i. zu beobachten. Daher scheinen die nachgeschalteten Effekte von IRP2 für die Beseitigung von Mtb und die Vermittlung von Immunreaktionen des Wirts in der frühen Phase der Mtb Infektion wichtig zu sein. Insgesamt entwickelten Mäuse, die eine eisenreiche Diät erhielten, und *Irp2*^{-/-} Mäuse einen Phänotyp der Eisenüberladung, der Entzündungen und Wachstum von Mtb fördert.

Um zu untersuchen, ob die beobachteten Phänotypen auf eine Unterschiede in der Zusammensetzung der Mikrobiota zurückzuführen sind, wurde ein Co-Housing-Ansatz mit keimfreien wt-Mäusen angewandt. Die Untersuchung des Zäkalmikrobiota mittels 16S rRNA-Gen-Sequenzierung ergab, dass im Vergleich zu wt-Mäusen wurden in *Irp1*^{-/-} Mäusen mehr Bakterien der Gattungen *Barnesiella* und *Turicibacter* beobachtet, un der Gattungen *Alloprevotella*, *Helicobacter*, and *Flavonifractor* in *Irp2*^{+/-} Mäusen. Der Bray-Curtis-Index

of dissimilarity zeigte eine vergleichbare Zusammensetzung der Zäkalmikrobiota zwischen Nachkommen keimfreien wt-Mäuse (Akzeptor-Mäusen), die mit entsprechenden wt-, *Irp1*^{-/-} und *Irp2*^{+/-} Mäusen gehalten wurden. Die Mtb-Infektion von Akzeptoren zeigte eine geringere Mtb-Belastung in den Lungen von IRP1-Akzeptor Mäuse im Vergleich zu wt-Akzeptor- und IRP2-Akzeptor Mäusen zu Beginn der Infektion eine geringere Mtb-Belastung in der Lunge, begleitet von niedrigerem Serum-TNF α and IFN γ sowie einer geringeren Anzahl von Monozyten im Blut der IRP1-Akzeptor Mäusen.

Diese Ergebnisse deuten auf einen von der Eisenverfügbarkeit abhängigen Effekt der Mikrobiota auf die Reaktion des Wirts auf eine Mtb Infektion, hin. Diese Ergebnisse deuten auf einen von der Eisenverfügbarkeit abhängigen Effekt der Mikrobiota auf die Reaktion des Wirts auf eine Mtb Infektion, hin. Dies ist unanabhängig von dem Eisenüberladungsphänotyp, der bei *Irp2*^{-/-} Mäusen beobachtet wurde, die ansonsten diese Mäuse anfälliger für Mtb-Infektionen machten. Diese Ergebnisse zeigen, dass IRP1 und IRP2 entgegengesetzte nachgeschaltete Effekte haben, die Wirtsreaktionen beeinflussen können, welche die Mtb-Replikation in Mäuse in der frühen Phase der Infektion kontrollieren. Die Daten in dieser Arbeit bilden die Grundlage für zukünftige Studien zur Ökologie mikrobieller Gemeinschaften und zur Analyse der Wechselwirkungen zwischen Eisen, Mikrobiota und Mtb-Infektion, die neue, auf den Wirt ausgerichtete Therapien zur wirksamen Bekämpfung von TB ermöglichen könnten.

Introduction

1.1 Iron Biology

Iron ranks among the most prevalent elements found in the Earth's crust [1]. As a transition metal, iron has oxidation states ranging from -2 to +7, with ferrous (Fe^{2+}) and ferric (Fe^{3+}) iron ions being the most common forms. Fe^{2+} is soluble in aqueous solutions at physiological pH and readily oxidized to Fe^{3+} . In contrast, Fe^{3+} steadily remains insoluble at neutral pH. Equally, iron is an essential micronutrient used by organisms of all domains of life. Due to its redox properties, iron participates in many electron transfer and redox reactions by forming complexes with iron-containing functional groups such as heme, iron-sulfur clusters, and iron-oxo centers to function as enzyme cofactors (**Table 1.1**). These cofactors are required for the activity of many enzymes [2, 3] to catalyze an array of essential biochemical processes and metabolic pathways vital for cell survival.

Table 1.1: Iron cofactors and their essential functions

Cofactor	Function
Heme	Oxygen transport (hemoglobin and myoglobin) Enzyme catalysis (such as nitric oxide synthases and oxidases) Electron transfer reactions (cytochromes)
Iron-sulfur cluster	Regulation of gene expression (bacterial transcription factors AirS, SoxR) Electron transfer and redox reactions (such as oxidative phosphorylation) Enzyme catalysis (such as aconitases) Nucleic acid metabolism in DNA/RNA synthesis and repair
Iron-oxo centre	Enzyme catalysis (ribonucleotide reductase) Oxygen transport (hemerythrin)

Despite being beneficial, surplus iron in an unbound labile form can be toxic by acting as a catalyst for forming reactive free hydroxyl radicals through the Fenton reaction. These radicals can cause protein oxidation, membrane lipid peroxidation, and mutagenesis of nucleic acids. To avoid these detrimental effects, organisms have developed highly controlled strategies to import, manage, store and export iron at both the cellular and systemic levels.

1.1.1 Iron acquisition, absorption, and homeostasis

On average, the iron content in a healthy adult human body typically ranges from 3-5g of iron, consisting of heme-bound iron and Fe^{2+} and Fe^{3+} iron ions. Most total body iron is present as heme, contained within hemoglobin (Hgb) in red blood cells (RBCs). Meanwhile, 10-15% is present as myoglobin in muscles and other tissues. The liver and spleen are the main iron reservoirs in the body as damaged, or senescent RBCs are phagocytosed by the bone marrow resident hepatic, and splenic macrophages (MØs). Effective mechanisms to excrete iron are lacking. Therefore, systemic iron homeostasis is regulated through iron recycling by MØs from these sources and via dietary iron absorption by duodenal enterocytes. In this way, healthy adults procure only 1-2mg of iron from their diet daily to compensate for unspecific losses. These losses occur through daily cell desquamation or elimination of body fluids such as sweat or urine [4].

Heme-bound iron is taken up by scavenger receptors (SRs). Of note, circulating ferritin is also imported via SR class A member 5 (SCARA5) [5]. SRs recognize and eliminate damaged and senescent RBCs, other forms of protein-bound iron, and by-products of RBC degradation [6]. For example, Haptoglobin, a liver-derived protein with high binding affinity to free Hgb in the blood, is taken up and cleared by the cluster of differentiation (CD) 163 (CD163), an SR of the cysteine-rich superfamily. Also, hemopexin, a plasma protein which binds free heme in plasma during intravascular hemolytic conditions such as infection-induced anemia, malaria, and sickle cell anemia, is internalized and cleared by CD91 [6, 7] (**Fig. 1.5C**).

Several transporters are involved in cellular heme transport, including the heme carrier protein 1 (HCP-1) and the feline leukemia virus subgroup C (FLVCR2) [8, 9]. HCP-1 is predominantly expressed in MØs and colocalizes with the Hgb-Hp complex, which is subsequently taken up by CD163, indicating that HCP-1 is involved in heme uptake. The cell surface receptor, FLVCR2, is also involved in heme uptake [8, 9]. Meanwhile, FLVCR1, a homologue of FLVCR2, and ATP-binding cassette transporter G2 (ABCG2) have been linked to heme export in mammalian cells [10, 11]. Another heme transporter is the heme-responsive gene-1 (HRG-1). HRG-1 transports heme from phagolysosomes and RBC degrading MØs into the cytoplasm. Mouse MØs deficient for *Hrg-1* show a decrease in heme transport from the phagolysosome, indicating that HRG-1 is essential for heme transport and iron recycling in MØs [12]. Primarily expressed by MØs, HRG-1 colocalizes with natural resistance-associated macrophage protein 1 (NRAMP1) to erythrophagolysosomes, a vesicle formed following the merging of RBC-containing phagosomes with lysosomal vesicles. NRAMP1 is expressed in the membrane of lysosomes in MØs and recruited to the phagosome membrane. NRAMP1 mediates iron import to the cytoplasm and maintains intracellular iron recycling following erythrophagocytosis [13, 14, 15].

In contrast to heme iron, most human non-heme iron, which exists as Fe^{3+} , is bound to iron-binding glycoproteins such as transferrin (TF) in plasma and lactoferrin in extracellular fluids such as breastmilk. This is why Fe^{3+} is poorly bioavailable and must first be reduced to Fe^{2+} before it is transported across the intestinal epithelium. Duodenal cytochrome b (DcytB), a membrane metalloredutase protein expressed on the apical surface of enterocytes, ensures the reduction of Fe^{3+} to Fe^{2+} (**Fig. 1.5A**). Recent studies have shown that the Zrt-Irt-like protein (ZIP) family of transporters, ZIP8 and ZIP14 have been identified as fundamental in transporting Fe^{2+} into the cytoplasm. This is achieved by the action of prion protein (PRNP), expressed on the surfaces of most nucleated cells, acting as a ferrireductase. A few authors have hypothesized that during digestion, the low pH of the stomach and ascorbic acid in the intestinal lumen contribute to the reduction of Fe^{3+} . Once reduced, Fe^{2+} binds to poly (rC)-binding protein-2 (PCBP2). PCBP2 is an iron chaperone which transports Fe^{2+} via divalent metal transporter-1 (DMT1), a significant iron transporter on the cell surface of

various cell types. Transported Fe^{2+} is delivered to the labile iron pool (LIP) which is composed of redox-active iron. Most of the iron from the LIP is delivered to the mitochondria, which are used for iron-sulfur cluster and heme group synthesis. Mediated by PCBP1 and PCBP2, iron from the LIP can also be inserted into cytoplasmic ferritin for storage. Another portion of iron from the LIP is destined for export into systemic circulation via ferroportin (FPN), the only known mammalian cellular iron exporter [16],[17].

Extracellularly, unbound Fe^{3+} atoms are scavenged by TF to become TF-bound iron (TBI). Interaction of TBI with transferrin receptor 1 (TFR1) expressed ubiquitously on the surfaces of most nucleated cells leads to its internalization by receptor-mediated endocytosis. As the pH of the endocytic vesicle drops, Fe^{3+} is released from TF and reduced to Fe^{2+} by six transmembrane epithelial antigen of the prostate 3 (STEAP3). STEAP3 is a ferrireductase essential for cellular iron uptake and homeostasis [18]. Fe^{2+} is mainly transported from the endosome into the cytoplasm by DMT1 or its homologue, solute carrier (SLC) 11A1, a member of the membrane transport protein family. In addition, ZIP14 transports TBI from the endosome to the cytoplasm [19]. Subsequently, Apo-TF (iron deficient TF form) and the TBI and transferrin receptor 1 complex are reprocessed for further iron binding and TBI endocytosis, respectively (**Fig. 1.5B**). Under physiological conditions, TF-mediated iron uptake is the most crucial pathway, particularly in developing erythroid precursors, due to their immense need for iron to support hemoglobin synthesis. However, in iron overload conditions, TF becomes heavily saturated with iron and circulating “free” iron (or non-transferrin bound iron (NTBI)) accumulates in blood circulation. NTBI is distributed to tissues through TF-independent mechanisms. Notably, mice and humans deficient in TF develop severe iron overload in the liver and pancreas, indicating distinct organ-specific transport mechanisms for NTBI. Studies have revealed that NTBI can be taken up by ZIP8 and ZIP14 into cells and stored within ferritin. There are also other mechanisms required for regulating iron transport, utilization, and storage. These mechanisms involve the synergistic action of iron-responsive elements (IREs) and iron regulatory proteins (IRPs) 1 and 2 (IRP1 and IRP2), which are critical in maintaining cellular iron homeostasis in vertebrates [20].

1.1.2 Regulation of cellular iron homeostasis via the IRE/IRP network

The IREs are highly conserved RNA motifs that form hairpin structures in the untranslated regions (UTRs) of various target mRNAs [20]. These mRNAs encode proteins involved in iron transport (TFR1, DMT1, FPN) and storage (ferritin light (L-) and heavy (-H), FtL and FtH, chains). The IRPs are predominantly located in the cytosol and encoded by the *IRP1* and *IRP2* genes. IRP1 and IRP2 are analogues of the tricarboxylic acid cycle enzyme mitochondrial aconitase (mACON) [20]. m-ACONs have a characteristic iron-sulfur (4Fe-4S) cluster required for the conversion of citrate to isocitrate. IRP1 and IRP2 regulate intracellular iron concentrations through different IRE-binding mechanisms.

IRP1 functions as a cytosolic aconitase (c-aconitase) using a catalytic 4Fe-4S cluster which is assembled under high iron conditions and prevents IRE-binding [21]. Under low iron conditions or in the presence of other oxidative signals such as reactive oxygen (ROS) and reactive nitrogen species (RNS) including nitric oxide (NO), hydrogen peroxide (H_2O_2), respectively, the 4Fe-4S cluster disassembles and induces IRP1 to acquire RNA-binding activity [21] (**Fig. 1.1A**).

Hypoxia stabilizes the IRP1 c-aconitase form by decreasing oxygen or ROS levels. A few studies have shown a protein kinase C phosphorylation site in IRP1-serine (S) 138. Notably,

S138 phosphomimetic mutants of IRP1 can assemble a Fe-S cluster leading IRP1 to display aconitase activity (**Fig. 1.1B**). Nevertheless, the Fe-S cluster is highly susceptible to the presence of oxygen, ROS, and H₂O₂ [22, 23]. Additionally, IRP1 acts as a substrate for F box and leucine-rich repeat protein 5 (FBXL5), an E3 ligase ubiquitin ligase subunit which regulates cellular and systemic iron homeostasis [24]. Particularly, FBXL5-dependent ubiquitination is promoted by iron during S138 phosphorylation or when Fe-S cluster biogenesis is compromised [25].

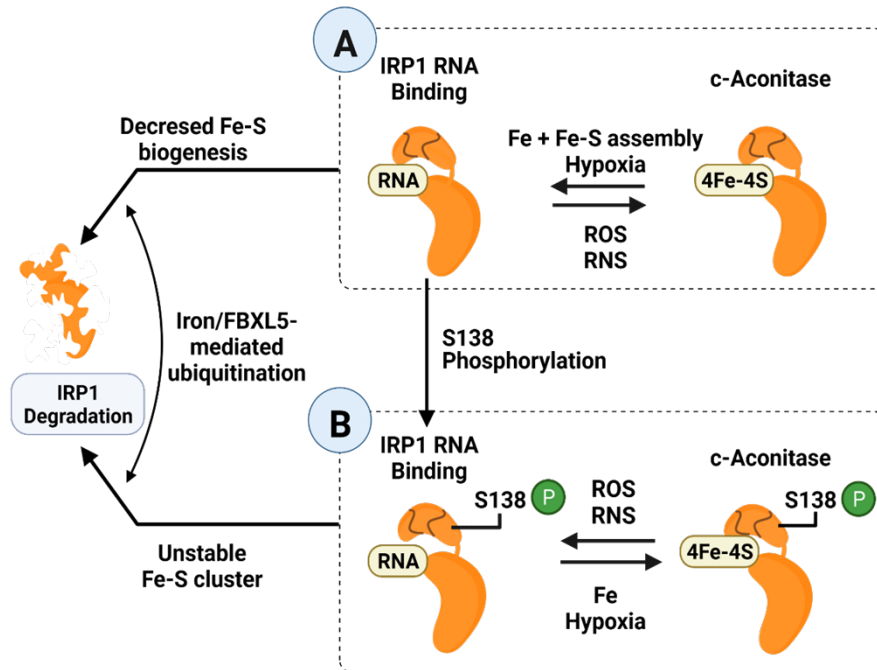


Figure 1.1: Mechanisms for IRP1 regulation. IRP1 can be regulated by the assembly or disassembly of the 4Fe-4S cluster resulting in the IRP1 functioning as either a c-aconitase or IRE-binding protein (A). Phosphorylation at S138 can also stimulate iron-sulfur assembly in IRP1 (B). Abbreviations: 4Fe-4S= iron-sulfur cluster, FBXL5= F-box and leucine-rich repeat protein 5, ROS= reactive oxygen species, RNS= reactive nitrogen species, Adapted from [26, 27]. Created with BioRender.com

Like IRP1, IRP2 is an RNA-binding protein but is enzymatically inactive and unable to assemble the 4Fe-4S cluster. The regulation of IRP2 primarily occurs at the protein stability level. Under iron-starved or hypoxic conditions, FBXL5 is marked for proteasomal degradation by an unknown E3 ligase leading to IRP2 stabilization and accumulation. In iron-replete conditions and hyperoxia, the FBXL5 hemerythrin domain binds to iron. This induces a conformational change that mediates FBXL5 stability triggering a cascade of events. These events include FBXL5 binding to IRP2, which connects with the S-phase kinase-associated protein 1, and culin 1 (SKPI-CUL1) complex to the RING domain-containing protein, RBX1 that binds an activated E2 conjugating enzyme. Ultimately, these events lead to IRP2 ubiquitination and degradation (**Fig. 1.2A**).

IRP2 activity can also be regulated by the phosphorylation at S157 via cyclin-dependent kinase 1 (CDK1/cyclinB1) and dephosphorylated by cell division cycle 14A (CDC14A), a protein-coding gene. Of note, phosphorylated and non-phosphorylated IRP2 can go through iron-dependent FBXL5-mediated degradation (**Fig. 1.2B**). Finally, IRP2 is also modulated in response to oxidative stress, primarily through ROS and RNS production [28].

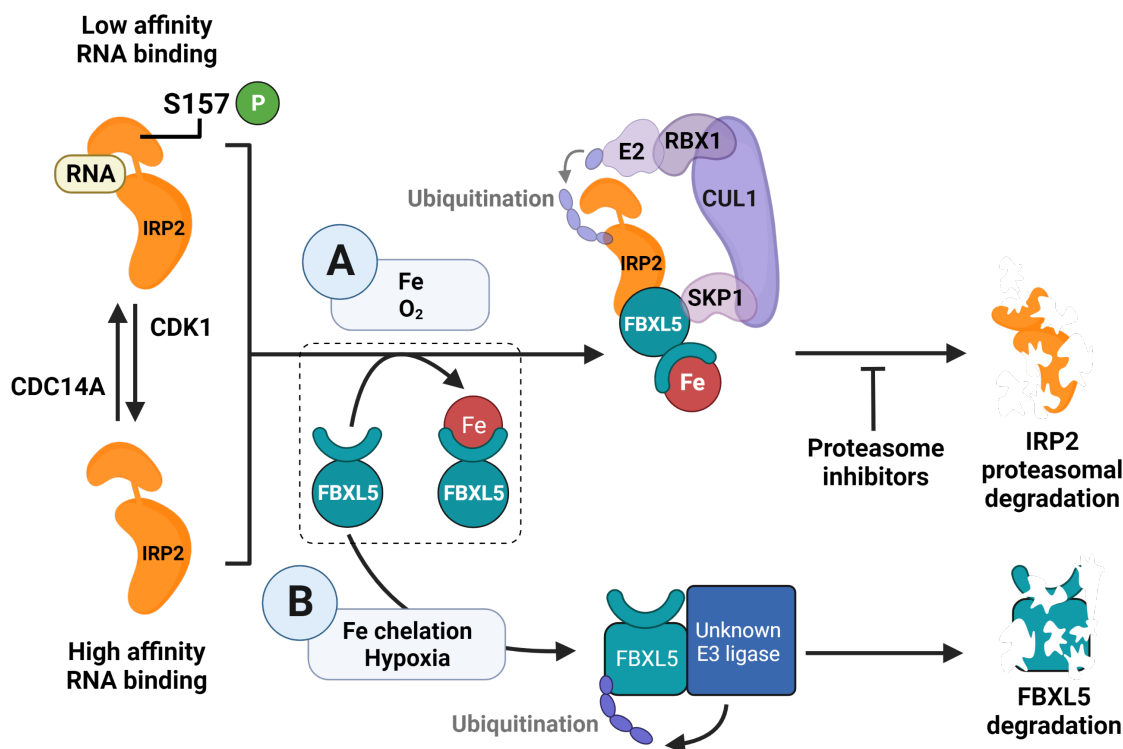


Figure 1.2: Mechanisms for IRP2 regulation. IRP2 is regulated at the level of protein stability in response to cellular iron and oxygen concentrations. In high iron and oxygen conditions, FBXL5 is stabilized, and IRP2 is degraded (A). Under iron or oxygen-deficient conditions, FBXL5 is destabilized, leading to an increase in IRP2 levels (B). Abbreviations: FBXL5= F-box and leucine-rich repeat protein 5, SKP1= S-phase kinase-associated protein 1, CUL1= culin 1, G2-M= Gap 2-mitosis, CDC14A= cell division cycle 14A, CDK1= cyclin-dependent kinase 1. Adapted from [26, 27]. Created with BioRender.com

Ultimately, under low cytoplasmic iron conditions, both IRP1 and IRP2 are active and bind to the IREs in the 5'-UTR of FPN, FtL, and FtH chains, and hypoxia-inducible factor (HIF)-2 α mRNAs to induce translational repression [29] (**Fig. 1.3A**). HIF-2 α belongs to the family of HIF transcription factors and mediates cellular responses to low oxygen concentrations [30]. When IRPs bind to 3'-UTR of TFR1 or DMT1 mRNAs, their degradation is impeded. Consequently, iron uptake is upregulated while iron storage and export are downregulated, leading to intracellular iron accumulation. When iron levels are abundant, IRP1 is converted to an iron-sulfur-containing cytosolic aconitase, whereas IRP2 undergoes proteasomal degradation [24]. Consequently, IRPs do not bind to IREs and allow FPN, FtL and FtH chains and HIF-2 α mRNA translation in the 5'URT. This promotes TFR1 and DMT1 mRNA degradation to prevent more iron uptake and avoid excess iron-induced damage [31] (**Fig. 1.3B**).

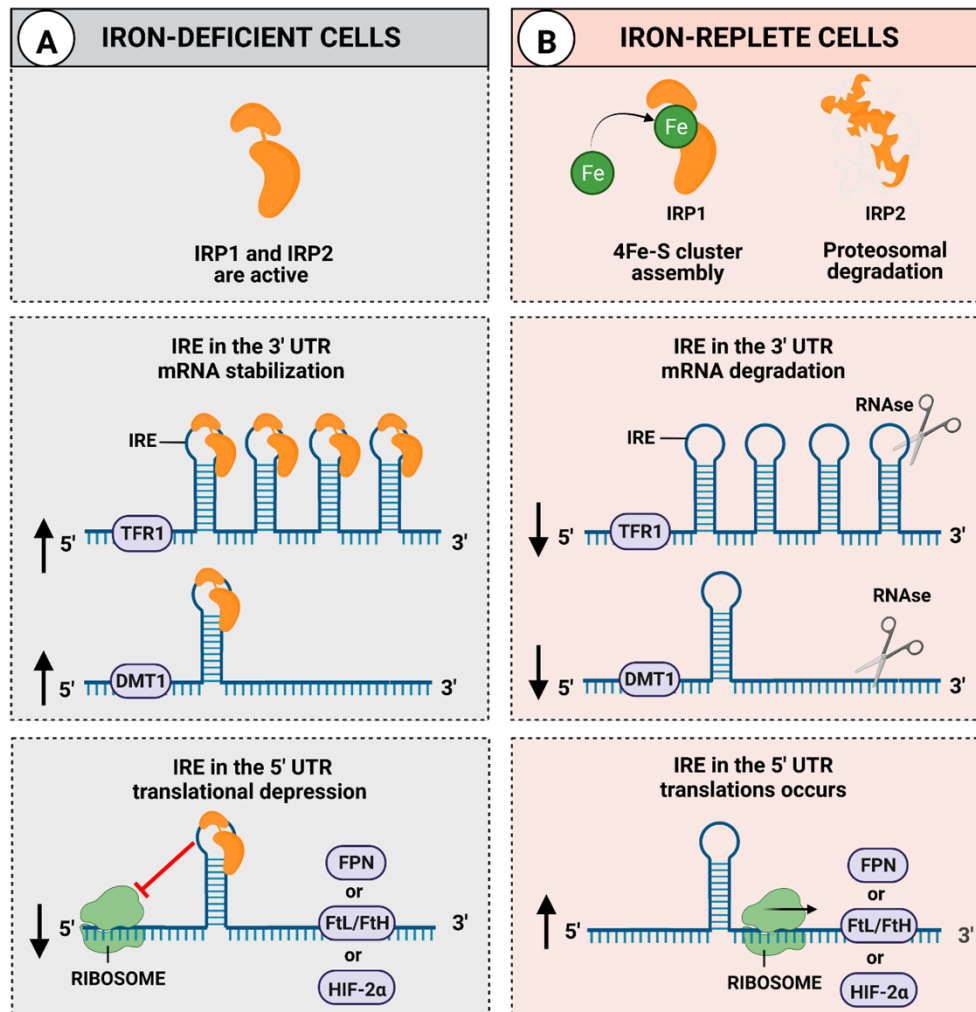


Figure 1.3: IRE/IRP regulatory system. The activity of IRPs is dependent on cellular iron concentrations. Under iron-deficient conditions, IRPs bind to IREs in 5'-UTR of the mRNA and translation of the target protein is repressed. Binding to 3'-UTR of the mRNA stabilizes and protects the transcripts from endonucleolytic cleavage and degradation (A). Under iron-replete conditions, IRP1 functions as a cytosolic aconitase cluster while IRP2 is degraded allowing for the translation of mRNA containing an IRE in the 5'-UTR and the degradation of mRNAs in the 3'-UTR (B). Abbreviations: IRP= iron regulatory protein, IRE= iron responsive element, UTR= untranslated region, TFR1= transferrin receptor 1, DMT1= divalent metal transporter 1, FPN= ferroportin, FtL/FtH= ferritin light and heavy chains, HIF-2α= hypoxia-inducible factor-2 alpha. Adapted from [32]. Created with BioRender.com

Some IRE/IRP system defects have been linked to human inheritable disorders [33, 34] summarized in **Table 1.2**. Meanwhile, genome-wide association studies (GWAS) have identified several genetic polymorphisms in *IRP1* and *IRP2*, which researchers have associated with a few human pathological conditions (see **Table 1.3**).

Table 1.2: Human disorders linked to IRE/IRP system defects. Modified from [35].

Disorder	Mutation	Phenotype
Hereditary hyperferritinemia-cataract syndrome	IRE motif of L-ferritin gene that obstructs IRP binding	Acute hyperferritinemia, no systemic iron overload or inflammation [33]
Sideroblastic-like anemia with iron overload	GBLX5 deficiency resulting in enhanced IRE-binding activity of IRP1 and ALAS2 mRNA repression	Sideroblastic-like anemia, microcytosis and systemic iron overload [36]
Autosomal dominant iron overload disorder in hepatocytes and Kupffer cells	A single mutation in the IRE motif of H-ferritin mRNA transcript which promotes IRP binding	H-ferritin mRNA repression resulting in iron overload disorder related to hemochromatosis [37]

Table 1.3: GWAS involving *IRP1* and *IRP2* polymorphisms. Modified from [35]

Gene	Disease	Association	Polymorphisms
<i>IRP1</i>	Cutaneous malignant melanoma	Cutaneous malignant melanoma risk	rs7855483, rs10813813, rs17288067 [38]
<i>IRP1</i>	Neuropathic pain in HIV-infected patients	Distal neuropathic pain in HIV patients on ART	rs2026739 [39]
<i>IRP2</i>	Lung cancer	Lung cancer	rs2036534 [40]
<i>IRP2</i>	Chronic obstructive pulmonary disease (COPD)	Increased mRNA and protein expression in patients with COPD	rs2568494, rs2656069, rs10851906, rs12593229, rs13180 [41, 42, 43, 44]
<i>IRP2</i>	Alzheimer's disease	Alzheimer's disease	rs2656070, rs13180 [45]
<i>IRP1</i> and <i>IRP2</i>	Age-related macular degeneration and migraine	Migraine susceptibility and macular degeneration typically in older individuals	rs867469, rs17483548 [46]

Abbreviations: w/= with HIV= Human immunodeficiency virus, ART= Antiretroviral therapy

IRP/IRE system interconnects with systemic iron metabolism through the regulation of FPN. FPN expression is also controlled at the post-transcriptional level by hepcidin, a key regulator of systemic iron homeostasis [47].

1.1.3 Systemic regulation of iron homeostasis by hepcidin

Hepcidin regulates iron availability by binding to and inactivating FPN leading to its clathrin-mediated internalization and proteolytic degradation [48]. Consequently, FPN-mediated iron export and uptake in duodenal enterocytes is hindered, leading to increased intracellular iron accumulation and hypoferrremia in plasma [49]. Ultimately, these events are commonly associated with anemia of inflammation (AI), usually seen in the setting of systemic inflammation [48]. Of note, IRPs may regulate hepcidin transcription under conditions of iron deficiency or hypoxia by controlling HIF-2 α mRNA translation.

Defect in regulating hepcidin expression leads to clinical conditions such as hereditary hemochromatosis (HH), "ferroportin disease", and iron-refractory iron-deficiency anemia (IRIDA). HH is a hereditary genetic disorder affecting genes encoding proteins involved in the signalling pathways

regulating hepcidin expression. Of these genes, the major ones include HFE (responsible for HH type I), HFE2 (or hemojuvelin (HJV) responsible for HH type IIA), and HAMP (responsible for HH type IIB) and TFR2 (transferrin receptor 2, responsible for HH type III). HH individuals have low hepcidin levels and unregulated dietary iron absorption reflected by increased intracellular iron and tissue iron overload in the liver, heart, and pancreas. Consequently, this leads to conditions such as liver cirrhosis, heart failure and diabetes [49]. However, iron-depleting remedies like iron chelation by deferoxamine, phlebotomy and bloodletting can rescue the condition but not rectify the primary disorder. “Ferroportin disease”, or HH type IV, is an autosomal-dominant genetic disorder. It is characterized by iron overload in the body caused by mutations in the *SLC40A1* gene encoding for FPN [49]. These mutations lead to reduced FPN plasma membrane localization or impaired hepcidin-induced FPN degradation. Mutations in the gene encoding for activin receptor-like kinase 2 (*ALK2*), the primary signal receptor suggested to induce hepcidin transcription and the transmembrane serine protease matriptase-2 (TMPRSS6), a negative regulator of hepcidin production (**Fig. 1.4A**), leads to iron-refractory iron deficiency anemia. Individuals with iron-refractory iron deficiency anemia have moderate to severe iron deficiency anemia with minimal response to oral iron supplementation.

Several intracellular signalling cascades trigger hepcidin upregulation by diverse mechanisms. Systemic iron availability and inflammatory and infectious signals are the most prominent of these mechanisms. For iron signalling, an increase in TF saturation in plasma and secretion of bone morphogenetic protein (BMP6) from liver sinusoidal cells induce hepcidin transcription via the BMP6/Small Mothers Against Decapentaplegic (SMAD) signalling pathways. Following the binding of TF to transferrin receptor 2 (TFR2), and BMP6 to BMP receptors, SMAD1/5/8 are phosphorylated and together with SMAD4 form a complex which is translocated to the nucleus and binds to BMP response elements in the *HAMP* promoter, thereby activating hepcidin transcription. This restricts iron availability to pathogens thereby linking iron metabolism and anti-microbial responses [47]. Successful hepcidin expression via iron signalling requires the action of HJV, which is also a BMP co-receptor, as well as HFE, which is negatively regulated by TMPRSS6 (**Fig. 1.4A**). Under infectious or inflammatory conditions, hepcidin expression is upregulated to limit iron availability to invading extracellular pathogens. Several stimuli initiate this, including LPS, interleukin (IL)-1, IL-6, or IL-22, partially through signal transducer and activator of transcription (STAT3). The IL-6/JAK/STAT (Janus kinase/Signal Transducer and Activator of Transcription) signalling pathway is the most studied one of these inflammatory mediators. IL-6 binds to IL-6 receptors, activates JAK1/2, and STAT3 is phosphorylated and translocated to the nucleus. Eventually, hepcidin transcription is stimulated through the binding of the STAT3-binding motif on the *HAMP* promoter [50] (**Fig. 1.4B**). In this way, plasma iron is decreased, and iron export from MØs is prevented, leading to increased intracellular iron accumulation in MØs. Ultimately, this prevents iron sequestration by pathogens, which depend on this essential micronutrient for growth and survival. Therefore, iron regulation by MØs is a vital defense strategy during infection [51].

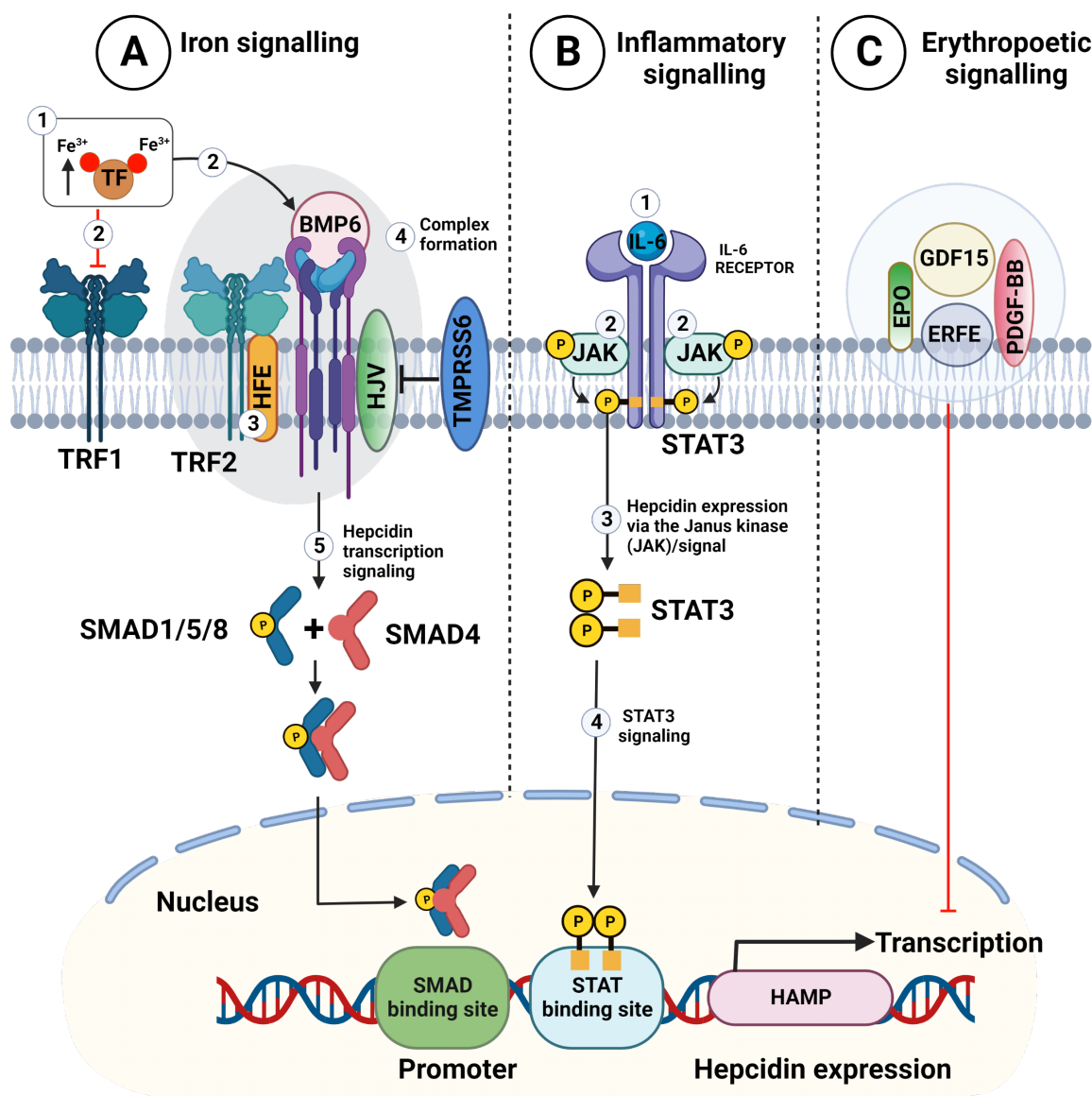


Figure 1.4: Major molecular mechanisms for hepcidin regulation. These include BMP6/SMAD (A) and IL-6/JAK/STAT (B) signalling pathways. Hepcidin expression is inhibited by hypoxia to stimulate iron recruitment and erythropoiesis. Other regulators such as erythropoietin (EPO), growth differentiation factor-15 (GDF15) and platelet-driven growth factor-BB (PDGF-BB) and erythroferrone (ERFE) both inhibit hepcidin expression [52, 53] and neutralize BMP6 [54] (C). Abbreviations: EPO= Erythropoietin, GDF15= Growth differentiation factor-15, PDGF-BB= Platelet-driven growth factor-BB, ERFE= Erythroferrone. Numbers and black arrows denote the sequence of events. Red arrows represent inhibitory effects. Adapted from [55]. Created with BioRender.com

1.1.4 Crosstalk between iron regulation and innate immunity

Iron homeostasis and MØ effector functions are closely connected. MØs are essential in maintaining iron homeostasis by recycling iron for storage and supplying 95% of iron needed during erythropoiesis. Iron plays two critical roles in MØ-pathogen interactions; first, by serving as a vital source of nutrients for intracellular pathogens such as *Salmonella* (*S.*) *enterica* serovar Typhimurium (referred hereon as *S.* Typhimurium), *Legionella pneumophila*, *Plasmodium falciparum*, *Coxiella burnetii* and *Mycobacterium* (*M.*) *tuberculosis* [56]. Second,

by acting as a catalyst promoting the production of antimicrobial effectors such as RNS and nicotinamide adenine dinucleotide phosphate-oxidase (NADPH)-generated ROS, contributing to the elimination of invading pathogens [57]. Notably, RNS and ROS modulate IRP1 and IRP2 binding activity [58, 28, 21]. In turn, this regulates the expression of DMT1 and TFR1, which limit iron uptake and ultimately restrict iron availability to intracellular pathogens. Through ROS generation, iron stimulates the binding activity of several transcription factors such as NF- κ B and Nrf2 (**Fig. 1.5**). NF- κ B serves as a critical mediator of inflammatory responses and induces the expression of several inflammatory cytokines including IL-1 β , IL-6, and tumor necrosis factor (TNF)- α [59, 60]. NF- κ B also promotes the transcription of HIF-1 α , which impedes NF- κ B-induced gene expression [61, 30]. In contrast to NF- κ B, the binding activities of HIF-1 α and nuclear factor for IL-6 expression (NF-IL-6) are inhibited by iron overload in vitro. Weiss et al. [62] reported that upon stimulation with interferon (IFN)-gamma (IFN γ) and LPS followed by treatment with Fe³⁺, NF-IL6 activation was decreased in the M \emptyset cell line, J774A.1 [62]. Interestingly, this reduced NF-IL6 activation also impaired nitric oxide synthase (NOS2) mRNA transcription and NO production [62]. In response to IFN γ , decreased intracellular heme-iron in M \emptyset s induces the expression of IL-6, IL-12, NOS2, TNF, and major histocompatibility complex (MHC) II [51]. IL-6 induces the expression of hepcidin which inactivates and degrades FPN. In M \emptyset s, FPN transcription is decreased by the toll-like receptor (TLR) 4 or TLR2/TLR6 signalling pathways leading to hypoferremia which is a host defense strategy to limit iron availability to invading pathogens. In the same line, IFN γ modulates TFR1 expression and intracellular ferritin concentration either in the absence or upon infection with various mycobacterial species (spp.), which can restrict iron availability to intracellular pathogens.

Taken together, within the M \emptyset , iron promotes the binding activities of several transcription factors, which regulate the expression of several inflammatory cytokines and iron transport and storage proteins, mediating host susceptibility or resistance to infections.

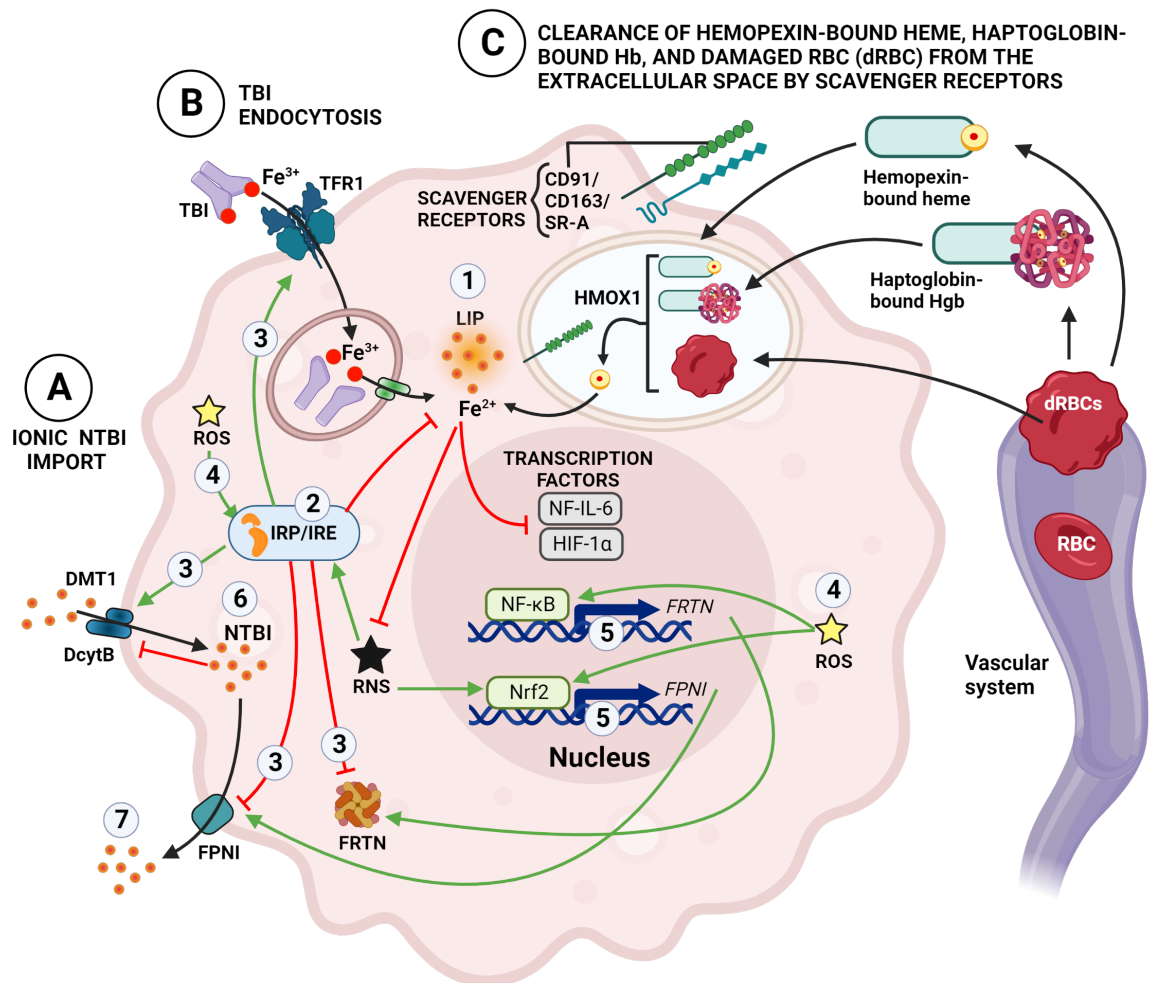


Figure 1.5: Iron metabolism in the macrophage. MØs can acquire iron from various sources including NTBI (A) and TBI uptake (B), and scavenger receptors (C). Excess labile iron generates ROS. ROS stimulates transcription factors' binding activities, which modulates the expression of several iron transport and storage proteins. In turn, the expression of these proteins is regulated posttranscriptionally by the IRPs. Abbreviations: HMOX1= heme oxygenase 1, TBI= transferrin-bound iron, NTBI= non-transferrin-bound iron, LIP= labile iron pool, FRTN= ferritin, FPNI= ferroportin; dRBCs= damaged RBCs, Hgb= hemoglobin. Numbers denote the sequence of events. Arrows represent iron movements (black), stimulatory effects (green), or inhibitory effects (red). Created with BioRender.com

1.2 Tuberculosis

TB ranks among the leading causes of death worldwide. In 2021, an estimated 10.6 million people developed TB worldwide, of which 1.6 million succumbed to the disease. TB predominantly causes a lung infection, but other sites such as meninges, pleura, lymphatic system, and bones can also be affected. Although some patients with active pulmonary TB and culture-positive results may be asymptomatic, typical symptoms include mild fever, generalized fatigue, persistent cough, chest pain, bloody sputum, weight loss, and drenching night sweats [63].

1.2.1 Microbiology of *M. tuberculosis* (Mtb)

M. tuberculosis (Mtb) and a group of phylogenetically closely related bacterial species assembled under the Mycobacterium tuberculosis complex (MTBC) are the causative agents for TB. While Mtb is the principal causative agent of human TB, *M. africanum* and *M. canettii* can also cause TB in humans in certain endemic regions of Africa [64]. First described in 1882 by Robert Koch, Mtb is a rod-shaped, aerobic, non-motile, non-spore-forming, facultative intracellular bacterium. Typically, slow-growing, the generation times of Mtb range between 18-54 h, and therefore, long culture times are required. Mtb is Gram-positive with a thick waxy cell wall, 60% of which comprises lipids. The cell wall consists of peptidoglycan and arabinogalactan layers with non-covalently attached macromolecules such as mycolic acids, trehalose dimycolate, glycoproteins and glycolipids [65]. Owing to this unique cell wall composition, mycobacteria are described as acid-fast bacteria as their lipid-rich cell wall repels water and soluble dyes and therefore, resists decolorization by acids or alcohols.

1.2.2 Epidemiology of TB

Currently, the epidemiology of TB varies depending on the geographical region as opposed to its global widespread until the mid-20th century. South-East Asia (43%), Africa (25%), and the Western Pacific (18%) are the most areas affected by TB. In 2020, the 30 high TB burden countries accounted for 86% of new TB cases. Of note, over 60 % of the people who developed TB worldwide were residents of 8 of the 30 high TB burden countries, including India (26%), China (8.5%), Indonesia (8.4%), the Philippines (6%), Pakistan (5.8%), Nigeria (4.6%), Bangladesh (3.6%) and South Africa (3.3%). In 2020, there were over 500 TB cases per 100 000 population in Lesotho, South Africa, Central Africa Republic, the Philippines and the Democratic People's Republic of Korea [63]. Some socio-economic factors account for the high TB incidence in some countries. These include malnutrition, poverty, overcrowded or poorly ventilated living or work spaces, poor sanitary conditions, mass migration due to geopolitical instability, and non-existent or low-quality health care systems [66]. There were 150-400 TB cases per 100 000 population in most of the 30 high TB burden countries and less than 10 TB cases per 100 000 population, mainly in Europe and the Americas (**Fig. 1.6**). Several factors such as alcoholism, tobacco smoking, indoor air pollution, prolonged exposure to silica dust, HIV infection, vitamin D deficiency, iron deficiency and iron overload of environmental or genetic origin are known risk factors for TB [67, 68, 69]. Interestingly, the male sex is a risk factor for TB, with a global male-to-female ratio of 1.75 [63].

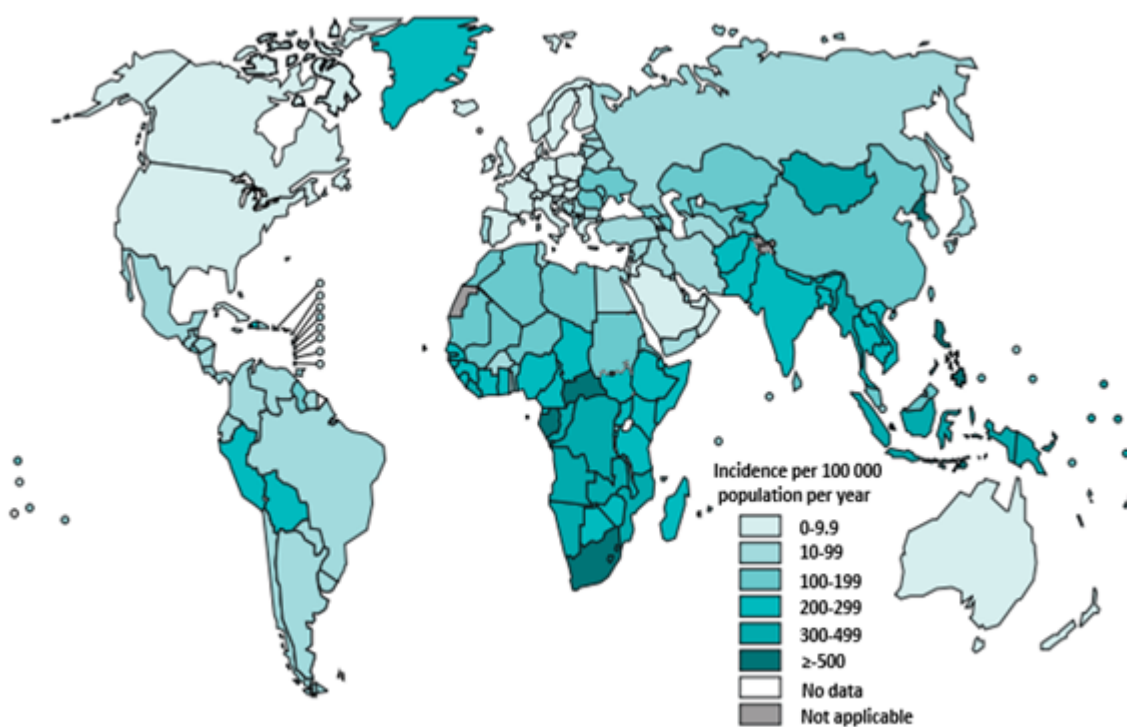


Figure 1.6: Estimated Global TB incidence rates in 2021 [63]

1.2.3 Pathogenesis and pathophysiology

According to the World Health Organization (WHO), approximately one-fourth of the global population is estimated to be infected with TB. Only 5-10% of those infected are predicted to develop active TB during their lifetime, while the remainder will maintain a latent TB infection (LTBI). Individuals with latent TB are asymptomatic and non-infectious, but they remain at risk of developing active TB at any point during their lifetime. HIV infection, autoimmune diseases, and immunosuppressive treatments such as anti-TNF therapy increase the likelihood of LTBI reactivation [63]. Aerosol particle production by coughing is the main route of pulmonary TB transmission [70]. Following inhalation, *Mtb* reaches the alveoli, where it encounters alveolar macrophages (aMØs), the niche for *Mtb*, and dendritic cells (DCs). This initial encounter can lead to immediate clearance by ingestion and destruction of the bacteria. Sometimes, these responses are enough to contain and eliminate *Mtb* in healthy persons. However, *Mtb* often evades initial destruction by phagocytes to ensure its survival and replication leading to either immediate onset of active disease following infection (primary TB) usually seen in small children and immunodeficient adults, LTBI, or reactivation in 5-10% of LTBI individuals later in life. Infected aMØs produce chemoattractants. These chemoattractants recruit resting innate immune cells such as neutrophils (or polymorphonuclear neutrophils, PMN), natural killer cells, and $\gamma\delta$ T-cells and blood monocytes to the initial infection focus. This initial immune response induces the formation of granulomas. The granuloma constitutes the major pathological hallmark of TB. At this point, monocytes can ingest the bacteria but fail to contain the bacilli. Professional antigen-presenting cells such as DCs and MØs transport the bacteria to local lymph nodes and present mycobacterial antigens to prime and activate specific T-cells. Specific T-cells relocate to the site of infection, further promoting the formation of

granulomas. T-cell derived $\text{IFN}\gamma$ can activate granuloma $\text{M}\phi$ s, which in turn can differentiate into either epithelioid cells, fuse to form multi-nucleated giant cells (MCG), or lipid-loaded “foamy macrophages” [71]. At this stage, the granuloma is encapsulated by well-organized rims comprising of DCs, B- and T-lymphocytes gathered around the $\text{M}\phi$ -rich area and surrounded by fibroblasts and a fibrotic cuff of collagen (**Fig. 1.7A**). In this way, the granuloma prevents further bacterial dissemination and tissue damage and thus contains the infection. In LTBI, the granuloma serves as a reservoir for *Mtb*, providing an environment for rapid bacterial proliferation when immunity is compromised. As the infection progresses, invading PMN alters the granuloma to a caseating granulomatous lesion with a central region of necrotic cells and damaged tissue (**Fig. 1.7B**). Interestingly, a few studies have reported necrotic centers of granulomas of human TB patients to contain a high concentration of host iron-withholding proteins and hypothesized that the host is establishing an iron-deprived environment for *Mtb*. However, at the same time, these iron-containing proteins could serve as an iron source for the bacteria upon proteolytic degradation [72]. Caseating granulomas can burst open and promote *Mtb* dissemination into the surrounding tissue, thereby rendering the host infectious and most often symptomatic. In extreme cases, pulmonary cavitation is characterized by liquefaction of the granuloma and destruction of lung tissue leading to reduced lung function can occur [73].

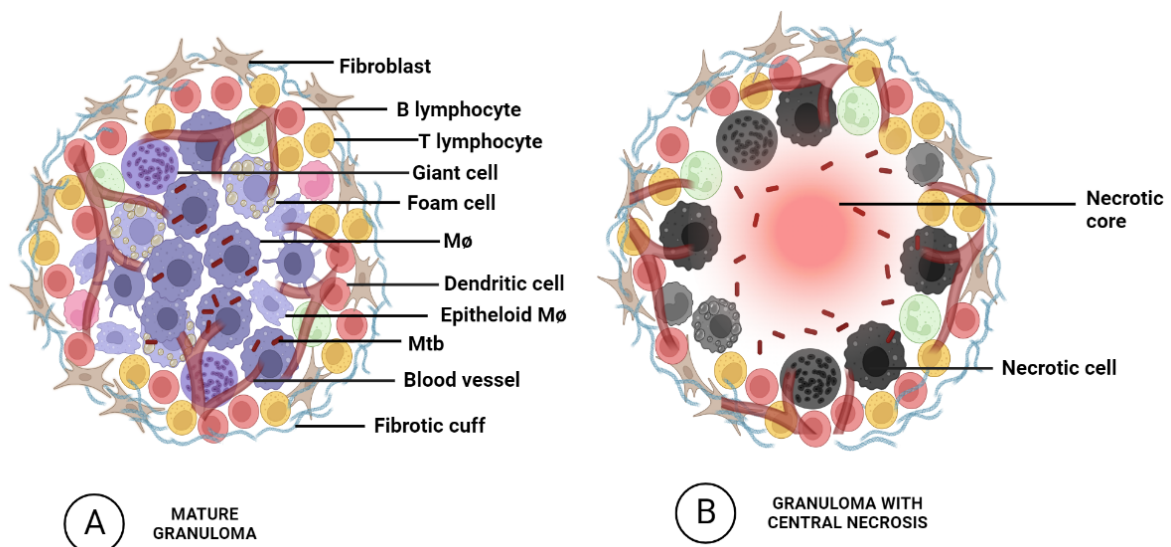


Figure 1.7: Granuloma formation during *Mtb* infection. *Mtb* infects a $\text{M}\phi$ s. This is followed by an influx of innate immune cells, such as PMNs, DCs, and NK cells, to the site of infection, leading to granuloma formation (A). Granuloma $\text{M}\phi$ s differentiate into giant cells and foamy $\text{M}\phi$ s. Surrounded by B- and T-lymphocytes and a fibrous cuff, the granuloma restricts *Mtb* dissemination (B). Created with BioRender.com

1.2.4 Treatment and vaccine

The standard anti-TB treatment regimen for drug-susceptible TB consists of a 2-month daily treatment with four first-line anti-TB drugs; rifampicin (RIF), isoniazid (INH), ethambutol (EMB), and pyrazinamide (PZA), followed by 4–7-month daily treatment with RIF and INH [63]. In the case of multi-drug resistant TB, treatment mostly requires prolongation for up to a year or even longer. Patient non-compliance with treatment regimens due to prolonged duration of drug therapy and drug-associated adverse effects are common causes of drug resistance in TB. Resistances against one of the first-line anti-TB drugs (drug-resistant TB),

or at least RIF and INH (multi-drug resistant TB, MDR-TB), or RIF and INH, fluoroquinolones (such as levofloxacin or moxifloxacin), and one of the second-line drugs such as capreomycin or kanamycin (extensively drug-resistant TB, XDR-TB) have become a menacing public health concern. In 2020, there were 500 000 reported new cases of RIF-resistant TB (RR-TB), of which 78% were attributable to MDR-TB. Shockingly, only one in three people with drug-resistant TB had access to treatment in 2020[63]. Therefore, there is a crucial need to shorten the duration of TB treatment, alleviate the associated side effects of anti-TB drugs to increase patient compliance during treatment and, most importantly, investigate supporting treatment methods such as host-directed therapies (HDT). HDTs are an emerging TB therapeutic strategy in which certain host immune response functions are modulated by interfering with host cell components or host metabolic pathways required by the pathogen for replication or survival [74]. Mtb requires iron for growth and survival and competes with the host for this micronutrient by utilizing several mechanisms to obtain host iron. One of such mechanisms includes the production of mycobactins, i.e. iron-chelating molecules, to scavenge iron from the host [75]. Therefore, targeting iron metabolism by interfering with Mtb iron acquisition mechanisms can be exploited as an HDT. Arnold et al. [72] identified IrtAB, an ATP-binding cassette transporter that imports and modifies mycobacterial siderophores, as a potential drug target against Mtb infection [72]. Also, targeting iron metabolism through iron chelation can be exploited as an HDT. Studies have shown that iron chelation directly inhibits the growth of Mtb and several mycobacterial spp. both *in vitro* and *in vivo* [76].

Furthermore, the combined administration of anti-TB drugs, HDTs, and iron chelators could potentially improve TB disease outcomes. For instance, retinoic acid, a vitamin A metabolite, significantly downregulates the transferrin receptors' expression on MØs limiting iron availability to Mtb [77]. Accordingly, Coleman et al. [78] reported that bone marrow-derived macrophages (BMMØs) and human MØs were less permissive to Mtb following treatment with retinoic acid [78]. Finally, targeting iron regulatory systems such as the hepcidin-ferroportin axis and IRE/IRP system to alter intra-and-extracellular iron concentration could also be exploited as promising HDT in TB.

Ultimately, HDT is essential because there is still no effective TB vaccine. The Bacille Calmette-Guérin (BCG) vaccine is currently the only available authorized vaccine against TB. The BCG vaccine is an attenuated strain of *M. bovis*, the agent of cattle TB. Although the BCG vaccine is protective against TB meningitis and disseminated TB in young children, it is ineffective in preventing pulmonary TB in adults [63]. Currently, several TB vaccine candidates are in clinical trials. However, developing new TB vaccines to improve BCG to achieve enhanced infection control or replace BCG is challenging as the antigen-specific T-cell responses relevant for inducing sufficient protective and sterile immunity against TB have still not been entirely determined.

1.2.5 Host response to Mtb and nutritional immunity

Developing a functional innate immune system that synergizes with the adaptive immune system is vital for the control and clearance of Mtb. Initiation of host innate defenses against Mtb starts with recognizing different mycobacterial ligands termed pathogen-associated molecular patterns (PAMPs) [79]. Pattern recognition receptors identify PAMPs (PRRs) predominantly expressed by immune cells such as MØs and DCs [80]. PRRs such as NOD-like receptors (NLRs) and C-type lectin receptors (CLRs), including mannose receptors, Mincle, and Dectin-1 have been implicated in PRR signalling pathways activating MØs and other myeloid cells such as DCs [81]. Toll-like receptor (TLR) 2 and TLR9 members of the PRR family also recognize mycobacterial lipopeptide-containing antigens and CpG motifs, respectively [82].

TLR2 signalling is inhibited by the early secreted antigenic target of 6kDa (ESAT-6), an abundantly secreted protein and critical virulence factor of Mtb. Engaging TLR2 and TLR9 leads to myeloid differentiation primary response gene 88 (MyD88)-mediated activation of NF- κ B, which stimulates the production of various cytokines and chemokines such as IL-18, CXCL1, CXCL2 needed to promote protective immunity against Mtb [83]. DCs also produce IL-12 and IL-18 which are important cytokines that determine the direction toward a Th1 response during immune activation. The production of these cytokines and chemokines leads to the recruitment of distinct immune cell populations to the site of infection in the lung. These chemokines (for example, CCL2, also known as monocyte chemoattractant protein-1 (MCP-1)) bind to G-protein-coupled receptors (GPCRs) and modulate the recruitment of leukocytes and monocytes, which migrate into the lung tissue in response to Mtb infection. TNF α also controls the expression of chemokine receptors and chemokines, such as CCL3 also known as macrophage inflammatory protein ((MIP)1- α), CCL4/MIP1- β , CCL2/MCP-1 and CCL5/RANTES, which are involved in the recruitment of immune cells from the blood to the site of the local infection in the lungs. TNF α and IFN γ promote monocyte differentiation into M ϕ s. Depending on their localization, M ϕ s can exhibit different phenotypes in response to priming. This M ϕ subset polarization can determine the outcome of the host response by either adopting the classical (M1) or the non-classical (alternative, M2) activation pathway. The development of a functional Th1 antigen-specific T-cell response leads to classical M1 activation of M ϕ s, resulting in a pro-inflammatory response involving the secretion of various cytokines. This changes the cell morphology and the secretory profile of M ϕ s, leading to the production of pro-inflammatory cytokines such as IL-1 β , IL-6, IL-12, IL-18, and TNF α [84].

Iron modulates M ϕ -mediated inflammatory responses during pathogenic infections. Most bacteria, be they commensal or pathogenic, require 10^{-8} - 10^{-6} M iron for optimal growth. As a defense strategy, the host limits free non-bound iron concentrations down to $< 10^{-9}$ M to 10^{-18} M to invading pathogens in a process called "nutritional immunity" [85]. An example is a host-mediated restriction of iron by SLC11A1, formerly referred to as NRAMP1. SLC11A1 impedes iron transport to the phagosome and pumps iron out of late phagosomes, thereby reducing the availability of the metal in the phagosome for mycobacteria. Several polymorphisms in *SLC11A1* gene in humans have been identified to increase susceptibility to TB [86, 87]. In murine M ϕ s, SLC11A1 mediates M ϕ resistance to intracellular pathogens, including *Leishmania donovani*, *S. enterica* subspecies (subsp.) serovar Typhimurium (hereon referred to as *S. Typhimurium*), as well as *M. avium*, and *M. bovis* (BCG) but not Mtb. This is achieved by limiting iron availability to these invading pathogens and eventually controlling intracellular microbial replication in M ϕ s.

Mtb, similar to many pathogenic bacteria has developed strategies to scavenge host iron sources for survival. These strategies include endocytic uptake of TF-bound iron, binding iron-loaded TF, uptake of cytoplasmic or heme-bound iron, or production of small organic molecules with high-iron binding affinity called siderophores such as mycobactin and carboxymycobactin, which can bind and recycle iron [88].

Another host strategy to prevent Mtb iron acquisition is through IFN γ -mediated M ϕ s activation which inhibits transcriptional expression of TfR, thereby diminishing uptake of TF-bound iron and its availability in the endosomes. IFN γ also promotes IRE/IRP binding and regulates the posttranscriptional expression of ferritin. TNF α stimulates the synthesis of ferritin and lactoferrin, which makes iron less inaccessible for intracellular as well as extracellular bacteria to scavenge iron, respectively [89]. In addition, IFN γ induces lipocalin-2 (LCN2) expression in M ϕ s, which is transferred into the phagolysosome. LCN2 can bind and inactivate mycobactin and carboxymycobactin [90, 91], thereby interfering with mycobacterial iron acquisition

system. MØs activated by IFN γ and TNF α also produce RNIs such as toxic NO generated by NOS2, which intoxicate intracellular Mtb [88]. Following NO production, MØs promote the upregulation of *Fpn* mRNA transcripts through the Nrf2 signalling pathway [92]. Mtb can bypass these host iron-withholding strategies through the direct modulation of FPN expression by inducing hepcidin expression. This eventually leads to increased intracellular iron, thereby enabling mycobacterial replication within aMØs [93].

A few studies suggest that pulmonary TB may be connected to changes in the resident microbial populations in the lung known as the lung microbiota [94, 95]. It has also been speculated that pulmonary TB may be ensuing a shift in microbial dynamics and homeostasis in the lung, which ultimately affects the gut microbial communities or vice versa. It has been suggested that this shift in the pulmonary microbial lung profile may affect the composition of these communities in the gut which rely on the availability of host nutrients such as iron [94].

1.3 The Microbiota

The human body is home to many microbes, including bacteria, fungi, protozoa, and archaea, together defined as the microbiota [96]. These microbes inhabit specific ecological niches and colonize biological surfaces including the skin and the epithelia of the oral-nasal cavity, lower respiratory tract (LRT), upper respiratory tract (URT), gastrointestinal tract (GIT), vagina and uterus [97, 98, 99, 100, 101].

1.3.1 The intestinal microbiota

With over 1000 distinct bacterial species [102], the microbial populations in the GIT expand from the stomach to the colon. Microbial colonization of the GIT in healthy humans begins at birth and is mainly influenced by the mode of delivery and feeding during infancy [99]. In the healthy human adult GIT, members of the phyla *Bacteroidetes* and *Firmicutes* are the most commonly identified ones based on their relative abundance. Other phyla present are *Proteobacteria*, *Actinobacteria*, *Verrucomicrobia*, *Fusobacteria* and *Cyanobacteria* [103, 104]. The gut microbiota (GM) functions in the biosynthesis of essential vitamins such as vitamin K, some B vitamins, and amino acids, which are critical for bacterial metabolism [105]. GM plays a vital role in the microbial fermentation of non-digestible substrates such as dietary fibers, complex carbohydrates, and host glycans into biologically active microbial metabolites. The primary metabolites (known as short-chain fatty acids (SCFAs)) include butyrate, acetate, and propionate and account for approximately 90-95% of the SCFAs in the colon [106]. SCFAs are mediators between the GM and immune system by activating “metabolite sensing” receptors GPCRs, including GPCR43, GPCR41, GPCR109A/HCAR2, and GPCR164, expressed on many cells. The GM also plays a role in the development and training of the immune system [107] and in modifying the nervous system [108]. Furthermore, the GM prevents bacterial overgrowth and provides colonization resistance by preventing the attachment of extracellular pathogenic bacteria to the wall of the GIT and inducing the production of host IgA. [109].

Diet, lifestyle, age, non-antibiotic drugs, host genome, infections, sanitary, environmental, and stress-related conditions can alter the homeostasis of the GM in a process termed “dysbiosis”. Several studies have shown that alterations in host iron homeostasis can also lead to gut dysbiosis. For example, most iron supplementation studies in humans have shown that orally administered iron leads to an increase in the abundance of *Escherichia* (*E.*) spps., *Shigella* spps., *Clostridium* spp., and pathogenic *E. coli* [110]. Additionally, increased enterobacteria/bifidobacterial ratio [111], lower abundance of *Bifidobacterium* accompanied by

increased gut inflammation [111], and increased incidence of diarrhea [112], hospitalizations and even mortality [113] have also been observed in the GM upon iron supplementation in human microbiome studies.

Alterations in the GM have been implicated in the development of diarrhea infections, and gut infections such as *Clostridiodes (C.) difficile*, *S. enterica*, and bowel disorders such as irritable bowel syndrome. GM dysbiosis has also been reported to be involved in type II diabetes, inflammatory bowel disease, and stress-related conditions, including depression and anxiety and neurological disorders such as autism [114, 115].

Interventions manipulating the GM composition have been successful in the treatment of certain GIT diseases in humans. For example, fecal microbiota transplantation (FMT), the administration of fecal matter from a healthy donor into the recipient's intestinal tract, has proven effective and safe in over 90% of *C. difficile* patients suffering from dysbiotic diarrhoea [116]. However, the mechanisms underlying the associated therapeutic effects of FMT have not been completely elucidated. An experimental strategy to manipulate the gut microbiota in mice is cohousing. Cohousing is used to investigate the influence of the GM on a phenotype of interest through microbiota transfer from "affected" or colonized animals (GM donors) to "unaffected" or germ-free animals (GM recipients or acceptors) [117, 118, 119, 120, 121]. The cohousing approach is based on the hypothesis that through the inter-grooming and coprophagic behaviour of murine cagemates, the element of the GM responsible for the phenotype of donor animals will be transferred to recipient animals. Therefore, cohousing experiments are an essential way to unravel the GM's influence on a phenotype that confers susceptibility or resistance to a particular disease.

Several studies show that GM influences lung immunity [122]. For instance, higher gut microbial diversity in childhood is protective against allergic asthma. Also, asthma, respiratory allergies and lung infections such as influenza virus, *Streptococcus pneumoniae* and *Klebsiella (K.). pneumoniae* [123, 124, 125] have been associated with gut dysbiosis. Conversely, the lung microbiota (LM) also affects the GM [126]. This bidirectional immunological link between gut and lung, also called the gut-lung axis [127], enables the transport of endotoxins, cytokines, hormones, soluble microbial components, and microbial metabolites into the bloodstream, thus connecting both niches.

1.3.2 The respiratory tract microbiota

Recent employment of culture-independent techniques to detect low abundant microbes has shown that the lungs harbour their own microbiomes in the healthy and diseased state [128, 129]. Dickson et al. [130] proposed that in health, the LM composition depends on immigration and the elimination of microbial community members [130]. Dickson et al. [130] interpreted this proposal that, at the steady-state, the rate of microbial immigration through microaspiration and inhalation of air equals the rate of microbial elimination through coughing, mucociliary clearance, and innate and adaptive immune defenses.

Numerous challenges are encountered in the investigation of the LM. These include low microbial biomass, nucleic acid extraction techniques, and sample type used (i.e. sputum, bronchoalveolar lavage (BAL) or tissue). In addition, contamination from multiple sources, such as contaminant DNA from the URT during sample collection and processing or from laboratory settings, "sterile" reagents and DNA/RNA isolation kits also account for challenges in LM studies. Cross-contamination from other samples and barcode cross-contamination during library preparation and sequencing runs are problems encountered in LM studies [131]. The healthy LM has a low density of microbial populations at $10^3 - 10^5$ CFU/g of lung tissue [132] and contains approx. 2.2×10^3 bacterial genomes per cm^2 . These populations mainly

consist of members of the phyla *Bacteroidetes*, *Firmicutes* and *Proteobacteria*, followed by *Actinobacteria* and *Fusobacteria* [133]. Several studies have shown that the LM composition significantly differs between the URT and the LRT in healthy individuals. Interestingly, the LRT microbiome in healthy individuals shares similarities to the oropharyngeal microbiota and is dominated by populations of the phyla *Firmicutes*, *Bacteroidetes* and *Proteobacteria* [134]. A few studies, though inconsistent in their findings, have shown that the microbiome might influence susceptibility to Mtb infection and even have a role in TB pathogenesis (i.e. progression from LTBI to active TB), treatment and outcome [94, 135]. Although these studies suggest that TB causes changes in microbiota communities, this connection remains elusive, whether directly through a local lung microbiota or indirectly through the gut-lung axis. Furthermore, it is still unclear if alterations in host iron metabolism first and foremost exert influence on the microbiota, eventually promoting TB susceptibility or driving pathogenesis or if Mtb infection alters the microbiota, which ultimately changes iron availability. Therefore, research must be carried out to comprehend the pathways and mechanisms that alter host iron metabolism and the homeostasis of the gut and lung microbiota in response to Mtb. Targeting alterations in host iron metabolism in the framework of gut and lung microbiota dysbiosis could be exploited as an HDT in TB and potentially improve the quality of treatment of TB patients globally.

1.4 Statement of intent and objectives

Many studies have identified the importance of iron availability for the pathogenesis of Mtb infection. Nevertheless, there are several knowledge gaps on the effects of alterations in iron metabolism on the susceptibility to mycobacterial infections. IRP1 and IRP2 have only been studied in the infection model of *S. Typhimurium*, a facultative intracellular pathogen which equally depends on host-derived iron sources as Mtb [136]. However, there are no studies yet on the role of these crucial regulators in response to Mtb infection. Therefore, the effects of IRP1 and IRP2 or dietary-mediated changes in iron availability on the outcome of experimental Mtb infection and homeostasis of the gut microbiota were investigated. The objectives of this study were to:

1. Examine the influence of the presence and absence of IRP1 and IRP2 on host iron status and host responses during experimental Mtb Infection *in vitro* and *in vivo*
2. Analyse the effects of changes in dietary iron metabolism on host responses and experimental Mtb infection outcome
3. Study whether iron status mediated differences in microbiota composition are linked to altered host responses

Materials

2.1 Chemicals and Reagents

Table 2.1: Chemicals and reagents used in this study

Chemical/Reagent	Supplier	Order-Nr.
Acetic acid	Carl Roth	3738.5
Albumin bovine Fraktion V, Protease-free	Serva	9048-46-8
Aqua destilata (Aq. dest.)	B. Braun	0082479E
Bovine serum	Biowest	S0250-500
BBL Middlebrook OADC Enrichment	BD Biosciences	21186
Carbol-fuchsin	Carl Roth	A130.1
Citric acid anhydrous	Sigma-Aldrich	C2404-100G
Chloroform	MP Biomedicals, LLC	MFCD00000826
cOmplete EDTA-free Protease Inhibitor	Roche	11873580001
Deferoxamine mesylate	Sigma-Aldrich	D9533
Difco Asparagine	BD Biosciences	214410
Difco Middlebrook 7H9 medium	BD Biosciences	262710
Difco 7H11 Agar	BD Biosciences	212203
Dimethyl sulfoxide (DMSO)	Carl Roth	D2650
DMEM (High D-Glucose, with sodium pyruvate, w/o L-glutamine)	PAN Biotech	P04-03600
DNase/RNase-free water	Gibco	10977-035
Donor horse serum	PAN Biotech	P30-0702
DPBS	PAN Biotech	P04-36500
Entellan	Merck KGaA	1.07961.0500
Eosin	Carl Roth	7089.2
Ethanol absolute for molecular biology	AppliChem	A3678,0500
Ethylenediaminetetraacetic acid (EDTA)	AppliChem	A2937,0500
Fetal calf serum (FCS)	PAN Biotech	P30-3306
Ferric Ammonium Citrate	Sigma-Aldrich	RES20400-A702X
Glycerol	Sigma-Aldrich	G5516
Goat serum	PAN Biotech	P30-1001

2. MATERIALS

Guanidine thiocyanate	Ambion	AM9422
Mayer's Haematoxylin	Carl Roth	T865.2
HEPES buffer solution	PAN Biotech	P05-01100
Hydrochloric acid (37 %)	Merck KGaA	1.00317.2500
Immersion oil for microscopy	Carl Roth	X8991
Iso-Pentane	VWR Chemicals	24872.298
Isopropanol	AppliChem	A3928
Kaiser's glycerol gelatin	VWR Chemicals	1.09242.0100
Ketamin	WDT	16D 257
L-Glutamin (200mM)	PAN Biotech	P04-80100
Liberase TL	Roche	05401020001
Loeffler's methylene blue solution	Carl Roth	AE64.3
MagSi-NGS Prep Plus	Magna Medics	MDKT00010075
Milli-Q water	In-house	N/A
N-(-1-Naphthyl) ethylene diamine dihydrochloride	Sigma-Aldrich	N9125-10G
Neutral red	PAN Biotech	MOLEM27400744
Oil Red O stain	Sigma-Aldrich	O0625
Ortho-phosphoric acid 85 %	Merck KGaA	100573.1000
Paraplast embedding agent for histology	McCorkick Scientific	502004
Parafilm M All-purpose laboratory film	Bemis	PM996
Paraformaldehyde (PFA)	Carl Roth	0335.3
Potassium hexacyanoferrate (II) Trihydrate	Merck KGaA	1.04984.0100
Recombinant murine IFN-gamma	PeproTech	315-05
RPMI 1640 w/o L-Glutamin	PAN Biotech	P04-17500
Saccharose	Carl Roth	9286.1
Sodium azide	Merck KGaA	8.22335.0100
Sodium citrate	Sigma-Aldrich	54641
Sodium hydroxide	Carl Roth	9356.1
Sulfanilamide	Sigma-Aldrich	S9251-100G
Tissue freezing medium	Leica	14020108926
Tween 20/-80	Sigma-Aldrich	P9416/- P8074
Triethyl Phosphate	Sigma-Aldrich	538728
TRI Reagent	Zymo Research	R2050-1-200
Triton X-100	Carl Roth	3052.3
Trizma base	Sigma-Aldrich	T6066
Trypan Blue	Carl Roth	CN76.1
Xylene	VWR Chemicals	28975.360
Xylazin	cp Pharma	16D 257

2.2 Consumables

Table 2.2: Consumables used in this study

Item	Supplier	Order-Nr.
25/10/5 mL serological pipettes	Corning Costar Stripette	-4489/-4488/-4487
1000/200 μ L Biosphere filter tips	Sarstedt AG & Co. KG	70.762.211/- .1130.210
20 μ L ART barrier tips	Thermo Scientific	2149P-HR
20/10/5 mL syringes	BD Discardit II	300296/309110/ 309050
0,1 mm Neubauer-counting chamber	Marienfeld GmbH&C0.KG	06 400 10
50/1 mL syringes	BD Plastipak	300865/303172
26G 3/8", 23G 1" cannulas	BD Bioscience	300300/ 300800
Serum separator 1,1 mL Z-Gel tubes	Sarstedt AG & Co. KG	41.1500.005F
Microvette 500 K3E	Sarstedt AG & Co. KG	20.1341
ZR Bashing Beads Lysis Tubes	Zymo Research	S6012.50
50 /15 mL tubes	Sarstedt AG & Co. KG	62.547.254/ 62.554.502
2/1/0,5 mL micro tubes	Sarstedt AG & Co. KG	73.694.006/- 692.005/-730.006
DNase/RNase free tubes	Sarstedt AG & Co. KG	72.706.200
TC Flask T25, Standard	Sarstedt AG & Co. KG	83.3910
Spin-X 0,22 μ m centrifuge tube filter	Costar	8160
0,20 μ m syringe pre-filter	BD Bioscience	83.1826.102
Stericup 500 mL Millipore Express PLUS 0.22 μ m PES	EMDMillipore Corporation	SCGPU05RE
70/100 μ m cell strainer	BD Bioscience	431751
96 round/96/ 48/24/ 12/ 6 flat well cell culture plates	Corning Costar	3596/3799/3548/ 3526/3513/3516
96-well 0.2 mL skirtless PCR plate/ Microseal film "A" adhesive seals	Bio-Rad	MLL9601/ MSA5001
Black flat bottom 96 well assay plate	Costar	3915
92 x 16 mm Petri dishes	Sarstedt AG &Co. KG	82.1472
Light Cyler 480 (LC480) multiwell plate 96, white/ LC480 sealing foil	Roche	04 729 692 001/04 729 757 001
92 x 16 mm Petri dishes	Sarstedt AG &Co. KG	82.1472
26 x 76 mm frosted microscope slides	R. Langenbrinck GmbH	03-0003
10 mm \varnothing microscope cover glasses	VWR Chemicals	ECN 631-1576
DynaMag-96 side skirted magnet	Thermo Scientific	12027
Parafilm	Bemis	PM 996
16 mm Cell Scraper	Sarstedt AG &Co. KG	83.1832
Embedding cassettes for histology	Carl Roth	K113.1
10 x 4 x 5 mm polystyrene cuvettes	Sarstedt AG &Co.	67.742
185 x 75 mm Whirl Pak plastic bags	Neo Lab- Whirl-Pak	1-7139
Vasofix Safety-Shielded IV catheter with injection port	B. Braun	00198137

2.3 Buffers, Solutions and Media

Table 2.3: Buffers, solutions and media used in this study

Buffer/Solution/Medium	Composition
Back Extraction buffer	4 mM Guanidine thiocyanate 50 mM Sodium citrate 1 mM Trizma base in PBS sterile filtered (0,20 μm syringe pre-filter)
Citrate buffer	10 mM citric acid anhydrous 0,05% (v/v) Tween 20 in Milli-Q water pH adjusted to 6.0 with 10 mM NaOH
Lung lysis buffer	0,05% (v/v) Tween 20 1 Protease inhibitor tablet in PBS sterile filtered (0,20 μm syringe pre-filter)
Spleen lysis buffer	0,1% (v/v) Tween 20 1 Protease inhibitor tablet in PBS sterile filtered (0,20 μm syringe pre-filter)
WTA buffer	1% (w/v) BSA 0,5% (v/v) Tween 80 in Aq. dest. sterile filtered (0,22 μm PES Sterricup)
4% PFA	4% (w/v) Paraformaldehyde (PFA) in PBS
DMEM- Full Medium	10% (v/v) h.i. FCS 1% (v/v) L929 cell supernatants 1% (v/v) HEPES-buffer solution in DMEM
Bone marrow-derived MØ medium	10% (v/v) h.i. FCS 5% (v/v) h.i. horse serum 20% (v/v) L929 cell supernatants 1% (v/v) HEPES-buffer solution 1% (v/v) L-Glutamine in DMEM sterile filtered (0,22 μm PES Sterricup)
7H11 Agar medium	1,9% (w/v) 7H11 Agar 0,5% (v/v) 7H11 Glycerine 0,1% (w/v) L-Asparagine in 900 mL Milli Q water
7H9 medium	0,05% (v/v) Tween 80 0,47% (w/v) 7H9 Agar in 1000 mL Milli Q water 10% (v/v) OADC medium prior to use

2.4 Kits

Table 2.4: Kits used in this study

Kit	Supplier	Order-Nr.
Avidin/Biotin Blocking Kit/ VECTASTAIN ABC HRP kit	Vector Laboratories, Inc	SP-2001/ PK-6100
DAB Peroxidase Substrate Kit	Vector Laboratories, Inc	SK-4100
Direct-zol RNA MiniPrep Plus	Zymo Research	R2072
Iron Assay Kit	Sigma-Aldrich	MAK025
Light Cycler 480 SYBR Green I Master	Roche	04 887 352 001
Linear Acylamide (1 mL, 5 mg/mL)	Invitrogen	AM9520
Maxima First Strand cDNA Synthesis Kit for quantitative w/ dsDNase	Thermo Scientific	K1672
Miseq Reagent Kit V3 (600 cycles)	Illumina	MS-102-3003
Mouse Ferritin-Light chain ELISA Kit	Abcam	Ab157713
Nextera XT index Kit v2 Set B	Illumina	15052164
Nextera XT index Kit V2 Set C	Illumina	15052165
OneStep PCR Inhibitor Removal Kit	Zymo Research	D6030
Pierce BCA Protein Assay Kit	Thermo Scientific	TG265238
PhiX Sequencing Control V3	Illumina	15017666
Phusion Hot start High-Fidelity (HiFi) DNA Polymerase	Thermo Scientific	F-549L
Red Taq DNA polymerase Master Mix	VWR Chemicals	5200300-1250
Total Iron Binding Capacity Kit	Abcam	Ab239715
Total Nitric Oxide Assay Kit	Cayman Chemical	780001
Quant-iT PicoGreen dsDNA Assay Kit	Thermo Fisher Scientific	P7589
U-plex Biomarker Group I (mouse) Multiplex Assay	Meso Scale Discovery	K15069L-2

2.5 Antibodies

Table 2.5: Antibodies used in this study for Immunohistochemistry

Antigen	Host species	Species	Dilution	Fluorophore	Supplier	Order-Nr.
NOS2	Rabbit	Mouse	1:200	N/A	Merck KGaA	ABN26
CD68	Rabbit	Mouse	1:250	N/A	Abcam	ab125212
IgG	Rat	Goat	1:500	Biotinylated	Jackson Immuno Research	111-066-047

2.6 Primers

Table 2.6: Primers used for Amplicon PCR

Primer	Sequence (5'→3')
Illumina-16S 357F	TCG-TCG-GCA-GCG-TCA-GAT-GTG-TAT-AAG-AGA-CAG-CCT-ACG-GGA-CGG-GCA-TGC-AG
Illumina-16S 806R	GTG-CTC-GTG-GGC-TCG-GAG-ATG-TGT-ATA-AGA-GAC-AGG-GAC-TAC-ATC-GAC-GGG-TAT-TCT-AAT

F and R indicate forward and reverse primer sequences, respectively

Table 2.7: qRT-PCR murine primer sequences used in this study

Transcript	Forward sequence (5'→3')	Reverse sequence (5'→3')
<i>Dmt1</i>	CTA-TCG-CCA-TCA-TCC-CCA-CC	GCA-ATC-CTC-CAG-CCT-ATT-CCA
<i>Fpn1</i>	CTC-CAA-CCC-GCT-CCC-ATA-AG	AGC-CTT-ATG-CCG-AAA-GAC-CC
<i>Frt-L</i>	CAC-CTA-CCT-CTC-TCT-GGG-CT	ACA-TCC-TGG-AAG-AGT-GCA-CG
<i>Hamp1</i>	GCC-ACC-ACA-CAA-GTC-CTT-AGA	TCT-CTT-CTG-CAT-TGG-TAT-CGC-A
<i>Hprt</i>	TCC-TCC-TCA-GAC-CGC-TTT-T	CAT-AAC-CTG-GTT-CAT-CAT-CGC
<i>Ifng</i>	TCA-AGT-GGC-ATA-GAT-GTG-GAA-GAA	TGG-CTC-TGC-AGG-ATT-TTC-ATG
<i>Il-6</i>	GAG-GAT-ACC-ACT-CCC-AAC-AGA-CC	AAG-TGC-ATC-ATC-GTT-GTT-CAT-ACA
<i>Irp1</i>	TGA-AGG-CGA-GTC-CAT-CCT-A	CGT-TCA-CTC-CCA-AAG-GCT-CT
<i>Irp2</i>	CTG-CAT-CCC-AGC-CTA-TTG-AAA-A	GCA-CTG-CTC-CTA-GCA-ATG-CTT-C
<i>Lcn2</i>	CCA-TCT-ATG-AGC-TAC-AAG-AGA-ACA-AT	TCT-GAT-CCA-GTA-GCG-ACA-GC
<i>Nos2</i>	CTG-CAG-CAC-TTG-GAT-CAG-GA	TCC-TTT-GAG-CCC-TTT-GTG-CT
<i>Tnfa</i>	CCA-CCA-CGC-TCT-TCT-GTC-TAC	AGG-GTC-TGG-GCC-ATA-GAA-CT
<i>Tfr1</i>	AGT-AGG-AGC-CCA-GAG-AGA-CG	GGT-ATC-CCT-CCA-ACC-ACT-CAG

2.7 Equipment

Table 2.8: Equipment used in this study

Equipment	Manufacturer
MSC-Advantage™ Class II Biological Safety Cabinet	Thermo Scientific
UVFS-AR DNA/RNA UV cleaner box	Biosan
099C A4224 Inhalation exposure system	Glas-Col, LLC
Hera cell 240 incubator	Thermo Scientific
Type KC-1 special biosafety cabinet	Kojair Tech Oy, Mänttä-Vilppula, FI
Heraeus Multifugue 3SR+	Thermo Scientific
LightCycler®480 Instrument II	Roche
BX41 Light Microscope	Olympus
LEICA EG 1140 C Paraffin dough station	Leica
Tissue float bath 1052	GFL
STP-120 Spin Tissue Processor Microm	Thermo Scientific
RM 2155 Rotary Microtome	Leica
Precision balance AY303 Sartorius	Sartorius AG
QTUM000EX Quantum EX Polishing Cartridge for Mill-Q system	Merck Chemicals GmbH
MiSeq next-generation sequencer	Illumina
Infinite® M200PRO NanoQuant	Tecan
FastPrep-24	MP Biomedicals, LLC
R2100 Antigen Retriever device	ProteoGenix, Schilitigheim
Meso QuickPlex SQ 120 instrument	Meso Scale Discovery
BioTek Synergy Multi-Mode Microplate Reader	Bio Tek Instruments
VetScan HM5	SCIL animal care company GmbH
Thermocycler	SensoQuest

2.8 Software

Table 2.9: Software used in this study

Software	Developer
Anaconda3 2021.05	Anaconda, Inc. (Austin, U.S.A)
BioRender 2022*	BioRender (Toronto, Canada)
GraphPad Prism version (v) 9.4.1.681.	GraphPad Software, Inc. (La Jolla, U.S.A)
Illumina Sequencing Analysis Viewer v2.1.8	Illumina (San Diego, U.S.A)
Illumina Experiment Manager v1.18.0	Illumina (San Diego, U.S.A)
LightCycler 480 v1.5.1.62	Roche (Mannheim, DE)
Magellan v7	Tecan Group Ltd (Männedorf, CH)
Mendeley Desktop v 1.19.8	Elsevier (London, UK)
i-Control microplate reader software	Tecan Group Ltd (Männedorf, CH)
pyRAT System v4.2-323	Scionics Computer Innovation GmbH (Dresden, DE)

cellSens Imaging software v3.3	Olympus Corporation (Tokyo, Japan (JP))
Discovery Workbench v4.0	Meso Scale Discovery (Rockville, U.S.A)
VetScan HM5-C software v2.2	Abaxis (Griesheim, DE)
R studio v.1.1.1.383	R Studio, PBC (Boston, U.S.A)

*Except Fig. 1.6, all figures in this study were created with biorender.com

2.9 Bacterial Strains

Table 2.10: Bacterial strains used in this study

Strain	Genotype	Source
<i>M. tuberculosis</i> H37Rv	Wild type	Albert Einstein College of Medicine, New York, USA (Prof. Dr. W.R. Jacobs)

2.10 Mice

Female mice homozygous for either iron regulatory protein 1 (*Irp1*^{-/-}) or 2 (*Irp2*^{-/-}) genes were generated as described in [137, 138, 139] and provided by Prof. Dr. Esther Meyron at the Technion - Israel Institute of Technology, Israel. Upon arrival at the Research Centre Borstel (RCB), these mice were mated with wild type (wt) C57BL/6J male mice to expand the breeding stock. From these matings, *Irp1*^{-/-}, *Irp2*^{-/-} and *Irp2*^{+/-} were generated and used in this study. Unless otherwise stated, 8-20-week-old female wt, *Irp1*^{-/-}, *Irp2*^{-/-} and *Irp2*^{+/-} mice were used for both *in vitro* and *in vivo* studies. 3-week-old female C57BL/6J mice purchased from Charles River (Suelzfeld, DE) were also used in this study. Pregnant Germ-free (GF) wt mice used in this study were a kind gift from Prof. Dr. Ulrich Steinhoff at the Philipps-University of Marburg, DE.

Table 2.11: Mice used in this study

Strain	Genotype	Health Status	Breeder	Reference
C57Bl/6J	wt	SPF	Animal facility, RCB	N/A
C57Bl/6J	<i>Irp1</i> ^{-/-}	SPF	Animal facility, RCB	[137]
C57Bl/6J	<i>Irp2</i> ^{-/-}	SPF	Animal facility, RCB	[139]
C57Bl/6J	<i>Irp2</i> ^{+/-}	SPF	Animal facility, RCB	N/A
C57Bl/6J	wt	SPF	Charles River, DE	N/A
C57Bl/6J	wt	GF	Philipps University of Marburg, DE	N/A

CHAPTER 3

Methods

3.1 *In vitro* Experiments

3.1.1 Isolation of mouse bone marrow-derived macrophages

Non-infected wt, *Irp1*^{-/-}, *Irp2*^{-/-} were used to generate all MØ types used in this study. Mice were euthanized by CO₂ exposure followed by cervical dislocation. Bone marrow-derived MØs (BMMØs) were isolated and differentiated as described in [140] with slight modifications. Femora and tibiae were isolated, and bone marrow cavities were flushed with a 10 mL BMMØ medium using a 0.5mm x 25 mm 25 G cannula loaded on a 10 mL syringe. The flushed cells were pelleted at 485 rcf for 5 mins at 4°C and resuspended in 1 mL BMMØ medium. Viable cells were counted by trypan blue dye exclusion test on a hemocytometer, adjusted to a concentration of 5 × 10⁶ cells in 10 mL BMMØ medium and plated onto 92 × 16 mm Petri dishes. Bone marrow MØ progenitors were allowed to proliferate and differentiate into mature BMMØs in a humidified chamber with 7.5% CO₂ at 37°C. 4 days after seeding the cells, 5mL BMMØ medium prewarmed at 37°C was added per petri dish and further incubated for another 4 days. On day 8, the culture supernatant (s/n) was collected in 50 mL tubes and stored temporarily on ice. Cells were detached by adding 5 mL ice-cold 1 × DPBS per petri dish before incubation at 4°C for 15 mins. Using a cell scraper, adherent cells were scraped, pooled with the previously collected s/n and centrifuged at 485 rcf for 5 mins at 4°C. Cells were resuspended in 1 mL DMEM-FM supplemented with 20% (v/v) heat-inactivated (h.i.) FCS and adjusted to a concentration 2 × 10⁷ cells/ mL. DMEM-FM supplemented with 20% (v/v) h.i. FCS and 20% (v/v) DMSO were used to cryopreserve freshly harvested BMMØs in a final concentration of 10⁷ cells/ mL. Cells were temporarily stored at -80°C for 24 h and then transferred to a liquid nitrogen tank for long-term storage.

3.1.2 Isolation of mouse peritoneal macrophages

Peritoneal lavages were performed as described in [141] with slight modifications. Using a 10 mL syringe and 0.9 mm x 40 mm 20 G cannula, 10 mL cold 1 × DPBS supplemented with 4% (v/v) h.i. FCS was injected into the peritoneal cavity. The abdominal cavity was gently massaged for approx. 30 s to displace the peritoneal cells. The injected fluid was aspirated from the peritoneum, centrifuged at 485 rcf for 5 mins at 4°C and resuspended in 1 mL DMEM-FM.

3.1.3 Isolation of mouse alveolar macrophages

Following euthanization by CO₂ exposure, aMØs were isolated as described in [142] with slight modifications. An incision was made on the animal's thorax, extending to the neck to expose the trachea. Using curved tip forceps, surgical suture thread was passed under the trachea and left untied at both ends. A Vasofix Safety-Shielded IV catheter with an injection port was gently inserted through the tracheal wall into the tracheal lumen. The surgical thread was knotted on the uppermost part of the trachea to secure the catheter in place firmly. The 20 G needle lodged within the catheter was carefully removed, leaving the plastic holder in place. 1 mL syringe prefilled with ice-cold 1 × DPBS supplemented with 0.2% (w/v) EDTA was attached to the catheter, and the buffer solution was infused into the lungs. The thorax was gently massaged for approx. 30 s, the injected fluid was aspirated from the lungs back into the syringe and collected into a sterile 50 mL tube on ice. The lung infusion step was repeated 7 times. Cells were pelleted at 485 rcf for 5 mins at 4°C and resuspended in 1 mL RPMI 1640 medium supplemented with 10% (v/v) h.i. FCS.

3.1.4 Treatment of mouse macrophages

For infection of BMMØs, previously cryopreserved cells were thawed in a water bath at 37°C. Thawed cells were transferred to 15 mL tubes containing 9 mL DMEM-FM, pelleted at 485 rcf for 5 mins at 4°C, and resuspended in 1 mL DMEM-FM. BMMØ and freshly isolated aMØs and peritoneal MØs (pMØs) were counted by trypan blue exclusion test for cell viability on a hemocytometer. Unless otherwise stated, MØs were adjusted to a concentration of 10⁵ cells. Cells were incubated overnight (o/n) in a humidified chamber with 7.5% CO₂ at 37°C prior to any further experiments. Where indicated, cells were stimulated 2 h after seeding with 500 U/mL of recombinant murine IFN- γ or treated with 100 μ M Ferric Ammonium citrate (FAC) and 100 μ M Deferoxamine (DFO). Furthermore, the phagocytosis rate of BMMØs was measured using the Phagocytosis assay kit (Cell Biolabs, San Diego, USA). This was achieved by treating cells with either 500 U/mL of recombinant murine IFN- γ or 10 μ M cytochalasin D before adding prelabelled Zymosan particles (MOI of 3:1) as per the manufacturer's protocol.

3.1.5 Culturing of Mtb for *in vitro* infections

Mtb stocks were grown in Middlebrook 7H9 broth supplemented with 10% (v/v) OADC enrichment medium. Bacterial cells were harvested at the mid-log phase of growth and frozen in 1 mL aliquots at -80°C for future use. For *in vitro* infections, frozen aliquots were thawed and grown in Middlebrook 7H9 broth supplemented 10% (v/v) OADC enrichment medium in a 1:10 dilution. After 3 days in culture, a 1:10 subculture in 7H9 broth supplemented with 10% (v/v) OADC enrichment medium was prepared and incubated in a humidified chamber at 37°C for an additional 4 days. On day 7, the bacterial culture was centrifuged at 3500 rcf for 10 mins at 4°C. The cells were washed with 10 mL 1 × DPBS and centrifuged again at 3500 rcf for 10 mins at 4°C. The resulting pellet was resuspended in 1 mL 1 × DPBS and the bacterial suspension was homogenized several times using a 0.4mm × 23 mm 27 G blunt end cannula loaded onto a 1 mL syringe to separate cell aggregates. The turbidity of the bacterial suspension was determined by measuring the optical density (OD) at 580 nm (OD₅₈₀). To calculate the OD, a 1:10 dilution of the bacterial suspension in 4% (w/v) PFA was made. Based on OD₅₈₀ measured and considering the dilution factor used, the concentration of the

bacteria per mL was calculated using the formula below.

$$\text{Bacteria [} \times 10^8/\text{mL]} = \text{OD}_{580} \times (5 \times 10^8) \times 10$$

3.1.6 Colony-forming unit (CFU) numeration assay

Unless otherwise stated, MØs were adjusted to a concentration of 10^5 cells in 100 μL DMEM-FM and infected with different multiplicity of infection (MOI) values of Mtb at various time points post-infection. Infected MØs were incubated in a humidified chamber with 5% CO_2 at 37°C. Colony-forming unit enumeration assays (CFU) were performed. Cell culture s/n were collected and stored at -80°C for future use. MØs were washed twice with cold 1 x DPBS and treated with 0.5% (v/v) Triton X-100 in PBS to permeabilize cell membranes. 10 μL Triton X-100 treated cells were tenfold serially diluted in 90 μL 0.05% (v/v) Tween 80 in PBS and plated onto 7H11 agar plates supplemented with 10% (v/v) h.i. bovine serum. Plates were incubated in a humidified chamber at 37°C and observed for 21-28 days. The highest countable dilution was chosen for all experimental groups, and the results were shown as CFU per mL.

3.1.7 Measurement of nitrite production

Nitrite production in cell culture s/n was measured using the Griess reaction [143]. 50 μL Griess reagent was added to 50 μL of cell culture s/n per well and incubated in the dark for 30 mins at room temperature (RT). Absorbance was measured at 540 nm using the Synergy 2 Multi-Mode Microplate Reader (Biotek Instruments, Inc., Winooski, USA), and a standard curve (0-100 μM) was established with NaNO_2 .

3.2 *In vivo* Experiments

3.2.1 Ethics statement

Animal handling and experimental protocols reported herein complied with the German Animal Protection Law and were approved by the Ethics Committee for Animal Experiments of the Ministry of Energy, Agriculture, Environment, Nature and Digitalization, State of Schleswig-Holstein, Germany, under licenses V 242- 24752/2018 (78-6/15) and V 241-32204/2018 (82-6/17).

3.2.2 Experimental animals

8-20-week-old female wt, *Irp1*^{-/-}, *Irp2*^{-/-} and *Irp2*^{+/-} mice were bred under specific-pathogen-free (SPF) conditions and maintained under a controlled temperature of 20-24°C, humidity 45-65°C and a constant 12-hour light/dark cycle. For the cohousing study, 20-week-old pregnant germ-free (GF) C57BL/6J mice from the Philipps University of Marburg (Marburg, DE) were transported to the Research Center Borstel (RCB) in the 2nd gestational week at E16 of embryonic development. GF mice were maintained under the same conditions described above. 3-5 mice were housed in type II long, individually ventilated cages (IVC) in the Biosafety level 3 (BSL-3) facility of the RCB. Cages and cage enrichment materials were changed every week. Mice were allowed free access to drinking water and fed a maintenance diet (ssniff Spezialdiäten GmbH, Soest, DE) ad libitum sterilized by 25 kGy/min γ -irradiation.

Drinking water was routinely examined (AGROLAB Agrar und Umwelt GmbH, Kiel, Prüfbericht 1776575-102794) to have an iron concentration of 0.016 mg/L and a pH value of 7.5. For the feeding study, 3-week-old female C57BL/6J cage mates were purchased from Charles River (Sülfeld, DE) and maintained under the conditions described above except for varying diet types. Upon arrival at RCB, C57BL/6J mice were acclimatized to a purified pellet diet of 46 mg/kg Fe (II) fumarate (S0647-E712) for 8 weeks. After that, mice were randomly assigned to three feeding groups. These groups consisted of an iron-rich diet (460 mg/kg Fe (II) fumarate (S0647-E716)), an iron-low diet (< 9 mg/kg Fe (II) fumarate (S0647-E724)) or maintained on the initial diet of 46 mg/kg Fe (II) fumarate for 16 weeks plus the duration of the infection for an additional 16 weeks. All diets were purchased from ssniff Spezialdiäten GmbH (Soest, DE), sterilized by 25 kGy/min gamma-irradiation, vacuum-packed, and stored at 4°C.

3.2.3 Infection of experimental animals with Mtb

Mice were allowed to acclimatize to the BSL-3 facility of the RCB for at least 2 weeks before infection with Mtb H37Rv. Mice were infected via the aerosol route in an inhalation exposure chamber (IEC) (Glas-Col, Terre Haute, USA). Mtb stocks prepared as described in **section 3.1.5** were thawed at RT and briefly vortexed. To achieve uptake of approx. 100 viable bacilli per mouse lung, the bacterial stock was thawed and homogenized several times using a 0.4mm x 23 mm 27 G blunt end cannula loaded onto a 1 mL syringe to separate cell aggregates. 200 µL of the bacterial stock was added to 6 mL Aq. Dest. and briefly vortexed. To measure the inoculum, 500 µL of the bacterial suspension was tenfold serially diluted up to 10⁻⁹ in 4.5 mL of 0.05% (v/v) Tween 80 in Aq. Dest. Dilutions were plated onto 7H11 agar plates supplemented with 10% (v/v) h.i. bovine serum and colonies were counted after incubating plates in a humidified chamber at 37°C for 21-28 days. To proceed with the infection of experimental animals, 5.5 mL of the bacterial suspension was introduced into the nebulizer-venturi unit attached to the IEC. The device was calibrated to include preheating, nebulizing, cloud decay, and decontamination programs which ran for 900 s, 2400 s, 2400 s and 900 s, respectively. Deeper decontamination of the IEC was performed under the exact settings mentioned above with 7% (v/v) optisept in 6 mL Aq. Dest. The in vivo target infectious dose was confirmed by measuring lung CFU in 4 Mtb infected C57BL/6J mice 24 h post-infection (p.i.) by plating homogenized lung tissue onto 7H11 agar plates supplemented with 10% (v/v) h.i. bovine serum.

3.2.4 Health monitoring

Mice were monitored for disease severity based on general behaviour, activity, appearance, and variations in weight as per an adapted protocol proposed by Morton and Griffiths [144] (**Table 3.1**). Based on an in-house identification system, 2 mm notches were made in mice ears. Animals reaching a score of 2 were monitored 2-3 times per week or daily for a score of 3. Animals with severe symptoms, getting a clinical score of 3.5 or more, were withdrawn from the experiment and sacrificed.

Table 3.1: Scoring scheme for experimental animals. Adapted from [144]

Score	Activity and stress levels	Body weight	General condition	Behaviour
1	Highly active, no stress	Unaffected or increase in body weight	Smooth, sleek, and shiny fur, kempt, shiny eyes	Alert, close physical interaction with cagemates
2	Active, mild stress	Slight weight change (<10%)	Change in posture, nasal discharge, reduced or excessive grooming	A slight deviation from the above-described behaviour
3	Less active, moderate stress	Reduced weight loss (<10 - 20%)	Dull fur, increased muscle tone, body cuts	Inactive or hyperactive response to stimuli, limited interaction with cagemates
4	Barely active, severe stress	Reduced weight loss (<20 - 30%)	Unkempt fur, crouched posture, dull cloudy eyes, shivering, piloerection	Lethargy, self-isolation, no response to stimuli, motor coordination disorders
5	Lethargic	Reduced weight loss (>30%)	Shivering, cramps, paralysis, abnormal breathing sounds	Auto aggression, painful shrieks on touch

3.2.5 Organ removal

Mice were sacrificed by an overdose cocktail of ketamine-xylazine (180 mg/kg body weight Ketamidor and 24 mg/kg body weight Xylavet) in 1 x DPBS administered intraperitoneally. To avoid cross-contamination, separate dissection tools were used to cut open the skin and dissect the organs. Blood was collected from the inferior vena cava using a 0.4 mm x 19 mm 27 G cannulae and a 1 mL syringe. Lung perfusions were performed using a 20 mL syringe, and 1.2 mm x 40 mm 18 G cannula by passing $\text{Ca}^{2+}/\text{Mg}^{2+}$ free HBSS supplemented with 1 mM EDTA through the right ventricle and pulmonary artery. Lungs, liver, spleen, and caeca were aseptically removed, briefly rinsed in 1 x DPBS, weighed, and allocated to different read-outs as outlined in **Table 3.2**.

Table 3.2: Allocation of organs to different experiments following organ harvesting

Organ	Read-out	Storage buffer/medium
Whole blood	Hematological analyses	K3 EDTA
Whole blood	Serological analyses	Clot activator
Superior lung lobe	Paraffin embedding and cryopreservation	4% (w/v) PFA for 24 h
Remainder of the lung lobes	1/2 of minced lung lobes for CFU and multiplex cytokine assays	1 mL lung lysis buffer
Remainder of the lung lobes	1/2 of minced lung lobes for RNA isolation for qRT-PCR	1 mL TRI Reagent
1/4 left liver lobe	Paraffin embedding	4% (w/v) PFA for 24 h
Left liver lobe (approx. 50-100 mg)	RNA isolation for qRT-PCR	1 mL TRI reagent
Right liver lobe	CFU assays	WTA buffer
Spleen	CFU assays and multiplex cytokine assays	1 mL spleen lysis buffer
Caecum	RNA isolation (16S rRNA sequencing)	1 mL TRI reagent

3.2.6 Colony-forming unit (CFU) enumeration assay

To determine the mycobacterial load in vivo, lungs, spleens, and livers were aseptically removed, and total organ weights were recorded. Organs were mechanically homogenized in Whirl Pak plastic bags prefilled with corresponding buffers indicated in **Table 3.2**. 50 μ L or 100 μ L organ homogenates were subjected to tenfold serial dilutions in WTA buffer and plated onto half, or whole Middlebrook 7H11 agar plates supplemented with 10% (v/v) h.i. bovine serum, respectively. After incubation in a humidified chamber at 37°C for 21-28 days, the number of colonies per plate were counted. The highest countable dilution was considered for results and standardized per gram of net organ weight.

3.2.7 Whole blood collection and serum preparation

Evaluation of hematological parameters was performed from whole blood on VetScan HM5-C hematology analyzer (Scil animal care company GmbH, Viernheim, DE) according to the manufacturer's user manual. Whole blood collected in serum separator tubes was centrifuged at 7000 rcf for 5 mins at 4°C to obtain a transparent barrier between the blood clot and serum. Using 0.22 μ m filter tubes, the serum was filtered by centrifugation at 7000 rcf for 3 mins at 4°C, transferred to 0.5 mL microtubes, and stored at -80°C until further use.

3.3 Histopathological and Immunohistochemical Analyses

Tissues were fixed in 5 volumes 4% (w/v) PFA to organ weight and incubated at 4°C for 24 h. The following day, samples were transferred to 0,1% (w/v) sodium azide in PBS and stored at 4°C until further processing.

3.3.1 Tissue processing for histopathology

Tissues were loaded onto embedding cassettes and dehydrated using the Spin Tissue Processor Microm STP-120 (Thermo Fisher Scientific, Walldorf, DE), consisting of graded ethanol baths. The dehydration steps included are shown in **Table 3.3**.

Table 3.3: Paraffin processing of tissues

Reagent	Immersion time (min) per cycle	Cycles
4% PFA	60	1
70% Ethanol	60	1
80% Ethanol	60	1
90% Ethanol	60	1
96% Ethanol	60	1
100% Ethanol	60	3
Xylol	60	2
Paraffin (65°C)	90	1

Paraffin-treated tissues were mounted on metal moulds and embedded in liquid paraffin at 65°C using the HistoStar Embedding Workstation (Thermo Scientific, Dreieich, DE). The paraffinized tissues were allowed to solidify into paraffin blocks for approx. 30 mins and sectioned at 4 μ m using a Leica RM 2155 rotary microtome (Leica Biosystems, Wetzlar, DE). Sections were placed to float in a 37°C water bath, mounted onto SuperFrostPlus microscope slides, and air-dried at 37°C o/n. All paraffin-embedded tissue sections were deparaffinized and rehydrated before treatment with any stain of interest. The deparaffinization and rehydration steps consisted of incubating the sections in 2 changes of xylol for 5 mins each, 2 changes of 100% Ethanol for 2 mins each, 2 changes of 96% Ethanol for 2 mins, once in 70% Ethanol for 1 min, and finally in Aq. Dest. for 2 mins followed by a brief rinse in PBS.

3.3.2 Cryopreservation of tissues

Deparaffinized tissues were incubated in varying concentrations of saccharose in PBS, as indicated in **Table 3.4**.

Table 3.4: Tissue processing for cryopreservation

Steps	Incubation time	Temperature
5% Saccharose	45 min	RT
5% Saccharose + 20% Saccharose (2:1)	45 min	RT
5% Saccharose + 20% Saccharose (1:1)	45 min	RT
5% Saccharose + 20% Saccharose (1:2)	45 min	RT
20% Saccharose	o/n	4°C
20% Saccharose + Tissue Tek (2:1) (infiltration solution)	30 mins	RT

Saccharose-treated tissues were loaded onto plastic cryo moulds containing 1 mL of the infiltration solution. For cryopreservation of tissues, tissue-loaded moulds were immersed into a beaker containing Isopentane cushioned on 19 mm dry ice pellets until frozen. For actual immunochemistry staining, frozen samples were mounted on a CM1850 cryostat-microtome

(Leica Biosystems, Wetzlar, DE), sectioned at 4 μm , and placed on SuperFrost Plus microscope slides and stored at -80°C until further use.

3.3.3 Hematoxylin and eosin (H&E) stain

4 μm deparaffinized tissue sections were stained with Mayer's Hematoxylin for 10 mins. Tissues were rinsed briefly in running tap water, then Aq. Dest. for 2 mins and counter-stained with 1% (w/v) Eosin in Milli-Q water for 1 min. Following brief rinsing in Aq. Dest., subsequent dehydration steps were performed to include incubation in; 96% Ethanol for 2 mins, 100% Ethanol for 4 mins and briefly in xylene. Sections were embedded in Entellan and examined under the BX41 light microscope (Olympus Corporation, Tokyo, JP). Hematoxylin stains the nuclei blue-purple while eosin stains the cytoplasm and extracellular matrix pink. Quantitative assessment of lesion size and lymphoid aggregates in Mtb infected lung, and liver tissue was performed by measuring the affected lung and liver areas using CellSensB microscopy imaging software (Olympus Corporation, Tokyo, JP).

3.3.4 Perl's stain

Paraffin sections were used for Perl's stain to demonstrate the presence of ferritin within cells in tissues. Deparaffinized and rehydrated sections were incubated at RT for 15 mins in a working solution consisting of equal parts of 4% (w/v) aq. potassium ferrocyanide and 4% (v/v) aq. HCl. Tissue sections were briefly rinsed in Aq. Dest. and tap water. Following treatment with 1% (w/v) filtered neutral red for 2 mins, tissue sections were rinsed in Aq. Dest, dehydrated in absolute alcohol, cleared with xylene and mounted with Entellan towards microscopy under the BX41 light microscope (Olympus Corporation, Tokyo, JP). Ferritin appears bright-to-deep blue, nuclei and cytoplasm appear pink-to-red, and erythrocytes appear yellow.

3.3.5 Ziehl-Neelsen (ZN) stain

ZN staining was used to identify *Mycobacterium* species in deparaffinized sections. Deparaffinization was done as outlined in **Table 3.5**.

Table 3.5: Treatment of tissue sections prior to ZN staining

Reagent	Time (min)	Temperature
Xylol I	5	RT
Xylol III	5	RT
Xylol III	5	RT
Xylol I/Ethanol 1:2	1, swivel lightly	RT
100% Ethanol I	5	RT
100% Ethanol I	5	RT
100% Ethanol II	dip briefly	RT
100% Ethanol III	dip briefly	RT
96% Ethanol	dip briefly	RT
70% Ethanol	dip briefly	RT
40% Ethanol	dip briefly	RT
Aq. dest.	5	RT

Sections were flooded with carbol-fuchsin and passed over a heat source until the appearance of fumes. After 5 mins of cooling, sections were washed in Aq. dest. and flooded with 0.5%

(v/v) HCl in 70% (v/v) Ethanol until the sections were decolorized to pale pink. After that, tissue sections were treated as indicated in **Table 3.6**.

Table 3.6: ZN staining

Reagent	Time (min)	Temperature
Aq. dest.	rinse briefly	RT
1:10 Loeffler's methylene blue solution	1 min	RT
Aq. dest.	rinse briefly	RT
96% Ethanol	dip briefly	RT
Isopropanol	dip briefly	RT
Xylol 1st wash	5 mins	RT
Xylol 2nd wash	5 mins	RT
Xylol 3rd wash	5 mins	RT

Finally, tissue sections were allowed to air dry and mounted in Entellan for microscopic examinations using the BX41 light microscope (Olympus Corporation, Tokyo, JP). Acid-fast mycobacteria stain hot pink-red.

3.3.6 Oil Red O stain

Oil red O (ORO) staining was used to identify triglycerides, triacylglycerols, and lipid droplets in cryosections. Sections were rinsed in PBS and treated with freshly prepared ORO working solution (0.5% (w/v) ORO stock solution in 60% triethyl phosphate, diluted to 0.35% (v/v) ORO in Aq. dest.) for 30 mins. Sections were washed thrice in Aq. Dest, stained with Mayer's Hematoxylin for 10 mins and briefly rinsed in Aq. Dest. Finally, slides were mounted in aq. Kaiser's glycerol gelatin in advance of microscopy using a BX41 light microscope (Olympus Corporation, Tokyo, JP).

3.3.7 Immunohistochemistry

Deparaffinized tissue sections were loaded in staining cuvettes prefilled with citrate buffer. Cuvettes were placed in a Retriever 2100 pressure cooker prefilled with water and treated for 45 min to unmask the antigenic epitopes. Tissues were allowed to cool at RT for approx. 20 mins and washed thrice with PBS. After that, sections were incubated with 1% (v/v) H₂O₂ in the dark at RT for 20 mins to block endogenous peroxidase activity. Sections were washed thrice with PBS and treated with 100 μ L 0,1% (v/v) Triton X-100 in 3% (w/v) BSA in PBS supplemented with 5% (v/v) normal goat serum (NGS) to block unspecific binding sites and permeabilize the cells for 10 mins at RT. This was followed by treatment with or without 100 μ L primary antibody (diluted in 2% (w/v) BSA in PBS) o/n at 4°C. Samples treated without the primary antibody served as negative controls. The following day, tissue sections were rinsed thrice with PBS and incubated in 100 μ L biotinylated goat anti-rabbit secondary antibody (diluted in 2% (w/v) BSA in PBS) for 45 mins in the dark at RT. Following three times rinsing with PBS, 100 μ L VECTASTAIN ELITE ABC kit reagents prepared according to the manufacturer's protocol were added to the tissue sections. Tissue sections were again washed thrice with PBS and treated with 200 μ L DAB peroxidase substrate per microscope slide. Finally, tissue sections were rinsed for 5 mins with Aq. Dest. after the desired stain intensity had been achieved when viewed under the light microscope. Sections were counterstained with

Gill's Hematoxylin for 5 mins, washed under running tap water for an additional 5 mins, and rinsed in Aq. Dest. Tissue sections were dehydrated as described in section 3.3.1, mounted in aq. Kaiser's glycerol gelatin and imaged with a BX41 light microscope (Olympus Corporation, Tokyo, JP).

3.4 Biochemical Analyses

3.4.1 Protein concentration measurement

Following organ homogenization as described in section 3.2.6, 300 μ L organ lysates were transferred to 0.22 μ m centrifuge filter tubes, centrifuged at 7000 rcf for 5 mins at 4°C, transferred to 0.5 mL microtubes and stored at -80°C until further experiments. Protein concentration in organ lysates was determined using the Pierce BCA protein assay kit (Thermo Fisher Scientific, Rockford, USA) according to the manufacturer's instructions and normalized before cytokine and chemokine measurements.

3.4.2 Enzyme-linked immunosorbent assay (ELISA)

Murine serum was used to quantify ferritin using mouse ferritin light chain kit (Abcam, Cambridge, United Kingdom (UK)) through ELISA per the manufacturer's protocol.

3.4.3 Determination of biochemical iron parameters

Total iron concentration in serum was measured using the Iron assay kit (Sigma-Aldrich, Steinheim, DE) as per the manufacturer's instructions. Total iron-binding capacity (TIBC) using the TIBC kit (Abcam, Cambridge, UK) was measured in murine sera per the manufacturer's instructions. Transferrin saturation in serum was not measured but calculated as a ratio of the serum iron concentration and the TIBC expressed as a percentage.

3.5 Molecular Biology Analyses

3.5.1 Total RNA extraction from tissue

Samples were collected in BashingBead™ lysis tubes (containing 0.1 and 0.5mm beads) pre-filled with 1 mL TRI reagent. Tissues were homogenized using the FastPrep 24 (MP Biomedicals, CA, USA) by performing 5 cycles of homogenization for 50 secs at a speed of 6.5 m/s. A 5 mins cool-down on ice was performed between each homogenization cycle. After that, samples were centrifuged at 12 000 rcf at RT for 1 min. RNA was isolated by the phase separation method [145] with slight modifications. 400 μ L of the tissue homogenate was transferred to a DNase/RNase free tube, and 80 μ L of Chloroform was added to the homogenate. Samples were briefly vortexed, incubated for 3 mins at RT, and spun at 12000 rcf for 15 min at 4°C. The upper aqueous phase containing the RNA was transferred into a new tube and processed using the Direct-zol RNA MiniPrep kit according to the manufacturer's protocol (Zymo Research, Freiburg, DE). The resulting RNA was purified using One-Step PCR Inhibitor Removal Kit (Zymo Research, Freiburg, DE) according to the manufacturer's protocol. RNA concentrations were determined at 260 nm on the Infinite M200Pro NanoQuant Plate reader (Tecan, Männedorf, CH), diluted to 100 ng/ μ L in DNase/RNase free water and stored at -80°C until further use.

3.5.2 Quantitative real-time reverse transcription (RT)- polymerase chain reaction (PCR) (qRT-PCR)

Reverse transcription

RNA was treated with dsDNase using the Maxima First Strand cDNA Synthesis kit with dsDNase (Thermo Fisher Scientific, Dreieich, DE) to eliminate contaminating genomic DNA (gDNA) as outlined in **Table 3.7**.

Table 3.7: dsDNase digestion reaction set-up

Components	Volume (μL)
10x dsDNAase buffer	1
dsDNAase	1
Template RNA	8
Total volume	10

The reaction was performed on the Labcycler (SensoQuest, Göttingen, DE) at 37°C for 2 min. The dsDNase treated RNA was transcribed into cDNA using the Maxima FirstStrand cDNA Synthesis kit with dsDNase (Thermo Fisher Scientific, Dreieich, DE) as per the manufacturer's instructions (**Table 3.8**) on the Labcycler (SensoQuest, Göttingen, DE) with the following thermal cycling conditions outlined in **Table 3.9**.

Table 3.8: cDNA synthesis reaction set-up

Components	Volume per sample (μL)
5x Reaction mix	4
Maxima enzyme mix	2
DNA/RNase-free water	4
Total volume	10

Table 3.9: Thermal cycling conditions for cDNA synthesis

Program	Temperature ($^{\circ}\text{C}$)	Time (hh:mm:ss)	Cycles
Denaturation	25	00:10:00	1
Annealing	50	00:15:00	1
Extension	85	00:05:00	1
Cooling	4	Hold	1

qRT-PCR

The expression of target genes at the RNA level was quantified by qRT-PCR on the LightCycler 480 Instrument (Roche Diagnostics, Mannheim, DE) using the fluorescent SYBR Green I dye, which intercalates double-stranded DNA (dsDNA). Primers used to amplify reference and target genes were designed using the NCBI tool Primer-BLAST and ordered from Sigma-Aldrich (Hamburg, DE). The primers for Nos2, Hprt, Irf1, and Frtn-L chain were provided by Coinfection group, RCB, Borstel, DE. 10 μM forward and 10 μM reverse primers for each gene were prepared, aliquoted, and stored at -20°C until further use. The efficiency of the amplification was determined by preparing titrations of cDNA of all test samples (100%, 50%, 10%, 5%, 1%, 0.5%, 0.1%, 0%) for both reference and target genes. The qRT-PCR was

performed using the LightCycler 480 SYBR Green I Master kit (Roche Diagnostics, Mannheim, DE) as per the manufacturer's instructions (**Table 3.10**) using the program settings outlined in **Table 3.11**.

Table 3.10: qRT-PCR reaction set-up

Components	Volume per sample (μL)
SYBR Green I Master	5
DNA/RNase-free water	3,8
Primer-Mix	0,2
cDNA template	1
Total volume	10

Table 3.11: Thermal cycling conditions for qRT-PCR

Program	Temperature ($^{\circ}\text{C}$)	Time (hh:mm:ss)	Cycles
Denaturation	95	00:10:00	1
Amplification	95	00:00:10	45
	63	00:00:10	45
	72	00:00:08	45
	72	00:00:01	45
	Melting curve	95	00:00:10
Melting curve	65	00:00:10	1
	97	-	1
	Cooling	37	00:00:01

For the actual qRT-PCR, primer pairs with specific melting curves and cDNA titration with mid-log phase around 10-20 cycles were selected. DNase/RNase-free water, non-template control, and cDNA samples without reverse transcriptase were used as controls. Mouse hypoxanthine-guanine phosphoribosyltransferase 1 (*Hprt1*) was used as the housekeeping gene. The qRT-PCR was performed using the same reaction volumes and cycling conditions in Tables 3.10 and 3.11, respectively. The relative quantification (RQ) of the target gene expression in the test sample was determined using the E-(Efficiency)-method (Roche Applied Sciences) based on the true efficiency of each reaction obtained from the titrations of the reference and target genes prepared as described above. The results were automatically calculated by LightCycler 480 software, v1.5.1. from the target and the housekeeping genes' cycle threshold (Ct) values.

3.5.3 DNA extraction of tissue

DNA was isolated from tissues using phase separation [145] and TRI reagent DNA/protein isolation protocols (Thermo Scientific). Following mechanical disruption using the FastPrep-24 (MP Biomedicals, LLC, Irvine, USA), tissues were processed as described in **Section 3.5.1**. The phenol-chloroform phase and interphase containing the DNA were used for DNA isolation. 200 μL back extraction buffer was added to the samples' 400 μL phenol-chloroform phase and interphase. The mixture was incubated for 10 mins at RT and centrifuged at 12000 rcf for 15 mins at 4°C to yield 2 phases. The upper aqueous phase containing the DNA was transferred to a new tube, and 2 μL of linear acrylamide was added to the samples to increase DNA yield. Samples were vortexed, and 160 μL isopropanol was added to the tubes. Again, samples were

vortexed, incubated for 5 mins at RT, and centrifuged at 12000 rcf for 5 mins at 4°C. The resulting pellet was resuspended in 1 mL 75% (v/v) Ethanol and incubated at 4°C o/n. The following day, samples were incubated for 15 mins at RT, gently mixed, and centrifuged at 12000 rcf for 5 mins at 4°C. The pellet was allowed to air dry for 15 mins and resuspended in 100 μ L 8 mM NaOH. Finally, samples were centrifuged at 12000 rcf for 5 mins at 4°C, and the s/n was transferred to a 96-well PCR plate. 1 μ L HEPES buffer was added to the DNA samples, which were further purified using MagSi-NGS Prep Plus (Magna Medics Diagnostics B.V., Geleen, Netherlands (NL)) following a protocol described in [146]. DNA concentration and purity were assessed by measuring the ratio of absorbance at 260 nm and 280nm on the Infinite M200Pro NanoQuant Plate reader (Tecan, Männedorf, CH). Caecum DNA samples were diluted to 10 ng/ μ L in DNase/RNase-free water and stored at -80°C.

3.5.4 Genotyping PCR

Genomic DNA was extracted from ear punch biopsies or liver tissue samples as described in **section 3.5.3** and diluted 1:10 in DNA/RNase-free water (Zymo Research, Freiburg, DE). The PCR was performed using the Red Taq DNA polymerase (TaqPol) master mix (VWR, Darmstadt, DE) as per manufacturer's instructions (**Table 3.12**) on the Labcycler (SensoQuest GmbH, Göttingen, DE) using the program settings outlined in **Table 3.13**.

Table 3.12: PCR reaction set-up

Components	Volume per sample (μ L)
TaqPol master mix	15
DNA/RNase-free water	10
Primer mix	1*
DNA template	1
Total volume	27

*2 μ L for IRP2 primer mix

Table 3.13: Thermal cycling conditions for PCR

Program	Temperature (°C)	Time (hh:mm:ss)	Cycles
Denaturation	94	00:05:00	1
Annealing	94	00:00:30	30
Extension	60,8	00:00:30	30
Extension	72	00:01:00	30
Extension	72	00:07:00	25
Cooling	4	Hold	

To separate DNA by size for visualization, agarose gel electrophoresis was used. For this, 2% agarose gel was used. 2 g agarose powder (Carl Roth, Karlsruhe, DE) was dissolved in 100 mL 1x TAE buffer by microwaving for 1-2 mins. The agarose solution was poured into a gel tray with well combs and allowed to solidify for 20-40 mins. Following gel solidification, the gel box was filled with 1x TAE buffer and 8 μ L 6x loading buffer (i.e., Generule 100bps (Thermo Scientific, Bremen, DE)) was loaded in the first and last of the wells of the gel. 20 μ L PCR product was mixed with 4 μ L 6x loading dye and 24 μ L in total was loaded into additional wells of the gel. Water was used as a negative control. The gel was run for 1h 35 mins at 100V. DNA bands were visualized by staining the gel in 1 μ g/mL Ethidium Bromide (EtBr)

staining solution (Carl Roth, Karlsruhe, DE) for 20-30 mins. EtBr intercalates with DNA double strands and fluoresces when excited with UV light at an emission maximum of 595 nm. Thereafter, gels were destained in ddH₂O for 5-10 mins to remove excess EtBr, exposed to UV light at 302 nm, and imaged using a photo documentation system (Biorad Laboratories GmbH, Munich, DE).

3.5.5 16S rRNA library preparation

Amplicon PCR

Bacterial 16S rRNA variable V3-V4 regions were amplified on the Labcycler (SensoQuest GmbH, Göttingen, DE) using the Phusion Hot Start II High-Fidelity (HiFi) DNA-Polymerase (Thermo Scientific, IL, USA) as indicated in Table **Table 3.14**.

Table 3.14: Amplicon PCR reaction set-up for one sample

Components	Volume (μL)
DNA/RNase-free water	14.75
5x Phusion HF buffer	5
dNTP-mix	0.5
Forward primer	1
Reverse primer	1
Phusion HotStart II HiFi DNA polymerase	0.25
DNA template	2.5
Total volume	25

The PCR program was run as follows: initial denaturation at 98°C for 30 s, followed by 25 cycles of denaturation at 98°C for 10s, annealing at 55°C for 20 s, extension at 72°C for 20 s for 25 cycles and a final extension step at 72°C for 420 s.

PCR Clean-up I and Index PCR

Following PCR amplification, MagSi-NGS Prep Plus (Magna Medics Diagnostics B.V., Geleen, NL) was used to purify the resulting v3-v4 amplicons based on the protocol described in [146]. Index 1 (i7) and index 2 (i5) adapters (Illumina, San Diego, U.S.A) were used to attach barcodes to amplicons through index PCR using the 2x KAPA HiFi HotStart ReadyMix (2x KAPA HiFi) kit (Roche, Karlsruhe, DE). The reaction set-up is indicated in **Table 3.15**.

Table 3.15: Index PCR reaction set-up for one sample

Components	Volume (μL)
DNA	5
Index 1 (i7) adapters	5
Index 2 (i5) adapters	5
PCR grade water	10
2x KAPA HiFi	25
Total volume	50

PCR program started with an initial denaturation at 95°C for 180 s, followed by 8 cycles of denaturation at 95°C for 30 s, annealing at 55°C for 30 s, extension at 72°C for 30 s and final extension at 72°C for 300 s.

PCR Clean-up II, Library quantification and standardization

DNA was again purified using MagSi-NGS Prep Plus, and DNA yield was quantified using Quant-iT PicoGreen dsDNA Assay (Thermo Scientific, Dreieich, DE) as per manufacturer's instructions. DNA was then diluted to a final concentration of 0.1 nM in 10 mM Tris HCl (pH 7), after which 3 μ L of each sample was used to create a pooled library.

Library denaturation and sequencing on the MiSeq platform

60 μ L 0.1 mM pooled library was added to 60 μ L NaOH and incubated at RT for 5 mins to allow denaturation. To achieve a 20 pM DNA pool, 60 μ L 200 mM Tris HCl (pH 7) was added to 120 μ L hybridization buffer (HT1). Of this, 240 μ L of the pool was mixed with 700 μ L HT1 and 60 μ L 20 pM PhiX. The dilution steps resulted in a 6 pM pool containing 20% denatured PhiX. Finally, 600 μ L of the final pool was added to the cartridge and loaded onto the MiSeq sequencer (Illumina, San Diego, U.S.A). Unless otherwise mentioned, all reagents and kits used for library preparation were purchased from Illumina, San Diego, USA.

3.6 Immunological Analyses

3.6.1 Multiplex cytokine assay

Sample protein concentrations were quantified as described in section 3.4.1 before assays. Cytokines and chemokines present in sera and organ lysates were measured using the MSD U-PLEX Biomarker Group 1 (mouse) Multiplex Assays (Meso Scale Discovery, Rockville, USA) according to the manufacturer's protocol. Samples were measured on the Meso QuickPlex SQ 120 instrument (Meso Scale Discovery, Rockville, USA) and data were acquired using the MSD Discovery Workbench software v4.0.

3.6.2 Measurement of reactive nitrogen species production

Nitrite production in murine serum and lung homogenates was measured using the Total Nitric Oxide and Nitrate/ Nitrite colourimetric assay kit (Cayman Chemical, Minneapolis, USA) according to the manufacturer's protocol.

3.7 Data Analyses

3.7.1 Bioinformatic analyses

Samples were sequenced using the MiSeq system (Illumina, San Diego, USA) at the Molecular and Experimental Mycobacteriology department at the RCB (Borstel, DE). FASTQ files containing the sequence data were processed using a pipeline of USEARCH (v11) commands [146]. For this study, the R code used for the analysis of the OTU tables was established by Dr. Matthias Hauptmann. Data were analyzed in Rstudio (v.1.1.1.383) and Anaconda (v3 2021.05). β -diversity was measured using the Bray-Curtis dissimilarity index based on principal coordinates analysis (PCoA). Within-and-between group dissimilarities were quantified using Wilcoxon Rank Sum Exact Test.

3.7.2 Statistical tests

Data are presented as mean \pm standard deviation and were analysed using GraphPad Prism v.9.1.2 (GraphPad Software, LaJolla, CA). Two-way analysis of variance (ANOVA) with Tukey's post hoc analysis was used to evaluate normally distributed data. Non-parametric Kruskal-Wallis test was used for data with a non-normal distribution. Differences were considered statistically significant at $p < 0.05$, $p < 0.01$, $p < 0.001$, and $p < 0.0001$.

CHAPTER 4

Results

4.1 Effects of Dietary Iron Manipulation in Mtb Infection *in vivo*

Increased iron availability of genetic, dietary, or environmental origins is considered a risk factor for developing and exacerbating active TB [147]. Many studies have inconsistent findings on the consequences of dietary iron supplementation and iron deficiency on the predisposition to pulmonary TB infection. To investigate whether long-term dietary iron supplementation or under-supply of iron in mice prior to and during experimental Mtb infection could influence TB disease outcome, C57BL/6J mice were fed iron-rich, iron-low, and iron-control diets to induce dietary iron overload and iron deficiency.

4.1.1 Investigation of host responsiveness to Mtb

To induce iron overload or iron deficiency anemia, SPF female C57BL/6J wt mice were kept on either iron-rich (460 mg/kg Fe (II) fumarate), iron-low (< 9mg/kg Fe (II) fumarate) or iron-control diets (46 mg/kg Fe (II) fumarate) for 16 weeks before infection. After that, mice were infected with 100 CFU Mtb H37Rv via aerosol route and maintained on the same diets for an additional 16 weeks post Mtb infection (p.i.) (**Fig. 4.1**).

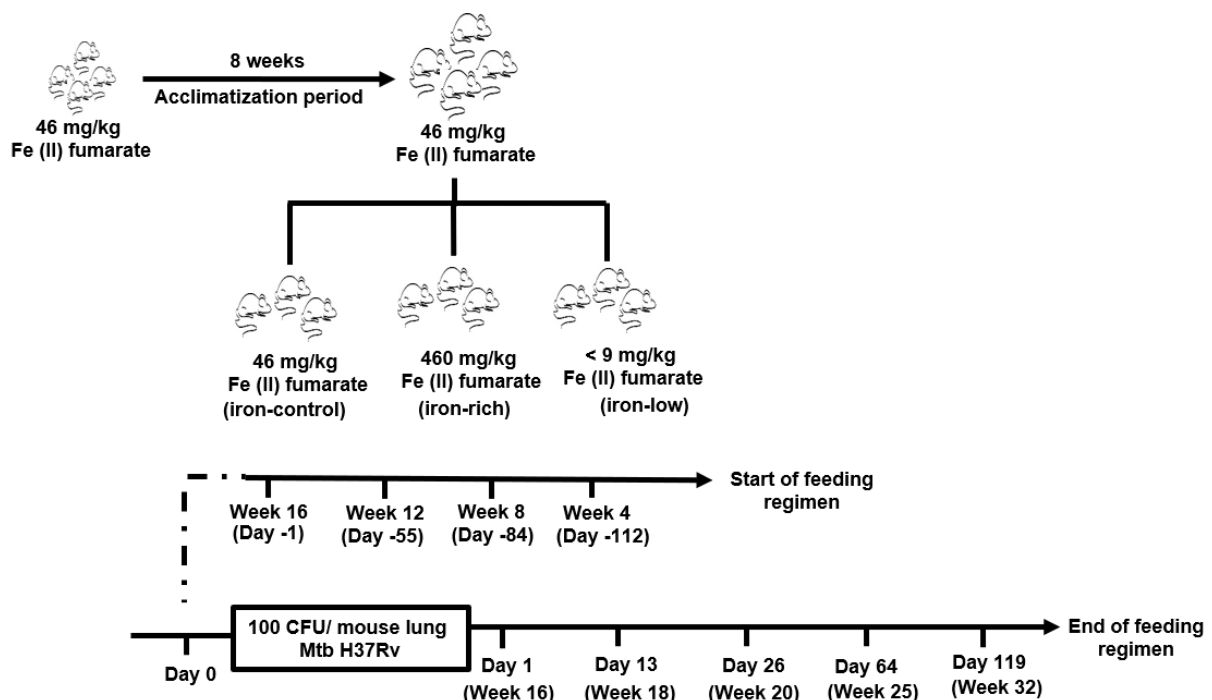


Figure 4.1: Experimental set-up for investigating dietary iron supplementation and iron under-supply in mice prior to and during experimental Mtb infection. 3-week-old female C57BL/6J mice were fed an experimental diet containing 46 mg/kg Fe (II) fumarate for 8 weeks for acclimatization. At 11 weeks of age, mice were assigned to 3 feeding groups: iron-control, iron-rich, and iron-low. Mice were sacrificed 8 weeks (d-84 p.i.) and 16 weeks (d-1 p.i.) after the start of the feeding regimen and infection with 100 CFU Mtb H37Rv via the aerosol route on day 0 was performed. The target infection dose was investigated in 8 mice (i.e., n=4 animals per experiment) in the iron-control group on day 1 p.i. Mice were maintained on the respective diets for additional 16 weeks and sacrificed at indicated time points.

On either day 13 or 16, 26 or 29, 63 or 64, and 119 or 120 p.i., mice in the different feeding groups were euthanized. Lungs, spleens, and livers were collected to assess Mtb loads via CFU enumeration assays. Mycobacterial replication was observed in the mice's lungs, spleens, and livers over time (**Fig. 4.2**). Higher Mtb loads were observed in the lungs of mice on the iron-rich diet compared to mice on iron-control and iron-low diets in the early phase of infection at days 13 and 26 p.i. (**Fig. 4.2A**). However, the bacterial load was reduced to similar levels at days 64 p.i. in all feeding groups demonstrating equal control of mycobacterial growth. Interestingly, in the late phase of infection at day 119 p.i., a surge in the mycobacterial growth was observed in the lungs of mice in all feeding groups, with the highest Mtb loads observed in mice on the iron-rich diet versus (vs) those in the other feeding groups (**Fig. 4.2B**). In the spleen, significantly higher Mtb loads were observed in spleens of mice on the iron-rich diet compared to mice on iron-control or iron-low diets at all time points (**Fig. 4.2D-F**), indicating that increased iron availability promoted Mtb replication. Higher Mtb loads were observed in the livers of mice on the iron-rich diet compared to those on iron-control or iron-low diets at days 26, 64, and 119 p.i. (**Fig. 4.2G-I**). These results show that increased iron availability promotes Mtb replication, whereas limited iron availability in the lungs, spleens, and livers inhibits Mtb growth.

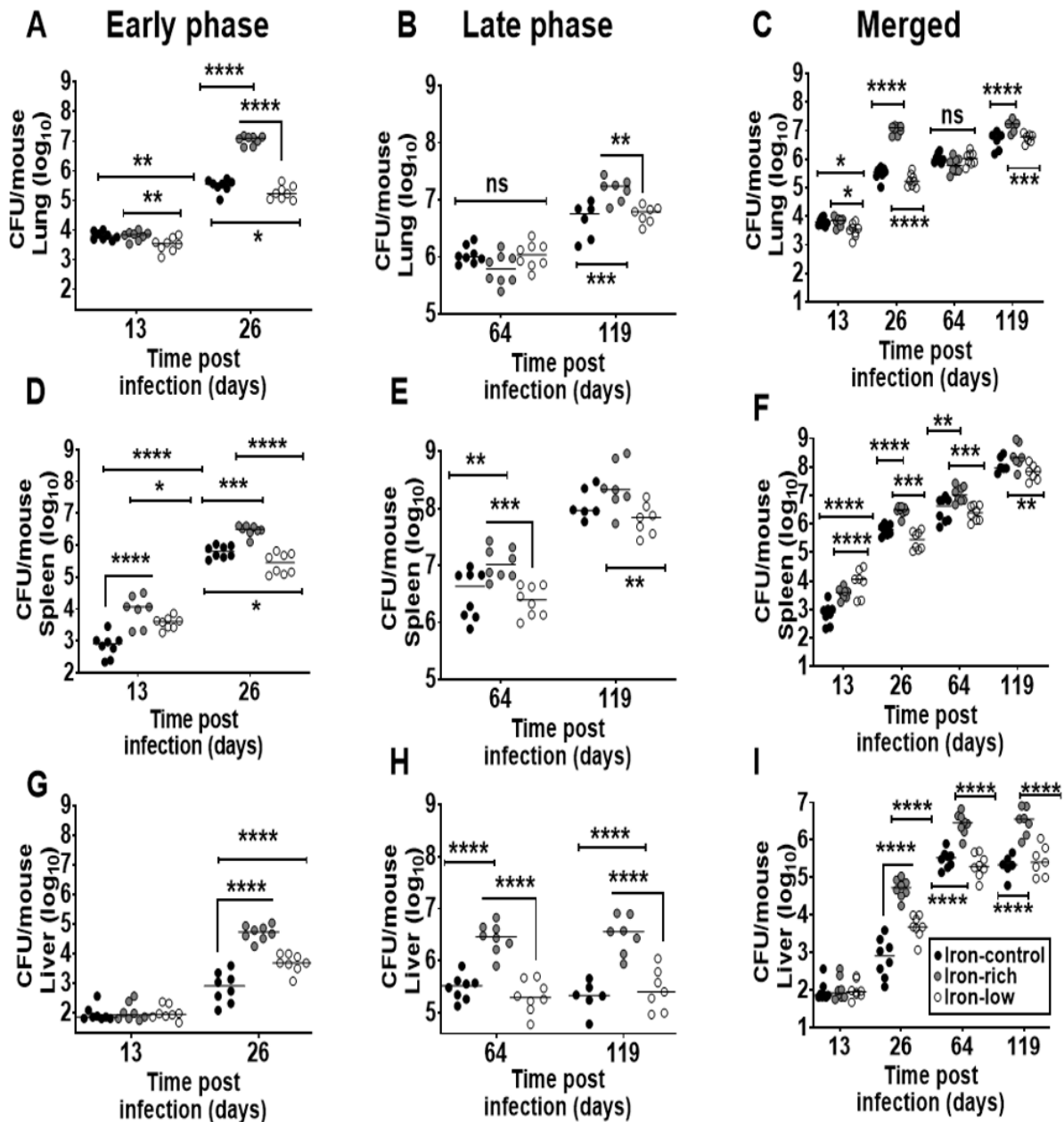


Figure 4.2: Mycobacterial loads in tissue homogenates from mice on iron-control, iron-rich and iron-low diets. SPF female C57BL/6J mice were treated as indicated in Fig. 4.1. CFU assays were performed, and mycobacterial loads in lungs (A-C), spleens (D-F) and livers (G-I) were determined at indicated time points. Each circle represents an individual sample (n=6-8 animals for all panels). Data pooled from 2 independent experiments representing both days 13/16, 26/29, 63/64, and 119/120 p.i. Data were log-transformed and as shown as mean ± SD. Statistical analysis was performed using two-way ANOVA with Tukey's multiple comparisons tests. * $p \leq 0.05$, ** $p \leq 0.01$, *** $p \leq 0.001$ and **** $p \leq 0.0001$ were considered statistically significant. ns represents statistically non-significant differences.

4.1.2 Histopathological analysis of lung tissue

To visualize the effect of the different diet types on TB histopathology in mice on iron-control, iron-rich, and iron-low diets, lung sections were stained with Hematoxylin and Eosin (H&E)

stain. No histopathological alterations were observed in the lungs of all mice in the different feeding groups before infection and on days 13/16 p.i. (**Fig. 4.3**). Increased cellular infiltration at the sites of infection and larger inflammatory lesions were observed in the lungs of Mtb-infected mice on an iron-rich diet at either day 26/29 or 119/120 p.i. when compared to mice on iron-control or iron-low diets thus reflecting lung CFU data.

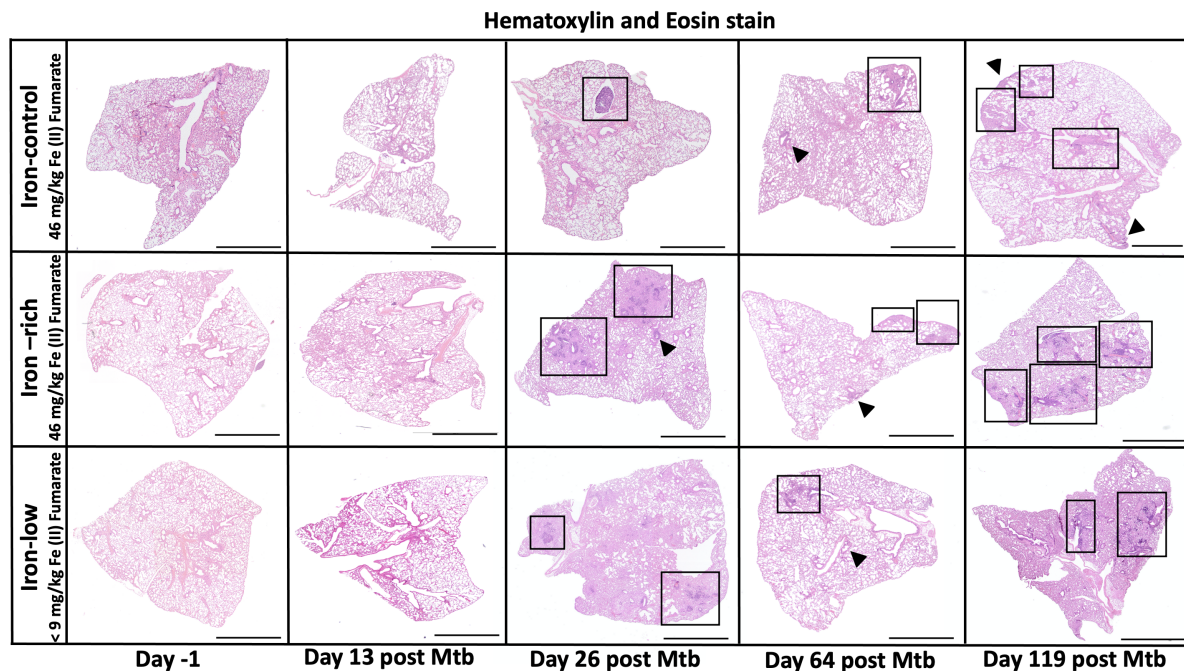


Figure 4.3: Histopathological analysis of lung tissue sections from mice on iron-control, iron-rich and iron-low diets. SPF female C57BL/6J mice were treated as indicated in Fig. 4.1. Superior lung lobes were collected, PFA fixed, and paraffin-embedded (PFPE). Tissue sections were stained at all time points with H&E stain and examined at indicated magnifications. Representative micrographs of 1 animal out of 8 per group are shown (i.e., from 2 independent experiments). Squares with a black outline and black arrows show inflammatory cellular infiltrates. Scale bars represent 1 mm taken with 4x objective.

4.1.3 Investigation of indicators of iron status

Several studies have linked host iron status to infection severity with TB [147]. Therefore, it was hypothesized that the increased availability of free iron could have driven increased mycobacterial loads observed in the mice on the iron-rich diet due to dietary iron supplementation. Consequently, indicators of host iron status such as serum iron and ferritin were investigated. No differences in total iron levels in serum were observed in all mice in the different feeding groups at all time points (**Fig. 4.4A-C**). Elevated serum ferritin concentrations were observed in mice on the iron-rich diet at day 26 p.i. compared to mice on iron-low diets and at day 119 p.i. to those on the iron control diet. Though insignificant, a trend towards higher serum ferritin concentrations was observed at days -84, -1, 13, and 64 p.i. in mice on the iron-rich in comparison to those on iron-control and iron-low diets (**Fig. 4.4D-F**). These results suggest that increased iron availability led to increased iron stores which served as a nutrient source for Mtb resulting in the higher Mtb loads observed in mice on the iron-rich diet at these time points.

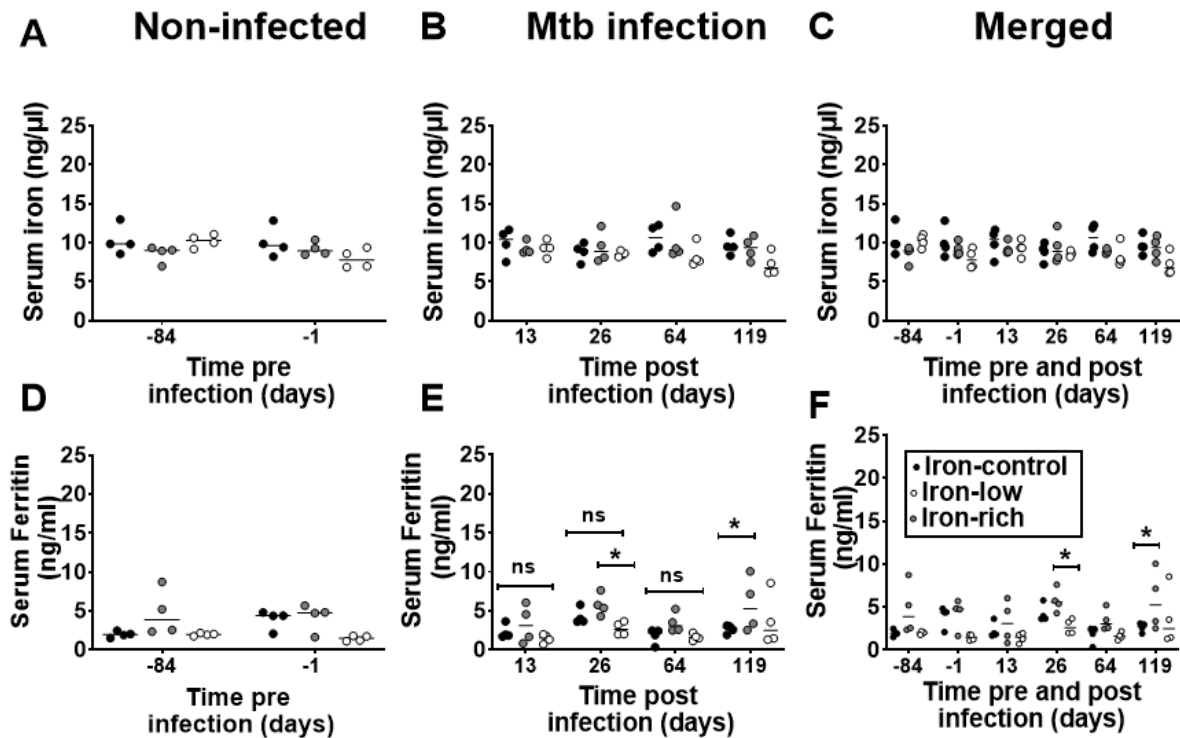


Figure 4.4: Evaluation of indicators of iron status in sera from mice on iron-control, iron-rich and iron-low diets. SPF female C57BL/6J mice were treated as indicated in Fig. 4.1. Serum was obtained from whole blood collected from the *vena cava caudalis* under terminal anaesthesia to investigate total serum iron (A-C) and serum ferritin (D-F) concentrations at indicated time points. Each circle represents an individual sample (n=4 animals). Data are from 1 experiment and shown as mean \pm SD. Statistical analysis was performed using two-way ANOVA with Tukey's multiple comparison tests. * $p \leq 0.05$, ** $p \leq 0.01$, *** $p \leq 0.001$ and **** $p \leq 0.0001$ were considered statistically significant. ns represents statistically non-significant differences.

4.1.4 Quantitative evaluation of expression of iron metabolism genes

To investigate the impact of dietary iron availability or insufficiency on the expression of iron metabolism genes in the liver, gene expression analyses were performed by qRT-PCR. Hepatic *Tfr1* mRNA transcript levels were significantly elevated in mice on the iron-low diet at all time points indicating augmented import of iron into the cells to meet the increased demand caused by the low-iron diets. Precisely, at days -84, -1, 13 and 26 p.i., higher *Tfr1* mRNA transcript levels observed in mice on the iron-low diet were in comparison to mice in the other feeding groups. At days 64 and 119 p.i., higher *Tfr1* mRNA transcript levels were observed in mice on the iron-low diet compared to those on the iron-rich diet but not controls (**Fig. 4.5A-C**). The expression of hepatic *Fpn1* remained unchanged in all feeding groups prior to Mtb infection. At day 13 p.i., hepatic *Fpn1* expression was upregulated in mice on the iron-control diet compared to those on the iron-rich diet. On days 26 and 64 p.i., *Fpn1* expression was elevated in mice on the iron-rich diet in comparison to those on the iron-low diet (**Fig. 4.5D-F**). Hepatic *Frtn-L* expression equally remained unchanged in all feeding groups during the entire feeding regimen and Mtb infection, except at day 64 p.i., wherein, hepatic *Frtn-L* expression was increased in mice on the iron-rich diet in comparison to those on the iron-control and iron-low diets (**Fig. 4.5G-I**). Finally, hepatic *Hamp1* expression was upregulated in mice on the iron-rich diet at all time points in comparison to mice on the iron-control and iron-low diets (**Fig. 4.5J-L**). In all,

these findings illustrate the impact of iron availability on the expression of iron metabolism genes (including *Tfr1*, *Fpn1*, *Frtn-L*, and *Hamp1*) in the liver prior to and during experimental Mtb infection.

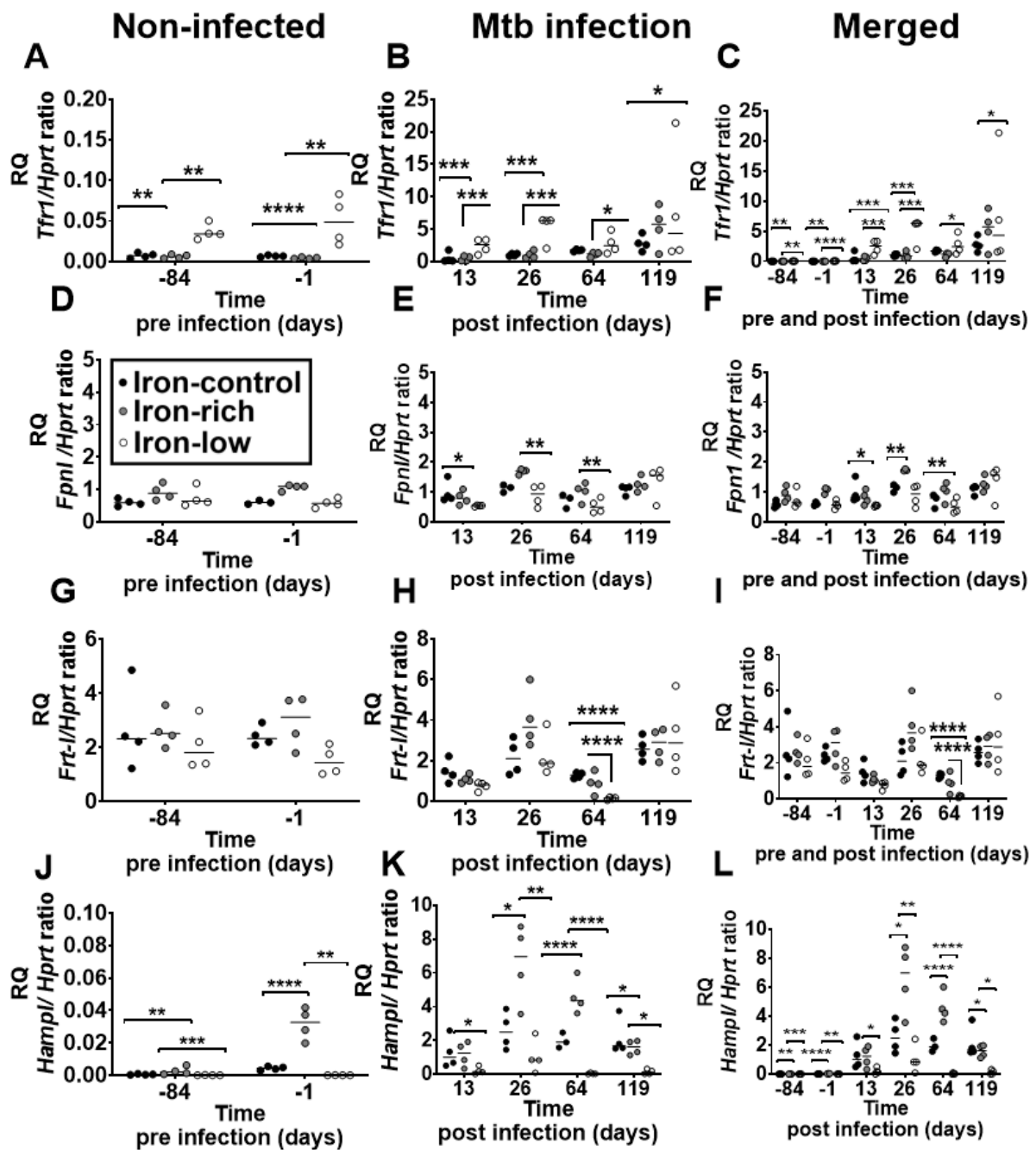


Figure 4.5: Quantification of iron metabolism genes in liver tissue from mice on iron-control, iron-rich and iron-low diets. SPF female C57BL/6J mice were treated as indicated in Fig 4.1. Livers were collected, total host cellular RNA was extracted, reverse transcribed to complementary DNA, and used for the quantification of *Tfr1* (A-C) *Fpn1* (D-F) *Frtn-L* (G-I) and *Hamp1* (J-L) gene expression by qRT-PCR. All mRNA expression levels were normalized against murine *Hprt* mRNA expression levels. Each circle represents an individual sample (n=4 animals). Data are from 1 experiment and shown as mean \pm SD. Statistical analysis was performed using two-way ANOVA with Tukey's multiple comparison tests. * $p \leq 0.05$ and ** $p \leq 0.01$ were considered as statistically significant. ns represents non-statistically significant differences. RQ = Relative quantification.

4.1.5 Investigation of mRNA and protein expression levels of inflammatory cytokines

Iron promotes ROS production, which influences NF κ B activity, a key transcription factor in initiating immune responses. To investigate if increased or decreased dietary iron availability modulates the expression of inflammatory cytokines including, *Ifng*, *Tnfa*, and *Il-6* involved in immunity against Mtb infection, lung tissues from mice fed different diets and handled as indicated in **Fig. 4.1** were analysed using qRT PCR. *Ifng* mRNA transcript levels were elevated in mice fed an iron-rich diet at day 13 p.i., compared to mice on the iron-low diet. At days 26 and 119 p.i., *Ifng* expression was upregulated in mice on the iron-rich diet compared to mice fed an iron-low diet but not in those on the iron-control diet (**Fig. 4.6A**). Meanwhile, *Tnfa* expression was upregulated in mice on the iron-rich diet at days -1 and 13 p.i., in comparison to mice on iron-low diet only. Though no differences were observed, there was an increase in the overall expression of *Tnfa* in all mice at days 26, 64, and 119 p.i. (**Fig. 4.6B**). Finally, *Il-6* was upregulated in mice fed an iron-rich diet only at day 13 p.i., compared to controls as well as mice on the iron-low diet (**Fig. 4.6C**). In all, these results indicate a general infective effect by Mtb, with prominent observations at days 26, 64 and 119 p.i.

Additionally, protein expressions of IFN γ and TNF α in lung homogenates of mice fed different diets and handled as indicated in **Fig. 4.1** were investigated using a customized immunoassay. Concentrations of IFN γ and TNF α were increased across all feeding groups at days 26, 64 and 119 p.i. These concentrations were compared to pre-infection levels at days -84 and -1, as well as during Mtb infection at day 13 p.i. Higher concentration of IFN γ was observed in lungs of mice on the iron-rich diet compared to both mice on the iron-control and iron-low diets at days 26 and 119 p.i (**Fig. 4.6D**). Although not statistically significant, a trend towards higher TNF α concentration was observed at day 26 p.i. in mice on the iron-rich in comparison to those on iron-control and iron-low diets. However, at day 119 p.i., TNF α was significantly elevated in lungs of mice fed an iron-rich diet vs those in the other feeding groups (**Fig. 4.6E**). Overall, these results show that dietary iron levels in mice, whether increased or decreased, have an impact on the modulation of *Tnfa*, *Ifng*, and *Il-6* mRNA and IFN γ and TNF α protein expression during experimental Mtb infection.

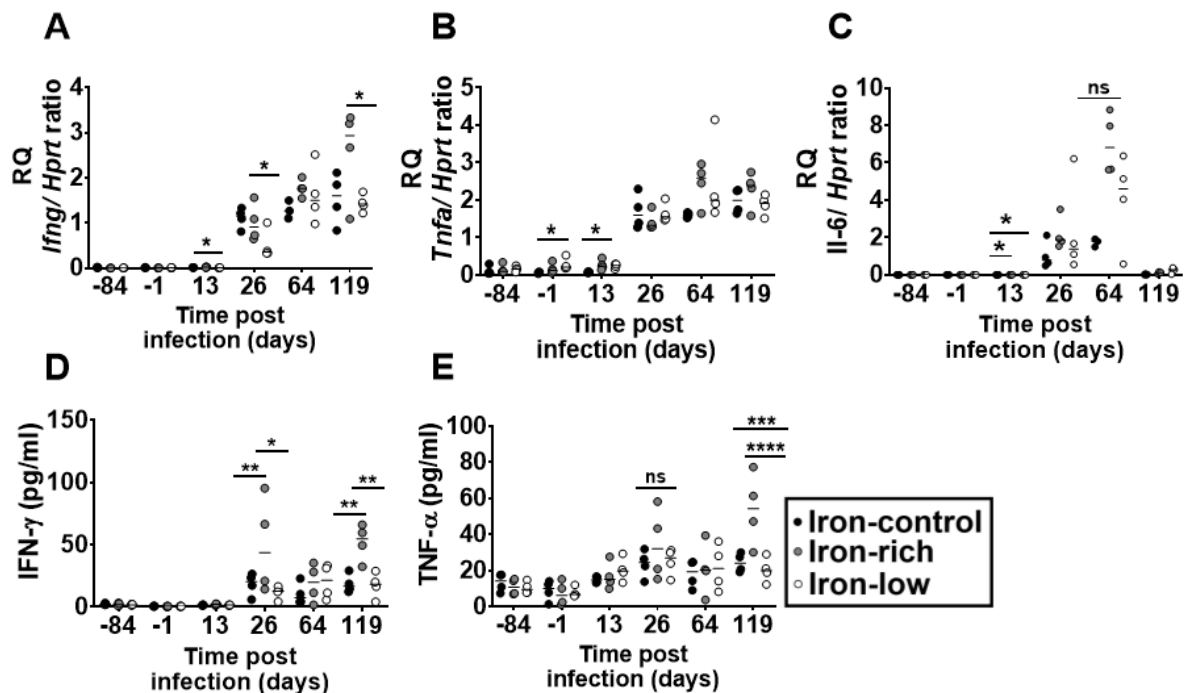


Figure 4.6: Quantification of mRNA and protein expression levels of inflammatory cytokines in lung tissue and homogenates from mice on iron-control, iron-rich and iron-low diets. SPF female C57BL/6J mice were treated as indicated in Fig. 4.1. Lungs were collected, total host cellular RNA was extracted, reverse transcribed to complementary DNA, and used for the quantification of *Ifng* (A), *Tnfa* (B) and *Il-6* (C) gene expression by qRT-PCR. All mRNA expression levels were normalized against murine *Hprt* mRNA expression levels. RQ = Relative quantification. In lung homogenates, the protein concentrations of IFN γ (A) and TNF α (B) were investigated. Each circle represents an individual sample (n=4 animals). Data are from 1 experiment and shown as mean \pm SD. Statistical analysis was performed using two-way ANOVA with Tukey's multiple comparison tests. * $p \leq 0.05$ and ** $p \leq 0.01$ were considered as statistically significant. ns represents non-statistically significant differences.

4.1.6 Histological analysis for iron deposits in lung tissues

Mtb resides in Ms, and mycobacterial growth requires (free) iron availability. To investigate whether iron promotes Mtb infection, Perl's stain was used to identify iron depositions in the lungs. Increased Prussian blue-positive cells were observed in the lungs of non-infected as well as Mtb infected mice on the iron-rich diet in comparison to mice on iron-control and iron-low diets at days -84 p.i. and 119 p.i., respectively (Fig. 4.7A-B).

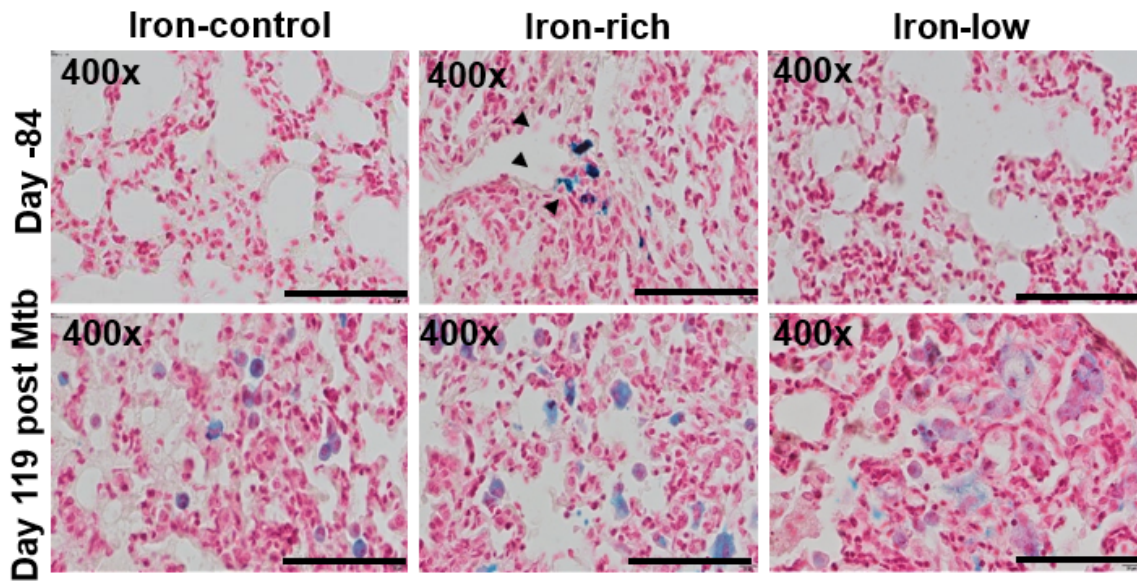
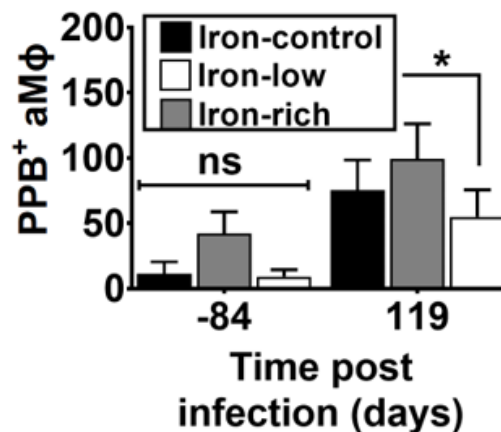
A. Perl's stain**B. Quantification of Perl positive macrophages in lung tissue**

Figure 4.7: Histological analysis of iron deposits in lung tissue sections from mice on iron-control, iron-rich and iron-low diets. SPF female C57BL/6J mice were treated as indicated in Fig 4.1. Superior lung lobes were collected, PFA fixed, and paraffin infiltrated at days -84 and 119 p.i. Tissue sections were stained with Perl's stain and examined under the BX41 light microscope at different magnifications (A). Iron deposits stain bright-deep blue while nuclei and cytoplasm stain pink-red. Representative micrographs of 1 animal out of 8 per group are shown. Black arrows indicate iron deposits stained bright blue. Scale bars represent 100 μm (400x magnification). Quantitative assessment of iron deposits (B). Data generated from quantification of iron deposits are from 1 experiment, $n=4$ animals. Statistical analysis was performed using two-way ANOVA with Tukey's multiple comparison tests. $*p \leq 0.05$ was considered as statistically significant. ns represents non-statistically significant differences. PPB⁺ aM ϕ = Perl Prussian blue positive alveolar macrophages.

The above results (**Figs. 4.1-4.7**) show significant findings regarding dietary iron manipulation in mice prior to and during infection with experimental Mtb. Regarding dietary iron supplementation in mice, my results show that increased dietary iron (i) promoted higher

Mtb loads in lungs, spleens, and livers (ii) worsened pulmonary pathology, (iii) increased iron deposits in aMØs and (iv) altered the expression of iron metabolism genes. Conversely, dietary iron-under supply in mice led to (i) lower Mtb loads in target organs and (ii) milder pulmonary pathology in comparison to mice on the iron-rich diet. Collectively, these results highlight the influence of manipulating iron metabolism on the outcome of experimental TB infection and subsequent expression of immune and iron metabolism-related genes.

To further explore the influence of alterations in iron metabolism on experimental TB, the role of 2 key regulators of cellular iron metabolism, IRP1 and IRP2, on host iron status and host immune responses during experimental Mtb Infection was investigated. For this, 2 mouse models deficient for either IRP1 or 2, i.e., *Irp1*^{-/-} or *Irp2*^{-/-}, respectively, were used to explore this aspect both *in vitro* and *in vivo*

4.2 The Role of Iron Regulatory Proteins 1 and 2 in Mtb H37Rv Infection in Macrophages *in vitro*

MØs are important to immune function in TB and essential to iron homeostasis [148]. In this study, aMØs, peritoneal (pMØs), and BMMØs obtained from non-infected wt, *Irp1*^{-/-} and *Irp2*^{-/-} mice were used to investigate the course of Mtb infection and the cellular response of IRP1 and IRP2-deficient MØs.

4.2.1 Assessment of tissue-resident macrophage numbers

Bone marrow cells, peritoneal and alveolar MØs were collected from non-infected wt, *Irp1*^{-/-} and *Irp2*^{-/-} mice and viable cells were counted by trypan blue dye exclusion test. A lower number of bone marrow cells and alveolar MØs (aMØs) were observed in *Irp1*^{-/-} and *Irp2*^{-/-} mice in comparison to wt but not between *Irp1*^{-/-} and *Irp2*^{-/-} mice. *Irp2*^{-/-} mice showed lower number of peritoneal MØs (pMØs) in comparison to wt but not *Irp1*^{-/-} mice (Fig. 4.8). These results suggest that the lack of *Irp1* and *Irp2* affects myelopoiesis resulting downstream in lower numbers of tissue-resident MØs.

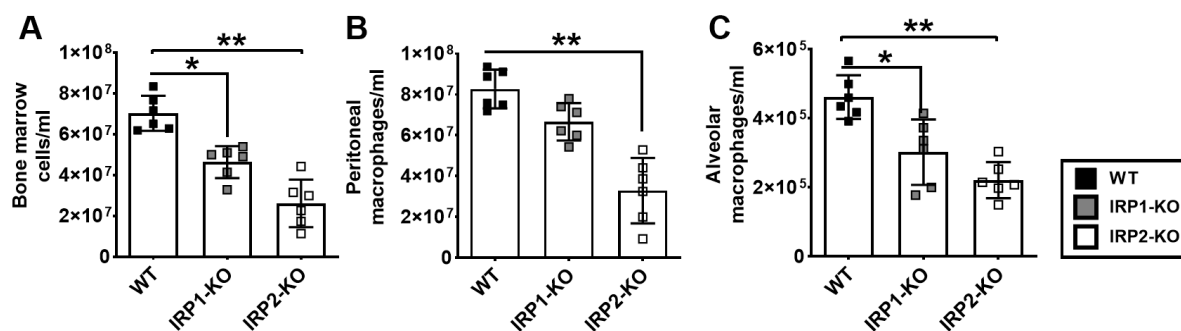


Figure 4.8: Tissue-resident macrophage numbers in wt, *Irp1*^{-/-} and *Irp2*^{-/-} mice. 12-16-week-old female wt, *Irp1*^{-/-} and *Irp2*^{-/-} mice were euthanized by CO₂ exposure. Bone marrow cells (A), pMØ (B) and aMØ (C) were collected, and viable cells were counted. Each square represents an individual sample (n=6 animals). Data pooled from 2 independent experiments and shown as mean ± SD. Statistical analysis was performed using Kruskal-Wallis' nonparametric test with Dunn's multiple comparisons test to compare experimental groups. *p ≤ 0.05 and **p ≤ 0.01 were considered statistically significant.

4.2.2 Investigation of macrophage responsiveness to Mtb

The response of IRP1 and IRP2-deficient MØs to Mtb has not yet been investigated. In line with this, BMMØs, pMØs and aMØs were isolated from non-infected wt, *Irp1*^{-/-} and *Irp2*^{-/-} mice and infected with Mtb at different time points indicated in **Figs. 4.9**. Increasing mycobacterial loads over an observation time of 72h were observed in all MØ types of all three mouse strains but increases were strongest in IRP2-deficient MØs (**Figs. 4.9A-I**).

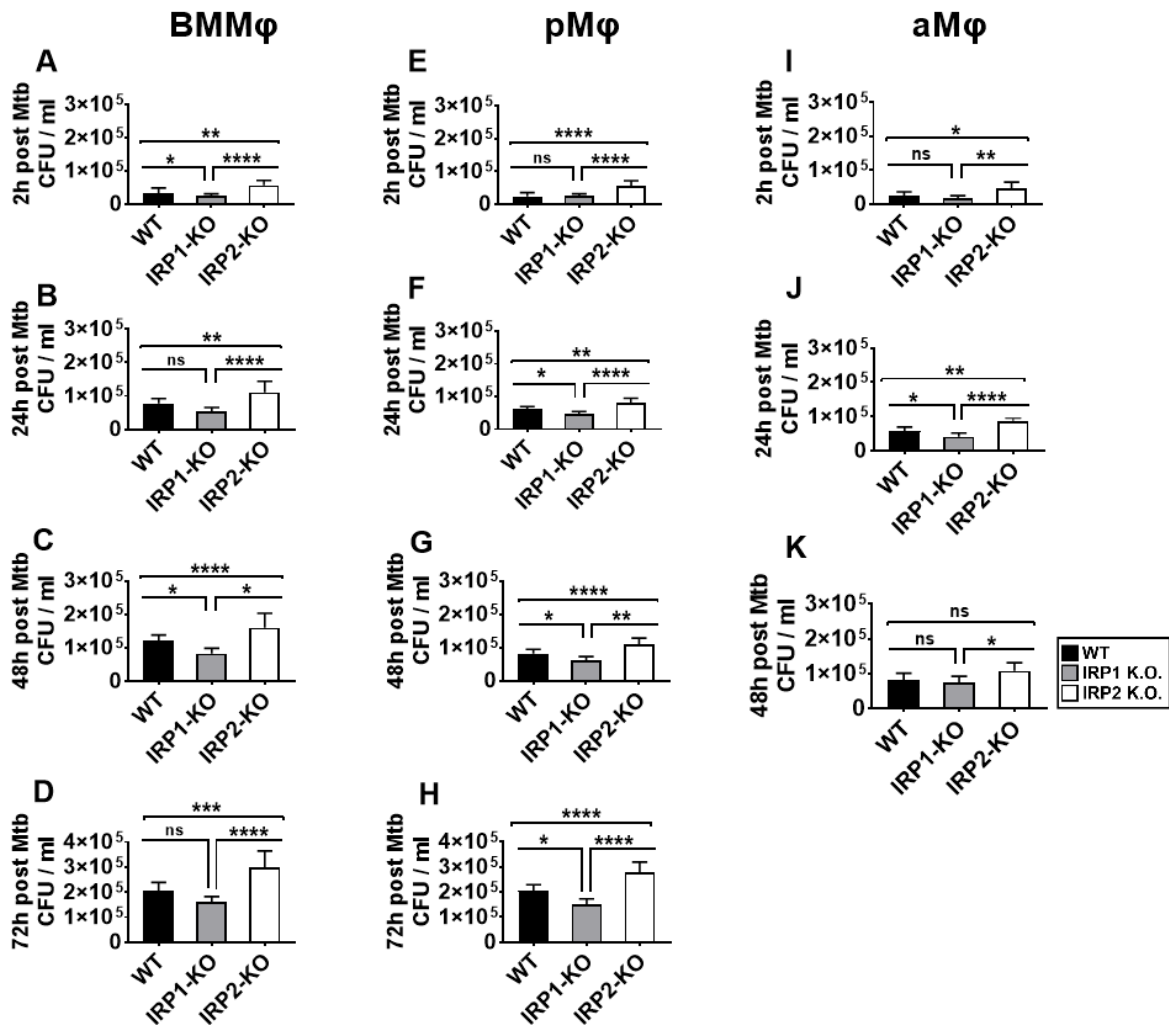


Figure 4.9: Mycobacterial loads in wt, *Irp1*^{-/-} and *Irp2*^{-/-} macrophages. Bone marrow cells were isolated from non-infected wt, *Irp1*^{-/-} and *Irp2*^{-/-} mice and allowed to differentiate to mature BMMØs. 10⁵ BMMØs (A-D), pMØ (E-H) and aMØ (I-K) were infected with Mtb H37Rv (MOI of 0.1:1) to determine the mycobacterial burden at indicated time points. Data pooled from 3 independent experiments with 3 technical replicates each and shown as mean ± SD. Statistical analysis was performed using ordinary one-way ANOVA with Tukey's multiple comparison tests, with single pooled variance. *p ≤ 0.05, **p ≤ 0.01, *** p ≤ 0.001 and **** p ≤ 0.0001 were considered statistically significant.

Upon IFN γ activation, mycobacterial replication was inhibited in all MØ types from all three mouse strains at all indicated time points (**Fig. 4.10A-K**). These observations suggest that the differential permissiveness of *Irp2*^{-/-} versus *Irp1*^{-/-} and wt MØs is overwritten by IFN γ -mediated activation, indicating the disruption of iron metabolism benefiting Mtb

growth in the absence of IRP1 or 2 is overwritten by IFN γ activation of anti-microbial effector molecules.

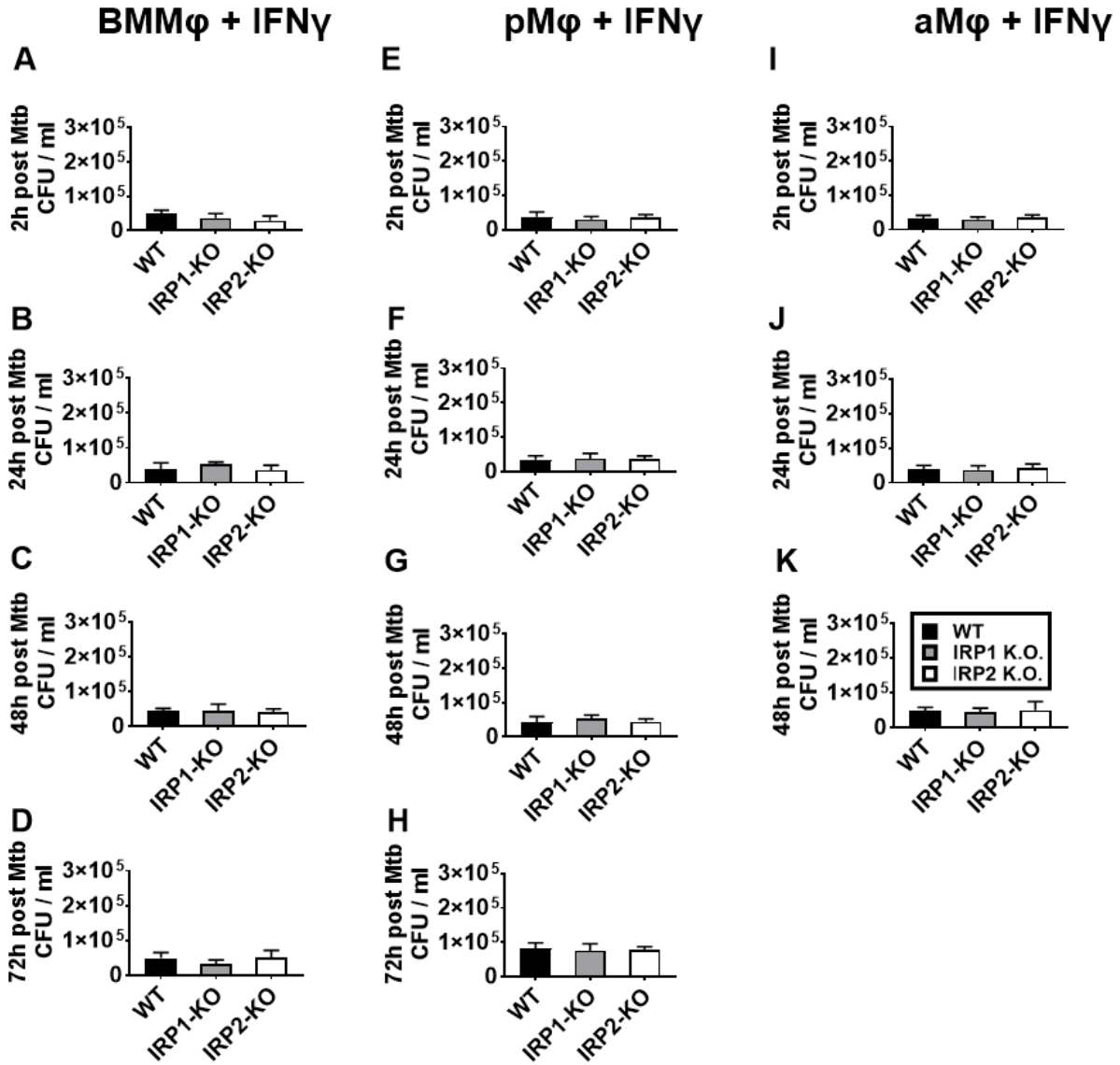


Figure 4.10: Mycobacterial loads in wt, *lrp1*^{-/-} and *lrp2*^{-/-} macrophages following IFN γ stimulation. Bone marrow cells were isolated from non-infected wt, *lrp1*^{-/-} and *lrp2*^{-/-} mice and allowed to differentiate to mature BMM ϕ s. 10⁵ BMM ϕ s (A-D), pM ϕ (E-H) and aM ϕ (I-K) were stimulated with 500 U/ml IFN γ and infected with Mtb H37Rv (MOI of 0.1:1) to determine the mycobacterial burden at indicated time points. Data pooled from 2 independent experiments with 3 technical replicates each and shown as mean \pm SD. Statistical analysis was performed using ordinary one-way ANOVA with Tukey's multiple comparison tests, with single pooled variance.

4.2.3 Determination of phagocytosis rate of bone marrow-derived macrophages

Based on the observed increased growth of Mtb in *lrp2*^{-/-} M ϕ s (Figs. 4.9), it was hypothesized that differential phagocytic abilities between wt, *lrp1*^{-/-} and *lrp2*^{-/-} M ϕ s might explain the differences in permissiveness to Mtb. To assess whether wt, *lrp1*^{-/-} and *lrp2*^{-/-}

MØs have different phagocytic activities, BMMØs isolated from non-infected wt, *Irp1*^{-/-} and *Irp2*^{-/-} mice were studied for uptake of Zymosan particles using an MOI of 3:1. No differences were observed in the phagocytic activity of all BMMØs from all mouse strains which were untreated with Zymosan particles and unstimulated with IFN γ (**Fig. 4.11A**). These BMMØs in (**Fig. 4.11A**) were used as experimental controls. Higher phagocytic activity was observed in *Irp2*^{-/-} BMMØs compared to wt and *Irp1*^{-/-} MØs upon adding Zymosan particles (**Fig. 4.11B**). Treatment of BMMØs with IFN γ equalized the phagocytic activity between all BMMØs (**Fig. 4.11C**) while Cytochalasin D inhibited phagocytosis in all MØs equally (**Fig. 4.11D**). These findings suggest that the higher phagocytic ability of *Irp2*^{-/-} BMMØs may have contributed to the higher mycobacterial loads in comparison to *Irp1*^{-/-} BMMØs.

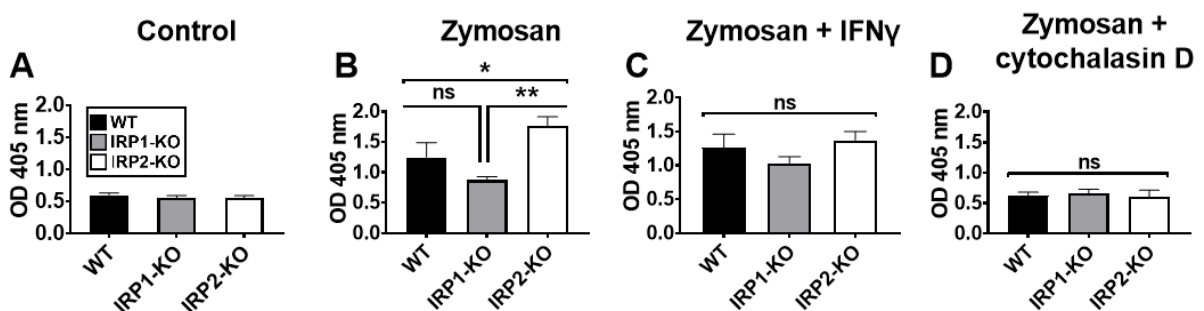


Figure 4.11: Determination of phagocytosis rate in wt, *Irp1*^{-/-} and *Irp2*^{-/-} macrophages. Bone marrow cells were isolated from non-infected wt, *Irp1*^{-/-} and *Irp2*^{-/-} mice and allowed to differentiate to mature BMMØs. 10⁵ BMMØs per well were seeded, and phagocytosis rate was measured in BMMØs which were either untreated with Zymosan particles and unstimulated with IFN γ (A), treated with only Zymosan particles (B), treated with Zymosan particles and stimulated with 500 U/ml IFN γ (C) or treated with Zymosan particles and 10 μ m Cytochalasin D (D). The phagocytosis rate was determined by colourimetric detection at 405 nm. Data are from 1 experiment and shown as mean \pm SD. Statistical analysis was performed using Kruskal-Wallis' nonparametric test with Dunn's multiple comparisons test to compare experimental groups. * $p \leq 0.05$ and ** $p \leq 0.01$ were considered statistically significant. ns represents statistically non-significant differences.

4.2.4 Evaluation of nitric oxide production in macrophages

During Mtb infection, MØs are activated to inhibit mycobacterial replication through the production of nitric oxide (NO) [149]. To investigate the ability of wt, *Irp1*^{-/-} and *Irp2*^{-/-} mice BMMØs to produce NO, BMMØs isolated from non-infected wt, *Irp1*^{-/-} and *Irp2*^{-/-} mice were used. No differences were observed in NO production in non-infected and unstimulated BMMØs indicated in **Figs. 4.12A-D**, as well as in non-infected BMMØs stimulated with IFN γ at all time points indicated in **Figs. 4.12E-H**.

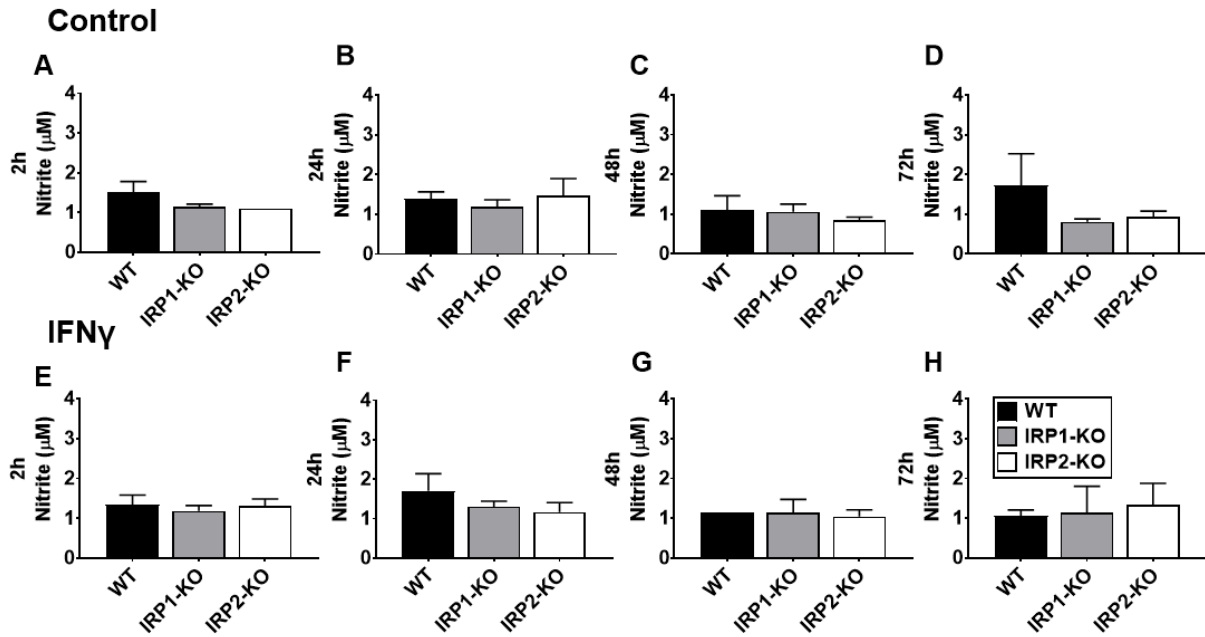


Figure 4.12: Nitric oxide quantification in wt, *lrp1*^{-/-} and *lrp2*^{-/-} non-infected macrophage supernatants. Bone marrow cells were isolated from non-infected wt, *lrp1*^{-/-} and *lrp2*^{-/-} mice and allowed to differentiate to mature BMM ϕ s. 10⁵ BMM ϕ s per well were seeded, and NO levels were estimated in non-infected and unstimulated BMM ϕ s (A-D), non-infected but stimulated with 500 U/ml IFN γ (E-H). Data pooled from 2 independent experiments with 3 technical replicates each and shown as mean \pm SD. Statistical analysis was performed using ordinary one-way ANOVA with Tukey's multiple comparison tests, with single pooled variance.

Following Mtb infection, higher NO production over an observation time of 48h was observed in *lrp1*^{-/-} in comparison to *lrp2*^{-/-} and wt BMM ϕ s (**Fig. 4.13A-D**). Upon activation with IFN γ followed by Mtb infection, higher NO production was observed in all BMM ϕ s, particularly in wt BMM ϕ s at 24-72h p.i. time points in comparison to *lrp1*^{-/-} and *lrp2*^{-/-} BMM ϕ s (**Fig. 4.13E-H**). These observations, particularly in **Fig. 4.13A-D**, suggest higher concentrations of NO produced by *lrp1*^{-/-} BMM ϕ s could account for the better reduction of mycobacterial growth in *lrp1*^{-/-} but not in wt and *lrp2*^{-/-} M ϕ s.

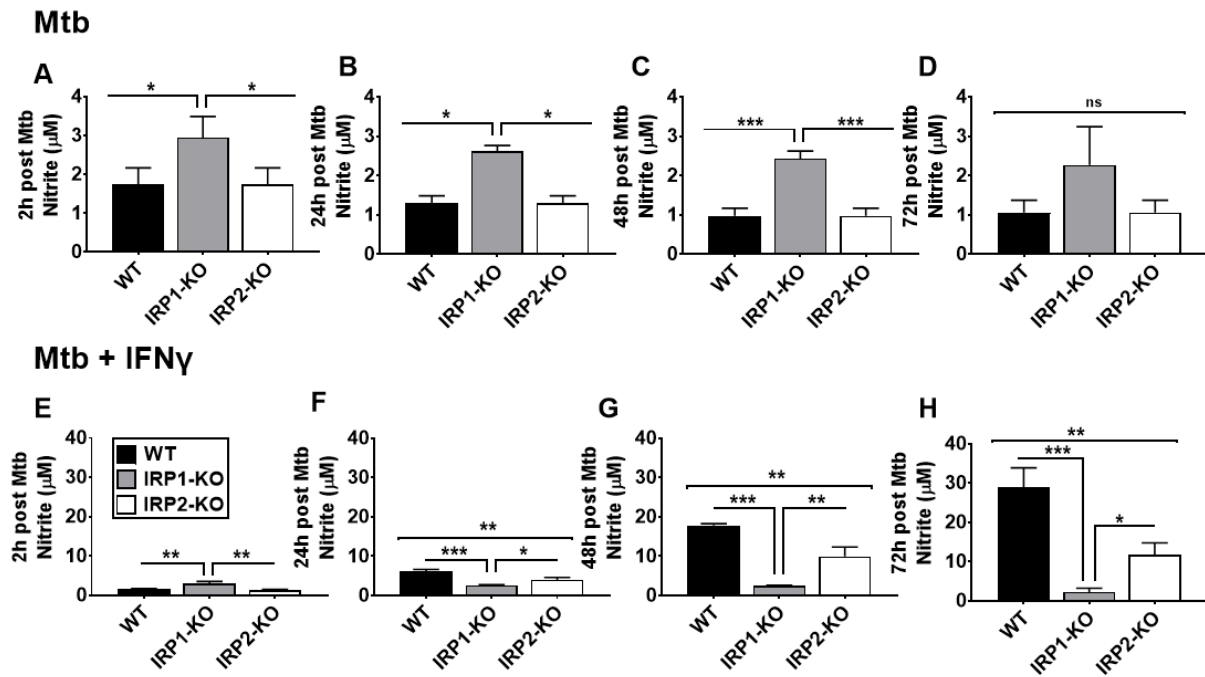


Figure 4.13: Nitric oxide quantification in wt, *lrp1*^{-/-} and *lrp2*^{-/-} Mtb infected macrophage supernatants. Bone marrow cells were isolated from non-infected wt, *lrp1*^{-/-} and *lrp2*^{-/-} mice and allowed to differentiate to mature BMM ϕ s. 10⁵ BMM ϕ s per well were seeded, and NO levels were estimated in BMM ϕ s which were either Mtb infected and unstimulated with IFN γ (A-D) or Mtb infected and stimulated with 500 U/ml IFN γ (E-H). Data pooled from 2 independent experiments with 3 technical replicates each and shown as mean \pm SD. Statistical analysis was performed using ordinary one-way ANOVA with Tukey's multiple comparison tests, with single pooled variance. *p \leq 0.05, **p \leq 0.01 and **** p \leq 0.0001 were considered statistically significant. ns represents statistically non-significant differences.

4.2.5 Permissiveness of macrophages to Mtb following iron supplementation and depletion

Several reports have demonstrated that the administration of exogenous iron increases mycobacterial growth *in vitro* in M ϕ s. Likewise, treatment of M ϕ s with iron-chelating agents has been reported to minimize mycobacterial growth *in vitro* [147]. Therefore, the response of *lrp1*^{-/-} and *lrp2*^{-/-} BMM ϕ s to Mtb infection upon treatment with ferric ammonium citrate (FAC) or deferoxamine mesylate salts (DFO) was investigated. Firstly, untreated BMM ϕ s isolated from non-infected wt, *lrp1*^{-/-} and *lrp2*^{-/-} mice were infected with Mtb to serve as controls. Here, increasing mycobacterial loads were observed over an observation time period of 72h from all mouse genotypes but increases were strongest in *lrp1*^{-/-} and *lrp2*^{-/-} BMM ϕ s (**Fig. 4.14A-D**). Similarly, all FAC-treated BMM ϕ s from all mouse genotypes showed augmenting Mtb loads but again, increases were strongest in *lrp2*^{-/-} BMM ϕ s at 2h, 48h, and 72h p.i. when compared to *lrp1*^{-/-} BMM ϕ s only (**Fig. 4.14E-H**). To demonstrate the consequences of iron chelation on IRP-deficient BMM ϕ s following Mtb infection, BMM ϕ s from non-infected wt, *lrp1*^{-/-} and *lrp2*^{-/-} mice were treated with 100 μ M DFO. DFO did not influence mycobacterial replication in all BMM ϕ s (**Fig. 4.14I-L**). These results confirm observations from other authors that increased iron availability promotes Mtb growth in M ϕ s. The observation that iron chelation is inefficient in decreasing Mtb growth could be due to

the lower affinity of DFO.

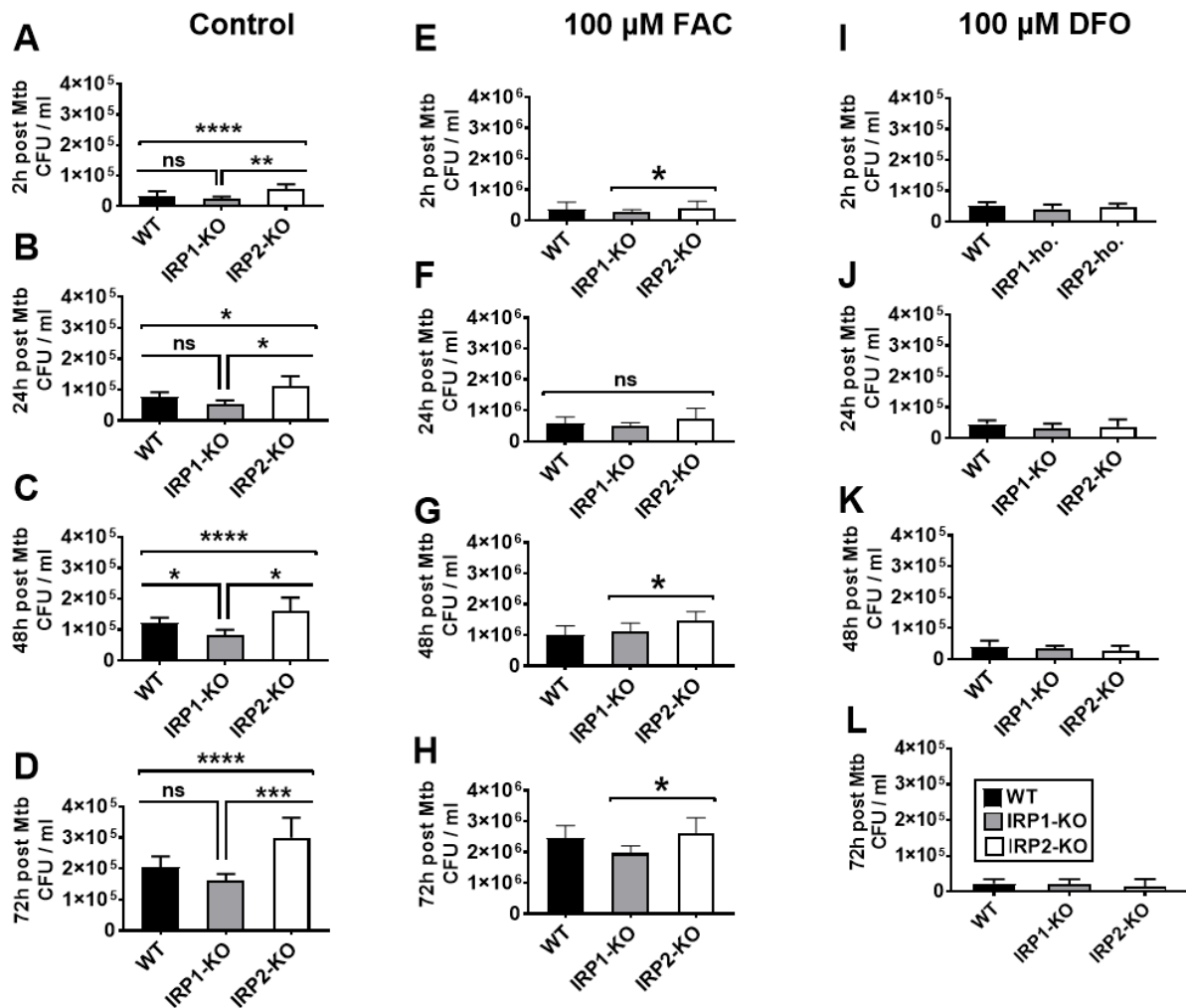


Figure 4.14: Mycobacterial loads in wt, *Irp1*^{-/-} and *Irp2*^{-/-} macrophages following FAC or DFO treatment. Bone marrow cells were isolated from non-infected wt, *Irp1*^{-/-} and *Irp2*^{-/-} mice and allowed to differentiate to mature BMMØs. 10⁵ BMMØs per well were infected with Mtb (MOI of 0.1:1) (A-D) and treated with either FAC (E-H) or DFO (I-L) to determine the mycobacterial burden at indicated time points. Data pooled from 2 independent experiments with 3 technical replicates each and shown as mean ± SD. Statistical analysis was performed using ordinary two-way ANOVA with Tukey's multiple comparison tests, with single pooled variance. *p ≤ 0.05, **p ≤ 0.01 and **** p ≤ 0.0001 were considered statistically significant. ns represents statistically non-significant differences.

4.3 The Influence of Iron Regulatory Proteins 1 and 2 on Host Responsiveness to Mtb Infection

Recently, the relevance of IRPs in mediating murine host resistance against experimental *S. enterica* serovar Typhimurium has been reported [136]. However, no study has investigated the role of IRPs in murine Mtb infection. Both Mtb and *S. Typhimurium* are intracellular pathogens which depend on host-derived iron sources [150, 151]. Given the similarities between Mtb and *S. Typhimurium*, with respect to their niche and reliance on iron, it was hypothesized that IRPs might contribute to host responsiveness to Mtb.

4.3.1 Investigation of host responsiveness to Mtb

To address this hypothesis, female wt, *Irp1*^{-/-} and *Irp2*^{-/-} mice were infected with 100 CFU Mtb via aerosol route and mycobacterial burdens were determined on days 13, 28 and 63 p.i. Mycobacterial replication was observed in the mice's lungs, spleens, and livers over time. Higher mycobacterial loads were observed in the lungs of *Irp2*^{-/-} mice compared to *Irp1*^{-/-} and wt mice at day 13 p.i. Interestingly, at day 28 p.i., *Irp2*^{-/-} mice showed three times higher bacterial load than *Irp1*^{-/-} and wt mice. At day 63 p.i., the bacterial load was equalized to similar levels in all three mouse genotypes indicating that *Irp2* contributes to the control of Mtb during the exponential mycobacterial growth phase (**Fig.4.15A**).

Compared to wt and *Irp1*^{-/-} mice, significantly higher CFUs were observed in spleens of *Irp2*^{-/-} mice at day 28 p.i. At day 63 p.i., significantly higher Mtb loads were observed between *Irp2*^{-/-} and wt mice only but not *Irp1*^{-/-} mice (**Fig.4.15B**).

In the liver, higher Mtb loads were observed in *Irp2*^{-/-} mice compared to wt and *Irp1*^{-/-} at days 28 and 63 p.i. (**Fig.4.15C**). Taken together, these results show that IRP1 and IRP2, though with different roles, are involved in host responses, which control Mtb replication.

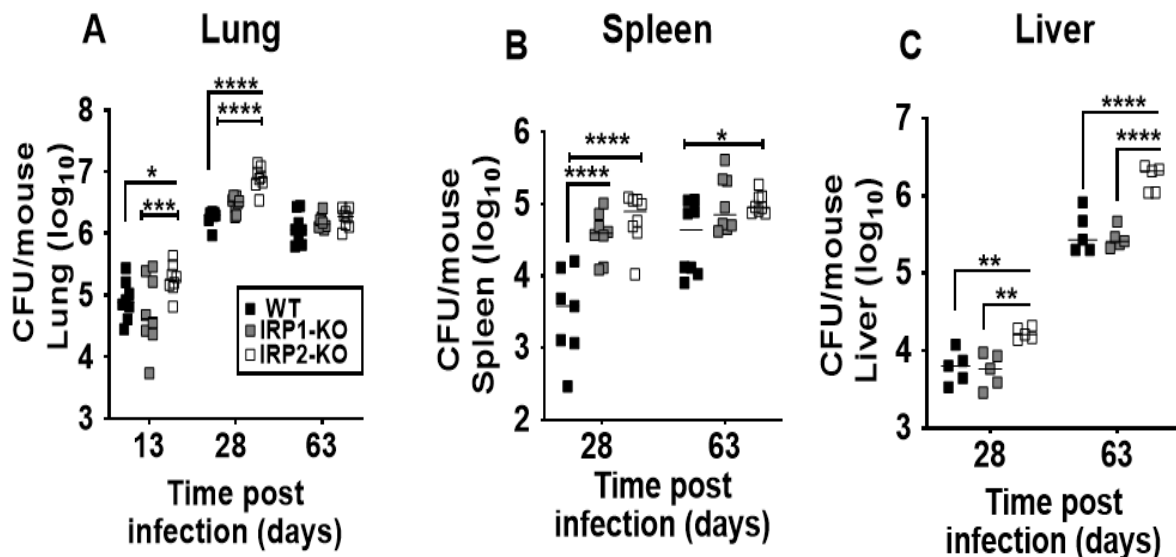


Figure 4.15: Mycobacterial loads in tissue homogenates from wt, *Irp1*^{-/-} and *Irp2*^{-/-} mice. 8-20-week-old female wt, *Irp1*^{-/-} and *Irp2*^{-/-} mice were infected with 100 CFU Mtb via the aerosol route. CFU assays were performed, and the mycobacterial loads in lungs (A), spleens (B), and livers (C) were determined at indicated time points. Each square represents an individual sample. Data pooled from 2 independent experiments (n=8 animals for panels A and B, n= 5 animals for panel C), log-transformed and as shown as mean ± SD. Statistical analysis was performed using two-way ANOVA with Tukey's multiple comparisons tests. *p ≤ 0.05, **p ≤ 0.01, ***p ≤ 0.001 and ****p ≤ 0.0001 were considered statistically significant.

4.3.2 Clinical and pathological signs of Mtb infection

Following experimental infection of wt, *Irp1*^{-/-} and *Irp2*^{-/-} mice with Mtb H37Rv via the aerosol route, mice were monitored for clinical signs of disease throughout the infection. Based on the clinical scoring scheme described in section 3.2.4, no clinically obvious symptoms were observed in Mtb infected wt, *Irp1*^{-/-} and *Irp2*^{-/-} mice. Mice were weighed weekly, and their body weights were recorded. A significant increase in overall body weight was observed in

Irp2^{-/-} mice at days 14-35, 49 and 63 p.i. in comparison to wt or *Irp1*^{-/-} mice (**Fig.4.16**). This data shows that *Irp2*^{-/-} mice gained weight despite the higher mycobacterial loads.

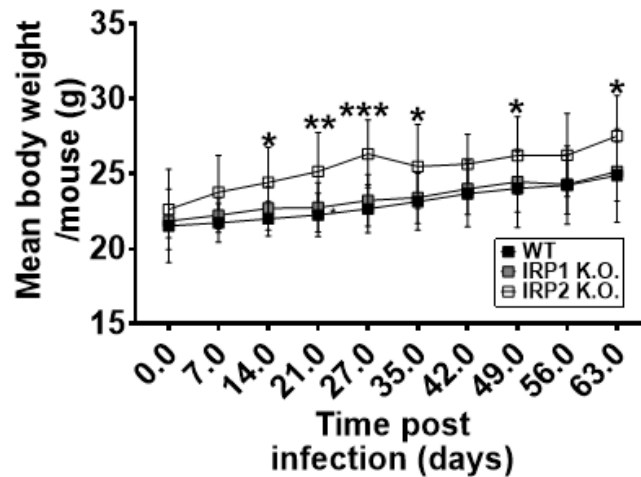


Figure 4.16: Mean body weights of wt, *Irp1*^{-/-} and *Irp2*^{-/-} mice. 8-20-week-old female wt, *Irp1*^{-/-} and *Irp2*^{-/-} mice were monitored for fluctuations in weight prior to and during infection with 100 CFU Mtb via the aerosol route. Data pooled from 2 independent experiments (n=7-8 animals) and shown as mean \pm SD. Statistical analysis was performed using two-way ANOVA with Tukey's multiple comparisons tests. *p \leq 0.05, **p \leq 0.01 and *** p \leq 0.001 were considered statistically significant.

Based on the differences observed between the overall body weights between the different mouse genotypes, a comparative analysis of lung and spleen weights and numbers of viable cells in these organs was investigated. A significant increase in lung weight and number of viable immune cells were observed in *Irp1*^{-/-} mice compared to wt mice but not *Irp2*^{-/-} mice at day 28 days p.i. (**Figs. 4.17A-C**).

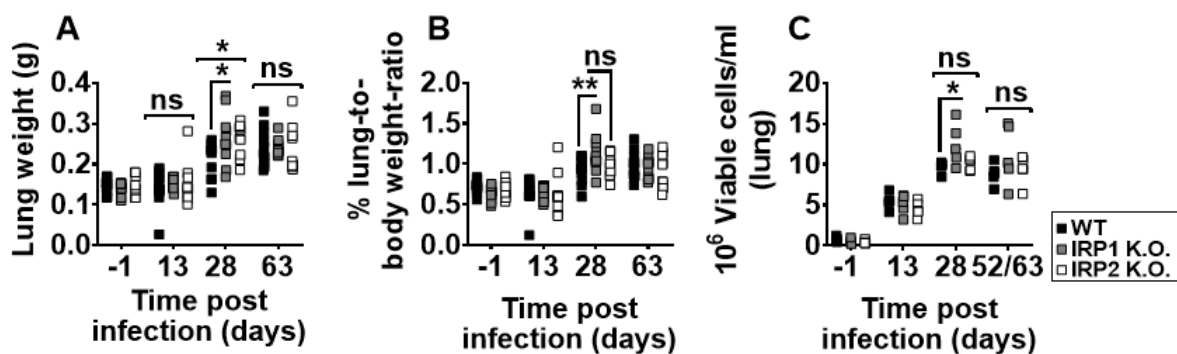


Figure 4.17: Relative organ weight and viable immune cell count in lungs from wt, *Irp1*^{-/-} and *Irp2*^{-/-} mice. 8-20-week-old wt, *Irp1*^{-/-} and *Irp2*^{-/-} mice were infected with 100 CFU Mtb via the aerosol route. Lungs were collected, and lung weights (A), lung-to-body weight-ratio (B) and the number of immune cells (C) were recorded. Each square represents an individual sample (n=7-8 animals for panels A and B, 5 animals for panel C). Data pooled from 2 independent experiments and shown as mean \pm SD. Statistical analysis was performed using two-way ANOVA with Tukey's multiple comparisons tests. *p \leq 0.05 and **p \leq 0.01 were considered statistically significant. ns represents statistically non-significant differences.

4.3. The Influence of Iron Regulatory Proteins 1 and 2 on Host Responsiveness to Mtb Infection

Though not statistically significant, splenomegaly was observed in non-infected *Irp1*^{-/-} mice compared to wt and *Irp2*^{-/-} mice confirming observations from other studies [137, 152]. Remarkably, at day 28 p.i., the splenomegaly phenotype was exacerbated in *Irp1*^{-/-} mice versus wt and *Irp2*^{-/-} mice (**Fig. 4.18 A-D**). Exacerbated splenomegaly was accompanied by a significant increase in spleen weight and number of viable immune cells (**Fig. 4.18A-c**). Nevertheless, this phenotype vanished at day 63 p.i. with no observable differences between wt, *Irp1*^{-/-} and *Irp2*^{-/-} mice.

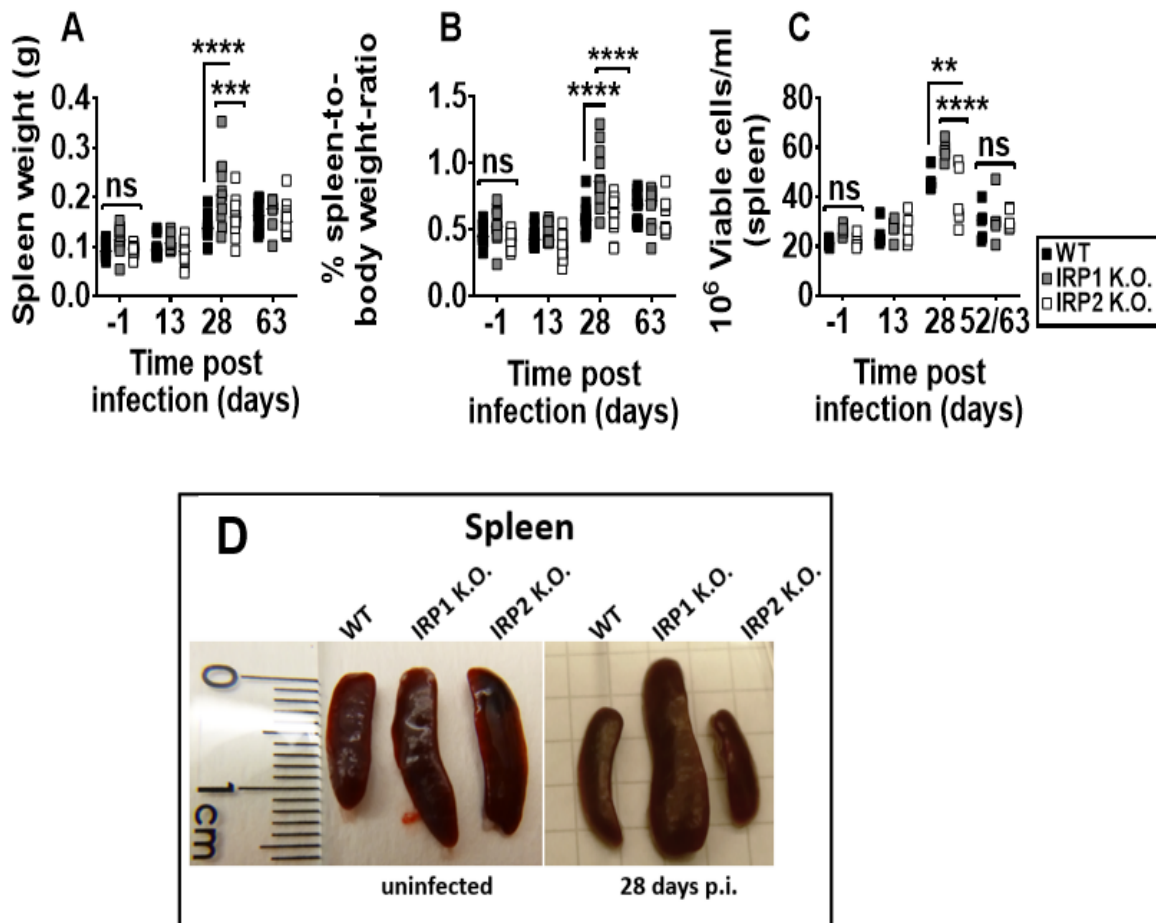


Figure 4.18: Relative organ weight and viable immune cell count in spleens from wt, *Irp1*^{-/-} and *Irp2*^{-/-} mice. 8–20-week-old wt, *Irp1*^{-/-} and *Irp2*^{-/-} mice were infected with 100 CFU Mtb via the aerosol route. Spleens were collected, and respective weights (A), spleen-to-body-weight-ratio (B) and number of viable immune cells (C) were recorded. Each square represents an individual sample (n=7-8 animals for panels A and B, 5 animals for panel C). Data pooled from 2 independent experiments and shown as mean ± SD. Statistical analysis was performed using two-way ANOVA with Tukey's multiple comparisons tests. *p ≤ 0.05 and **p ≤ 0.01 were considered statistically significant. ns represents statistically non-significant differences. Macroscopic assessment of mice spleens was performed (D). Representative photograph of 1 animal spleen per mouse strain out of 8 per group are shown, i.e., from 2 independent experiments.

4.3.3 Cytokine and chemokine quantification

Pro-inflammatory cytokines such as IL-1 β , IL-6, IL-12, TNF α , and IFN γ are crucial in host immunity against mycobacterial infections [153]. Following the differential responses of wt, *Irp1*^{-/-} and *Irp2*^{-/-} mice to Mtb infection, the cytokine and chemokine profiles in the lung and spleen tissue homogenates of non-infected and Mtb infected wt, *Irp1*^{-/-} and *Irp2*^{-/-} were investigated using a customized immunoassay. In all mouse strains, the proinflammatory cyto- and chemokines were increased by Mtb infection primarily at day 28 p.i. (**Fig. 4.19 and 4.20**).

In the lungs, higher concentrations of inflammatory mediators such as IFN γ , TNF α , IL-1 β , and IL-6 were observed in lungs of *Irp2*^{-/-} compared to wt and *Irp1*^{-/-} mice at day 28 p.i. (**Fig. 4.19A-D**). Additionally, chemokines such as Keratinocyte chemoattractant (KC/GRO), monocyte chemoattractant protein (MCP-1), and macrophage inflammatory protein 2 (MIP-2) and were significantly elevated in lungs of *Irp2*^{-/-} mice at day 28 p.i. compared to wt and/or *Irp1*^{-/-} mice (**Fig. 4.19F-H**). Of note, KC/GRO and MIP-2 concentrations were elevated in lungs of *Irp2*^{-/-} mice at day 28 p.i, compared to wt but not *Irp1*^{-/-} mice lungs (**Fig. 4.19F and H**). Similarly, higher concentrations of the MCP-1 were observed in *Irp2*^{-/-} compared to wt but not *Irp1*^{-/-} mice at day 28 p.i. (**Fig. 4.19G**).

At day 63 p.i., lower concentrations of all these cyto- and chemokines were observed in all mouse strains (**Fig. 4.19A-G**), indicating a reduction in inflammation which correlates with lung CFU data (**Fig. 4.15A**). Nevertheless, higher concentrations of IFN γ , TNF α and MCP-1 were observed in *Irp2*^{-/-} mice compared to wt and *Irp1*^{-/-} mice at this time point (**Fig. 4.19A, B and G**). These results show that Mtb infection promotes increased production of pro-inflammatory cytokines and chemokines which was higher in *Irp2*^{-/-} compared to wt and *Irp1*^{-/-} mice in the early phase of infection when compared to the late stage of infection.

In the spleens, higher concentrations of inflammatory mediators such as IFN γ (**Fig. 4.20A**) and IL-6 (**Fig. 4.20D**) were observed in spleens of *Irp2*^{-/-} compared to wt and *Irp1*^{-/-} mice at day 28 p.i. Augmented concentrations of IL-1 β (**Fig. 4.20C**) and IL-17A (**Fig. 4.20F**) were observed in spleens of *Irp2*^{-/-} compared to wt but not *Irp1*^{-/-} mice at day 28 p.i. Furthermore, chemokines such as KC/GRO (**Fig. 4.20G**) and MCP-1 (**Fig. 4.20H**) were significantly elevated in spleens of *Irp2*^{-/-} mice at day 28 p.i. compared to wt and *Irp1*^{-/-} mice at day 28 p.i.

At day 63 p.i., lower concentrations of all these cyto- and chemokines were observed in all mouse strains (**Fig. 4.20A-I**), showing a reduction in inflammation. However, higher concentrations of IFN γ , KC/GRO and MCP-1 were observed in *Irp2*^{-/-} mice compared to wt mice at this time point (**Fig. 4.20A, G and H**). Interestingly, no differences in the concentration of IL-10 were observed in all mouse genotypes at all time points (**Fig.4.20E**). These findings indicate that Mtb infection enhances the production of pro-inflammatory cytokines and chemokines, particularly in the early stage of infection, with higher levels observed in *Irp2*^{-/-} mice as compared to both wt and *Irp1*^{-/-} mice.

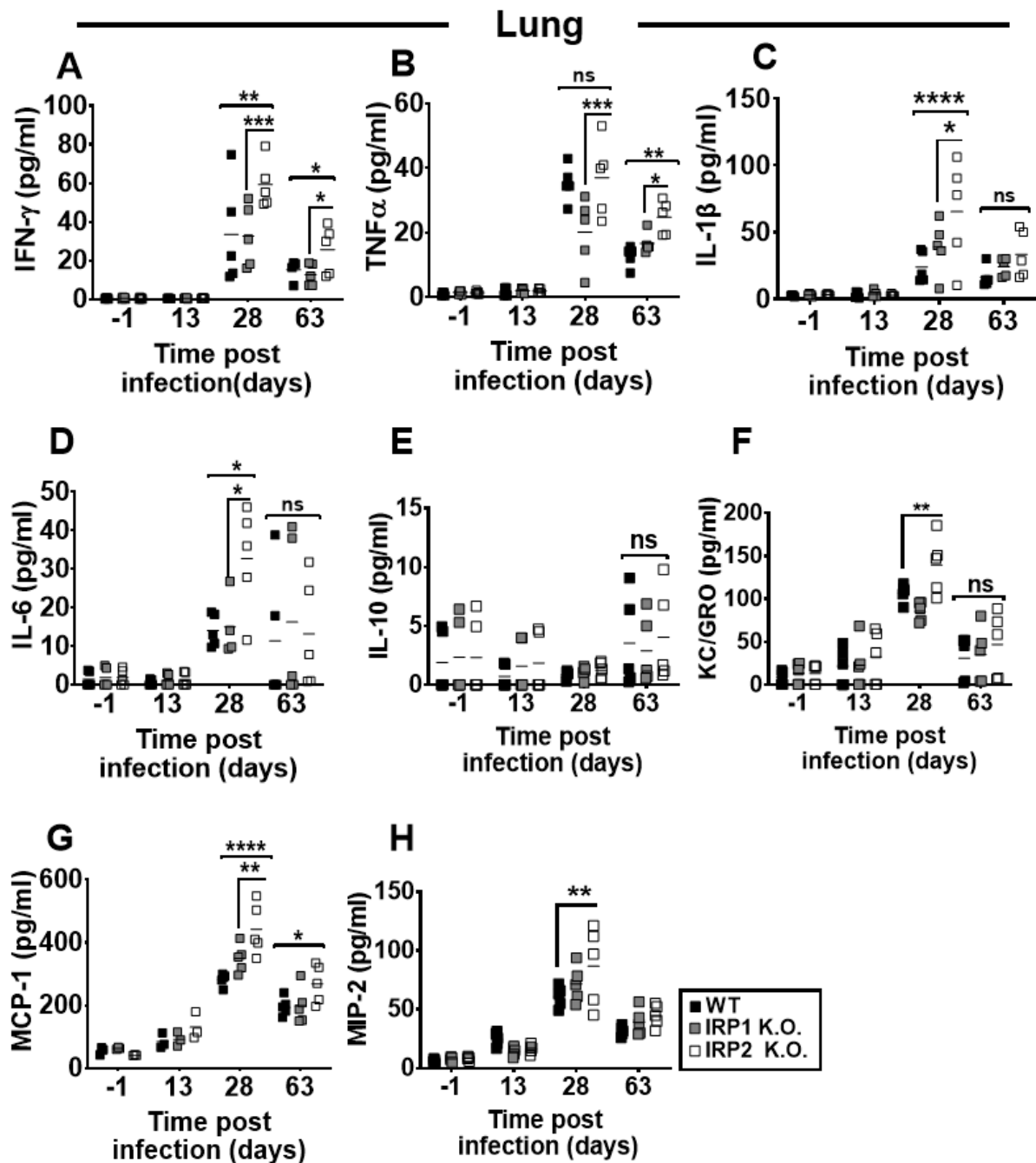


Figure 4.19: Cytokines and chemokine quantification in lung homogenates from wt, *lrp1*^{-/-} and *lrp2*^{-/-} mice. 8-20-week-old female wt, *lrp1*^{-/-} and *lrp2*^{-/-} mice were infected with 100 CFU of Mtb via the aerosol route and sacrificed at indicated time points. Lungs were collected and homogenized for the investigation of IFN γ (A) TNF α (B) IL-1 β (C) IL-6 (D) IL-10 (E) KC/GRO (F) MCP-1 (G) MIP-2 (H) production. Each square represents an individual sample (n=5 animals). Data pooled from 2 independent experiments and shown as mean \pm SD. Statistical analysis was performed using two-way ANOVA with Tukey's multiple comparisons tests. * $p \leq 0.05$, ** $p \leq 0.01$, *** $p \leq 0.001$ and **** $p \leq 0.0001$ were considered statistically significant. ns represents statistically non-significant differences.

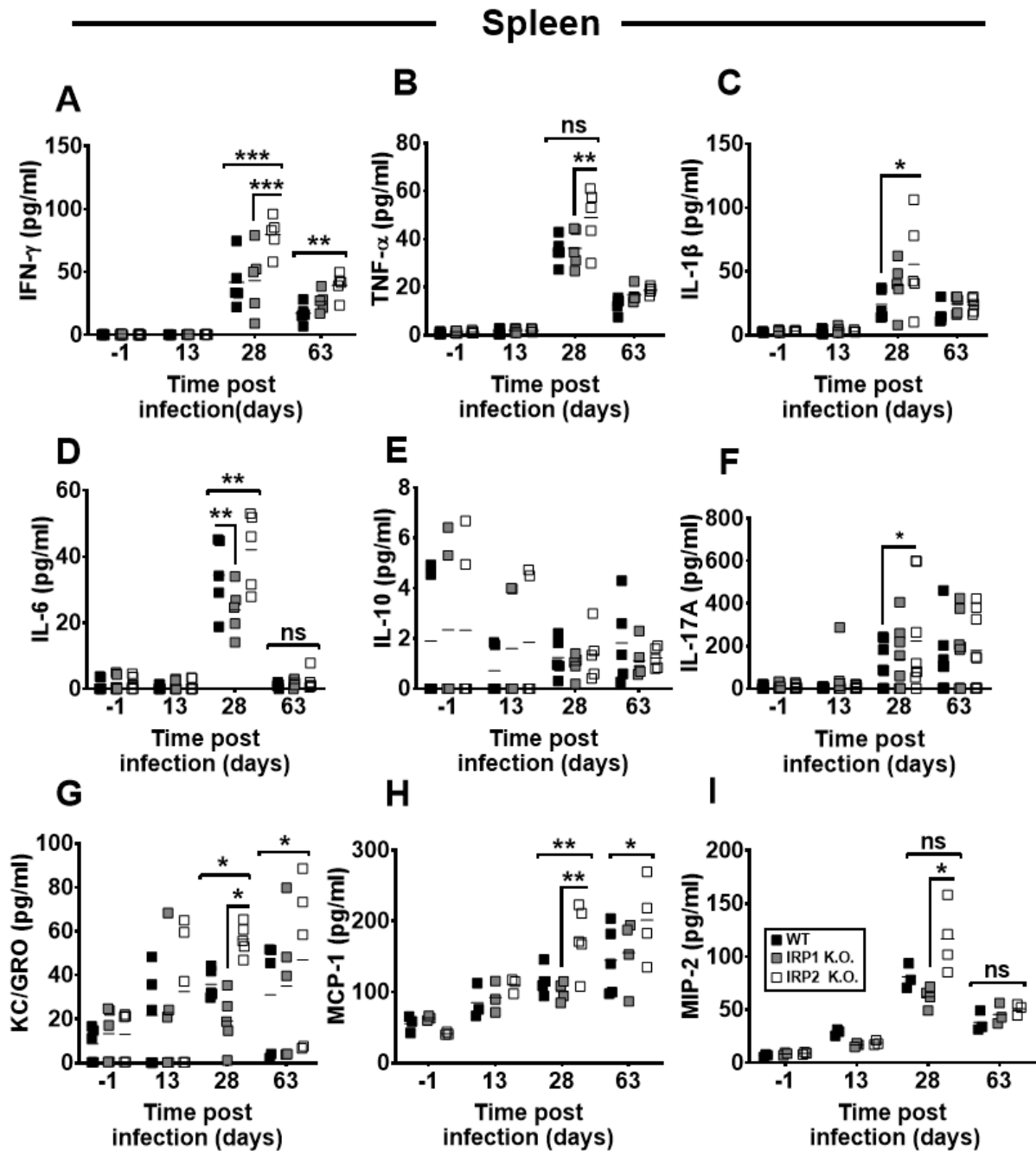


Figure 4.20: Cytokines and chemokine quantification in spleen homogenates from wt, *lrp1*^{-/-} and *lrp2*^{-/-} mice. 8-20-week-old female wt, *lrp1*^{-/-} and *lrp2*^{-/-} mice were infected with 100 CFU of *Mtb* via the aerosol route and sacrificed at indicated time points. Spleens were collected, and homogenates were used for the investigation of IFN γ (A), TNF α (B), IL-1 β (C), IL-6 (D), IL-10 (E), IL-17A (F), KC/GRO (G) MCP-1 (H) MIP-2 (I) production. Each square represents an individual sample (n=5 animals). Data pooled from 2 independent experiments and shown as mean \pm SD. Statistical analysis was performed using two-way ANOVA with Tukey's multiple comparisons tests. * $p \leq 0.05$, ** $p \leq 0.01$, *** $p \leq 0.001$ and **** $p \leq 0.0001$ were considered statistically significant. ns represents statistically non-significant differences.

4.3.4 Determination of iNOS

Host antimicrobial effector mechanisms are important in mounting an immune response during TB infection. One of such mechanisms is the production of nitric oxide from L-arginine by iNOS upon stimulation by inflammatory cytokines such as $\text{TNF}\alpha$, $\text{IFN}\gamma$ and members of the IL-1 family [153]. To investigate the histopathological implications of pro-inflammatory cytokines such as $\text{IFN}\gamma$ levels in $\text{Irp2}^{-/-}$ mice, lung tissues were stained with anti-NOS2 antibody to detect NOS2 in MØs. Slightly more NOS2-positive aMØs was observed in $\text{Irp2}^{-/-}$ mice compared to wt and $\text{Irp1}^{-/-}$ mice lungs at day 28 p.i. (**Fig.4.21**). These differences were diminished in all mice genotypes at days 63 p.i. (data not shown).

Anti-NOS2 IHC stain

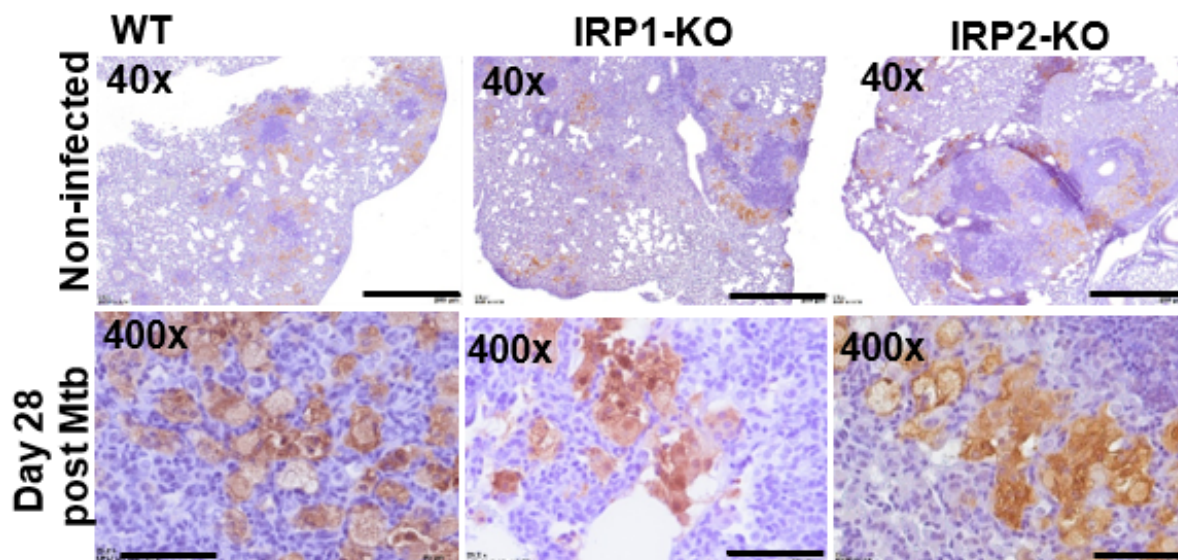


Figure 4.21: Immunohistological staining for NOS2-positive macrophages in lung tissue sections from wt, $\text{Irp1}^{-/-}$ and $\text{Irp2}^{-/-}$ mice. 8-20-week-old female wt, $\text{Irp1}^{-/-}$ and $\text{Irp2}^{-/-}$ were infected with 100 CFU of Mtb H37Rv via the aerosol route. Superior lung lobes were collected, PFA fixed, and paraffin-embedded. NOS2 in lung tissue sections was detected by anti-NOS2 antibody followed by treatments with biotinylated goat anti-rabbit secondary antibody, avidin-biotin complex, and DAB peroxidase substrate. Sections were counterstained with Gill's Hematoxylin and examined under the BX41 light microscope. Gill's Hematoxylin stains the nuclei purple while anti-NOS2 antibody stains the NOS2 within MØs copper brown. Representative micrographs of 1 animal out of 4 per group are shown. Scale bars represent 500 μm and 100 μm . Abbreviation: IHC= immunohistochemistry.

To quantify *Nos2* gene expression in the lungs of these mice, qRT-PCR was performed. Though statistically insignificant, a trend toward higher *Nos2* expression was observed in $\text{Irp2}^{-/-}$ mice at days 13 and 63 p.i. However, at day 28 p.i., higher *Nos2* mRNA transcripts levels were observed in $\text{Irp2}^{-/-}$ mice compared to wt and $\text{Irp1}^{-/-}$ mice (**Fig.4.22A**), thereby confirming the NOS2 stain data (**Fig.4.21A**). Similarly, higher nitric oxide concentrations were observed in lung homogenates of $\text{Irp2}^{-/-}$ mice in comparison to wt and $\text{Irp1}^{-/-}$ mice at day 28 p.i. but not on days 13 or 63 p.i. (**Fig.4.22B**). Though these findings show that $\text{Irp2}^{-/-}$ mice have higher nitric oxide levels and increased *Nos2* mRNA transcripts at day 28 p.i., these results also suggest a delay or defect in effector mechanisms in $\text{Irp2}^{-/-}$ mice in controlling Mtb replication.

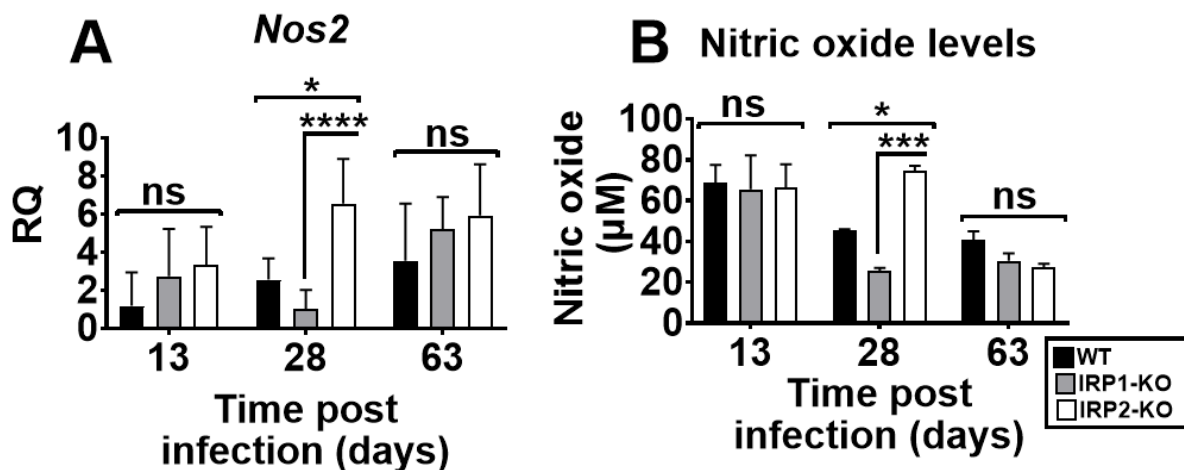


Figure 4.22: Determination of RNI in lungs from wt, *lrp1*^{-/-} and *lrp2*^{-/-} mice. 8-20-week-old female wt, *lrp1*^{-/-} and *lrp2*^{-/-} mice were infected with 100 CFU of Mtb H37Rv via the aerosol route and sacrificed at indicated time points. Lungs were collected, and total host cellular RNA was extracted. Complementary DNA was synthesized and used to quantify *Nos2* gene expression via qRT-PCR (A). All mRNA expression levels were normalized against murine *Hprt* mRNA expression levels. In lung homogenates, the protein concentrations of nitric oxide was also measured (B). Data are from 1 experiment (n=4 animals) and shown as mean ± SD. Statistical analysis was performed using two-way ANOVA with Tukey's multiple comparison tests. *p ≤ 0.05, *** p ≤ 0.001 and **** p ≤ 0.0001 were considered statistically significant. ns represents non-statistically significant differences. Abbreviations: RQ = Relative quantification, Nos2= Nitric oxide synthase 2.

4.3.5 Histopathological analysis of lung and liver tissue

In line with the higher bacterial loads observed in the lungs and livers of *lrp2*^{-/-} mice compared to wt and *lrp1*^{-/-} mice, the question was asked whether histopathological alterations reflect these differential bacterial loads. Here, lung sections of wt, *lrp1*^{-/-} and *lrp2*^{-/-} mice were stained with H&E. Inflammatory cellular infiltration at the sites of infection and larger inflammatory lesions (black squares and black arrows) were observed in the lungs of Mtb infected *lrp2*^{-/-} mice at day 28 p.i., which were larger compared to those in wt and *lrp1*^{-/-} mice (**Fig. 4.23A and C**). However, wt mice developed large areas of pulmonary inflammation occurring mainly at the rim of the lung and *lrp1*^{-/-} mice formed larger "granuloma-like" structures containing large necrotic areas while the *lrp2*^{-/-} mice had smaller cellular infiltrates, which were however more numerous in comparison to *lrp1*^{-/-} mice but also contained central necrotic areas. On day 63 p.i., no differences in histopathological alterations were observed in any of the three mouse strains (**Fig. 4.23B and C**).

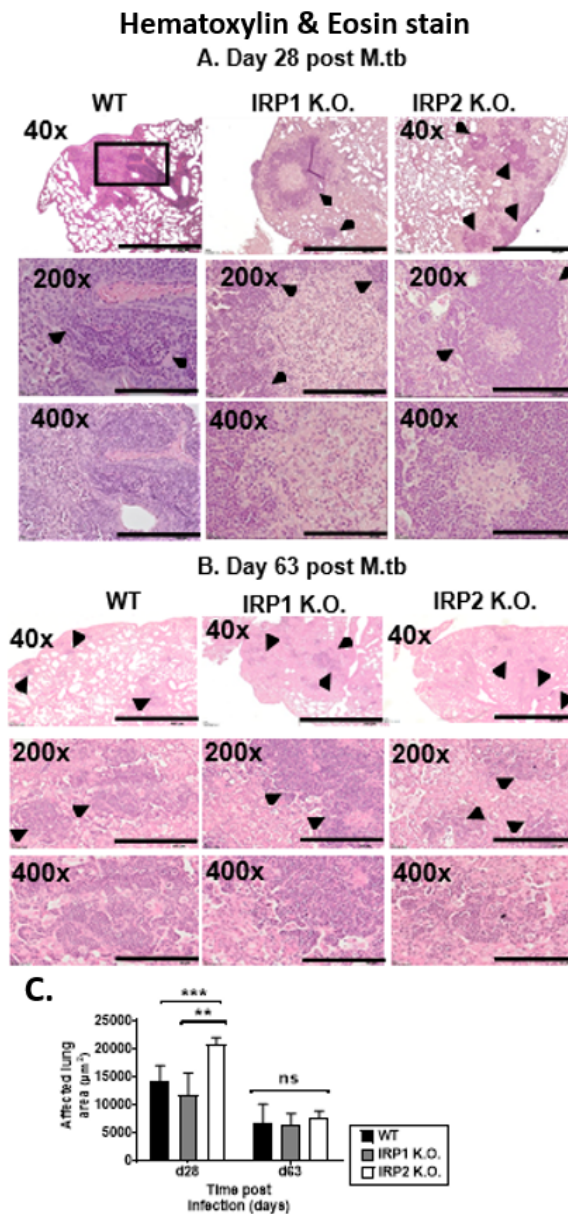


Figure 4.23: Histopathological analysis of lung tissue sections from wt, *Irp1*^{-/-} and *Irp2*^{-/-} mice. 8-20-week-old female wt, *Irp1*^{-/-} and *Irp2*^{-/-} mice were infected with 100 CFU of Mtb via the aerosol route. Superior lung lobes were collected, PFA fixed, and paraffin-embedded. Tissue sections were stained at days 28 (A) and 63 p.i. (B) with H&E stain and examined at indicated magnifications. Representative micrographs of 1 animal out of 8 per group are shown, i.e., from 2 independent experiments. Black squares and arrows show inflammatory cellular infiltrates. Scale bars represent Scale bars represent 500 µm, 200 µm and 50 µm (40x, 10x and 40x magnification, respectively). Quantitative assessment of cellular infiltrates and lesions of lung tissue (C). Data generated from quantification is from 1 experiment (n=4 animals). Statistical analysis was performed using two-way ANOVA with Tukey's multiple comparisons tests. **p ≤ 0.01 and ***p ≤ 0.001 were considered statistically significant, and ns represents statistically non-significant differences

In the liver, immune cell infiltration was observed in all mouse genotypes at days 28 and 63 p.i. However, at day 63 p.i. more cellular infiltrates were observed in liver sections of *Irp2*^{-/-} mice compared to wt or *Irp1*^{-/-} mice (Fig. 4.24 A-B), thereby reflecting the differential

liver CFU data (Fig. 4.15C)

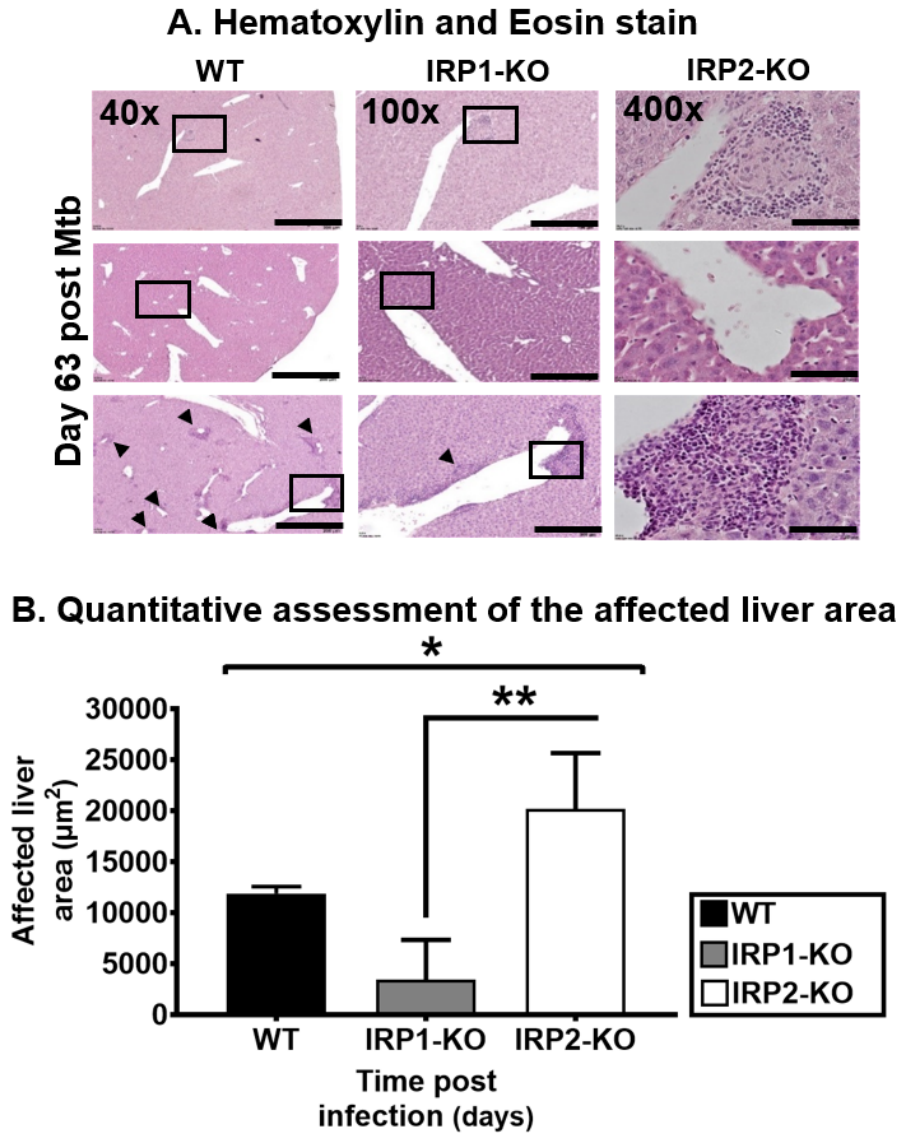


Figure 4.24: Histopathological analyses of liver tissue sections from wt, *Irp1*^{-/-} and *Irp2*^{-/-} mice. 8-20-week-old female wt, *Irp1*^{-/-} and *Irp2*^{-/-} mice were infected with 100 CFU of Mtb H37Rv via the aerosol route. Left liver lobes were collected, PFA fixed, and paraffin infiltrated at 63 days p.i., stained with H&E stain, and examined under the BX41 light microscope (A). Hematoxylin stains the nuclei blue-purple while eosin stains the cytoplasm and extracellular matrix pink. Representative micrographs of 1 animal out of 8 per group (i.e., from 2 independent experiments) are shown. Scale bars represent 500 µm, 200 µm and 50 µm (40x, 10x and 40x magnification, respectively). Black squares and arrows indicate inflammatory cellular infiltrates. Quantitative assessment of cellular infiltrates and lesions of lung tissue (B). Data generated from quantification is from 1 experiment, n=4 animals. Statistical analysis was performed using two-way ANOVA with Tukey's multiple comparisons test tests. **p ≤ 0.01 and *** p ≤ 0.001 were considered statistically significant, and ns represents statistically non-significant differences.

Mtb thrives in “foamy” MØs rich in lipid droplets within granulomas. Reportedly, Mtb utilizes these host lipids as a Carbon source [154]. Therefore, lipid droplets in the lungs of wt, *Irp1*^{-/-}

and *Irp2*^{-/-} mice were investigated using Oil Red O (ORO), a neutral lipid stain. Higher numbers ORO positive “foamy” MØs were observed in the lungs of Mtb-infected *Irp2*^{-/-} mice at day 63 p.i. when compared to *Irp1*^{-/-} and wt mice (**Fig. 4.25**). This suggests that Mtb stimulated the production of these lipid droplets to support its growth during the late phase of infection in *Irp2*^{-/-} mice.

Oil Red O stain

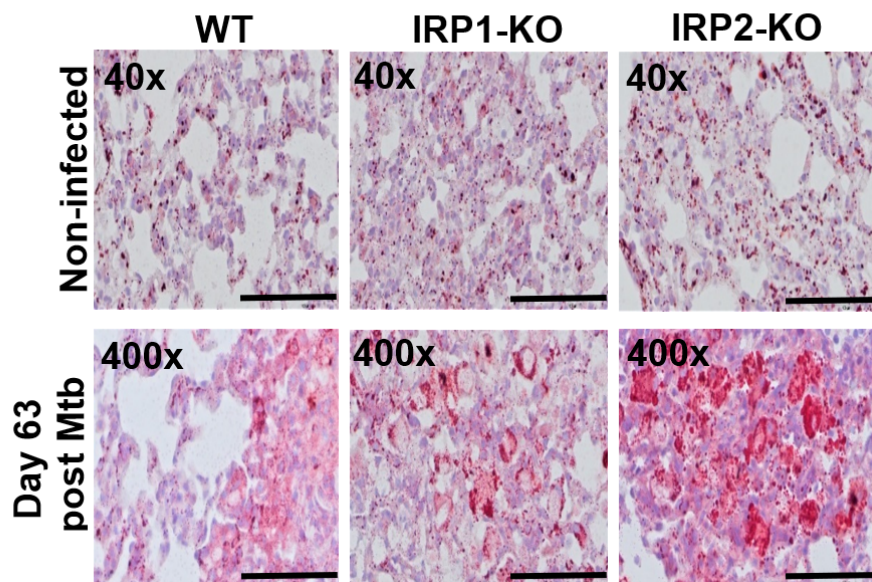


Figure 4.25: Histopathological determination of neutral lipids in lung tissue sections from wt, *Irp1*^{-/-} and *Irp2*^{-/-} mice. 8-20-week-old female wt, *Irp1*^{-/-} and *Irp2*^{-/-} mice were infected with 100 CFU of Mtb via the aerosol route. Superior lung lobes were collected, PFA fixed, and paraffin-embedded. Tissue sections were stained with ORO stain to visualize lipid droplets and examined at indicated magnifications. ORO stains neutral lipids red containing lipid droplets and hematoxylin stains the nuclei blue-purple. Representative micrographs of 1 animal out of 3 per group are shown, i.e., from 1 experiment. Scale bars represent 500 μm and 100 μm .

4.4 The Role of Iron Regulatory Proteins 1 and 2 on Host Iron Status during Mtb Infection

4.4.1 Quantitative evaluation of expression of iron metabolism genes

To investigate the effect of *Irp*-deletion on the expression of iron metabolism-associated genes during Mtb infection, non-infected and Mtb-infected wt, *Irp1*^{-/-} and *Irp2*^{-/-} mice were used. For this, the expression of genes of interest in the lung and liver were quantified via qRT-PCR analysis. No differences were observed in the expression of key iron metabolism genes in the lungs of all mouse genotypes (**Fig. 4.26A-F**). This indicates that Mtb infection does not modulate the expression of iron transport genes, hepcidin and lipocalin in the absence of either IRP1 or IRP2 in the lungs.

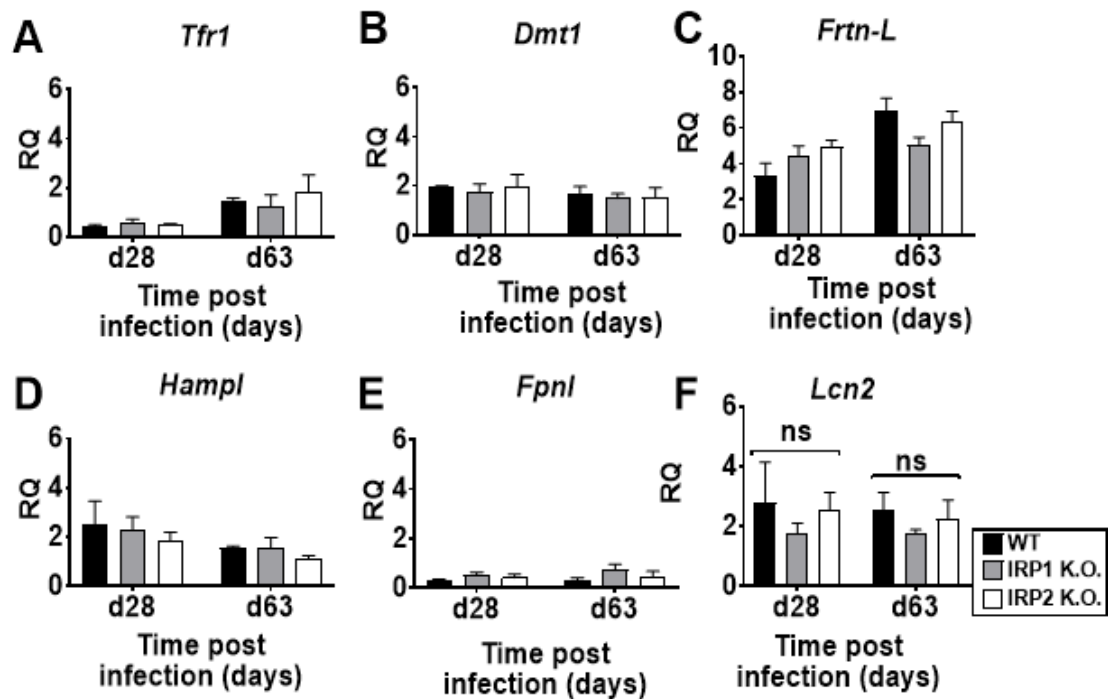


Figure 4.26: Quantification of iron metabolism genes in lung tissue from wt, *Lrp1*^{-/-} and *Lrp2*^{-/-} mice. 8-20-week-old non-infected and Mtb infected female wt, *Lrp1*^{-/-} and *Lrp2*^{-/-} mice were sacrificed at indicated time points. Lungs were collected, and total host cellular RNA was extracted. Complementary DNA was synthesized and used for the quantification of *Tfr1* (A) *Dmt1* (B) *Frtn-L* (C) *Hamp1* (D) *Fpn1* (E) and *Lcn2* (F) gene expression via qRT-PCR. All mRNA expression levels were normalized against murine *Hprt* mRNA expression levels. Data are from 1 experiment (n=4 animals) and shown as mean ± SD. Statistical analysis was performed using two-way ANOVA with Tukey's multiple comparison tests. ns represents statistically non-significant differences. Abbreviations: RQ= Relative quantification, *Tfr1*= transferrin receptor 1, *Dmt1*= divalent metal transporter, *Frtn-L*= ferritin-light chain, *Hamp1*= hepcidin, *Fpn1* = ferroportin, *Lcn2* =lipocalin 2.

Similarly, no changes were observed in the hepatic expression of *Tfr1*, *Frtn-L*, and *Fpn1* (Figs. 4.27A, C and F, respectively). Interestingly, hepatic *Dmt1* was upregulated in *Lrp1*^{-/-} mice at day 63 p.i. compared to *Lrp2*^{-/-} mice but not wt mice hepatic *Dmt1* (Figs. 4.27B). Meanwhile, hepatic *Il-6* (Figs. 4.27D) and *Hamp1* (Figs. 4.27E) mRNA transcript levels were elevated in *Lrp2*^{-/-} mice at day 28 p.i. when compared to wt and *Lrp1*^{-/-} mice but remained unchanged in all mouse genotypes at day 63 p.i. These results indicate that at day 28 p.i., Mtb infection triggered IL-6 production, which induced increased hepatic hepcidin synthesis in wt and *Lrp2*^{-/-} mice livers but not *Lrp1*^{-/-} mice.

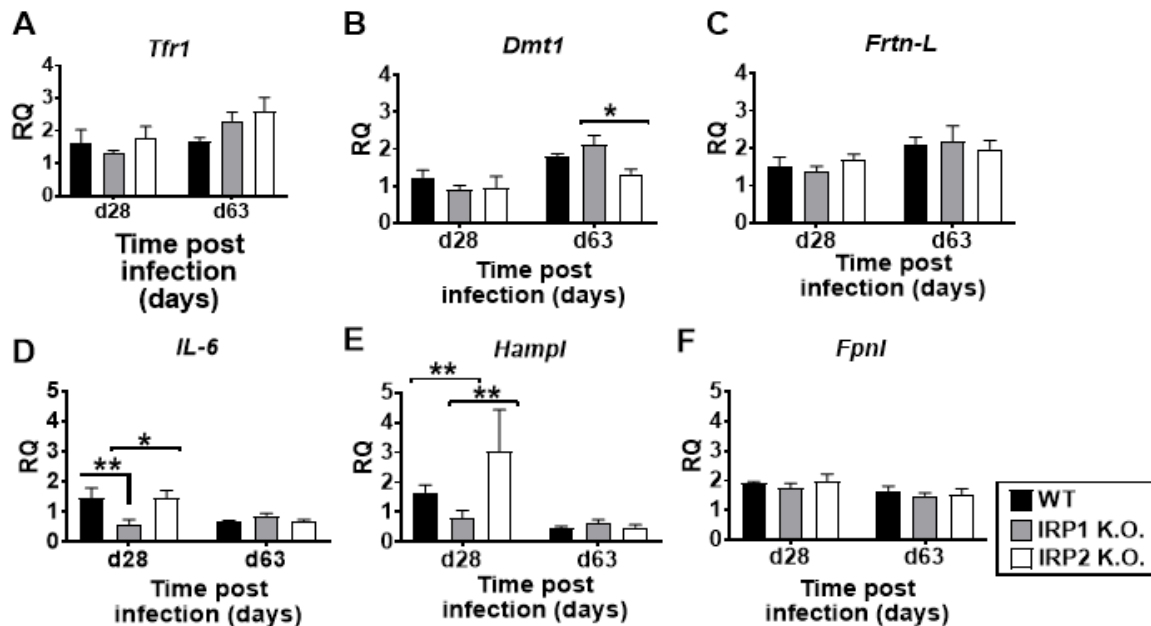


Figure 4.27: Quantification of iron metabolism genes in liver tissue from wt, *Irp1*^{-/-} and *Irp2*^{-/-} mice. 8-20-week-old non-infected and Mtb infected female wt, *Irp1*^{-/-} and *Irp2*^{-/-} mice were sacrificed at indicated time points. Livers were collected, and total host cellular RNA was extracted. Complementary DNA was synthesized and used for the quantification of *Tfr1* (A) *Dmt1* (B) *Frtn-L* (C) *Il-6* (D) *Hamp1* (E) *Fpn1* (F) gene expression via qRT-PCR. All mRNA expression levels were normalized against murine *Hprt* mRNA expression levels. Data are from 1 experiment (n=4 animals) and shown as mean ± SD. Statistical analysis was performed using two-way ANOVA with Tukey's multiple comparison tests. ns represents statistically non-significant differences. Abbreviations: RQ= Relative quantification, *Tfr1*= transferrin receptor 1, *Dmt1*= divalent metal transporter, *Frtn-L*= ferritin-light chain, *Il-6*= Interleukin-6, *Hamp1*= hepcidin, *Fpn1* = ferroportin.

4.4.2 Histological analysis for iron deposits in lung, liver and spleen tissues

Elevated levels of free circulating iron in the human and murine host have been linked to increased growth of Mtb reported to exacerbate TB disease and affect treatment outcomes [69, 155]. Furthermore, *Irp2*^{-/-} mice have been described to have altered iron distribution in tissues. This includes mild iron accumulation in the duodenum and liver, iron overload in neurons and iron deficiency in the spleen and no pulmonary phenotype [137, 139]. Still, the influence of this phenotype coupled with Mtb infection has not yet been investigated. Therefore, 8-12-week-old non-infected and Mtb infected wt, *Irp1*^{-/-} and *Irp2*^{-/-} mice were sacrificed at different time points, and lungs, livers and spleens were collected. Tissue sections were stained with Perl's Prussian blue (PPB) stain to demonstrate the presence of ferric iron. Non-infected *Irp2*^{-/-} mice had substantial iron deposits in aMØs in the pulmonary alveoli compared to the wt and *Irp1*^{-/-} mice (Fig. 4.28A). However, upon Mtb infection, iron deposits were observed in wt, *Irp1*^{-/-} and *Irp2*^{-/-} mice lungs at all time points but the highest number of Perl's positive MØs were observed in *Irp2*^{-/-} mice on days 28 and 63 days p.i. (Fig. 4.28A-B).

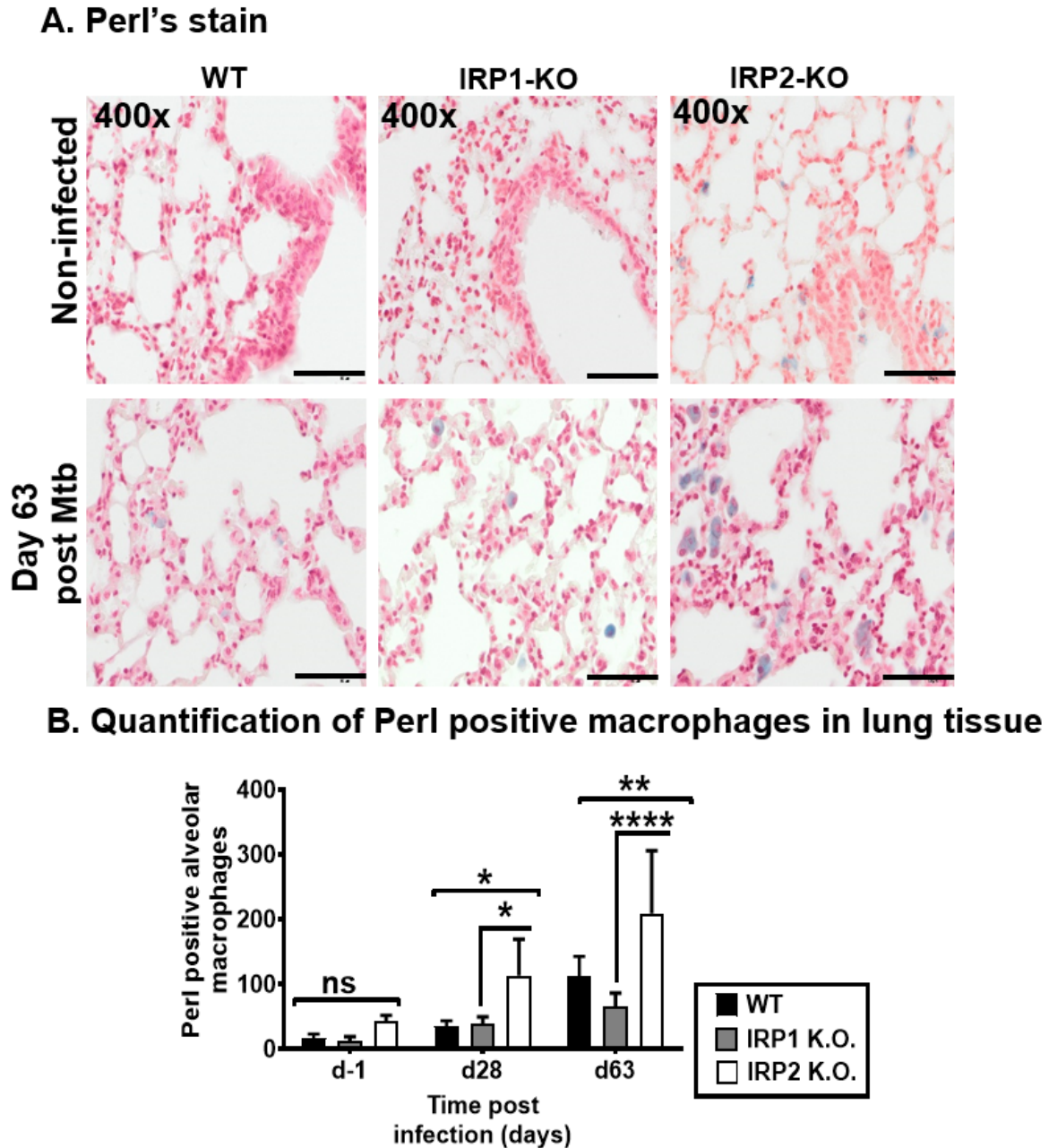
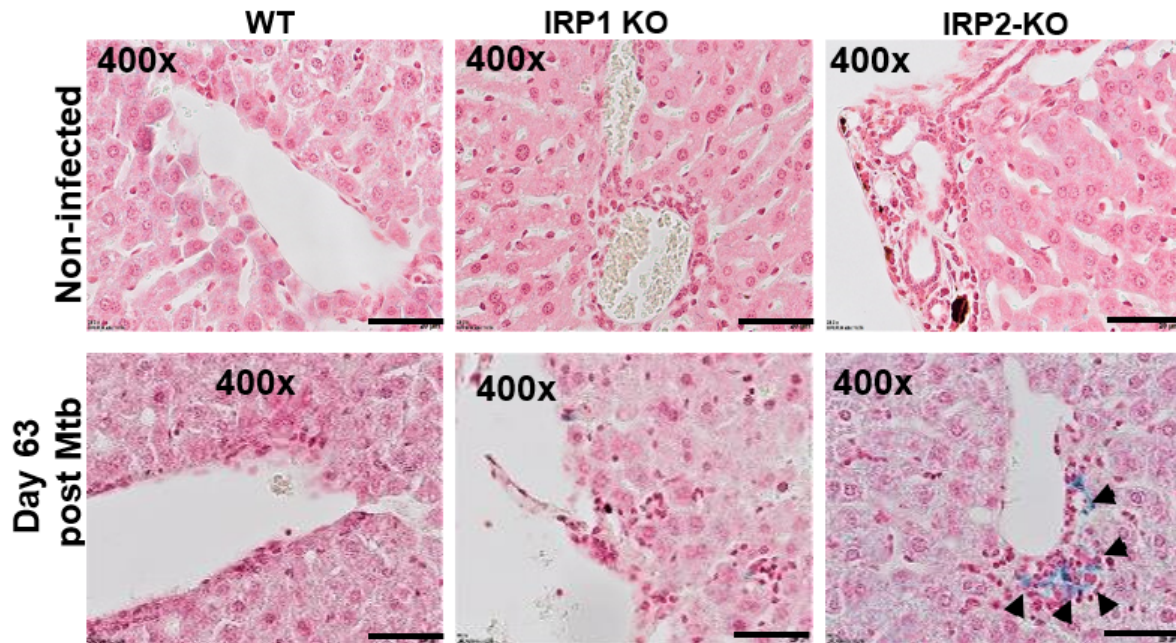


Figure 4.28: Histological analysis of iron deposits in lung tissue sections from wt, *Irp1*^{-/-} and *Irp2*^{-/-} mice. 8-20-week-old female wt, *Irp1*^{-/-} and *Irp2*^{-/-} mice were infected with 100 CFU of Mtb via the aerosol route. Superior lung lobes were collected, PFA fixed, and paraffin-embedded. Tissue sections were stained with Perl's stain and examined at indicated magnifications (A). Iron deposits stain bright-deep blue while nuclei and cytoplasm stain pink-red. Representative micrographs of 1 animal out of 8 per group are shown. Scale bars represent 100 μ m. Quantitative assessment of iron deposits (B). Data generated from quantification is from 1 experiment (n=4 animals). Statistical analysis was performed using two-way ANOVA with Tukey's multiple comparison tests. * $p \leq 0.05$, ** $p \leq 0.01$ and **** $p \leq 0.0001$ were considered statistically significant. ns represents statistically non-significant differences

In the livers, more iron deposits were observed in hepatic M ϕ s around the central vein and sinusoids in *Irp2*^{-/-} mice at day 63 p.i. as opposed to little-to-no iron accumulation in hepatic

MØs of wt and *Irp1*^{-/-} mice (Fig. 4.29A-B).

A. Perl's stain



B. Quantification of PPB positive MØ in liver tissue

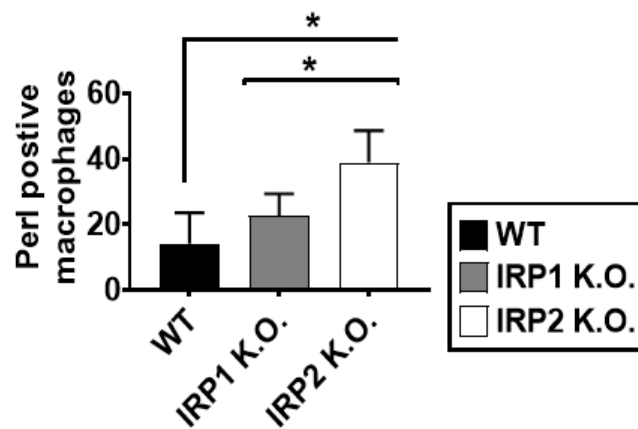


Figure 4.29: Histological analysis of iron deposits in liver tissue sections from wt, *Irp1*^{-/-} and *Irp2*^{-/-} mice. 8-20-week-old female wt, *Irp1*^{-/-} and *Irp2*^{-/-} mice were infected with 100 CFU of Mtb via the aerosol route. Left liver lobes were collected, PFA fixed, and paraffin-embedded. Tissue sections were stained with Perl's stain and examined at indicated magnifications (A). Iron deposits stain bright-deep blue while nuclei and cytoplasm stain pink-red. Representative micrographs of 1 animal out of 8 per group are shown. Scale bars represent 100 μ m. Quantitative assessment of iron deposits (B). Data generated from quantification is from 1 experiment (n=4 animals). Statistical analysis was performed using two-way ANOVA with Tukey's multiple comparison tests. * $p \leq 0.05$ was considered statistically significant

In the spleen, iron deposits were observed in the red and white pulp of wt and *Irp1*^{-/-} mice before and during Mtb infection. However, no iron deposits were found in spleens of

non-infected and Mtb-infected *Irp2*^{-/-} mice (**Fig. 4.30**) confirming reports from other authors [156, 137].

A. Perl's stain

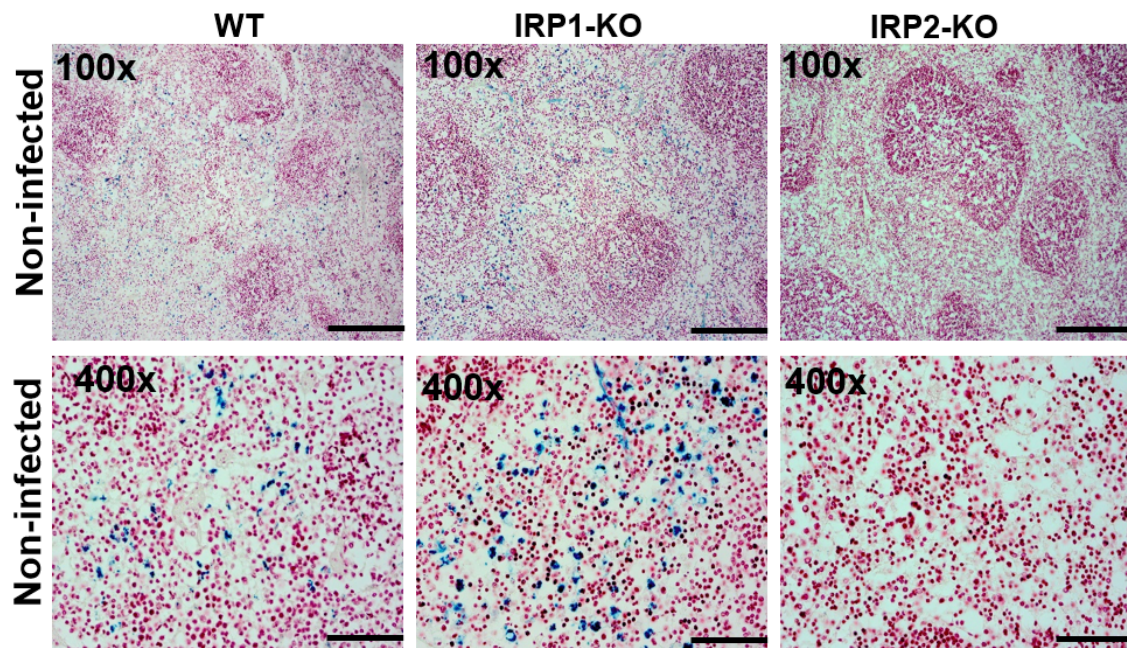


Figure 4.30: Histological analysis of iron in spleen tissue sections from wt, *Irp1*^{-/-} and *Irp2*^{-/-} mice. 8-20-week-old non-infected female wt, *Irp1*^{-/-} and *Irp2*^{-/-} mice were sacrificed, spleens were collected, PFA fixed, and paraffin-embedded. Tissue sections were stained with Perl's stain and examined at indicated magnifications. Iron deposits stain bright-deep blue while nuclei and cytoplasm stain pink-red. Representative micrographs of 1 animal out of 4 per group are shown. Scale bars represent 200 μm and 100 μm .

From these observations in **Fig. 4.28-30**, it can be concluded that *Irp2*^{-/-} mice have an altered iron distribution in the lungs, liver and spleens. Interestingly, the altered iron distribution phenotype in the lungs and livers of *Irp2*^{-/-} mice was further exacerbated upon Mtb infection. Considering that there are no reports on the influence of either IRPs on iron homeostasis during experimental Mtb infection in mice, the iron metabolic status of *Irp*-deficient mice was investigated.

4.4.3 Assessment of red blood cell parameters

For this, whole blood was collected from wt, *Irp1*^{-/-} and *Irp2*^{-/-} mice prior to experimental Mtb infection and at days 13, 28, and either 52 or 63 (denoted day 52/63) p.i. (**Fig. 4.31**) was used to assess blood cell count and RBC indices in these mice.



Figure 4.31: Experimental design. 20-week-old female wt, *Irp1*^{-/-} and *Irp2*^{-/-} mice were infected with 100 CFU of Mtb H37Rv via aerosol route and sacrificed at indicated time points.

No differences in RBC counts, hemoglobin, and hematocrit were observed between non-infected wt and *Irp1*^{-/-}, wt and *Irp2*^{-/-} as well as between *Irp1*^{-/-} and *Irp2*^{-/-} mice (**Fig. 4.32A-D**). This is contrary to previous studies which have shown differences in hematological parameters between these mouse genotypes [157, 158, 156]. However, the average volume (size) of RBC represented as the mean cell volume was observed to be lower in *Irp1*^{-/-} compared to wt mice (**Fig. 4.32D**). *Irp2*^{-/-} mice showed a significant decrease in RBC counts, hemoglobin, and hematocrit at day 28 p.i. compared to wt but not *Irp1*^{-/-} mice (**Figs. 4.32A-C**). In addition, hemoglobin was decreased at days 28 and 52/63 p.i. which is suggestive of anemia in *Irp2*^{-/-} mice in the early and late phases of infection. Though not statistically significant, a trend towards decreased RBC counts and hematocrit was observed in *Irp2*^{-/-} at day 52/63 p.i. The mean cell volume remained unchanged in all three genotypes at days 13 and 28 p.i. Interestingly, a significant increase in the mean cell volume was observed in *Irp2*^{-/-} mice at day 52/63 p.i. indicating larger RBC in *Irp2*^{-/-} mice pointing towards macrocytosis at the late phase of infection.

Measuring the average mass of hemoglobin per RBC represented as the mean corpuscular hemoglobin (MCH), the *Irp2*^{-/-} mice had decreased MCH compared to the wt mice on day 13 p.i. (**Figs. 4.32E**). However, the average amount of hemoglobin in RBCs represented as the MCH concentration (MCHC) was elevated in *Irp1*^{-/-} mice compared to wt mice prior to infection and at day 13 p.i. On days 28 and 63 p.i., *Irp2*^{-/-} mice had decreased MCHC compared to *Irp1*^{-/-} mice and wt mice (**Figs. 4.32F**). Finally, to investigate RBC variation in terms of size and volume, the RBC distribution width (RDWc) was measured. Though not statistically significant, a trend towards decreased RDWc was observed in *Irp2*^{-/-} mice at day 28 p.i. compared to wt mice. At day 63 p.i., decreased RDWc was observed in *Irp2*^{-/-} mice at 52/63 days p.i. compared to *Irp1*^{-/-} and wt mice (**Figs. 4.32G**).

Together, these data suggest that Mtb induces anemia, particularly at day 28 p.i. in Mtb-infected *Irp2*^{-/-} mice. Meanwhile, the hematological parameters of wt and *Irp1*^{-/-} mice remained within the normal range before and during Mtb infection, particularly at day 28 p.i.

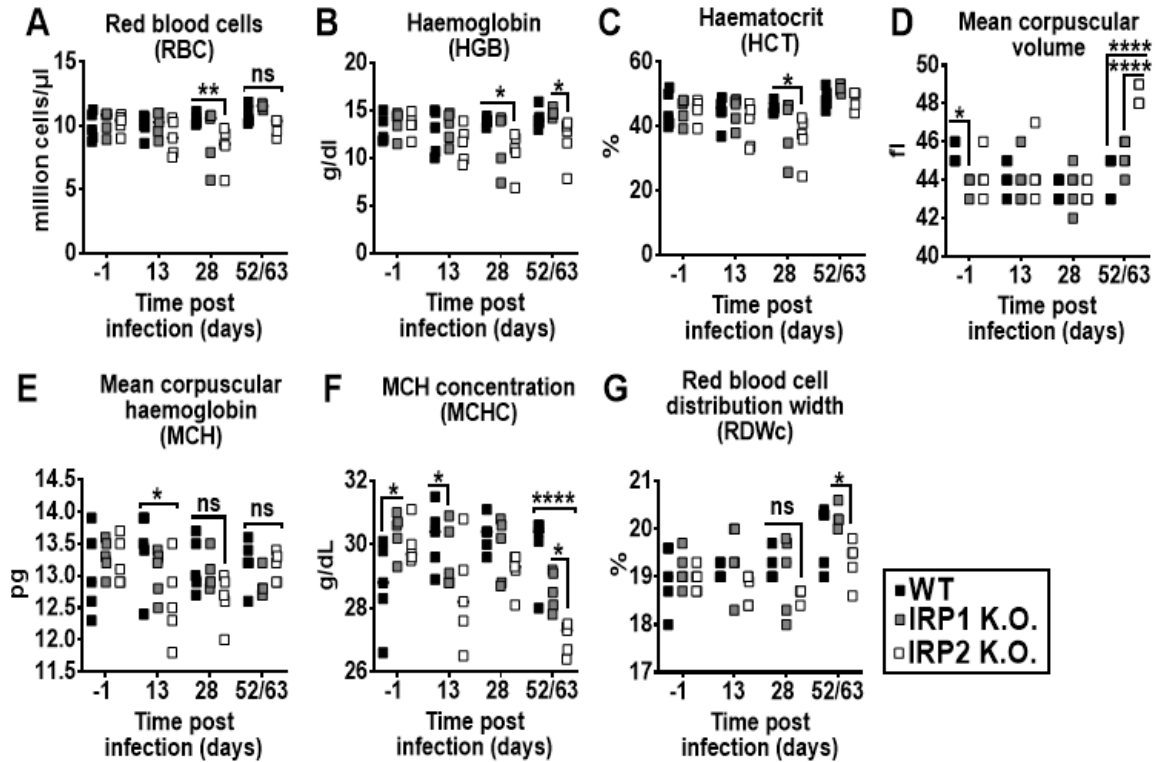


Figure 4.32: Measurement of blood cell count and RBC indices in whole blood from wt, *lrp1*^{-/-} and *lrp2*^{-/-} mice. 20-week-old non-infected and Mtb infected female wt, *lrp1*^{-/-} and *lrp2*^{-/-} mice were sacrificed. Blood was obtained from the *vena cava caudalis* under terminal anaesthesia for investigation of RBC (A), HGB (B), HCT (C), MCV (D), MCH (E), MCHC (F) and RDWc (G) at indicated timepoints. Each square represents an individual sample (n=5 animals). Data pooled from 2 independent experiments and shown as mean \pm SD. Statistical analysis was performed using two-way ANOVA with Tukey's multiple comparison tests. *p \leq 0.05, **p \leq 0.01 and **** p \leq 0.0001 were considered statistically significant. ns represents statistically non-significant differences.

In light of the above findings in **Fig. 4.32**, the absence of differences in RBC parameters between non-infected *lrp1*^{-/-} and *lrp2*^{-/-} mice raised questions regarding the validity of the mouse strains used. This discrepancy in my study contradicts previous studies from other authors [157, 158, 156]. In order to investigate if the wrong strains of mice were used to for analyzing RBC blood cell parameters, liver samples were collected from these mice and subjected to PCR genotyping. Mice presumed to be *lrp1*^{-/-} mice showed identical alleles at the *lrp1* gene locus as indicated by a single DNA fragment on the gel, confirming that these mice are IRP1 homozygous mutants (**Fig. 4.33B and E**). Among the mice presumed to be *lrp2*^{-/-}, 14 out of 20 mice used RBC parameter analysis showed two different alleles at the *lrp2* gene locus represented by 2 different DNA fragments of varying sizes on the gel (**Fig. 4.33C, lanes 5-16 and Fig. 4.33F, lanes 5-7**). This suggests that these mice were heterozygous mutants for IRP2 (i.e., *lrp2*^{+/-}). Interestingly, the remaining 6 mice presumed to be *lrp2*^{-/-} were observed to be wt (**Fig. 4.33F, lanes 8-12**). These results indicate that *lrp2*^{-/-} strain in our mouse collection at the RCB has been lost during the breeding process. These genotyping PCR results provide an explanation for the discrepancy between my hematology data and the findings reported by other authors [157, 158, 156].

4.4. The Role of Iron Regulatory Proteins 1 and 2 on Host Iron Status during Mtb Infection

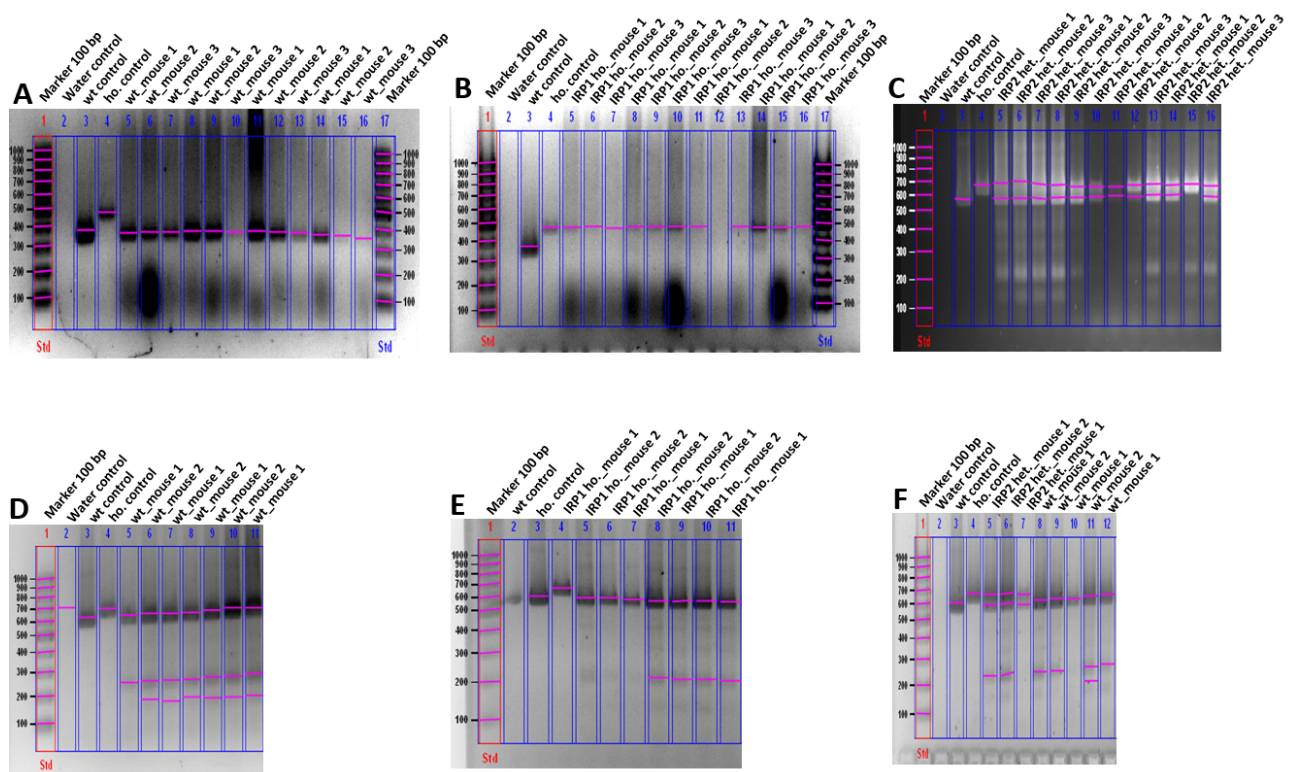


Figure 4.33: Genotyping by PCR from liver tissues from mice presumed to be wt, *lrp1*^{-/-} and *lrp2*^{-/-} mice. Non-infected and Mtb infected female mice presumed to be wt, *lrp1*^{-/-} and *lrp2*^{-/-} mice were sacrificed at indicated time points. Livers were collected, and total host cellular DNA was extracted, amplified by PCR and separated by size for visualization by agarose gel electrophoresis. Photographs of 2% agarose gels showing DNA bands from wt (A and D), *lrp1*^{-/-} (B and E) and "*lrp2*^{-/-}" (C and F) mice. Std= standard, i.e., 100 bp Marker, wt control= wild type control, ho.= homozygous, het.= heterozygous.

With the new knowledge that 14 out of the 20 mice presumed to be *lrp2*^{-/-} mice were actually *lrp2*^{+/-} mice, the data in **Figs. 4.33** was reanalyzed after excluding 6 of the wt mice (**Figs. 4.33F, lanes 8-12**) from the data set. Although not statistically significant, a trend towards decreased RBC counts, hemoglobin, and hematocrit was observed in *lrp2*^{+/-} mice, particularly at days 28 and 52/63 p.i., in comparison to wt and *lrp1*^{+/-} mice (**Fig. 4.34A-C**). Additionally, the mean cell volume was observed to be higher in *lrp2*^{+/-} compared to wt and *lrp1*^{-/-} mice at day 52/63 p.i. (**Fig. 4.34D**). *lrp2*^{+/-} mice showed decreased MHC at day 13 pi., as well as decreased MCHC at days 13 and 52/63 p.i. compared to to wt and *lrp1*^{-/-} mice (**Fig. 4.34E-F**). It is important to note that this experiment was conducted once with a sample size of 4-5 mice per group, and a repetition of this experiment is necessary to draw a definitive conclusion. Nevertheless, the data highlights the importance of IRP2 in iron metabolism and also reveals for the first time that Mtb infection alters iron metabolic status in *lrp2*^{+/-} mice.

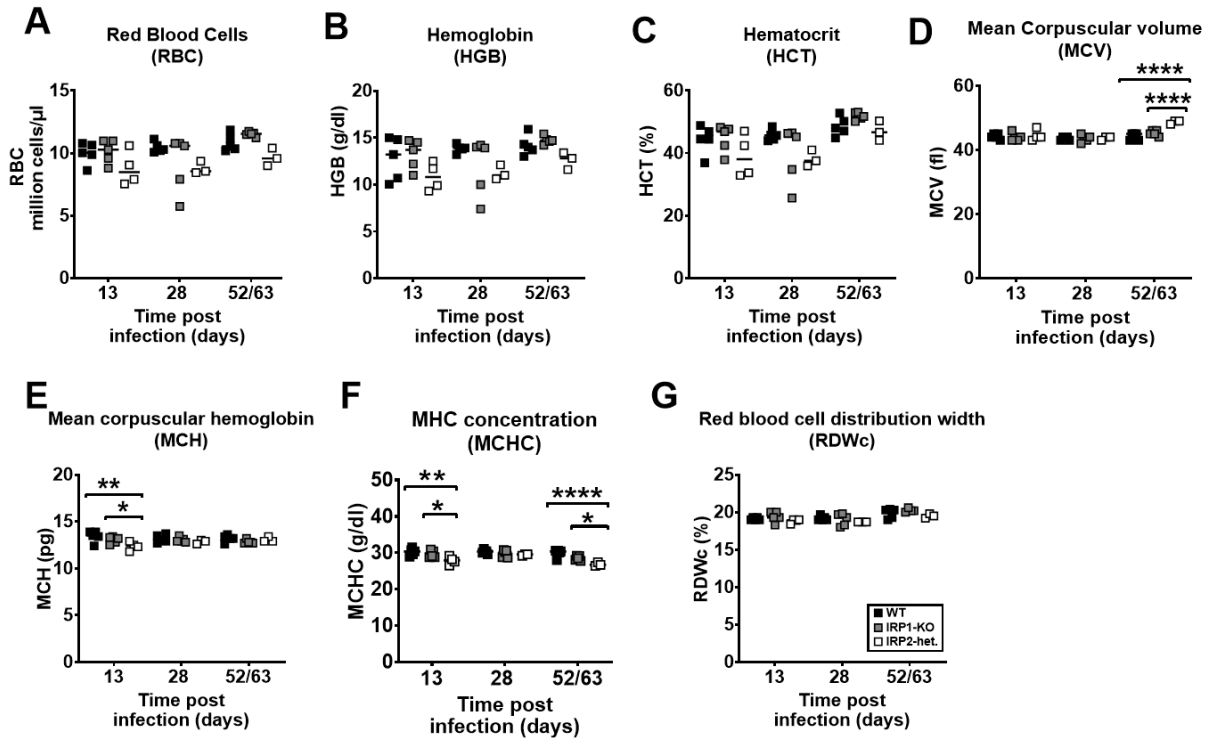


Figure 4.34: Measurement of blood cell count and RBC indices in whole blood from wt, *Irp1*^{-/-} and *Irp2*^{+/-} mice. 20-week-old female wt, *Irp1*^{-/-} and *Irp2*^{+/-} mice were infected with 100 CFU of Mtb via aerosol route. Blood was obtained from the *vena cava caudalis* under terminal anaesthesia for investigation of RBC (A), HGB (B), HCT (C), MCV (D), MCH (E), MCHC (F) and RDWc (G) at indicated timepoints. Each square represents an individual sample (n=5 animals). Data pooled from 2 independent experiments and shown as mean \pm SD. Statistical analysis was performed using two-way ANOVA with Tukey's multiple comparison tests. * $p \leq 0.05$, ** $p \leq 0.01$ and **** $p \leq 0.0001$ were considered statistically significant. ns represents statistically non-significant differences.

4.4.4 Evaluation of indicators of iron status

Clinical iron parameters were measured to investigate the iron status of non-infected and Mtb-infected wt, *Irp1*^{-/-}, *Irp2*^{-/-} and *Irp2*^{+/-} mice. These parameters included total serum iron (which measures how much iron is present in serum), total iron-binding capacity (TIBC, which measures TF levels), TF saturation (% TF sat, which is the value of serum iron divided by TIBC to indicate how much iron is bound to transferrin) and serum ferritin (indicates the amount of ferritin secreted into the blood). Here, total serum iron was decreased to statistically significant levels in the sera of *Irp2*^{-/-} mice compared to wt mice at day 13 p.i., as well as at day 28 p.i., compared to wt and *Irp1*^{-/-} mice (**Fig.4.35A**). Though statistically insignificant, a trend towards lower TIBC was observed in sera of non-infected and Mtb-infected *Irp2*^{-/-} compared to wt but not *Irp1*^{-/-} at days 13 and 63 p.i. However, a significant decrease in TIBC was observed in *Irp2*^{-/-} mice compared to wt but not *Irp1*^{-/-} mice at day 28 p.i. (**Fig.4.35B**). Transferrin saturation was significantly decreased in *Irp2*^{-/-} compared to wt but not *Irp1*^{-/-} mice at days 13, 28 and 63 p.i. (**Fig.4.35C**). Lastly, serum ferritin was measured, revealing a significant increase in ferritin levels in the *Irp2*^{-/-} mice compared to *Irp1*^{-/-} and wt mice at all time points (textbfFig.4.35D). These findings indicate a hypoferremic response in *Irp2*^{-/-} mice in the early phase of infection at day 28 p.i.

No differences were observed in total serum iron, TF saturation, TIBC, and serum ferritin between wt, *Irp1*^{-/-} and *Irp2*^{+/-} mice (data not shown).

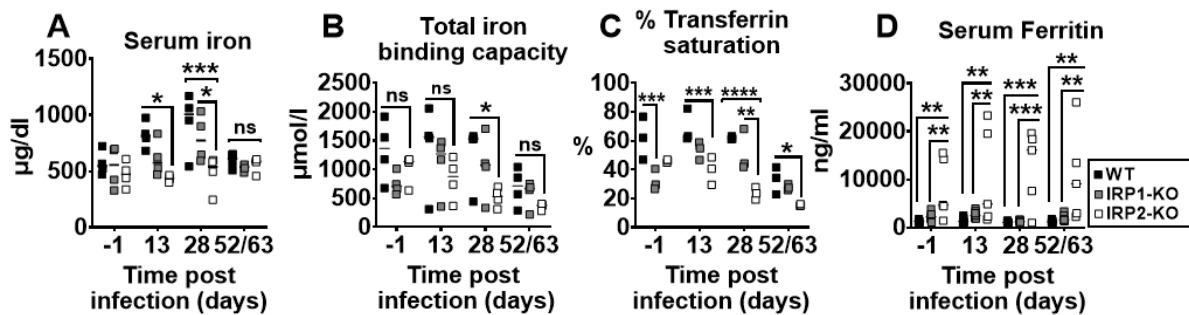


Figure 4.35: Evaluation of indicators of iron status in sera from wt, *Irp1*^{-/-} and *Irp2*^{-/-} mice 20-week-old female wt, *Irp1*^{-/-} and *Irp2*^{-/-} mice were infected with 100 CFU of Mtb via the aerosol route. Serum was obtained from whole blood collected from the *vena cava caudalis* under terminal anaesthesia for investigation of serum iron (A), total iron-binding capacity (B), transferrin saturation (C), and serum ferritin (D) at indicated timepoints. Each square represents an individual sample (n=3-5 animals). Data are from 1 experiment and shown as mean \pm SD. Statistical analysis was performed using two-way ANOVA with Tukey's multiple comparison tests. * $p \leq 0.05$, ** $p \leq 0.01$ and *** $p \leq 0.001$ were considered as statistically significant. ns represents statistically non-significant differences.

4.5 The Influence of Microbiota Composition on Host Phenotypic Variation during Mtb infection

Iron has been shown to influence microbiota composition. A few studies also show that the microbiota has significant phenotypic effects on the host [159, 160, 161], but studies so far show the limited influence of the microbiota on TB outcome [94, 135]. This led to the hypothesis that the differential microbiota composition in wt, *Irp1*^{-/-} and *Irp2*^{-/-} mice could be responsible for the phenotypic variation observed between the different mouse genotypes. However, since as the *Irp2*^{-/-} strain in our mouse collection at the RCB has been lost (**Fig. 4.33C and F**), the question was posed if wt, *Irp1*^{-/-} and *Irp2*^{+/-} mice have different microbiota compositions which could cause phenotypic variations between the different mouse genotypes prior to and following infection with experimental Mtb. To investigate this, pregnant germ-free (GF) C57Bl/6J mice were cohoused with SPF wt, *Irp1*^{-/-} and *Irp2*^{+/-} mice as outlined in **Fig. 4.36**.

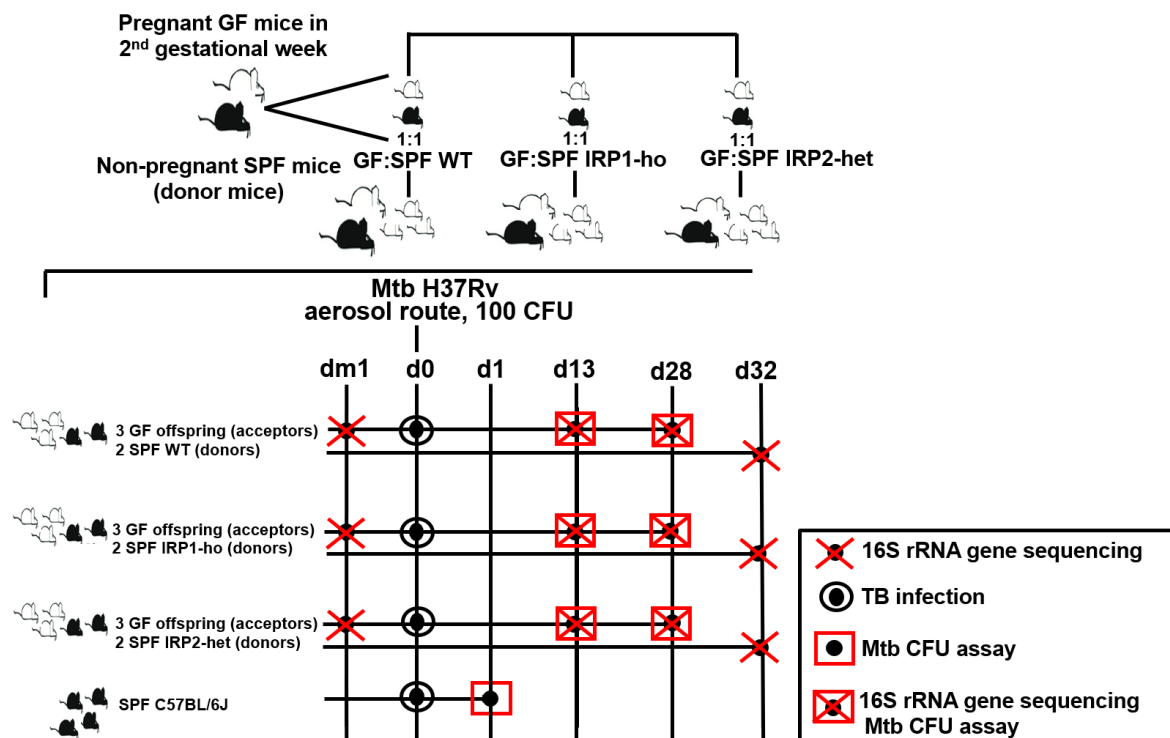


Figure 4.36: Cohousing experimental approach to investigate the influence of microbiota composition on host phenotypic variation during Mtb infection. Pregnant GF mice in the 2nd gestational week were cohoused in a 1:1 ratio per cage with wt, IRP1 homozygous (ho or *Irp1*^{-/-}) and IRP2 heterozygous (het or *Irp2*^{+/-}) mice (referred to as donors) from SPF housing conditions. After the birth of pups, all mice were cohoused for 4 weeks before weaning. Afterwards, female pups (referred to as acceptors) from ex-GF mice were cohoused in a 3:2 ratio per cage with the same donor mouse genotypes before weaning. At 6 weeks of age, only acceptors were infected with 100 CFU of Mtb via aerosol route and further cohoused with non-infected donors. Before infection (i.e. at day -1 (dm1)) and at days 13 and 28 p.i., acceptor animals were sacrificed. Non-infected donor animals were sacrificed at day 32 p.i. (i.e., at the end of the study). Experimental set-up illustrates one experiment, n=8 animals per donor genotype and 3-4 per acceptor genotype.

4.5.1 Visualization of differences or similarities in caecal microbiota composition

Caecal microbiota analysis was performed in all donor mouse genotypes at day 32 p.i. as well as in all acceptor mouse genotypes at day -1 p.i. and at days 13 and 28 p.i. using 16S rRNA sequencing. To visualize differences in the microbiota composition between the donors and acceptors, a principal coordinates analysis (PCoA) based on Bray-Curtis (BC) dissimilarity index was performed. PCoA revealed considerable variability in the ordination of samples from all donor and acceptor mouse genotypes. Samples from donor genotypes ordinated closer to each other indicating that wt, *Irp1*^{-/-} and *Irp2*^{+/-} mice do not have distinct microbiota compositions (**Fig. 4.37A**). This can be explained by the effects of cohousing or coprophagy being stronger thereby levelling out the genotype effect. For the acceptor mice, PCoA revealed that samples from the wt-acceptor mice clustered closer to each other irrespective of the time point. This indicates that the wt-acceptor mice have more comparable microbiota to each other across all time points compared to IRP1-acceptors and IRP2-acceptors (**Fig. 4.37B**),

implying that wt-, IRP1 - and IRP2-acceptors have different microbiota compositions

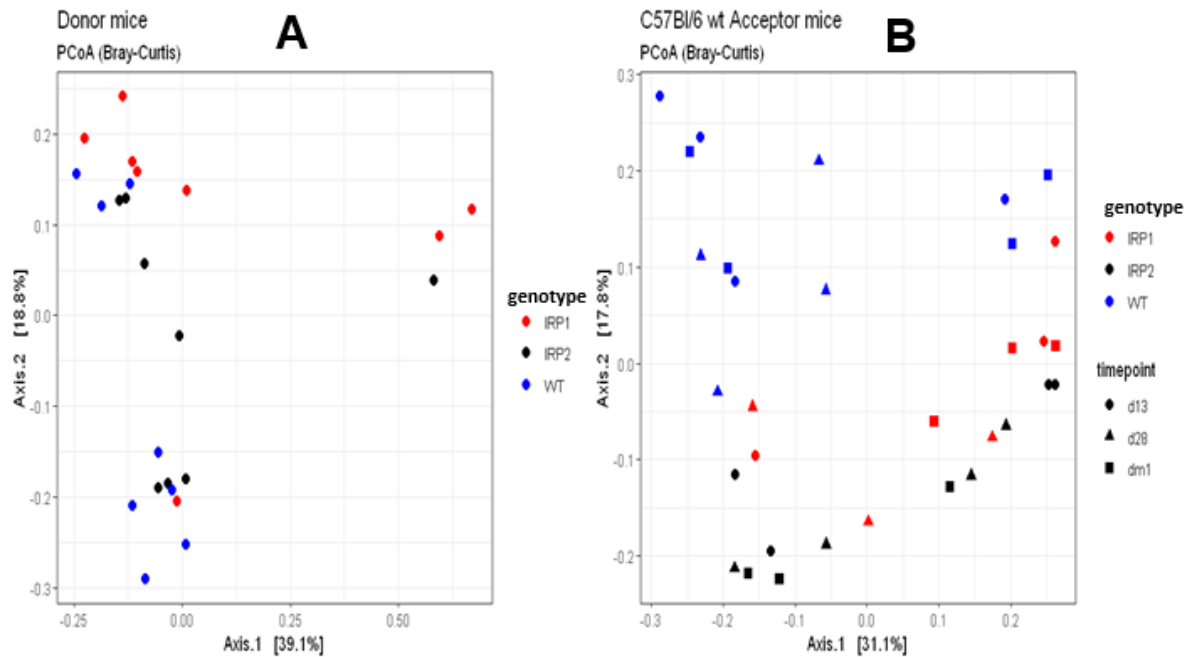


Figure 4.37: Visualization of differences in the caecal microbial community structure of donor and acceptor mice. 6-week-old female acceptors were cohoused with non-infected donors in a genotype-specific manner and infected with 100 CFU of Mtb via the aerosol route. All mice were sacrificed at indicated time points, and their caecal content was collected for 16S rRNA sequencing. Distinct clustering of samples was observed between the donors (A) and acceptors (B). Data from 1 experiment are shown, n=8 animals per donor genotype and 3-4 per acceptor genotype.

The BC dissimilarity index was used to comprehend the differences between donor mouse genotypes. The between-group dissimilarity of IRP1- compared to WT-donor mice was not at the same level as the within-group dissimilarity of both groups (**Fig. 4.38A**), indicating differences in the microbiota compositions of IRP1- compared to wt-donor mice. Similarly, highly significant differences were observed for IRP2- compared to wt-donor mice (**Fig. 4.38B**). These results show that IRP1- and IRP2-donor mice have different caecal microbiota compositions.

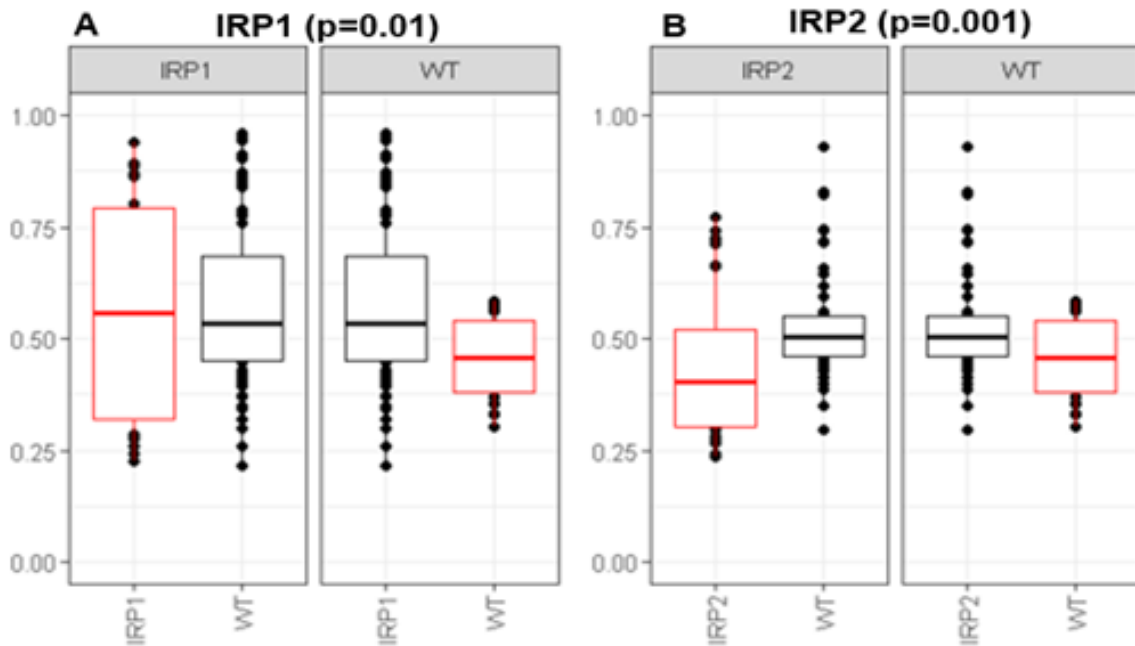


Figure 4.38: Within-group and between-group dissimilarities in the caecal microbial community structure of donor mice. Non-infected wt-, IRP1- and IRP2-donor mice were sacrificed at the end of the experiment and caecal contents were collected for 16S rRNA sequencing. Differences in microbiota compositions were observed between IRP1- (A) and IRP2- (B) compared to wt donor mice were observed. Data from 1 experiment are shown, n=8 animals per donor genotype and 3-4 per acceptor genotype. Significance was tested using the adonis function from the vegan package in R; ** and *** indicate $p \leq 0.01$ and $p \leq 0.001$, respectively.

Next, the caecal microbial composition differences between donors and acceptors were investigated. First, the between-group dissimilarity of wt-donors and wt-acceptors was at the same level as the within-group dissimilarities of both groups (**Fig. 4.39A**) indicating that both wt-donor and wt-acceptor mice have comparable microbiota compositions. Second, the between-group dissimilarity of the IRP1-donor and IRP1-acceptor mice was at the same level, but the within-group dissimilarity of IRP1-donor and IRP1-acceptor mice was at different levels indicating differential microbiota compositions within the IRP1-acceptor mice but not between the IRP1-donor and IRP1-acceptor mice (**Fig. 4.39B**). Third, the between-group dissimilarity of IRP2-donor and IRP2-acceptor mice was at the same level as the within-group dissimilarities of both groups, which were at similar levels (**Fig. 4.39C**), indicating that IRP2-donor, as well as IRP2-acceptor mice, have comparable microbiota compositions.

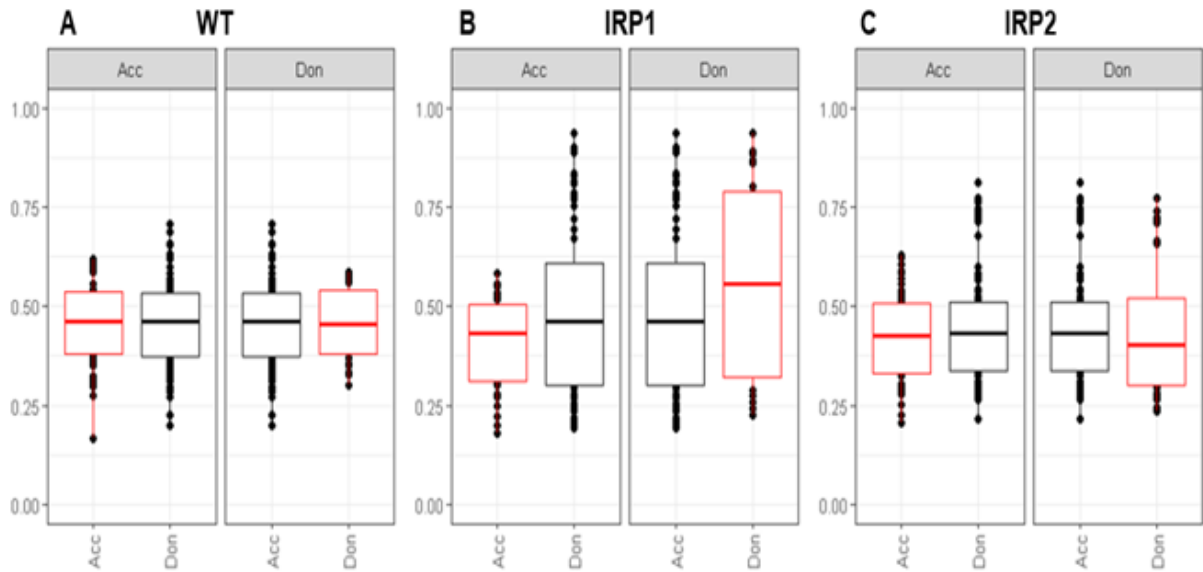


Figure 4.39: Within-group and between-group dissimilarities in the caecal microbial community structure of donor vs acceptor mice. 6-week-old female acceptors were cohoused with non-infected female donors in a genotype-specific manner prior to and following Mtb H37Rv infection via the aerosol route. All mice were sacrificed at specific time points, and caecal content was collected for 16S rRNA sequencing. Comparable microbiota compositions between and within wt-acceptors and -donors (A), dissimilar microbiota compositions between but not within IRP1-acceptors and -donors (B), and comparable microbiota compositions between and within IRP2-acceptors and -donors (C) were observed. Data from 1 experiment are shown, $n=8$ animals per donor genotype and 3-4 per acceptor genotype. Significance was tested using the adonis function from the vegan package in R; ** and *** indicate $p \leq 0.01$ and $p \leq 0.001$, respectively. Abbreviations: Acc= acceptor, Don= donor.

Last, the genotypic differences between acceptor mice were investigated. Significant differences were observed in the within-group dissimilarity of both the IRP1-acceptors (**Fig. 4.40A**) and IRP2-acceptors (**Fig. 4.40B**) compared to the between-group dissimilarity of WT-acceptors. These results show differences in the caecal microbiota compositions between acceptor mouse genotypes. This indicates a successful transfer of the genotype-specific microbiota from the donor mice to the respective acceptor mice genotypes. In all, these results revealed that (i) *Irp1*^{-/-} and *Irp2*^{+/-} mice have distinct microbiota, (ii) microbiota between donor and acceptor mouse genotypes are comparable and (iii) IRP1- and IRP2-acceptors have different microbiota compositions.

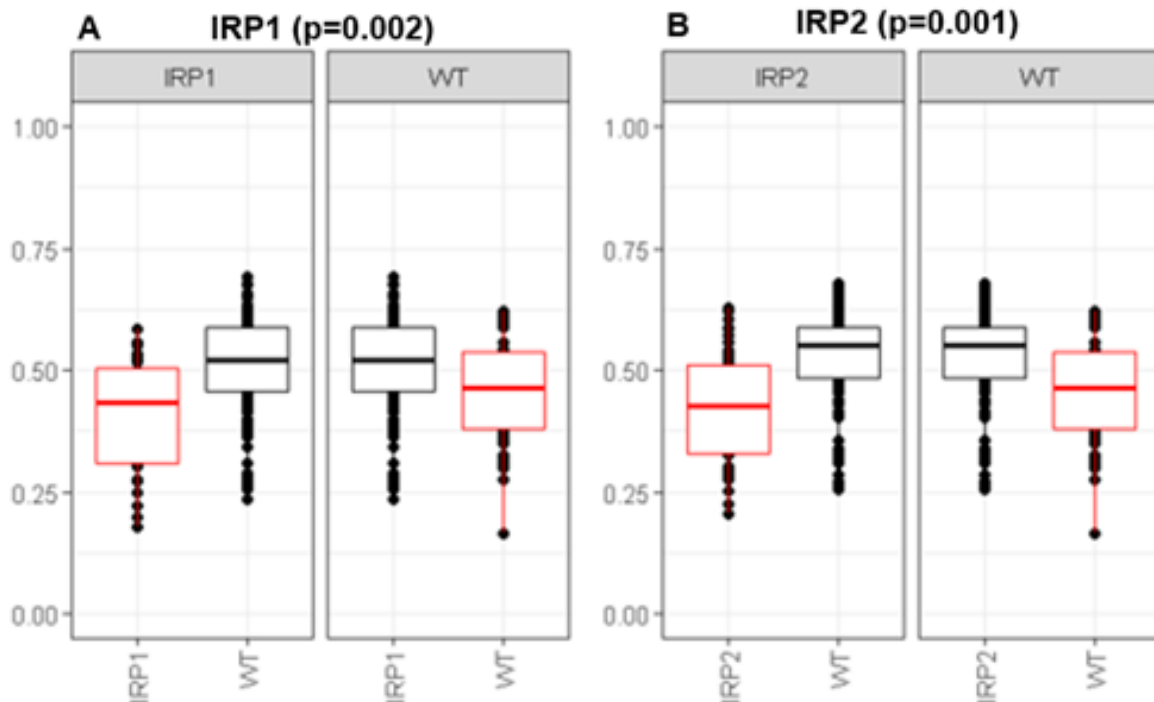


Figure 4.40: Within-group and between-group dissimilarities in the caecal microbial community structure of acceptor mice. 6-week-old female acceptors were cohoused with non-infected donors in a genotype-specific manner. Acceptors were infected with 100 CFU of *Mtb* via aerosol route, sacrificed at specific time points, and caecal content was collected for 16S rRNA sequencing. Data from 1 experiment are shown, $n=3-4$ animals. Significance was tested using the `adonis` function from the `vegan` package in R; ** and *** indicate $p \leq 0.01$ and $p \leq 0.001$, respectively. Abbreviations: Acc= acceptor, Don= donor.

4.5.2 16S rRNA taxonomy analysis

At the family level, the main taxa identified with a p -value ≤ 0.2 among the most abundant families were *Rikenellaceae*, *Anaeroplasmataceae*, *Ruminococaceae*, *Coriobacteriaceae*, *Desulfovibrionaceae*, an unclassified (uncl.) member of the *Clostridiales* order, an uncl. member of the *Bacteroidales* order, and an uncl. member of the *Clostridia* order. The most significant differences in IRP1- in comparison to wt-donors were a higher representation of *Rikenellaceae* as well as a lower representation of *Anaeroplasmataceae*, *Ruminococaceae*, *Coriobacteriaceae*, *Desulfovibrionaceae*, an unclassified (uncl.) member of the *Clostridiales* order, an uncl. member of the *Bacteroidales* order, and an uncl. member of the *Clostridia* order. Interestingly, *Bacteroides*, uncl. member of the order *Clostridia*, *Acetobacter* and unclassified members of the family *Coriobacteriaceae* had somewhat similar abundances in the wt-donors as in the IRP1-donors (Fig. 4.41).

4.5. The Influence of Microbiota Composition on Host Phenotypic Variation during Mtb infection

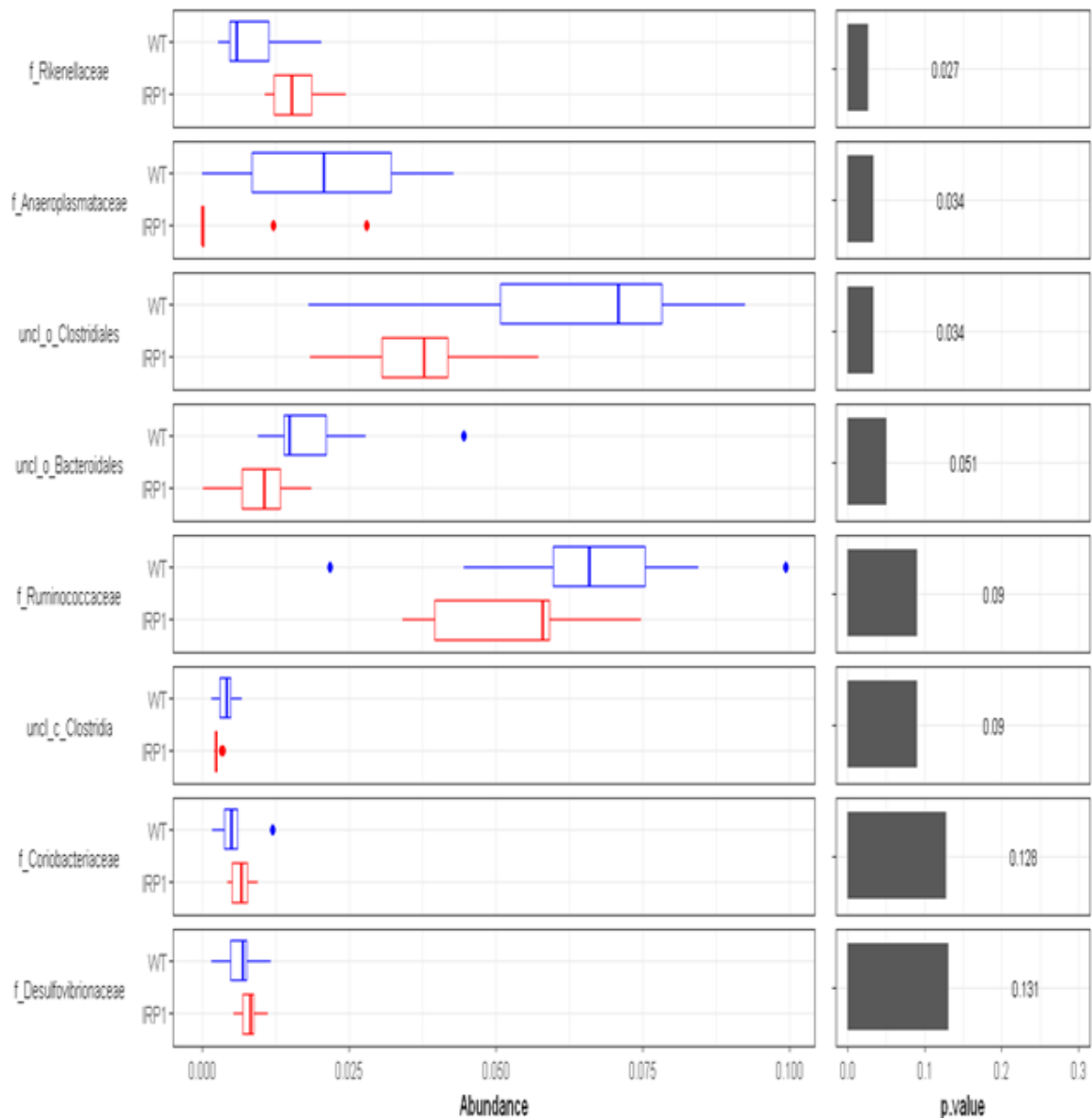


Figure 4.41: Differentially abundant families in caeca from IRP1- vs wt-donor mice. IRP1-donors from SPF animal husbandry were cohoused in a 1:1 ratio per cage with pregnant GF mice and handled as indicated in Fig. 4.36. All non-infected IRP1 donor- and wt-donor mice were sacrificed and caecal contents were collected for 16S rRNA sequencing. Only families with a p-value ≤ 0.2 are shown. Data from 1 experiment are shown, n=3-4 animals. Abbreviations: f= family, o= order, c= class, o= order, uncl= unclassified. Significance was tested using the exact Wilcoxon test.

Differences were observed in the caecal microbiota of wt- and IRP2-donors at the family level. *Helicobacteraceae*, *Prevotelleceae*, *Rikinellaceae* and *Lactobacillaceae* were the main taxa identified among the most abundant families. Of these families, *Helicobacteraceae*, *Prevotelleceae* and *Rikinellaceae* were highly represented in IRP2 -donors compared to wt-donors. Meanwhile, *Lactobacillaceae* family was observed to be lower in IRP2-donors in comparison to wt ones (**Fig. 4.42**).

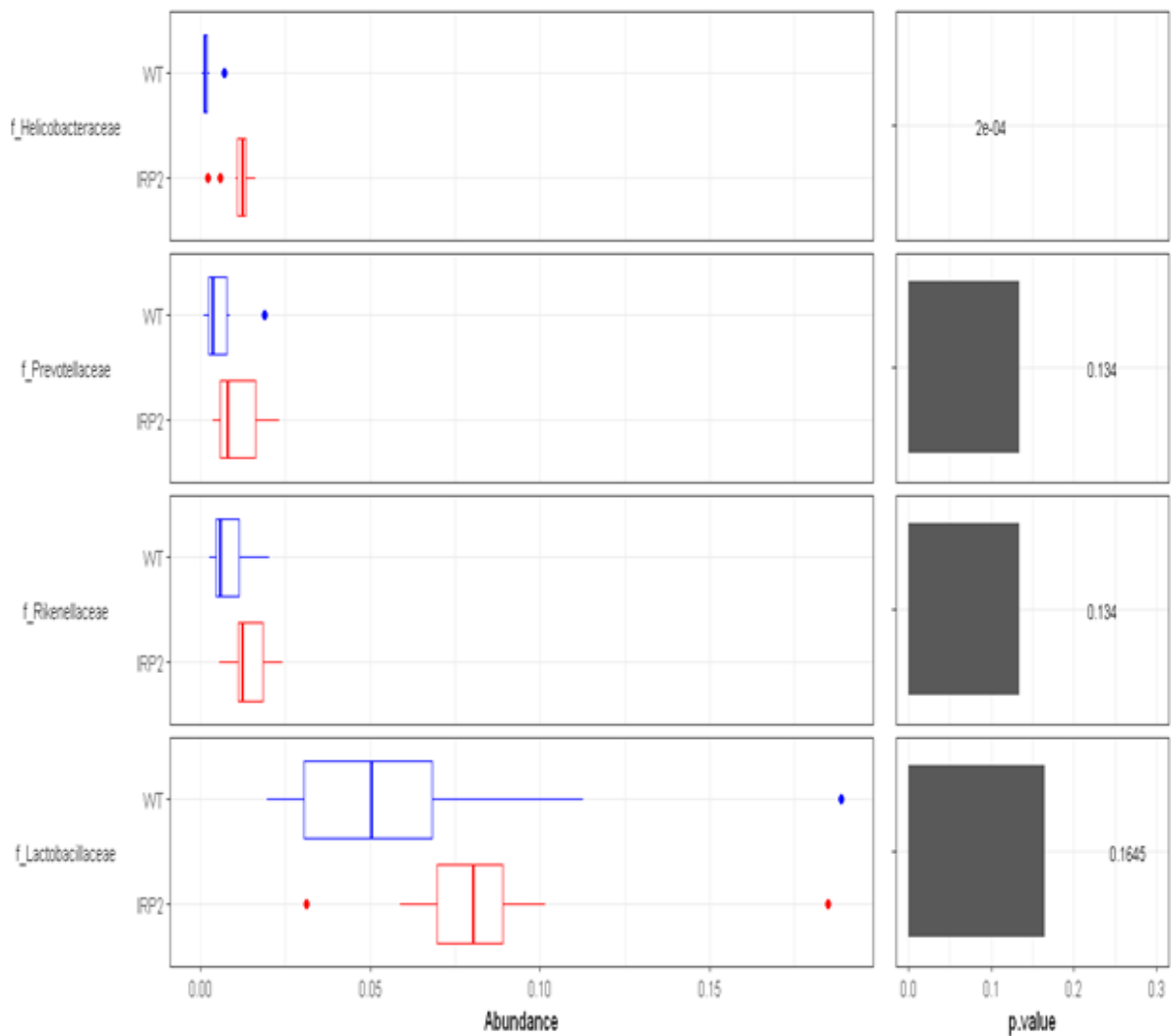


Figure 4.42: Differentially abundant families in caeca from IRP2- vs wt-donor mice. IRP2-donors from SPF animal husbandry were cohoused in a 1:1 ratio per cage with pregnant GF mice and handled as indicated in Fig. 4.36. All non-infected IRP2 donor- and wt-donor mice were sacrificed and caecal contents were collected for 16S rRNA sequencing. Only families with a p-value ≤ 0.2 are shown. Data from 1 experiment are shown, n=3-4 animals. Abbreviations: f= family, o= order, c= class, o= order, uncl= unclassified. Significance was tested using the exact Wilcoxon test.

At the genus level, the most significant differences in IRP1- vs. wt-donors were a higher representation of *Barnesiella* and *Turicibacter* and a lower representation of *Odoribacter*, *Anaeroplasma*, *Clostridiales*, an uncl. member of the order *Bacteroidales*, an uncl. member of the family of *Ruminococaceae*. Interestingly, *Bacteroides*, uncl. member of the order *Clostridia*, *Acetobacter* and uncl. members of the family *Coriobacteriaceae* had somewhat similar abundances in the wt- as in the IRP1-donors (**Fig. 4.43**).

4.5. The Influence of Microbiota Composition on Host Phenotypic Variation during Mtb infection

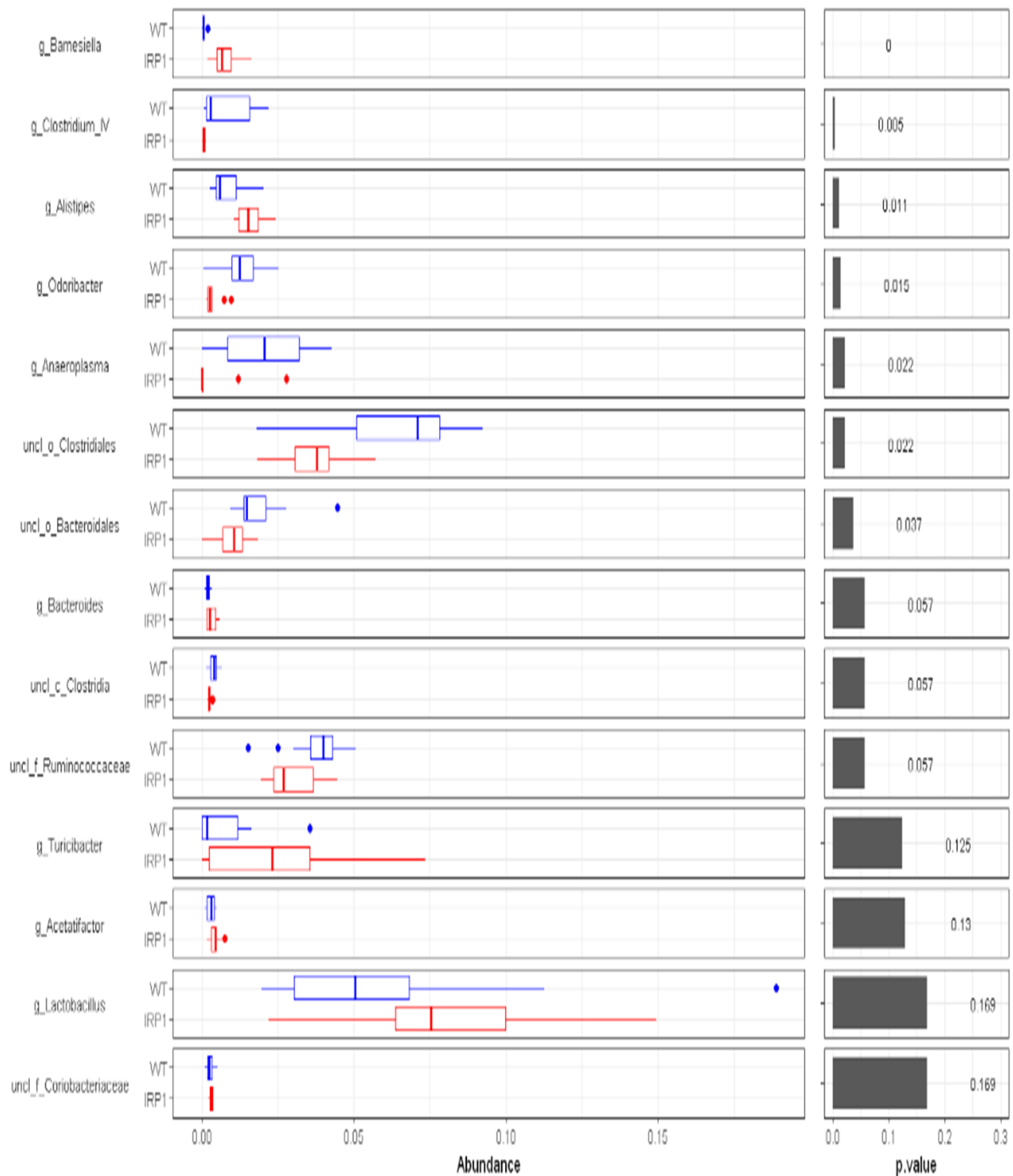


Figure 4.43: Differentially abundant genera in caeca from IRP1- vs wt-donor mice. IRP1-donors from SPF animal husbandry were cohoused in a 1:1 ratio per cage with pregnant GF mice as indicated in Fig. 4.36. All non-infected IRP1- and wt-donor mice were sacrificed and caecal contents were collected for 16S rRNA sequencing. Only families with a p-value ≤ 0.2 are shown. Data from 1 experiment are shown, n=3-4 animals. Abbreviations: c= class, o= order, f= family, g= genus, uncl = unclassified. Significance was tested using the Wilcoxon Signed-Ranks Tests; $p \leq 0.2$.

The most significant differences in IRP2-donors compared to wt-donors were a higher representation of the genera, *Alloprevotella*, *Barnesiella*, *Helicobacter*, *Bacteroidetes* and *Flavonifractor* as well as a lower representation of *Odoribacter* (Fig. 4.44).

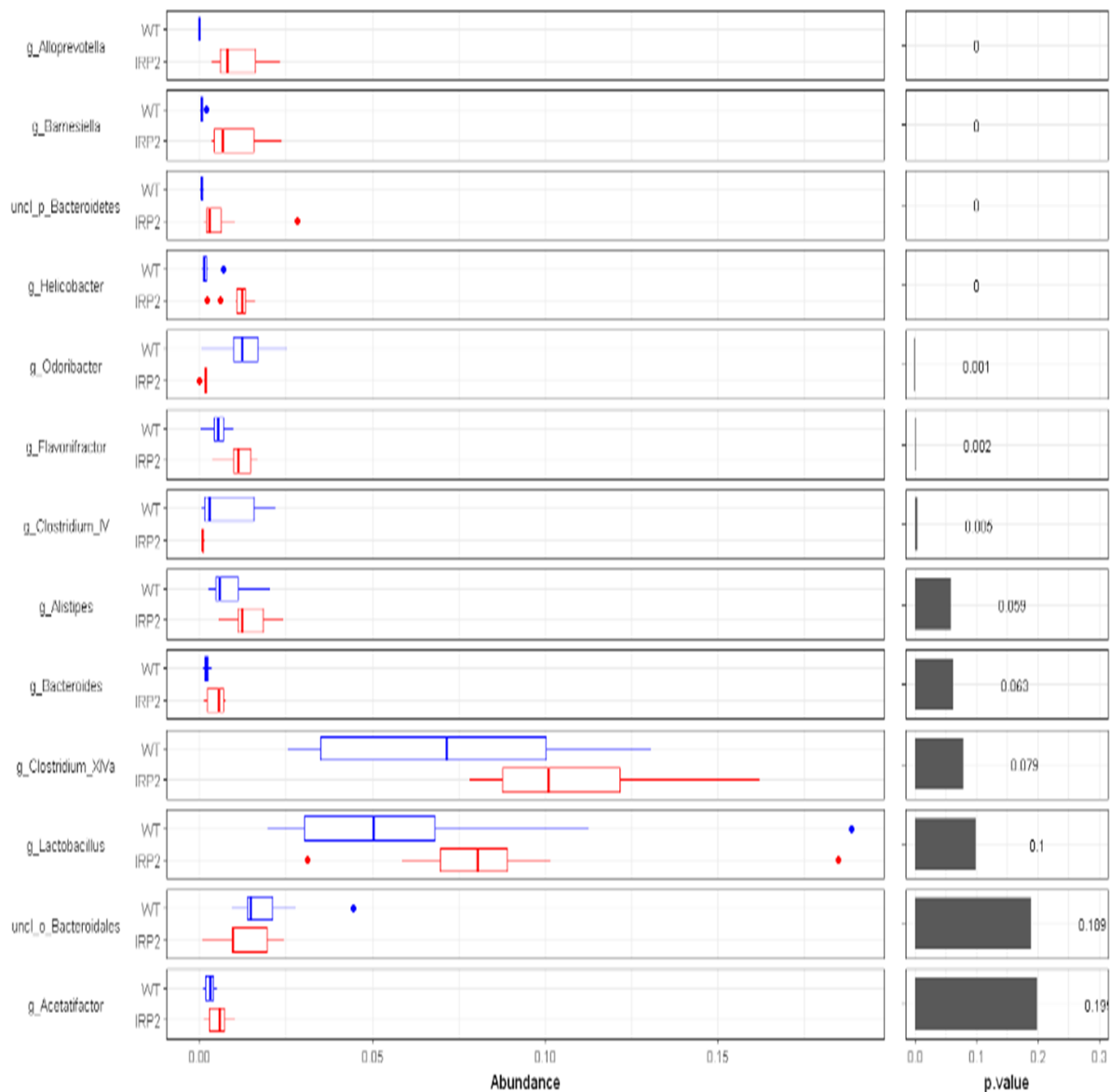


Figure 4.44: Differentially abundant genera in caeca from IRP2- vs wt-donor mice. IRP2-donors from SPF animal husbandry were cohoused in a 1:1 ratio per cage with pregnant GF mice as indicated in Fig. 4.36. All non-infected IRP2-donor and wt-donor mice were sacrificed and caecal contents were collected for 16S rRNA sequencing. Only families with a p-value ≤ 0.2 are shown. Data from 1 experiment are shown, n=3-4 animals. Abbreviations: c= class, o= order, f= family, g= genus, uncl= unclassified. Significance was tested using the Wilcoxon Signed-Ranks Tests; $p \leq 0.2$.

4.5.3 Investigation of host responsiveness to *Mtb* following cohousing

Studies have shown that the gut microbiota influences host phenotype and vice versa [162, 163]. To investigate whether the differences observed in the caecal microbial communities of these mice might influence the outcome of *Mtb* infection, female wt-, IRP1-, and IRP2-acceptors were infected with 100 CFU *Mtb* via aerosol route and CFU assays were performed at days 13 and 28 p.i. Mycobacterial replication was observed in the mice's lungs, spleens, and livers over time. Interestingly, at day 13 p.i., lower bacterial loads were observed in the lungs of

IRP1-acceptors compared to the wt-acceptors but not IRP2-acceptors (**Fig. 4.45A**). On day 28 p.i., no differences in mycobacterial replication were observed in all mice (**Fig. 4.45B**). Similarly, no differences in CFUs were observed in spleens (**Fig. 4.45C**) and livers (**Fig. 4.45D**) of all acceptor mouse genotypes at day 28 p.i.

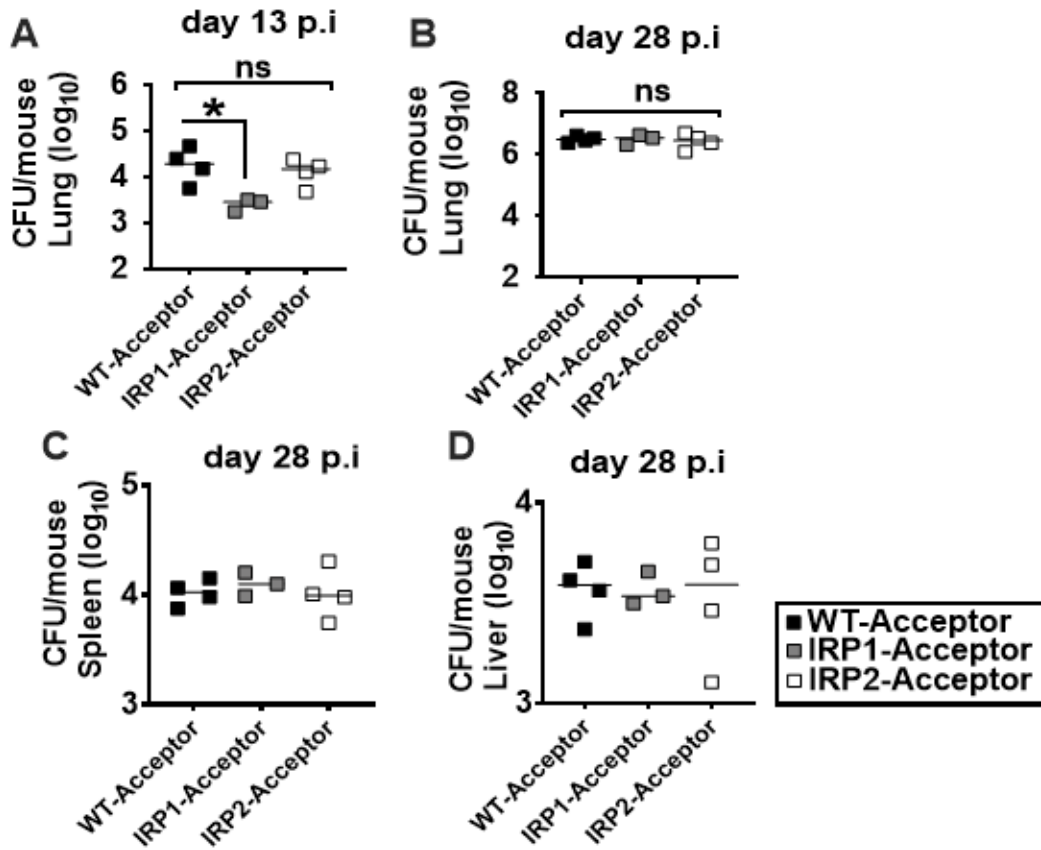


Figure 4.45: Mycobacterial loads in tissue homogenates from wt-, IRP1- and IRP2-acceptor mice. 6-week-old wt-, IRP1-, and IRP2-acceptor mice handled as indicated in Fig. 4.36 were infected with 100 CFU of Mtb via the aerosol route. Mice were sacrificed, lungs (A and B), spleens (C), and livers (D) were collected, and CFU assays were performed at indicated time points. Data from 1 experiment are shown. Each square represents an individual sample (n=3-4 animals) with horizontal lines indicating the median. Statistical analyses were performed using Kruskal-Wallis with Dunn's posttest to compare experimental groups *p = 0.0272 was considered statistically significant. ns represents statistically non-significant differences

4.5.4 Histopathological analysis of lung tissue

To investigate whether the decreased Mtb loads in lungs of IRP1-acceptor mice could be accompanied by any histopathological changes in lung cellular structure, lung tissue was examined using H&E staining. The onset of immune cell infiltration to the sites of infection was observed in all three mouse genotypes at day 13 p.i. Though not statistically significant, IRP1-acceptor seemed to have slightly fewer cellular infiltrates when compared to wt- and IRP2-acceptor mice at this timepoint. As the infection progressed to the 28th day (data not shown), increased numbers of cellular infiltrates could be observed in all three mouse genotypes with no apparent differences like lung CFU data (**Fig. 4.46A-B**)

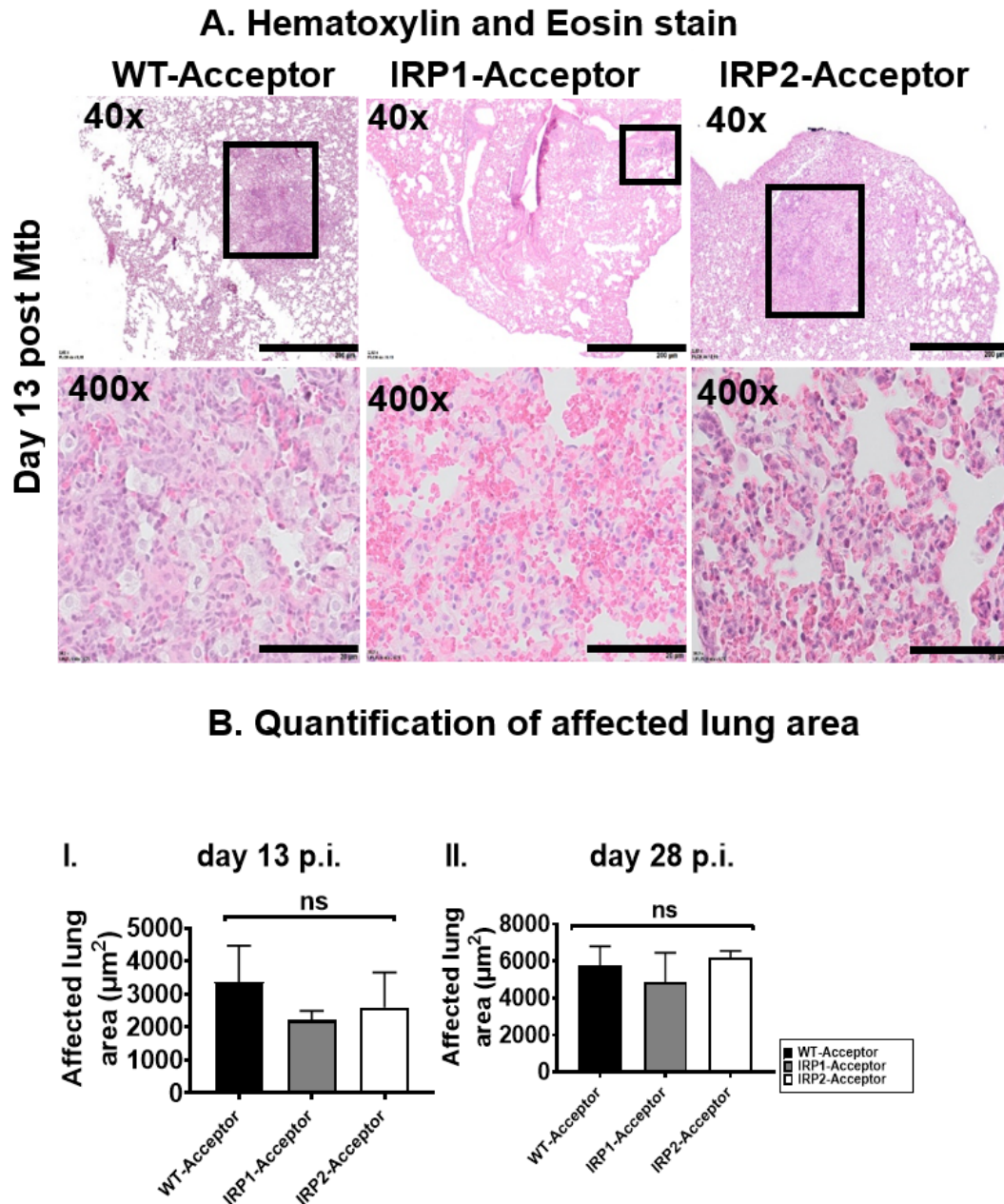


Figure 4.46: Histopathological analysis of lung tissue sections from wt-, IRP1- and IRP2-acceptor mice. 6- week-old female wt-, IRP1- and IRP2-acceptor mice handled as indicated in Fig. 4.36 were infected with 100 CFU Mtb H37Rv via the aerosol route and sacrificed at day 13 p.i. Superior lung lobes were collected, PFA fixed, paraffin infiltrated, stained with H&E stain, and examined under the BX41 light microscope (A). The affected lung area was measured using the cellSens software. Representative micrographs of 1 animal out of 3 per group are shown (i.e., from 1 experiment). Black squares indicate inflammatory cellular infiltrates. Scale bars represent 200 μm (4 x magnification, upper panel), 20 μm (40 x magnification, lower panel). Quantitative assessment of cellular infiltrates and lesions of lung tissue of wt-, IRP1-, and IRP2-acceptor mice at days 13 and 28 p.i (B). Statistical analysis was performed using Kruskal-Wallis' non-parametric test with Dunn's post-test to compare experimental groups; ns represents not-statistically significant differences.

4.5.5 Assessment of red blood cell parameters

To investigate if differences in microbial community structure could influence hematological parameters, whole blood from non-infected and Mtb-infected wt-, IRP1- and IRP2-acceptor was collected at indicated time points and analyzed. No differences were observed in total RBC counts, hematocrit, mean cell volume and mean corpuscular haemoglobin (Fig. 4.47A, B and D-E) of all acceptor mouse genotypes before infection and at days 13 and 28 p.i. On day 28 p.i., lower hemoglobin (Fig. 4.47B) and mean corpuscular haemoglobin concentration (Fig. 4.47F) were observed in the IRP2-acceptor vs wt-acceptor but not IRP1-acceptor mice. This data shows that the altered iron status observed in Mtb-infected wt and *Irp1*^{-/-} and *Irp2*^{+/-} mice (Fig. 4.34) could not be seen in acceptor mouse genotypes indicating that the differences in the caecal microbiota did not significantly influence RBC indices.

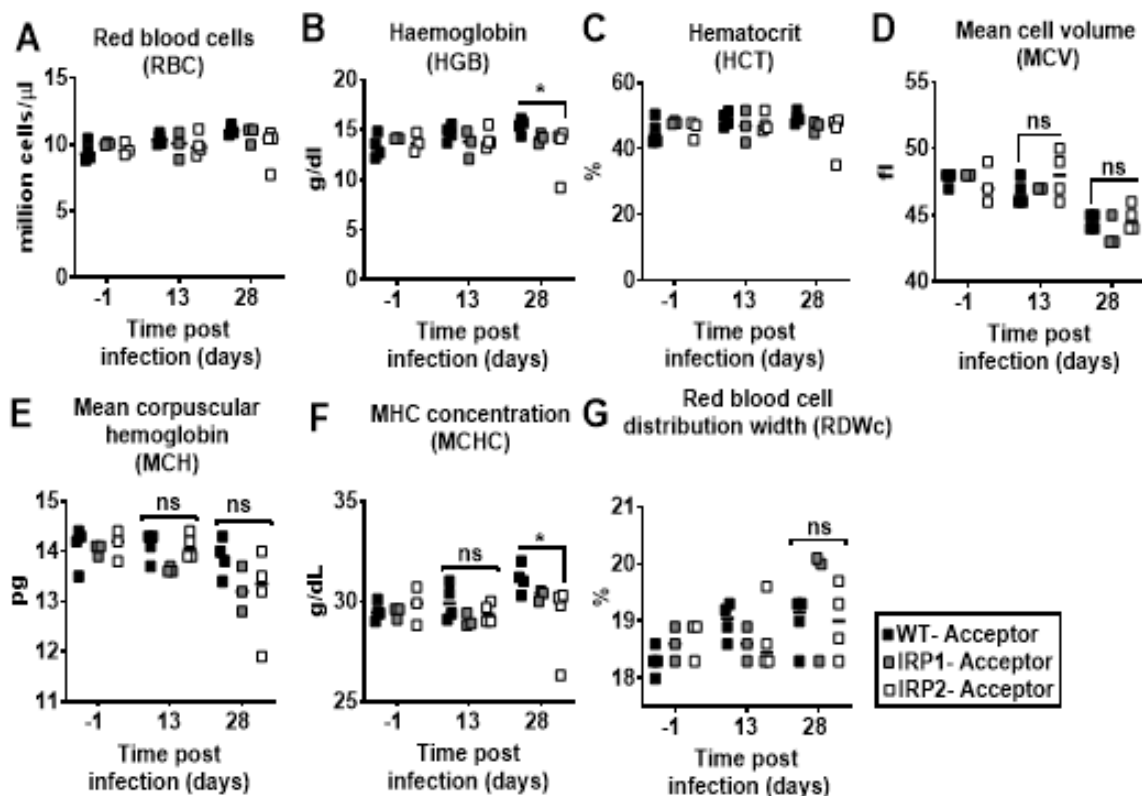


Figure 4.47: Measurement of blood cell count and RBC indices in whole blood from wt-, IRP1- and IRP2-acceptor mice. 6-week-old female wt-, IRP1- and IRP2-acceptor mice were handled as indicated in Fig. 4.36 and infected with approx. 100 CFU Mtb H37Rv via aerosol route. Blood was obtained from the inferior vena cava under terminal anaesthesia for the investigation of RBC (A), HGB(B), HCT (C), MCV (D), MCH (E), MCHC and (F) RDWc (G) indicated timepoints. Each square represents an individual sample (n=3-4 animals). Data from 1 experiment are shown. Statistical analysis was performed using two-way ANOVA with Tukey's multiple comparison tests. * $p \leq 0.05$ were considered statistically significant; ns represents non-statistically significant differences.

4.5.6 Measurement of immune blood cells

Published reports have shown that the gut microbiota influences the overall immune system development and maturation [164]. To investigate the influence of differential microbiota

composition on the immune status of all acceptor mouse genotypes, whole blood was collected, and immune blood cell parameters were analysed. An increase in white blood cells (WBC) (**Fig. 4.48A**) and lymphocyte count (**Fig. 4.48B**) was observed in IRP2-acceptors before Mtb infection and at day 13 p.i., compared to wt- and IRP1-acceptors. However, this increase was not observed at day 28 p.i. in all acceptor mouse genotypes. Furthermore, a higher number of monocytes (**Fig. 4.48C**) was observed only in non-infected IRP2-acceptor mice. No difference in the neutrophil count was observed in all acceptor genotypes (**Fig. 4.48D**).

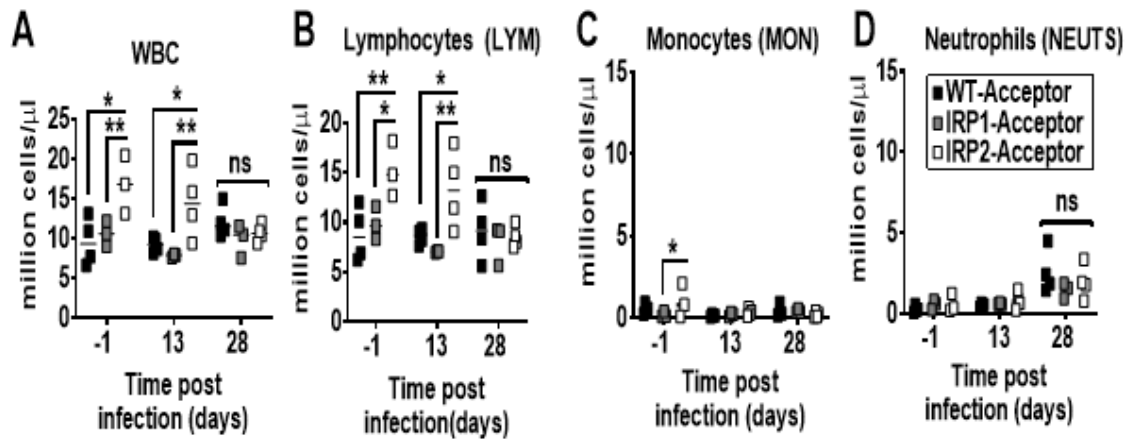


Figure 4.48: Measurement of immune cells in whole blood from wt-, IRP1- and IRP2-acceptor mice. 6-week-old female wt-, IRP1- and IRP2-acceptor mice handled as indicated in Fig. 4.36 were infected with 100 CFU Mtb H37Rv via aerosol route. Whole blood was obtained from the inferior *vena cava caudalis* under terminal anaesthesia for the investigation of blood immune cells WBC (A), Lymphocytes (B), Monocytes (C) Neutrophils (D) at indicated timepoints. Each square represents an individual sample (n=3-4 animals) with horizontal lines indicating the median. Data from 1 experiment are shown. Statistical analysis was performed using two-way ANOVA with Tukey's multiple comparison tests. * $p \leq 0.05$ were considered statistically significant; ns represents non-statistically significant differences.

4.5.7 Cytokine quantification

Following the differences observed in blood immune cells in IRP2- compared to wt- and IRP1-acceptor mice prior to and following infection with experimental Mtb at day 13 p.i. (**Fig. 4.49**), $\text{IFN}\gamma$ and $\text{TNF}\alpha$ concentrations were quantified in the sera of these mice at indicated time points. In all acceptor mouse genotypes, $\text{IFN}\gamma$ and $\text{TNF}\alpha$ were increased by Mtb infection predominantly at day 28 p.i. (**Fig. 4.49A-G**). Though not statistically significant, a trend towards lower $\text{IFN}\gamma$ concentration was observed in sera of IRP1-acceptor mice compared to wt- and IRP2-acceptor mice at day 28 days p.i. (**Fig. 4.49A**). Higher $\text{TNF}\alpha$ concentration was observed in sera of IRP2-acceptor mice compared to and wt- and IRP1-acceptors at days 28 p.i. (**Fig. 4.49B**), indicating the increased inflammatory response of IRP2-acceptor mice to Mtb. These results also show that the higher mycobacterial load in IRP1-acceptor mice is not reflected by the inflammatory responses measured.

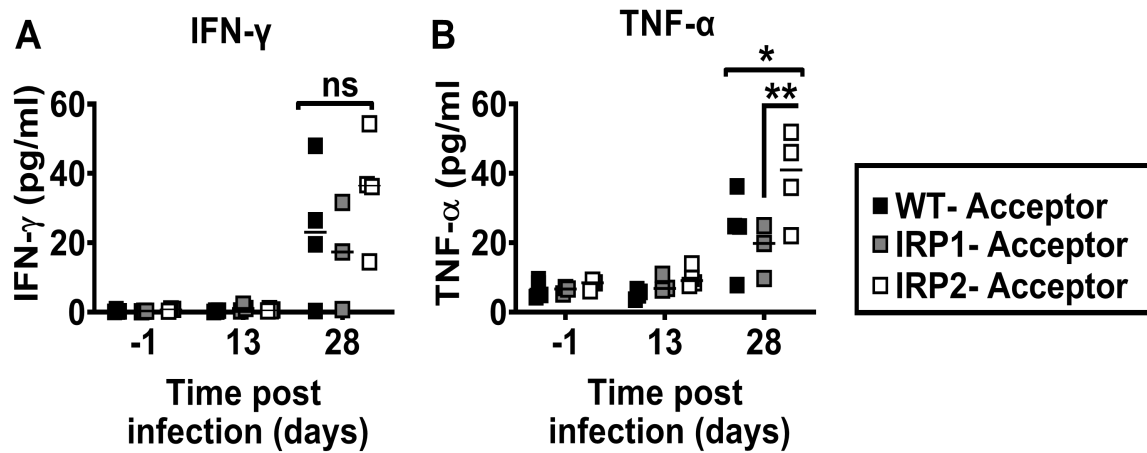


Figure 4.49: Quantification of cytokine concentrations in sera from wt-, IRP1- and IRP2-acceptor mice. 6- week-old female wt-, IRP1- and IRP2-acceptor mice handled as indicated in Fig. 4.36 were infected with approx. 100 CFU Mtb H37Rv via aerosol route and sacrificed at indicated time points. Serum was obtained from whole blood collected from the *vena cava caudalis* under terminal anaesthesia and used to investigate IFN γ (A) and TNF α (B) production. Each square represents an individual sample (n=3-4 animals) with horizontal lines indicating the median. Data from 1 experiment are shown. Statistical analysis was performed using two-way ANOVA with Tukey's multiple comparison tests. * $p \leq 0.05$ and ** $p \leq 0.01$ were considered statistically significant; ns represents non-statistically significant differences.

CHAPTER 5

Discussion

Iron is an essential micronutrient for both, the host and its microbial colonizers, beneficial and pathogenic. Therefore, regulation of iron availability and maintenance of its homeostasis is important for many biological processes. Alterations in iron homeostasis leading to either iron overload or deficiency can cause dysbiosis in the gut microbiome and influence susceptibility to infection. In TB, iron overload has been associated with an increased risk of developing active disease, exacerbated disease outcomes, and effects on gut and lung microbiota diversity. The role of iron and several genes involved in iron regulation and metabolism has been the focus of a number of TB studies. Still, the role of two main regulatory gene products, IRP1 and IRP2, in TB is unknown.

This study aimed to provide evidence for the impact of dietary-mediated changes in iron availability as well as identify the roles of IRP1 and IRP2 on antimicrobial host defenses in murine TB infection. Here, dietary iron supplementation and systemic deletion of *Irp2* altered iron regulation and distribution in non-infected mice leading to increased iron accumulation in alveolar MØs. This iron overload phenotype was further exacerbated upon Mtb infection and was associated with higher bacterial loads in target organs indicating that iron as a micronutrient source for Mtb is responsible for better growth of Mtb during dietary iron supplementation or in the absence of *Irp2*. Higher bacterial loads were also recorded in lungs and spleens of *Irp2*^{+/-} compared to wt mice. This was associated with lower total RBC counts, hemoglobin, and hematocrit but normal mean corpuscular volume, indicating anemia in the early versus late phase of Mtb infection in *Irp2*^{+/-} but not in wt and *Irp1*^{-/-} mice. Higher concentrations of the pro-inflammatory cytokines TNF α and IFN γ were observed in the early phase of Mtb infection and associated with higher Mtb loads and worsened pathology in lungs and livers of *Irp2*^{-/-} mice and mice on an iron-rich diet compared to wt controls or those on iron-low or iron-control diets. These observations demonstrate that higher iron stores impair host immune responses against Mtb. In addition, the iron overload phenotype coupled with increased production of IL-1 β , IL-6, and TNF α indicating a bias to pro-inflammatory host responses in the absence of *Irp2*. These results show that IRP2 is important for host defense functions, clearing of intracellular Mtb and downstream protective immunity against Mtb. IRP1, though, could also be relevant for host resistance to Mtb through compensatory mechanisms. Although the mechanistic roles of IRP1 and IRP2 during Mtb infection are still unclear requiring further investigations, this study provides critical insight into the differential roles of IRP1 and IRP2 during experimental Mtb infection. It reveals that increased iron availability impairs host immune responses, and promotes the growth of Mtb and inflammation, while iron deficiency reduces inflammation and Mtb replication.

Finally, the distinct iron regulation phenotypes of wt, *Irp1*^{-/-} and *Irp2*^{+/-} mice showed altered gut microbiota composition as revealed by 16S rRNA analysis indicating that the gut microbiota could have contributed to phenotypic variations between the mouse strains regarding TB outcome.

5.1 The Effects of Altered Iron Regulation On Host Iron Status During *Mtb* Infection

Healthy human adults produce approx. 2 million RBC per second. This indicates that erythroid precursor cells in the bone marrow require large amounts of iron to sustain demand in order to complete the process of erythropoiesis, which ultimately ends in mature RBC production. The maturation from erythroid precursor cells to mature RBC is driven by erythropoietin (EPO) [165]. EPO is a glycoprotein produced predominantly in the kidney and in minute amounts in the liver, that regulates RBC production in response to changes in tissue oxygenation [166]. EPO is regulated by HIF2 α and is transcriptionally activated under conditions of low oxygen concentrations (or hypoxia) in tissues. Under normal oxygen concentrations, HIF2 α is hydroxylated by iron-dependent enzymes, known as prolyl hydroxylases (PHDs), and degraded through the proteasomal pathway [167, 168]. However, under hypoxic or low iron conditions, PHD activity decreases, stabilizing HIF2 α . Stabilized HIF2 α translocates to the nucleus, binds as a heterodimer to HIF1 β subunit to hypoxia response elements on the EPO promoter, and activates EPO expression [169]. Systemic deletion of HIF2 α in mice leads to anemia [170], meanwhile, hepatocyte-specific deletion reduces hepatic EPO expression [166], thereby linking erythropoietic activity and iron metabolism.

Notably, HIF2 α is also regulated by the IRPs at the post-transcriptional level, as it contains an iron-responsive element (IRE) in the 5' UTR of its mRNA [171]. This suggests that the IRP/IRE system can control EPO expression through HIF2 α and decrease RBC production under low iron conditions, preventing the generation of hypochromic microcytic erythrocytes, which are smaller in size and contain less hemoglobin than normal RBCs.

While the *in vivo* interaction of IRP, HIF2 α , EPO, and erythropoiesis requires further study, the physiological role of IRP1 and IRP2 has been investigated through the generation and characterization of mouse models with *Irp1* or *Irp2* gene deletion [139, 172, 137, 173]. Complete deletion of both, *Irp1* and *Irp2* in mice (*Irp1*^{-/-}*Irp2*^{-/-}) results in a lethal phenotype during the blastocyst phase of embryonic development, thus indicating the critical role of IRPs in early development [172]. However, single *Irp1* and *Irp2* mice, as well as mice lacking one copy of *Irp1* and both copies of *Irp2* (i.e. *Irp1*^{+/-}*Irp2*^{-/-}) are viable and fertile, indicating that these IRPs are functionally redundant and can compensate for the loss of one other [139]. Despite this functional redundancy, *Irp1*^{-/-} and *Irp2*^{-/-} mice have distinct phenotypes, and mice lacking those genes systemically also show different phenotypic outcomes compared to those with tissue-specific deletions, as summarized in **Table 5.1**.

Table 5.1: Distinct phenotype features of mouse models with complete or tissue-specific deletion of *Irp1* and *Irp2*. Adapted from [35]

Mouse model	Site of modification	Phenotype
<i>Irp1</i> ^{-/-} <i>Irp2</i> ^{-/-}	Systemic	Embryonic lethality at blastocyst phase [172]
<i>Irp1</i> ^{-/-} <i>Irp2</i> ^{-/-}	Hepatocyte-specific	Postnatal death within 1-2 weeks after birth [174]
<i>Irp1</i> ^{-/-} <i>Irp2</i> ^{-/-}	Duodenal enterocytes-specific	Postnatal death within 4 weeks after birth, growth retardation, increased <i>Frtn</i> , <i>Fpn</i> , and <i>Dmt1</i> expression [175]
<i>Irp1</i> ^{+/-} <i>Irp2</i> ^{-/-}	Systemic	More prominent axonal degeneration in cerebellum, misregulation of <i>Frtn</i> and <i>TfR1</i> , microcytic anemia, increased serum ferritin levels, <i>TfR1</i> levels significantly decreased in erythroid precursors compared to <i>Irp2</i> ^{-/-} mice
<i>Irp1</i> ^{-/-}	Systemic	Polycythemia, stress erythropoiesis, splenomegaly, increased HIF2 α protein expression and serum EPO levels [157, 137, 176]
		Cardiac hypertrophy and fibrosis, pulmonary hypertension, increased polycythemia upon consumption of iron-deficient diet resulting in death by peritoneal hemorrhage [137]
		High duodenal <i>Dmt1</i> , <i>Fpn</i> , <i>Dcytb</i> mRNA expression, increased <i>Fpn</i> expression in splenic M ϕ s, decreased hepatic <i>Hamp1</i> mRNA transcripts, misregulation of <i>Frtn</i> and <i>TfR1</i> in the kidney and brown fat [157, 139, 176]
<i>Irp2</i> ^{-/-}	Systemic	Microcytic hypochromic anemia, iron overload in duodenum, liver, neurons but an iron deficiency in the spleen and bone marrow [158, 156]
		Increased protoporphyrin IX levels, decreased <i>TfR1</i> expression and iron levels in erythroblasts, increased <i>Frtn</i> levels in all tissues [158]
		Progressive neurodegeneration, mild neurological and behavioural deficits [177]
<i>Irp2</i> ^{-/-}	Macrophage-specific	No overt pathology
<i>Irp2</i> ^{-/-}	Hepatocyte-specific	Mild hepatic iron overload
<i>Irp2</i> ^{-/-}	Intestinal-specific	Mild duodenal iron overload

The phenotype of *Irp1*^{-/-} mice shows that *Irp1* functions as a central regulator of HIF2 α expression at the level of mRNA translation. It is noteworthy that *Irp1*^{-/-} mice have been reported to exhibit an overexpression of HIF2 α . This overexpression includes increased EPO production, leading to splenomegaly and secondary polycythemia due to extramedullary erythropoiesis [137, 176, 157]. Extramedullary erythropoiesis refers to the production of RBCs which occurs outside the medulla of the bone marrow, typically in the spleen or liver, as a result of elevated EPO production. In line with findings by other authors [137, 176, 157], *Irp1*^{-/-} compared to wt and *Irp2*^{-/-} mice in my study displayed splenomegaly at baseline. This phenotype was further exacerbated at day 28 p.i. (**Fig. 4.18**), suggesting that Mtb infection in the early phase significantly increases EPO production, leading to downstream splenomegaly. HIFs, particularly HIF1 α have been implicated in TB immunity and are being considered a potential target for therapeutic intervention against TB [178, 179]. However, there is no existing data on HIF2 α overexpression following Mtb infection in the context of the IRP/IRE system. Therefore, quantification of EPO protein expression as one of the indicators of HIF2 α overexpression, in kidney homogenates of Mtb infected *Irp1*^{-/-} mice using western blot is required to reveal whether experimental Mtb infection induces EPO upregulation, particularly at day 28 p.i.

HIF2 α overexpression is also manifested in patients with Chuvash polycythemia, a hereditary disease caused by mutations in the von Hippel-Lindau (VHL) gene (i.e., VHL^{R200W}) which prevents proteasomal degradation of HIF2 α , resulting in increased HIF2 α protein expression [180, 181]. Polycythemia is the body's response to an increased demand for oxygen. Typically, polycythemia is characterized by higher hemoglobin and hematocrits values, along with decreased mean cell volume and mean corpuscular hemoglobin values. Chronic inflammatory lung diseases such as chronic obstructive pulmonary disease (COPD), which includes emphysema and chronic bronchitis can cause low oxygen tension in the blood, resulting in polycythemia [182]. Further studies are required to investigate the potential interplay between TB and polycythemia and whether Mtb influences polycythemia and vice versa.

In *Irp1*^{-/-} mice, secondary polycythemia, which occurs due to high levels of EPO, has been explained by IRP1-regulated translational derepression of HIF2 α mRNA, which upregulates EPO and endothelin-1 expression driving reticulocytosis and downstream polycythemia [157]. The polycythemia phenotype in *Irp1*^{-/-} is exaggerated upon consumption of an iron-deficient diet, leading to sudden death by peritoneal hemorrhage. This highlights the important role of IRP1 in systemic iron homeostasis and erythropoiesis [137]. Previous reports by other authors show that adult *Irp1*^{-/-} mice have higher total RBC counts and hematocrits of 50% compared to 45% in wt mice [137], while some studies have shown that 4-6 week-old *Irp1*^{-/-} mice have hematocrits above 70% [183]. However, all studies agree that hematocrits of *Irp1*^{-/-} mice decrease with age, with vanishing differences in hematocrit levels between *Irp1*^{-/-} and wt mice starting around 6 weeks of age. The findings in my study regarding the iron status of *Irp1*^{-/-} mice do not entirely align with findings of other authors. In my study, no differences were observed in terms of total RBC counts, hemoglobin, and hematocrits between non-infected *Irp1*^{-/-} and wt mice (**Fig. 4.32**). This observation suggests that at the age of 20 weeks, the juvenile polycythemia phenotype of *Irp1*^{-/-} mice has passed. This hypothesis supports observations made by Zhang et al. [183], where hematocrits of *Irp1*^{-/-} mice of various ages ranging from 4 weeks to 14 months old were investigated [183]. In their study, no significant decrease in the hematocrits was reported in *Irp1*^{-/-} mice older than 8 weeks. To reveal this phenotype, younger mice under 8 weeks should have been used in my study. Nevertheless, I did observe lower mean cell volume (MCV) (**Fig. 4.32D**) and % transferrin saturation (**Fig. 4.35B**) in *Irp1*^{-/-} compared to wt mice, which is consistent with previous reports [157, 137, 152], indicating a reduced capacity for oxygen transport in RBCs

of *Irp1*^{-/-} compared to wt mice at baseline.

The described phenotype of *Irp2*^{-/-} mice indicates that *Irp2* functions as a key regulator in other facets of erythropoiesis and is not involved in the regulation of HIF2 α . *Irp2*^{-/-} mice have been described to display microcytic hypochromic anemia [158, 156]. This is characterized by decreased hemoglobin, hematocrits, and MCV despite total RBC counts being within a normal range. Clinically, anemia is classified as either microcytic (MCV less than 80 fl), normocytic (MCV 80-100 fl) and macrocytic (MCV greater than 100 fl) based on the MCV or hypochromic (MCH less than 26 pg) or normochromic (MCH greater than equal to 26 pg) based on MCH values [184]. In *Irp2*^{-/-} mice, microcytic anemia is associated with high serum ferritin, normal to slightly elevated transferrin saturation, and normal serum iron and total iron-binding capacity (TIBC). Cooperman et al. [158] observed that the microcytic, hypochromic anemia in *Irp2*^{-/-} mice was established as a result of iron-limited erythropoiesis due to down-regulation of TfR in erythroid precursors and empty bone marrow iron stores, despite normal transferrin saturation levels [158]. This is supported by mice with either hepatocyte-, enterocyte-, or macrophage-specific deletion of *Irp2*, which do not develop hematological defects [137], indicating that the microcytic hypochromic anemia of *Irp2*^{-/-} mice is due to a defect in RBC precursors.

A slight decrease, though not statistically significant, in total serum iron, total iron-binding capacity (TIBC), and % transferrin saturation but high serum ferritin were observed in *Irp2*^{+/-} compared to wt mice (**Fig. 4.35**). Genotyping by PCR revealed that these mice were heterozygous (*Irp2*^{+/-}) and not homozygous (*Irp2*^{-/-}) for *Irp2* allele (**Fig. 4.33C-F**), thereby explaining why no differences could be seen between these mice. As the described microcytic hypochromic anemia phenotype of non-infected *Irp2*^{-/-} could not be investigated in my study, further experiments are required.

So far, the iron phenotypes of *Irp1*^{-/-} and *Irp2*^{-/-} have not yet been analyzed in the context of experimental TB. Even though the *Irp2*^{-/-} strain was lost from our mouse collection, *Irp2*^{+/-} mice exhibited distinct iron phenotypes upon Mtb infection when compared to wt but not *Irp1*^{-/-} mice. In my study, *Irp2*^{+/-} mice developed normocytic normochromic anemia at day 28 p.i., characterized by decreased total RBC counts, hemoglobin and hematocrits but normal MCV (**Fig. 4.34**). The anemia phenotype of *Irp2*^{+/-} mice upon Mtb infection is comparable to numerous studies showing anemia as a consequence of several infectious diseases such as TB, Malaria, and Brucellosis [185, 155]. In particular, the normocytic normochromic anemia of *Irp2*^{+/-} mice at day 28 p.i. correlated with higher Mtb loads in the lungs, spleens and livers compared to wt and *Irp1*^{+/-} mice. These results align with the study by Rodrigues et al. [186], which demonstrated that iron-overloaded BALB/c mice infected with *M. avium* exhibited normocytic anemia and higher bacterial loads in livers and spleen [186]. These results also correlate with several clinical studies showing anemia as recurrent comorbidity of TB, affecting up to 94% of patients diagnosed with TB [187, 188]. Anemia is associated with an increased risk of delayed sputum smear conversion in pulmonary TB patients, poor TB outcomes and increased mortality in TB patients [189, 190, 191]. Normocytic normochromic anemia has been reported to be a common anemia type in most pulmonary TB patients. Notably, Mendonca et al [192] showed that 60.8% of TB patients enrolled in a study in Brazil were diagnosed with normocytic normochromic anemia ranging from mild-to-moderate forms, and anemia was severe in disseminated and meningeal TB, suggesting that anemia may serve as a biomarker of TB severity.

Anemia in TB patients has been reported to be due to anemia of inflammation (AI) rather than iron deficiency anemia, although both types of anemias frequently co-exist [193, 194]. As exacerbated inflammation is a characteristic feature of TB, hepcidin drives the onset of

AI through iron-restricted erythropoiesis. Typically, this is reflected by tissue iron release restriction, reduced serum iron and total iron-binding capacity (TIBC), and elevated serum ferritin levels. The findings in my study align with these characteristic features of AI. The normocytic normochromic anemia observed in Mtb infected *Irp2*^{+/-} mice correlated with low serum iron, low total iron-binding capacity (TIBC), and % transferrin saturation, but high serum ferritin concentrations on days 28 and 63 p.i. (**Fig. 4.35**), pointing towards anemia of inflammation, AI.

The altered iron metabolism observed in *Irp2*^{+/-} mice can be hypothesized to be a component of the host defense system against invading pathogens, and it is inferred to be mediated by several inflammatory cytokines discussed in detail in **section 5.3**. While IRP1-mediated secondary polycythemia has not yet been reported in humans, polymorphisms in IRP1 have been associated with cutaneous malignant melanoma [38]. Also, the association between HIF2 α and IRP1 in TB pathogenesis remains unexplored. My research establishes a regulatory link between the IRE/IRP system and TB, which stems from the critical role of IRPs in maintaining iron balance. Any disruption to this balance can result in oxidative stress, ultimately contributing to the growth and proliferation of benign or malignant neoplasms. The results of my study show a gene dosage effect, as the deletion of one allele of *Irp2*, as well as systemic deletion of IRP2, alters iron metabolism. This can be interpreted as a host defense strategy against Mtb, indicating that there is a protective role of IRP2 in TB pathogenesis in the context of iron homeostasis.

5.2 The Influence of Iron Availability on Mtb Growth in Macrophages and Mice

Iron is an indispensable micronutrient required for the growth, survival, and virulence of Mtb [72, 150]. Notably, Esx-3, a type VII secretion system implicated in mycobactin-mediated iron acquisition in Mtb, has been suggested to interfere with host functions that limit iron availability. Mtb mutants lacking *esx3* showed decreased iron uptake [195]. Similarly, Mtb mutants with single deletions in *mbtK*, a mycobactin synthase gene involved in siderophore production, showed defects in iron acquisition and reduced growth *in vitro* and in infected mouse lungs [196], supporting the notion of the importance of iron acquisition for Mtb growth and virulence.

Several authors have shown evidence that iron availability has an influence on mycobacterial growth *in vitro* [150, 151], in mice [76, 197] and humans [147]. Exogenous iron such as ferrous sulfate or ferric ammonium citrate (FAC) has been shown to enhance Mtb, *M. avium* and *M. bovis* growth in M ϕ s [48]. Conversely, supplementation of serum-free medium with apo-transferrin or bovine lactoferrin limits Mtb, *M. avium* and *M. bovis* growth, while treatment with iron-chelating agents such as deferoxamine shows a mycobacteriostatic effect, reducing mycobacterial growth in M ϕ s. The findings in my study confirm and expand on these previous observations by other authors by demonstrating that excess iron can further enhance mycobacterial growth in M ϕ s. Furthermore, *Irp2*^{-/-} M ϕ s have iron overload phenotype, which can only be achieved in wt and *Irp1*^{-/-} M ϕ s by adding exogenous iron (**Fig. 4.14**). Notably, FAC even further enhanced mycobacterial growth in *Irp2*^{-/-} M ϕ s (**Fig. 4.14E-H**) while DFO proved to be inefficient in decreasing Mtb growth (**Fig. 4.14I-L**) thus demonstrating a direct link between mycobacteria growth and iron availability.

Similar to *in vitro* studies, most reports, though contradictory, show that excess iron enhances mycobacterial growth *in vivo* [197, 198, 76]. However, the majority of these studies report on non-tuberculous mycobacteria such as *M. avium* allowing for scant evidence on the effects of iron availability on Mtb growth in mouse models. Here, I provide evidence on the effects of iron availability on Mtb growth using dietary iron supplementation which leads to higher Mtb growth in mice. In addition, I present new evidence on the influence of disruptions in iron metabolism on Mtb growth using MØs and mice deficient for either *Irp1* or *Irp2*, which leads to differential Mtb growth in target host cells and organs, respectively.

In my study, experimental iron overload or iron deficiency (ID) was induced in mice via the enteral route by feeding iron-rich (460 mg/kg Fe (II) fumarate) or iron-low (< 9 mg/kg Fe (II) fumarate) diets, respectively (**Fig. 4.1**). Prussian blue staining revealed increased iron accumulation in the lungs of mice on an iron-rich diet compared to those on control (4 mg/kg Fe (II) fumarate) and iron-low diets before and after Mtb infection, with the highest differences at day 120 p.i. (**Fig. 4.7**). This observation correlated with higher Mtb loads in the lungs, livers, and spleens of mice on iron-rich diets compared to those on iron-control and iron-low diets (**Fig. 4.2**). These results build on existing evidence from several *in vivo* studies showing that increased iron stores from iron supplementation, either per oral administration of iron salts in diets or drinking water, or intravenously as iron-carbohydrate complexes, increases the severity of mycobacterial infections [199, 147]. For instance, Dhople et al. [199] reported that BALB/c mice fed standard chow enriched with ferric ammonium citrate showed elevated iron saturation in sera which correlated with increased mycobacterial loads in the lungs, spleens, and livers following intravenous infection with (10^6) *M. avium* infection compared to controls [199]. In another study, Lounis et al. [198] reported that BALB/c mice treated with 50 mg/kg intraperitoneal injections of polymaltose ferric hydroxide, an oral iron preparation used to treat ID and iron deficiency anemia (IDA), three times a week for 2 weeks before intravenous infection with (7.2×10^3 CFU) Mtb H37Rv, showed higher mycobacterial loads in lungs and spleens compared to controls [198]. Similarly, B6 wt mice injected intraperitoneally with (approx. 4mg iron per animal) ferric hydroxide-dextran complex, equally used to treat iron deficiency (ID), for 20 days before infection with (10^6 CFU) *M. avium* via intravenous route exhibited increased mycobacterial loads in the lungs, spleen, and liver [151]. Clinical studies have also shown that increased iron stores from iron supplementation may result in iron overload, which may predispose individuals to the develop active TB [200, 69]. In a pioneer study, Murray et al. [147] found that oral administration of 900 mg ferrous sulfate per day, for 30 days in iron-deficient Somali nomads led to increased incidence rates of several infections, including Mtb [147].

Oral iron supplementation in the form of ferrous iron salts, e.g., ferrous fumarate, ferrous sulfate, ferrous gluconate, and the amino acid chelate, ferrous bisglycinate is routinely used to treat ID with or without anemia [201], which is prevalent in patients with TB, particularly in sub-Saharan African populations [202]. In these populations, dietary iron overload often occurs due to the consumption of traditional fermented beers brewed in steel containers. Generally, this is characterized by iron depositions in both MØs and hepatic parenchymal cell. Of note, the iron overload disorder in the sub-Saharan African population has been linked to poor TB outcome. Most studies on iron supplementation have been or are currently being carried out in sub-Saharan Africa where nutritional iron deficiency is highly prevalent. Nutritional ID, which arises when the diet does not provide enough bioavailable iron to meet up with the body's demand, is the primary risk factor for developing ID/IDA. ID has been described to modulate host immune responses but can also be detrimental to the host as immune responses are hampered [76, 199]. Murray et al. [147] showed that Somali nomads

entering a feeding camp did not contract infections if they were iron deficient, in contrast to a high infection rate in those with normal iron status. In my study, mice fed iron-low diets demonstrated lower Mtb replication in lungs, spleens, and livers (**Fig. 4.2**). These results are in line with reports by other authors which have shown that iron deprivation is protective [150, 203, 76]. For example, both B6 wt and B6 immunodeficient beige mice fed an iron-poor diet (6.7mg/kg) for 2 weeks prior to infection with (10^6 CFU) *M. avium* via intravenous route showed inhibited *M. avium* growth in lungs, spleens and livers [150]. However, in another study, B6 wt mice fed an iron-deficient diet (2-6 ppm iron) for 6 weeks prior to aerosol infection with Mtb Erdman (50-100 CFU) did not show any significant impact on mycobacterial growth in their lungs and spleens compared to controls [203]. Similarly, intranasal administration of lactoferrin (1 mg/mL twice weekly) did not alter Mtb growth in wt mice 22 p.i. [76]. While these studies, along with my own findings, highlight that increased iron availability promotes mycobacterial growth *in vivo*, it is also important to consider other factors are highly involved in determining TB outcome. These factors include; the route of iron supplementation (nteral versus intraperitoneal), choice of iron compounds, dosing and duration of iron treatment, Mtb strain used, route of infection, and overall experimental design. Therefore, investigators must carefully consider all these parameters when designing iron supplementation studies. Similarly, in a clinical setting, iron treatment should be carefully designed to avoid inducing iron overload, which can promote Mtb replication. Nevertheless, clinical trials are needed to ascertain the optimal timing and dosage of iron supplements in TB patients with anemia of inflammation and IDA.

In vivo studies by other authors have shown that disruptions in iron metabolism influence the outcomes of several types of infections [136, 76, 203, 204]. For instance, Nairz et al. [136] demonstrated that mice with an MØ-specific deletion of both IRPs developed hyperferritinemia, exhibited higher *S. Typhimurium* burdens in livers and spleens and succumbed earlier to the infection, indicating that IRPs are involved in innate immunity [136]. My data demonstrates increased iron deposits in Mtb infected aMØs (**Fig. 4.28**) and MØs in hepatic infiltrates (**Fig. 4.29**) in all three mouse strains, but more detected in *Irp2*^{-/-} mice at days 28 and 63 p.i. compared to wt and *Irp1*^{-/-} mice. These findings correlated with higher Mtb loads in lungs, livers, and spleens of *Irp2*^{-/-} mice compared to wt and *Irp1*^{-/-} ones (**Fig. 4.15A-C**), indicating that increased iron deposits serve as a micronutrient source for Mtb. These results build on existing evidence from similar studies using iron overload mouse models [136, 76]. For example, *Hfe*^{-/-} mice with hepatic iron overload showed increased *M. avium* loads in livers and spleens. Additionally, Beta-2 microglobulin (*β2m*^{-/-}) mice with parenchymal iron deposition were more susceptible to Mtb than wt controls, a phenotype which was rescued by iron sequestration through exogenous lactoferrin administration [76]. *Hfe* is the equivalent mouse gene of the human hemochromatosis gene HFE that binds to the transferrin receptor to facilitate internalization and recycling. HFE is a MHC Class-I-like molecule not covalently bonded to (*β2m*) [205, 206, 207]. However, my results contradict the claims of Harrington-Kandt et al. [203], who showed that Mtb Erdman infection of *Hamp1* mouse with an iron overload phenotype was not different from wt mice in terms of mycobacterial growth in lungs and spleens indicating that hepcidin deletion does not affect Mtb growth *in vivo*. Importantly, my study revealed increased iron deposits in aMØs in non-infected *Irp2*^{-/-} lungs compared to wt and *Irp1*^{-/-} lungs (**Fig. 4.28**). Ferring-Appel et al. [208] showed that mice with hepatocyte-specific or intestinal-specific deletion of *Irp2* display an iron overload phenotype to cell-autonomy traits in enterocytes and hepatocytes. The same interpretations by Ferring-Appel et al. can also be applied to my study. Therefore, it can be speculated that

iron overload in phenotype in *Irp2*^{-/-} lungs and livers, resulting in higher Mtb loads could have given a survival and marked replicative advantage for Mtb.

The differential Mtb loads in lungs, spleens, and livers of wt, *Irp1*^{-/-}, *Irp2*^{-/-} and *Irp2*^{+/-} mice at different time points after infection may be attributed to the varying sequestration of iron by specialized MØs in the respective tissues. MØs direct the production of RBCs during erythropoiesis and ultimately phagocytose old and damaged RBC at 120 days of age [6, 7]. Although the precise mechanisms which drive MØs to phagocytose RBCs are not fully understood, a few studies have suggested that pro-inflammatory cytokines such as TNF α and IFN γ , produced in response to infections, recruit and activate MØs to phagocytose RBCs, leading to increased intracellular iron within MØs [209, 210, 211]. Fundamentally, these alterations in iron metabolism upon immune activation are mostly dependent on IL-6 and hepcidin and will be extensively discussed in **section 5.3**.

Alterations in systemic iron homeostasis can also occur independent of IL-6 but require the exclusive action of PRRs. For example, *Fpn1* transcription is inhibited by TLR2, -4, and -6 ligation, allowing for downregulation of *Fpn1* mRNA transcripts via a hepcidin-independent mechanism. As a case in point, *S. Typhimurium*, can activate TLR4 via its PAMP lipopolysaccharide (LPS), enabling MØs to phagocytose RBCs, thereby increasing the intracellular iron pool [209].

In my study, higher concentrations of IL-6, TNF α , and IFN γ were observed in *Irp2*^{-/-} lung tissue homogenates at days 28 and 63 p.i. (**Fig. 4.19**), corresponding to higher Mtb loads in lungs (**Fig. 4.15**) and increased iron deposits in lungs and livers after Mtb infection (**Fig. 4.28**). To this end, it can be speculated that Mtb induced higher concentrations of IL-6 in *Irp2*^{-/-} MØs leading to hepatic *Fpn1* transcription inhibition, which resulted in increased intracellular iron levels as reflected by elevated iron deposits in *Irp2*^{-/-} lung and liver MØs. Consequently, this increased iron availability could serve as a micronutrient source for Mtb. However, it remains to be investigated whether Mtb infection or Mtb PAMPs can also induce erythrophagocytosis. Hence, the relevance of TLR2 or Mtb-specific PRR in this context cannot be ignored and requires further investigation. Some evidence suggests that RBC clearance is associated with a pro-inflammatory cytokine response, while other studies show an anti-inflammatory role for these MØs. On that account, flow cytometry studies will be necessary to explore the erythrophagocytic functions of *Irp1*-deficient and *Irp2*-deficient MØs at baseline and in the setting of an infection with Mtb H37Rv.

Moreover, my results also suggest that the higher Mtb loads observed in *Irp2*^{-/-} BMMØs could be attributed to their increased phagocytic rate, as seen in the uptake of pre-labeled Zymosan particles (**Fig. 4.11**). While this observation suggests that deletion of *Irp2* results in enhanced phagocytic ability, further flow cytometry investigations must be done to determine whether this also holds true for the uptake of mycobacteria.

5.3 The Role of Iron in Immunity against Mtb Infection

Beneath pulmonary inflammatory lesions, TB causes a chronic state of systemic inflammation, which can trigger hepatic hepcidin synthesis and ultimately influence iron homeostasis [212, 213]. Several clinical studies have reported elevated hepcidin concentrations in patients with active pulmonary TB with or without HIV [214]. Here, I found higher Mtb loads in *Irp2*^{-/-} mice livers at day 28 p.i. (**Fig. 4.15C**), which correlated with elevated hepatic *Il-6* and *Hamp1* mRNA transcripts (**Fig. 4.27C-D**). These observations suggest that higher Mtb loads enhanced *Il-6* expression which can promote hepatic hepcidin transcription as an

attempt to restrict peripheral iron availability for extracellular pathogens. Hepcidin promotes iron sequestration within MØs, as evidenced in this study by increased iron deposits in Kupffer cells and inflammatory cell infiltrates in livers of *Irp2*^{-/-} mice (**Fig. 4.29**) but decreased total serum iron (**Fig. 4.35D**), indicating a hypoferremic response. However, this iron withholding strategy within MØs provides a survival and replication advantage to intracellular Mtb, as iron is an essential micronutrient for Mtb. These results confirm data from studies by other authors that a wide range of infectious agents, including Influenza A virus, *S. Typhimurium*, *Vibrio vulnificus*, and *Candida albicans* strongly induce hepatic hepcidin transcription in mice [215, 216]. Indeed, IL-6 production and *Hamp1* transcription are triggered early following an infectious or inflammatory stimulus. However, higher hepatic *Hamp1* gene expression at day 28 p.i. in *Irp2*^{-/-} mice, rather than in the early phase of infection at day 13 p.i., suggests delay of induction of hepatic hepcidin or suppression of IL-6 mediated hepcidin production in the early stages of Mtb infection. However, the molecular basis underlying this phenotype remains unclear.

Consistent with previous studies by other authors [217], decreased hepatic *Hamp1* was observed in *Irp1*^{-/-} compared to *Irp2*^{-/-} mice (**Fig. 4.27D**). Viatte et al. [217] reported that *Irp1*^{-/-} and *Irp2*^{-/-} mice show similar hepcidin mRNA induction and associated reductions in serum iron levels upon treatment with turpentine oil, which was used to induce a local inflammation. This study showed that the lack of either IRP is not a disadvantage to inflammation triggered by hepatic hepcidin production [217]. However, in my study, systemic deletion of *Irp2* upon Mtb H37Rv infection induces *Hamp1* transcription, while, no effect is observed in the absence of *Irp1*. This discrepancy in *Hamp1* expression between Kupffer cells and inflammatory cell infiltrates in *Irp1*^{-/-} and Kupffer cells and inflammatory cell infiltrates in *Irp2*^{-/-} mice upon Mtb infection can be explained by the differential Mtb loads in these respective mouse genotypes, which is required to trigger *Hamp1* expression in the absence of IRP2 but not IRP1. In contrast to non-infected *Irp2*^{-/-} mice with an iron overload phenotype, non-infected mice on an iron-rich diet showed increased *Hamp1* mRNA expression when compared to mice on iron-control and -low diets (**Fig. 4.5J-L**). This observation is in line with studies showing that *Hamp1* mRNA expression was increased in response to enhanced dietary iron in mice [218, 219].

Besides infectious stimuli, hepcidin production can also be influenced by anemia [47, 220]. Several studies have shown that anemia decreases the production of hepatic hepcidin, which releases iron from MØs and enables iron to be utilized for compensatory erythropoiesis. For example, Nicolas et al. [47] demonstrated that anemia induced by repeated phlebotomies or acute hemolysis from phenylhydrazine treatment suppressed hepatic hepcidin mRNA [47]. In my study, infection-induced anemia in *Irp2*^{+/-} mice did not downregulate hepatic hepcidin production at day 28 p.i., indicating that through its proinflammatory stimuli, Mtb can overwrite anemia-mediated suppression of hepcidin at this time point. Additionally, the cytokines produced during Mtb infection can directly hinder erythropoiesis and lead to anemia. Hepcidin drives the onset of AI through iron-restricted erythropoiesis. Iron-restricted erythropoiesis can be due to functional iron deficiency, absolute iron deficiency, or iron sequestration. In my study, Mtb infected *Irp2*^{+/-} mice presented certain features of anemia of inflammation only at day 28 p.i. These features include normocytic anemia (**Fig. 4.34**), decreased total serum iron despite adequate iron stores represented by higher serum ferritin levels. Meanwhile, *Irp2*^{-/-} mice showed increased iron accumulation in aMØs, hepatic inflammatory infiltrates and Kupffer cells in the lungs and livers, respectively (**Fig. 4.28-29**). Although these features are indicative of anemia of inflammation in Mtb infected *Irp2*^{+/-} mice at day 28 p.i., other

factors such as shortened RBC survival and direct suppression of erythropoiesis could also contribute to the pathogenesis of anemia of inflammation but were not investigated in this study. Whether these factors affect anemia of inflammation in Mtb infected *Irp2*^{+/-} mice at day 28 p.i. remains a topic of future studies. The possibility of their contribution to the above-described phenotype cannot be ignored. Therefore, studies on RBC lifespan and suppression of erythropoiesis during experimental Mtb must be performed to understand the establishment of anemia in *Irp2*^{+/-} mice. In addition, the RBC indices of non- and Mtb infected *Irp2*^{-/-} mice need to be investigated in further studies, to fully understand, if Mtb infection induces anemia in mice deficient for IRP2, which further exacerbates disease.

In addition to IL-6 which induces hepcidin transcription, IL-1 β stimulates the expression of CCAAT enhancer-binding protein, a transcription factor, to promote hepcidin transcription through interactions with the hepcidin promoter [221]. Higher IL-1 β and IL-6 concentrations were observed in *Irp2*^{-/-} mice lungs compared to wt and *Irp1*^{-/-} mice, particularly in the early phase of infection (**Fig. 4.19**). In mice fed an iron-rich diet, an increase in *Il-6* gene expression was observed following Mtb infection (**Fig. 4.5C**). Despite higher protein concentrations of IL-1 β and IL-6 in the lungs of *Irp2*^{-/-} mice, increased *Hamp1* expression was not observed in the lungs of these mice (**Figs. 4.26**). An explanation to justify the surprising lack of *Hamp1* upregulation might be that IL-6 and IL-1 β produced by lung cells did not reach a threshold sufficient to trigger hepcidin expression. This hypothesis is supported by several reports suggesting that other cells such as monocytes, splenic and aM ϕ s and other tissues such as the kidney and adipose tissue [48] produce lower amounts of hepcidin than hepatocytes, which are the primary producers of hepcidin upon systemic inflammatory stimuli. Another explanation could be that *Hamp1* mRNA expression in the lung was suppressed by a mechanism, which did not involve the IL-6 signalling pathway. In support of this hypothesis, Nemeth et al. [48] showed that TNF α significantly suppressed *Hamp1* mRNA expression in Hep3B human hepatoma cell line through an IL-6 independent pathway [48]. Hypothetically, the higher concentration of IFN γ and TNF α in the lungs of mice deficient for IRP2 (**Fig. 4.19A-B**) or mice fed an iron-rich diet (**Fig. 4.6**) due to the higher bacterial load could have downregulated hepcidin production in these mice. To address this hypothesis, further studies investigating the induction of genes involved in the SMAD or STAT3 pathway using qRT-PCR are necessary to address this hypothesis.

Understanding the functions of cytokines and chemokines and how they intercommunicate is key to comprehending how to curb TB. Cytokines and chemokines are pivotal in initiating and organizing the recruitment and activation of immune cells to the site of infection during Mtb infection. Following phagocytosis of Mtb, aM ϕ s are stimulated, chiefly by the action of TLR2, to secrete proinflammatory cytokines, namely TNF α , IL-1 β , IL-6, and IL-12 [153]. IL-12 drives T helper type I (Th1) differentiation and IFN γ production, which plays a critical role in protective immunity against mycobacteria and other intracellular pathogens [222]. Defects in genes involved in IL-12-dependent IFN γ -mediated immunity in humans is associated with increased risk for mycobacterial disease and Mendelian susceptibility to mycobacterial diseases (MSMD) [223, 224]. Patients with either autosomal complete recessive mutations in IFN γ receptor 1 (IFN γ R1) or IFN γ R2 deficiency show a predisposition to chronic mycobacterial infections [225].

Studies by other authors have demonstrated that mice deficient for IFN γ (*Ifng*^{-/-}) have impaired M ϕ activation and downstream functions, fail to contain mycobacterial replication and become more susceptible to infection [222, 226, 227]. Consistent with these findings, the *in vitro* results in my study confirm the protective role of IFN γ , wherein, M ϕ s deficient for IRP2 which showed higher Mtb loads (**Fig. 4.9A-K**) became less permissive to Mtb following

treatment with IFN γ (**Fig. 4.10A-K**).

The findings from my *in vivo* study do not align with the commonly described protective role of IFN γ during Mtb infection, as shown across many studies. In my study, I showed higher IFN γ concentrations in the lungs of mice deficient for IRP2 (**Fig. 4.19A**) and mice fed an iron-rich diet (**Fig. 4.6A**) despite the higher pulmonary Mtb loads. These results indicate that higher IFN γ concentration alone was not sufficient to control the infection in these mice and suggest higher concentrations of IFN γ as a correlate of the higher Mtb loads. These observations in my study are in agreement with several studies by other authors that have shown that while IFN γ is necessary, it is insufficient for protection against Mtb infection in mice [228, 229]. Specifically, reports have shown that IFN γ produced by CD4 $^{+}$ T cells and or other T cell subsets, like CD8 $^{+}$ T cells, is protective against Mtb, whereas IFN γ produced by innate immune cells does not provide sufficient protection against exacerbating infections. For instance, Green et al. [230] developed an adoptive transfer model in which the presence or absence of CD4 $^{+}$ T cells from wt or *Ifng* $^{-/-}$ mice were assessed for their ability to control Mtb infection. The authors of this study showed that although CD4 T cells are important for the control of Mtb infection, IFN γ from CD4 $^{+}$ T cells is necessary for host survival and effective long-term control of the mycobacterial load especially as IFN γ produced by CD4 $^{+}$ T cells promotes robust CD8 T cell response [230]. Similarly, Sakai et al. [231] showed that when naïve CD4 $^{+}$ T cells isolated from either wt or *Ifng* $^{-/-}$ mice were transferred to Mtb infected mice deficient for RAG-1 (*Rag1* $^{-/-}$), the *Rag1* $^{-/-}$ mice that received CD4 $^{+}$ T cells from wt mice showed increased production of IFN γ in lungs, which was, however, accompanied by increased Mtb loads between day 21 and 42 p.i., and premature death before day 50 p.i. However, this study by Sakai et al. [231] also shows that pulmonary IFN γ prevents severe immune-mediated pathology [231]. Although other cells including CD8 T and NK cells can also produce IFN γ , CD4 $^{+}$ T cells are the main source of IFN γ during the adaptive immune response to Mtb infection and are essential for host persistence in the acute and chronic stage of infection [232]. For instance, mice deficient for CD4 and MHC-II showed increased susceptibility to Mtb and died faster than wt mice but, interestingly, survived twice as long as *Ifng* $^{-/-}$ and *Nos* $^{-/-}$ mice [232, 233, 226], again indicating that CD4 T cells are required for protective immunity against Mtb. In line with these observation from other authors, one hypothesis to explain the higher concentrations of IFN γ being insufficient to control infection in my study is that systemic deletion of *Irp2* as well as iron supplementation in mice may have reduced CD4 $^{+}$ T cell activation during the initial phase of the infection, leading to delayed IFN γ and NOS-2 production (**Fig. 4.21-22**) at day 13 p.i. However, as the infection progressed, other cells such as NK cells might have potentially produced IFN γ , but this was still inadequate to efficiently control the infection, particularly at days 28 p.i., in *Irp2* $^{-/-}$ and mice and at days 28 and 120 p.i in mice fed an iron-rich diet. Further studies using flow cytometry to identify the lymphocytic source of IFN γ production are needed to address this open question.

NK cells, $\gamma\delta$, CD4 and CD8 T cells can produce Th17 cytokines, such as IL-17A, which mediate proinflammatory and antibacterial responses in TB [234, 235, 234]. In my study, augmented IL-17A production which correlated with increased production of IL-6, CXCL1/KC/GRO, and CXCL2/MIP-2 was observed in *Irp2* $^{-/-}$ mice when compared to wt ones at day 28 p.i. (**Fig. 4.22**). The higher concentration of these cytokines and chemokines at this time point correlated with exacerbated pulmonary pathology in *Irp2* $^{-/-}$ mice as characterized by more extensive areas of inflammatory infiltrates (**Fig. 4.23**). These findings are consistent with a study by Schneider et al. [83], which demonstrated that increased IL-17 production induced IL-6 and several chemokines, including CXCL1/KC/GRO) and CXCL2/MIP-2, in mice deficient

for IL-18 upon Mtb infection, which triggered the influx of neutrophils into infected lungs [83]. Neutrophils are reported as the most abundantly infected cell type present in sputum and BAL samples from patients with active TB [236]. However, the role of neutrophils in TB is still a topic of discussion, as several studies have shown that they contribute to disease progression by driving exacerbation of inflammation, tissue destruction, and contributing to respiratory distress, rather than controlling the infection and providing protection [236, 237]. In my study, despite higher concentrations of CXCL1/KC/GRO and CXCL2/MIP-2 in *Irp2*^{-/-} mice by Mtb, increased neutrophil counts were not observed in the lungs of these mice based on histopathological analysis (**Fig. 4.23**). This suggests that neutrophils may not be responsible for the exacerbated pulmonary pathology in *Irp2*^{-/-} mice. This hypothesis is supported by previous studies demonstrating that neutrophils do not significantly contribute to Mtb-induced histopathological alterations in the C57BL/6J TB mouse model [237, 238].

Iron plays a key role in the functioning of neutrophils. Particularly, neutrophils require iron for the production of ROS and the formation of neutrophil extracellular traps (NETs) to fight microbial invasion. Neutrophils also express TfR1, FTH, and FPN which indicates that they modulate iron transport and storage protein expression upon stimulation [239]. Furthermore, hepcidin-induced FPN degradation leads to an increase in intracellular iron, which upregulates CXCL1 expression in keratinocytes thereby increasing neutrophil recruitment [240]. In a recent report by Bonadonna et al. [241], it was revealed that mice with conditional deletion of both IRP1 and IRP2 experienced a reduction in myeloid cell and erythrocyte counts in their peripheral blood, along with impaired neutrophil development and differentiation in the bone marrow, resulting in the production of immature neutrophils. This study by Bonadonna et al. highlights the importance of IRP function not only in erythrocyte differentiation but also in the differentiation of other hematopoietic cell lineages, such as neutrophils [241]. However, there is a lack of information regarding neutrophil differentiation, IRP activity, and their interaction with Mtb. Furthermore, data on iron regulating neutrophils, their recruitment, and function in the setting of an Mtb infection is scant. For this, flow cytometry analysis or analysis of iron-metabolism mediated gene expression in neutrophils isolated from non-infected and Mtb infected *Irp2*^{-/-} at various time points, particularly at day 28 p.i, when increased Mtb loads in lungs were observed, are required. Moreover, investigations into the contribution of NET-containing antimicrobial peptides released by neutrophils such as elastase, myeloperoxidase (MPO), lactoferrin (LF), lipocalin-2 (LCN-2), of which iron is also an important component, need to be conducted. For example, LCN-2 binds and inactivates mycobactin and carboxymycobactin, thereby interfering with mycobacterial iron acquisition [90, 91]. Mice deficient for LCN-2 (*Lcn-2*^{-/-}) showed higher Mtb growth in alveolar epithelial cells compared to controls, demonstrating that LCN-2 scavenges iron and inhibits the growth of Mtb. *Lcn-2*^{-/-} mice were more susceptible to infections with Gram-negative bacteria such as *Klebsiella*, *E. coli* or *Salmonella* spp. Nairz et al. [242] reported LCN-2-mediated protective mechanisms of IRPs with selective deletion of both IRPs in MØs upon infection with a lethal dose of *S. Typhimurium* [242]. In my study, I did not observe any differences in *Lcn-2* mRNA transcripts (**Fig. 4.26F**). As LCN-2 promotes neutrophil recruitment, thereby contributing to innate immunity against Mtb, it can be hypothesized that the lack of increased LCN2 production in my study could also be responsible for the lack of neutrophil recruitment, at least at the histopathological level, in mice deficient for IRP2.

IL-1 β , TNF α , and IFN γ produced by Th1 cells can induce expression of nitric oxide (NO) synthases (NOS-2) and subsequent NO by MØs, which can contribute to controlling Mtb [243]. However, in my study, despite the higher NO concentrations and *Nos2* mRNA transcripts as observed in *Irp2*^{-/-} mice lungs when compared to wt and *Irp1*^{-/-} mice (**Fig. 4.21-22**),

Mtb replication was not controlled during the early phase of infection. RNIs production by NOS-2 is an innate defense mechanism of MØs to target pathogen DNA, lipids, and proteins. Of these RNIs, NO produced by activated MØs kills Mtb, thereby modulating resistance to Mtb in several mouse models [243]. *Ifng*^{-/-} and *Nos-2*^{-/-} mice which fail to generate RNI are highly susceptible to Mtb, highlighting the importance of RNIs in protective immunity against Mtb. Some studies have shown that NO synthesized by NOS-2 inhibits neutrophil migration [244], and its absence leads to increased neutrophil recruitment and subsequent necrosis at the site of infection [245]. Based on these studies from other authors, it can be hypothesized that higher concentrations of TNF α , IFN γ and IL-1 β in *Irp2*^{-/-} mice lung tissue could have triggered higher *Nos2* expression which impaired neutrophil accumulation. To support this hypothesis, staining lung sections with an anti-Ly-6G monoclonal antibody, which specifically marks neutrophils, would provide information on whether neutrophil accumulation was impaired.

CCL2/MCP-1 is a chemoattractant for monocytes and T cells, both cell types which are important in granuloma formation which contains the bacteria. Higher CCL2/MCP-1 concentrations were observed in *Irp2*^{-/-} mice lungs when compared to wt and *Irp1*^{-/-} mice at days 28 and 63 p.i., indicating increased recruitment of MØs and monocytes to the site of infection (**Fig. 4.19**). Also, higher CCL2/MCP-1 concentration correlated with slightly higher CD68 positive MØs and increased Perl positive MØs in *Irp2*^{-/-} mice lungs (**Fig. 4.28**). However, to conclude whether these iron deposits were visualized in MØs, a co-staining of Perl's stain and anti-CD68 should be performed to identify these cells. Additionally, since MØs serve as a niche for Mtb, an increase in their numbers implies more host cells available for Mtb, leading to enhanced pathology. Interestingly, MCP-1 has been implicated in reactive oxygen species (ROS) production, as shown in a study on mice with ovariectomy-induced metabolic disturbance, where MCP-1 deficiency reduced elevated levels of ROS and oxidative stress [246]. Therefore, considering the elevated levels of CCL2/MCP-1 at days 28 and 63 p.i. in lungs of mice deficient for IRP2, it can be hypothesized that increased recruitment of MØ to the lungs of *Irp2*^{-/-} mice resulted in the production of high levels of ROS but failed to effectively control the infection due to the lack of IFN γ or TNF α for activation. Ultimately, higher CCL2/MCP-1 concentrations coupled with iron overload in these MØs could have contributed to increased ROS production which exacerbated pathology in these mice, suggesting that MØs may be responsible for the exacerbated pulmonary pathology in *Irp2*^{-/-} mice. To support this hypothesis, further studies should analyze ROS production via flow cytometry in MØs deficient for IRP2 and infected with Mtb.

IFN γ downregulates TFRs making iron to be less available for Mtb [247]. Salmeron et al. [247] showed that TFRs play an essential role in activating T cells and contributing to signal transduction of T cell receptor-mediated stimulation through interactions with CD3 co-receptor, thereby interfering with IFN γ production. In my study, higher IFN γ in *Irp2*^{-/-} mice and mice on an iron-rich diet correlated with unaltered or lower *TfR1* expression, respectively, both, in wt mice (**Fig. 4.27**) and mice fed iron-control and iron-low diets (**Fig. 4.5**), suggesting that high IFN γ concentration can hamper the expression of *TfR1* in these mice. Meanwhile, higher *TfR1* expression was observed in mice on an iron-low diet before and during Mtb infection than in mice fed an iron-low diet, indicating that *TfR1* was upregulated to meet the increased iron demand for metabolic processes in the cells.

5.4 The Influence of the Gut Microbiota on Host Phenotypic Variation during Mtb Infection

A few studies have identified the mouse microbiome composition as a potential cause of phenotypic variations between different mouse strains and sub-strains of mice [160, 161]. Fittingly, the activation or inactivation of genes is only associated with minor changes in the gut microbial composition, indicating that the host genotype equally influences microbiota composition [248, 249]. For instance, Buhnik-Rosenblau et al. [163] reported high levels of iron and higher abundance of *Lactobacillus (L.) murinus* and *L. intestinalis* in the feces of *Irp2*^{-/-} compared to wt and *Hfe*^{-/-} mice. Meanwhile, *Enterococcus faecium* spp. cluster and an unknown spp. most similar to *Olsenella* spp. were highly represented in *Hfe*^{-/-} mice, and *L. johnsonii* was highly abundant in wt controls. This study by Buhnik-Rosenblau et al. [163] demonstrates that host genetics impacts microbiota composition [163].

In my study, analysis of 16S rRNA sequencing data revealed distinct microbiota compositions of wt, *Irp1*^{-/-} mice and *Irp2*^{+/-} mice (**Fig. 4.37-44**), indicating that iron metabolism determined differences drives the differential abundance and occurrence of resident bacterial communities in the caeca of these mice. The main differences in *Irp1*^{-/-} mice compared to wt mice were a higher representation of the genera *Turicibacter* and *Barnesiella*, along with a lower representation of *Odoribacter* (**Fig. 4.43**).

Turicibacter spp. are Gram-positive, anaerobic bacteria which have been commonly identified in the GIT and feces of humans and animals. These bacteria belong to the phylum *Firmicutes* (class *Erysipelotrichia*, order *Erysipelotrichiales* and family *Turicibacteraceae*). Several studies have associated the abundance of *Turicibacter* abundance with obesity or non-alcoholic fatty liver disease [250], as well as in the production of butyrate, a SCFA produced in the gut microbiome, *in vivo* in mice and rats and *in vitro* models [251] [251]. Nishitsuji et al. [252] showed that an increased abundance of *Turicibacter* in fecal microbiota correlated with elevated plasma butyrate levels in Tsumura Suzuki obese diabetes (TSOD) mice, which suddenly developed obesity and obesity-related metabolic syndrome [252]. In another study, the authors showed a higher abundance of *Turicibacter* correlated with higher intestinal butyric acid in rats fed barley malt [251]. Butyrate plays several beneficial roles in the GIT and influences the gut flora [251]. It serves as a primary energy source for colonocytes, possesses antibacterial activity, and exhibits immunomodulatory effects [253, 254]. For example, Furasawa et al. [254] demonstrated that butyrate stimulates the differentiation of colonic regulatory T cells to anti-inflammatory effector cells by decreasing the concentrations of pro-inflammatory cytokines such as TNF α and IL-8 [254]. In another *in vitro* study, Andoh et al. [255] found that administration of sodium butyrate to the human intestinal epithelial cell line HT-29 cells inhibited TNF α in a dose-dependent manner, thereby triggering IL-8 secretion [255]. These observations suggest that the higher abundance of *Turicibacter* observed in *Irp1*^{-/-} mice may have resulted in increased butyrate production with known anti-inflammatory properties. Currently, scarcely any information on the role of *Turicibacter* on TB pathogenesis is available, further research is needed to clarify its metabolism and interaction with the host in the GIT during Mtb infection. Consequently, measuring the metabolites produced by these bacteria during Mtb infection and conducting functional investigations would be valuable.

Barnesiella, a genus of the family of *Barnesiellaceae*, order *Bacteroidales*, and class *Bacteroidia*, was one of the major abundant genera observed in the caecal microbiota of *Irp1*^{-/-} mice (**Fig. 4.44**). Members of the genus *Barnesiella* are Gram-negative, anaerobic bacteria which are typically found in low levels in the gut and constitute 1% of a healthy human adult gut bacteria [256]. The abundance of *Barnesiella* has been associated with the presence of

several immunoregulatory cells. Specifically, Presley et al., [257] reported a positive correlation between levels of *Banisiella* in the colon with the abundance of marginal zone B cells and invariant natural killer T cells in the spleen and liver, suggesting a role for *Banisiella* in modulating host immune responses [257]. Studies in mice and humans using 16S rRNA analysis have demonstrated that a microbiota *Banisiella* species can restrict the colonization of the intestinal tract by vancomycin-resistant *Enterococcus faecium* (VRE), which is an antibiotic-resistant pathogenic bacterium commonly observed in hospitalized patients [258]. Furthermore, a direct association has been made between a shift in microbial composition favoring *Banisiella* and resistance to arthritis in mice [258]. Arthritis-resistant mice are characterized by microbiota enriched with *Banisiella*, *Bifidobacterium* and *Parabacteroides* spp., with *Banisiella* being the most abundant genus. In the context of colitis development in *IL-10^{-/-}* mice, higher levels of a specific *Banisiella* phylotype were found to correlate with reduced disease activity [259]. Abnormally elevated *Banisiella* densities have also been observed in HIV-infected individuals compared to non-infected individuals, and these elevated densities were associated with systemic inflammation [260]. In recent years, numerous new sequences isolated from human and animal intestines and have been assigned to the genus *Banisiella* [261, 262]. Bacteria belonging to the order *Bacteroidales*, which contributes to carbohydrate degradation and compete with pathogenic bacteria, thereby preventing their colonization of the intestine. Although *Banisiella* belong to the major bacterial genera in mice, their representation in human microbiota is minor [263]. Changes in the abundance of *Banisiella* have not yet been reported in association with TB. Further research is needed to whether *Banisiella* modulates the host immune response to tuberculosis (TB) infection and to determine whether these findings can be translated into the development of novel TB therapies. These studies collectively underscore the importance of the gut microbiota in TB pathogenesis and highlight the potential of manipulating the gut microbiota as a therapeutic approach for TB.

In the case *Irp2^{+/-}* mice, the caecal microbiota exhibited a higher abundance of *Alloprevotella* and *Helicobacter* compared to wt mice (**Fig. 4.45**). Members of the *Alloprevotella* genus belong to a novel group within the *Prevotellaceae* family and phylum of *Bacteroidota*. They are Gram-negative, obligate anaerobic bacilli, which support host metabolism by producing SCFAs including high amounts of succinate moderate quantities of acetate [264]. Members of the *Alloprevotellaceae* family, particularly *Alloprevotella rava* have been implicated in oral cavity dysbiosis, leading to infections such as dental caries and periodontitis. The abundance of *Alloprevotella* has been found to correlate with TB outcome [265]. Wu et al. [266] demonstrated a lower abundance of *Alloprevotella*, *Catonella*, *Coprococcus*, *Treponema* and *Leptotrichia* in the lung microbiota of adult patients with TB in comparison to healthy controls [266]. Also, reduced abundance of the *Prevotella* genus was observed in patients with newly diagnosed active TB and recurrent TB compared to healthy individuals. The underlying mechanism linking this potential association between *Alloprevotella* and TB is not yet fully understood. However, it has been hypothesized that the altered gut microbiota composition and higher abundance of *Alloprevotella* observed in TB patients could affect the immune system's response to TB infection. For instance, *Alloprevotella* has been shown to produce SCFAs and polysaccharide A (PSA). SCFAs are known to promote the differentiation and activation of regulatory T cells (Tregs), which play a crucial role in modulating the immune response to infections. PSA, on the other hand, has been shown to induce the production of anti-inflammatory cytokines, which could also regulate host immune response to infections. In another study, higher serum concentrations of SCFAs such as propionate and butyrate were associated with a higher risk to develop active TB. Interestingly, this increase in SCFAs correlated with a higher abundance of *Prevotella* and lower production of IFN γ and IL-17A,

cytokines associated with protective immunity against Mtb [133]. Also, Ohseop Kwon et al. [267] showed that *Rag*^{-/-} mice treated with feces from wt donor mice showed increased presence of *Prevotellaceae* and *Helicobacteraceae*, which was correlated with increased myelopoiesis, i.e. higher numbers of bone marrow cells and hematopoietic stem and progenitor cells [267]. Further studies are needed to clarify the link between *Alloprevotella* and TB and to investigate the potential mechanisms underlying this association. These findings highlight the importance of investigating the gut microbiota's role in TB pathogenesis and suggest that targeting the gut microbiota could be a promising approach for new TB prevention and treatment strategies.

Helicobacters are another group of microorganisms which were highly abundant in *Irp2*^{+/-} mice compared to wt mice (**Fig. 4.44**). *Helicobacters* are non-spore-forming Gram-negative bacteria within the *Helicobacteraceae* and phylum *Campylobacterota*. Several *Helicobacter* other than *Helicobacter (H.) pylori*, the most common species of the *Helicobacters* genus, have been reported to cause gastritis, gastric ulcers and hepatitis in humans and animals [268]. In humans, a high abundance of *(H.) pylori* in the stomach during childhood has been reported to lower the risk of asthma by 40-60% [269]. Several reports show that Mtb and *(H.) pylori* co-exist, and *(H.) pylori* infection is associated with enhanced Th1 response to TB infection in rodents, humans, and non-human primates [270, 271]. Some studies have shown that *(H.) pylori* infection can modulate the Th1/Th2 balance towards a Th1 response, which may contribute to the protective effect against TB [270, 271]. Several epidemiological studies have shown an association between *(H.) pylori* infection and TB incidence. For example, Alemu et al. conducted a study in Ethiopia and found that the prevalence of *(H.) pylori* infection was significantly lower in TB patients compared to non-TB controls. Perry et al. [271] showed that *H. pylori* infection correlated with a higher concentration of IFN γ and a Th1-like profile of cytokine responses to TB in humans [271]. However, other studies have suggested that *H. pylori* infection may increase the risk of TB infection. A study conducted in South Africa found that *H. pylori* infection was associated with an increased risk of TB infection in HIV-positive individuals. Another study conducted in India also found that *H. pylori* infection was associated with an increased risk of TB infection in individuals with chronic obstructive pulmonary disease (COPD). These findings suggest that the relationship between *H. pylori* and TB may be complex and may depend on other factors such as the host immune status and the presence of other co-morbidities. The potential link between *H. pylori* and Mtb infections has important implications for the management of these diseases. If *H. pylori* infection does indeed protect against TB infection, then the eradication of *H. pylori* may increase the risk of TB. On the other hand, if *H. pylori* infection increases the risk of TB, then the eradication of *H. pylori* may be beneficial for the prevention of TB. Further studies are needed to clarify the relationship between *H. pylori* and TB, and to determine the potential implications for clinical practice.

In this study, I used a cohousing approach [117, 118] to investigate whether the phenotypic variation observed between non-infected and Mtb infected wt, *Irp1*^{-/-} and *Irp2*^{+/-} (donor) mice could be caused indirectly by differences in microbiota composition. Here, offspring from germ-free C57Bl/6J (acceptor) mice were cohoused with respective donor mouse genotypes (**Fig. 4.36**) to facilitate the transfer of microbiota. In my study, the microbiota composition of *Irp1*^{-/-} donor mice was comparable to that of IRP1-acceptor mice (**Fig. 4.39**), suggesting the successful transfer of the microbiota from the former to the latter. This outcome aligns with previous studies employing the cohousing approach, demonstrating the transfer of microbiota between mice. For example, Macia et al. [272] showed that cohousing of wt mice with *Gpr43*^{-/-} mice fed high fiber diets or SCFA acetate significantly improved dextran

sulfate sodium-induced colitis in *Gpr43*^{-/-} mice through the binding of SCFA to GPR43 and GPR109A [272]. In another study, cohousing of obese and lean mice averted increased adiposity and weight in obese mice and altered the metabolic profile of obese mice to look like that of lean mice [119]. In my study, it can be hypothesized that the successful transfer of the microbiota from *Irp1*^{-/-} donor mice to IRP1-acceptor mice may have contributed to decreased concentrations of TNF α in the sera IRP1-acceptors at day 28 p.i. (**Fig. 4.49**), and subsequently to better control of Mtb replication, as evidenced by lower Mtb loads in the lungs of IRP1-acceptor mice at day 13 p.i. (**Fig. 4.45**). Additionally, the lower monocyte counts observed in non-infected IRP1-acceptor mice (**Fig. 4.48**) may indicate the reduced availability of target cells for Mtb, resulting in lower Mtb growth at day 13 p.i. (**Fig. 4.45**). Based on the hypothesis that a higher abundance of *Turicibacter* led to butyrate production, it is possible that butyrate enhanced the bactericidal function of phagocytes, thereby contributing to the lower mycobacterial CFUs observed in the lungs of IRP1-acceptors mice at day 13 p.i. To support this hypothesis, some studies have demonstrated that butyrate can influence M ϕ s phagocytosis of bacteria by driving M ϕ s towards anti-inflammatory or anergic phenotype [273, 253, 274, 275]. Particularly, Fernando et al. [253] showed that M ϕ s differentiated by IL-4 suppressed colitis and treatment of these M ϕ s with butyrate promoted phagocytosis and killing of *E. coli* [253]. Given the potential of butyrate and other metabolites to modulate Mtb replication and the expression of iron metabolism associated or immune response genes, it could be hypothesized that the abundance of *Turicibacter* is associated or even indirectly responsible for lower Mtb loads in IRP1-acceptor mice.

Considering the comparable microbiota composition between IRP2-donor and IRP2-acceptor mice, and that adult bone marrow hematopoietic stem cells are precursors to blood cell lineages such as RBCs, platelets, and WBCs, it is possible that the higher abundance of *Prevotellaceae* and *Helicobacteraceae* may have stimulated increased production of blood cells, resulting in higher white blood cell counts, lymphocytes, and monocytes in non-infected and Mtb-infected IRP2-acceptor mice at day 13 p.i. (**Fig. 4.48**). Previous studies have associated higher WBC counts with reduced gut diversity in individuals with obesity, promoting chronic but (low-grade) inflammation corroborating this notion. In addition, it can be speculated that the high abundance of *Helicobacter* in caecal microbiota of IRP2-acceptor mice may have contributed to elevated concentrations of serum IFN γ , potentially leading to lower Mtb loads in the lungs.

Although it is important to acknowledge that the cohousing experiment was performed once with a small sample size of 3-4 mice per group, a repetition of this experiment is necessary to draw a definitive conclusion. However, based on the preliminary data, an interesting hypothesis arises. It suggests that the microbiota of the acceptor mice may compensate for certain host metabolic functions through the production of microbial metabolites, which could directly or indirectly influence iron homeostasis and contribute to decreased susceptibility of IRP1-acceptor mice to experimental Mtb in the early phase of infection. In support of this hypothesis, Deschemin et al. [276] showed that the gut microbiota competed with the host for iron, predominantly in iron-depleted conditions. The authors used germ-free and conventional mice fed iron-rich and iron-deficient diets and showed the gut microbiota effect on systemic iron homeostasis [276]. They explained that this was achieved by inhibiting pathways involved in intestinal iron absorption and promoting cellular iron storage through the production of bacterial metabolites such as 1,3-diaminopropane and reuterin. These metabolites inhibited HIF-2 α activity through heterodimerization inhibition and subsequently reduced systemic iron overload [277].

Overall, I show the impact of cohousing has on the course of experimental Mtb infection

likely by transferring a pathogenic microbiota associated with the IRP2 genotype. This study also offers a potential contribution of bacterial metabolites to TB pathogenesis. Therefore, elucidating the benefits of individual bacterial metabolites in mice deficient for IRP1 and IRP2 in the non-infected and Mtb-infected state is essential. Further experiments focusing on individual bacterial metabolites in mice deficient for IRP1 and IRP2 in both non-infected and Mtb-infected conditions are essential. These investigations will provide insights into whether the microbiota compensates for certain host genetic deficiencies and how these metabolites influence iron metabolism and immune responses during Mtb infection.

5.5 Conclusion and Outlook

The work presented here sought to reveal how a dysregulated iron metabolism influences host responses to and pathogenesis of experimental TB in mice. In non-infected mice, the absence of IRP2 resulted in slightly reduced total serum iron but higher serum ferritin concentrations and increased iron accumulation in the lung and liver, and iron deficiency in the spleen, indicating that without *Irp2* function, body iron distribution is altered. Meanwhile, in non-infected mice deficient for IRP1, splenomegaly was observed. Upon Mtb infection, the respective phenotypes of these mice were further exacerbated, leading to higher Mtb loads in lungs, spleens, and livers in *Irp2*^{-/-} when compared to wt and *Irp1*^{-/-} mice. Enhanced iron availability very likely contributed to stronger Mtb replication. On day 28 p.i., mice deficient for IRP2 exhibited certain features of a hypoferremic response such as higher hepatic *Hamp1* mRNA expression, and lower total serum iron but increased iron stores. The pathogenesis of *anemia of inflammation* has been attributed to hypoferremia due to impaired mobilization of iron stores from MØs and reduced iron absorption to withhold iron from pathogens. However, iron-independent factors such as a shortened RBC lifespan and suppression of erythropoiesis could also contribute to anemia development. To find out if the anemic phenotype observed can be classified as *anemia of inflammation*, further experiments need to be performed. These include; I. Evaluation of hematological parameters in wt, *Irp1*^{-/-}, *Irp2*^{-/-} and *Irp2*^{+/-} mice upon Mtb infection as indicators of anemia. II. Measurement of EPO concentrations in sera of mice deficient for either IRP1 or IRP2 following infection with Mtb for the differential diagnosis of anemia by immunoassays. III. Determination of the concentration of zinc protoporphyrin, a metabolite formed during heme synthesis, through hematofluorometry to investigate the suppression of erythropoiesis in mice deficient for IRP2. IV. Assessment of RBC survival using an RBC biotinylation assay to compare the RBC lifespan between Mtb infected wt, *Irp1*^{-/-}, *Irp2*^{-/-} and *Irp2*^{+/-} mice, particularly at day 28 p.i.

Multiplex cytokine assay analysis showed higher concentrations of IFN γ , TNF α , IL-1 β and IL-6 in lungs and spleens of *Irp2*^{-/-} when compared to wt mice, which correlated with higher nitric oxide levels in lung homogenates and *Nos2* mRNA gene expression in lungs of *Irp2*^{-/-} versus wt mice. In addition, despite higher Mtb loads, *Irp2*^{-/-} mice had higher concentrations of CXCL1/KC, CXCL2/MIP-2 and CCL2/MCP-1 which correlated with larger areas of inflammatory cell infiltrates in their lungs when compared to wt mice. However, at day 63 p.i., higher IFN γ and TNF α concentrations in *Irp2*^{-/-} mouse lungs were associated with now reduced Mtb loads and lung inflammation when compared to day 28 p.i. These findings suggest that the higher concentrations of these pro-inflammatory cytokines are a correlate of higher Mtb loads in the absence of IRP2. Notably, higher IFN γ concentrations, which could have been added by innate immune cells such as MØs and NK cells were insufficient to control Mtb replication effectively. Interestingly, immune responses at day 28 p.i., failed to control Mtb replication. At that time point, host responses are still primarily driven by innate immune

cells and their effector functions are likely hampered by the IRP2 defect, defective innate immunity, and limited or delayed T cell responses of *Irp2* deficient mice at this time point. To address these hypotheses, further studies using flow cytometry to identify CD4⁺ and CD8⁺ T cells secreting IFN γ are necessary. Higher IFN γ , TNF α , IL-1 β and IL-6 concentrations coupled with increased iron deposits in *Irp2*^{-/-} but not in wt and *Irp1*^{-/-} mice suggest an M1-driven pro-inflammatory phenotype in the IRP2. Further studies should therefore assess M1 and M2 cell populations in the lungs and spleens by flow cytometry.

16S rRNA sequencing analysis revealed differences in the caecal microbiota composition between *Irp1*^{-/-} and *Irp2*^{+/-} mice when compared to wt mice. Using a cohousing approach, the transfer of the IRP1 microbiota lowered the susceptibility to Mtb infection. It should be noted that this was only seen in one experiment performed. However, this observation raises the question of whether the microbiota can compensate for specific host metabolic functions through the production of metabolites, which could influence iron homeostasis and, in turn, alter immune responses and the course of experimental Mtb infection either directly or indirectly. To test this hypothesis, further studies should therefore investigate the gut microbial metabolome of acceptor mice. This can be achieved using either nuclear magnetic resonance (NMR) or mass spectrometry (MS) based metabolomics in correlation with iron metabolism and immune biomarkers. Biomarkers of host iron status (such as serum iron, serum ferritin concentration, transferrin saturation and total iron-binding capacity) and iron metabolism gene regulation, including IRP1 and IRP2 transcriptions should be examined in WT, IRP1 and IRP2-acceptor mice, using RNA-seq differential gene expression analysis. Finally, further cohousing experiments with GF wt, *Irp1*^{-/-} and *Irp2*^{-/-} mice housed under isolator conditions following Mtb infection are required to reveal microbiota-driven signals that may influence host iron metabolism alterations and ultimately, experimental TB.

As this study did not show whether alterations in iron homeostasis have an influence on the gut and lung microbiota composition promoting Mtb infection, or vice versa (i.e., causality dilemma), further studies are required. First, the murine microbiota in the upper and lower respiratory tract and gut under different iron statuses following Mtb infection should be monitored using 16S rRNA sequencing. Second, using biochemical and MS approaches, microbiota-derived metabolites in the framework of iron metabolism should be investigated to see if they play a role in TB pathogenesis, which could explain the phenotypes of *Irp1*^{-/-} and *Irp2*^{-/-} in contrast to wt mice.

IRP1 and 2 determine cellular iron availability through post-transcriptional modulation of iron transport and storage protein expression. No studies to date have shown whether individuals with IRE/IRP system defects are susceptible to Mtb infection. GWAS need to be performed to identify any genetic polymorphisms in *IRP1* and *IRP2*, which may be associated with TB. However, individuals with IRE/IRP system defects display certain phenotypes (reviewed in Table 1.3) such as increased ferritin stores and iron overload disorders, which have been associated with developing active pulmonary TB. My study reveals that systemic deletion of *Irp2* in mice leads to changes in host iron status indices and alters body iron distribution thus promoting Mtb replication. These results provide evidence of the role of IRP2 in maintaining adequate host iron stores and mediating host resistance against Mtb through yet an unknown mechanism. In addition, my data suggest a potential role of IRP2 in mitigating TB-associated anemia of inflammation, but further experiments need to be performed. Therefore, there is potential for iron metabolism as a therapeutic target in TB.

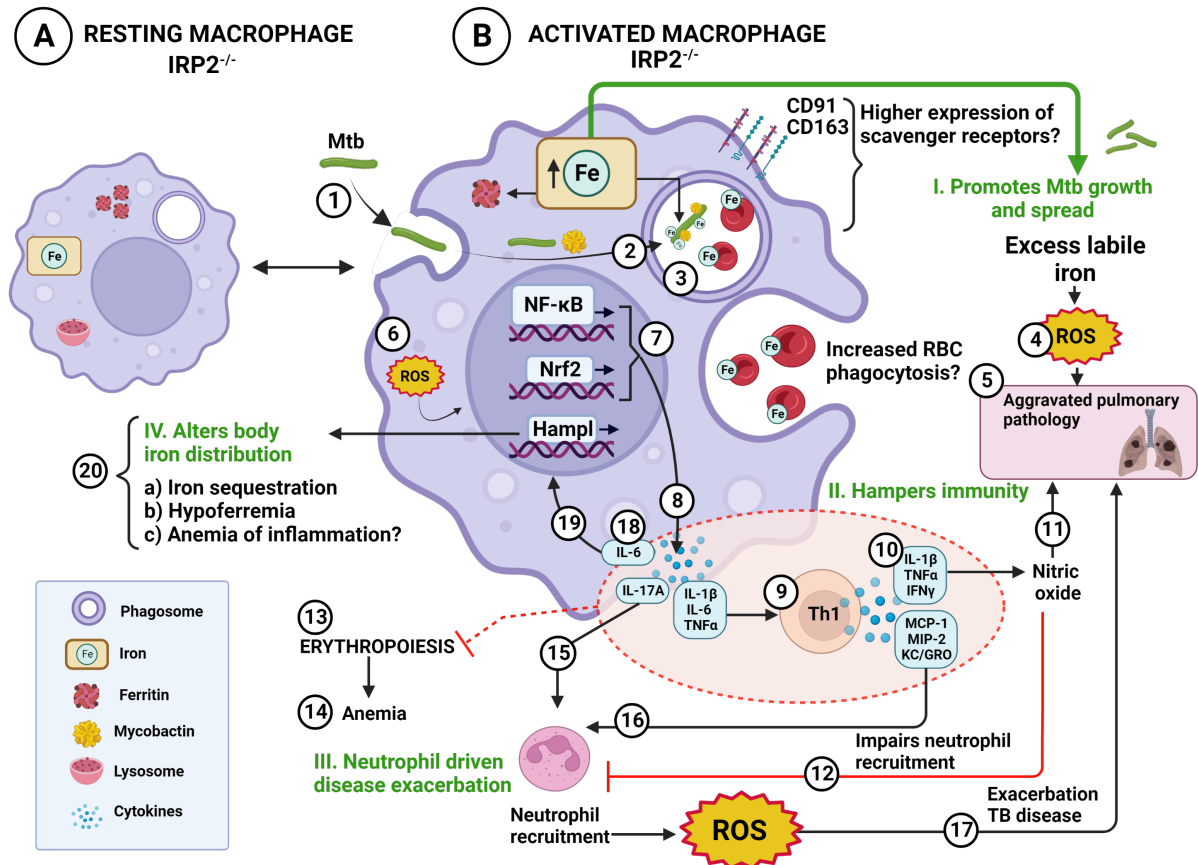


Figure 5.1: Hypothetical scheme of dietary iron supplementation and IRP2-mediated function during experimental TB: In mice deficient for IRP2 and mice on an iron-rich diet, non-infected and resting M ϕ s showed higher iron accumulation (A). In activated M ϕ s (B), **I. Increased iron concentration acts as a micronutrient source, promotes higher Mtb loads and spread:** Higher expression of scavenger receptors e.g., CD91, CD163, or increased phagocytosis of RBCs potentially enhances increased the iron accumulation phenotype. During Mtb infection (1), Mtb is phagocytosed and resides in iron-rich phagosomes (2). Mtb relies on iron for growth and uses its iron-chelating molecules called mycobactins to take iron from the host (3). Excess labile iron (4) generates ROS which aggravates pulmonary pathology (5). **II. Iron also hampers immunity:** This occurs through ROS (6) which stimulates binding activity of transcription factors such as NF κ B and Nrf2 (7) to induce the higher expression of cytokines such as IL-1 β , IL-6, and TNF α (8). Th1 cells (9) produce IL-1 β , TNF α , and IFN γ (10) which can induce expression of nitric oxide (11) by M ϕ s, which can contribute to controlling Mtb but can also aggravate pulmonary pathology (5). Higher nitric oxide also impairs neutrophil recruitment (12). Production of proinflammatory cytokines and chemokines produced hinders erythropoiesis (13) which induces anemia (14). **III. Iron leads to neutrophil-driven disease exacerbation:** IL-17A (15) induces neutrophil recruitment (16). Neutrophils produce ROS which exacerbates TB disease (17) and leads to aggravated pulmonary pathology (5) **IV. IRP2 deficiency alters body iron distribution:** This is achieved by higher IL-6 concentrations (18) which induce *Hampl* mRNA transcripts (19) which results in (a) iron sequestration within macrophages leading to iron overload which rather provides a survival advantage for Mtb and exacerbates pathology, (b) hypoferremia (c) potentially anemia of inflammation (20). Created with BioRender.com

Bibliography

- [1] P. A. Frey and G. H. Reed, "The Ubiquity of Iron," *ACS Chemical Biology*, vol. 7, pp. 1477–1481, Sept. 2012. Publisher: American Chemical Society.
- [2] M. Kolberg, K. R. Strand, P. Graff, and K. K. Andersson, "Structure, function, and mechanism of ribonucleotide reductases," *Biochimica et Biophysica Acta (BBA) - Proteins and Proteomics*, vol. 1699, pp. 1–34, June 2004. Publisher: Elsevier.
- [3] T. L. Poulos, "Structural biology of heme monooxygenases," *Biochemical and biophysical research communications*, vol. 338, pp. 337–345, Dec. 2005. Publisher: Biochem Biophys Res Commun.
- [4] T. Ganz, "Systemic iron homeostasis," *Physiological Reviews*, vol. 93, pp. 1721–1741, Oct. 2013. Publisher: Physiol Rev.
- [5] J. Y. Li, N. Paragas, R. M. Ned, A. Qiu, M. Viltard, T. Leete, I. R. Drexler, X. Chen, S. Sanna-Cherchi, F. Mohammed, D. Williams, C. S. Lin, K. M. Schmidt-Ott, N. C. Andrews, and J. Barasch, "Scara5 is a Ferritin Receptor Mediating Non-Transferrin Iron Delivery," *Developmental cell*, vol. 16, p. 35, Jan. 2009. Publisher: NIH Public Access.
- [6] M. Kristiansen, J. H. Graversen, C. Jacobsen, O. Sonne, H. J. Hoffman, S. K. A. Law, and S. K. Moestrup, "Identification of the haemoglobin scavenger receptor," *Nature*, vol. 409, pp. 198–201, Jan. 2001. Publisher: Nature.
- [7] J. G. Mohanty, E. Nagababu, and J. M. Rifkind, "Red blood cell oxidative stress impairs oxygen delivery and induces red blood cell aging," *Frontiers in Physiology*, vol. 5, p. 84, 2014. Publisher: Frontiers Media SA.
- [8] S. B. Keel, R. T. Doty, Z. Yang, J. G. Quigley, J. Chen, S. Knoblauch, P. D. Kingsley, I. D. Domenico, M. B. Vaughn, J. Kaplan, J. Palis, and J. L. Abkowitz, "A heme export protein is required for red blood cell differentiation and iron homeostasis," *Science (New York, N.Y.)*, vol. 319, pp. 825–828, Feb. 2008. Publisher: Science.
- [9] M. Shayeghi, G. O. Latunde-Dada, J. S. Oakhill, A. H. Laftah, K. Takeuchi, N. Halliday, Y. Khan, A. Warley, F. E. McCann, R. C. Hider, D. M. Frazer, G. J. Anderson, C. D. Vulpe, R. J. Simpson, and A. T. McKie, "Identification of an intestinal heme transporter," *Cell*, vol. 122, pp. 789–801, Sept. 2005. Publisher: Cell.
- [10] E. Desuzinges-Mandon, O. Arnaud, L. Martinez, F. Huché, A. D. Pietro, and P. Falson, "ABCG2 Transports and Transfers Heme to Albumin through Its Large Extracellular Loop," *The Journal of Biological Chemistry*, vol. 285, p. 33123, Oct. 2010. Publisher: American Society for Biochemistry and Molecular Biology.

- [11] J. G. Quigley, Z. Yang, M. T. Worthington, J. D. Phillips, K. M. Sabo, D. E. Sabath, C. L. Berg, S. Sassa, B. L. Wood, and J. L. Abkowitz, "Identification of a Human Heme Exporter that Is Essential for Erythropoiesis," *Cell*, vol. 118, pp. 757–766, Sept. 2004. Publisher: Elsevier.
- [12] C. White, X. Yuan, P. J. Schmidt, E. Bresciani, T. K. Samuel, D. Campagna, C. Hall, K. Bishop, M. L. Calicchio, A. Lapierre, D. M. Ward, P. Liu, M. D. Fleming, and I. Hamza, "HRG1 is essential for heme transport from the phagolysosome of macrophages during erythrophagocytosis," *Cell metabolism*, vol. 17, pp. 261–270, Feb. 2013. Publisher: Cell Metab.
- [13] C. Delaby, C. Rondeau, C. Pouzet, A. Willemetz, N. Pilard, M. Desjardins, and F. Canonne-Hergaux, "Subcellular localization of iron and heme metabolism related proteins at early stages of erythrophagocytosis," *PloS one*, vol. 7, July 2012. Publisher: PLoS One.
- [14] J. R. Forbes and P. Gros, "Iron, manganese, and cobalt transport by Nramp1 (Slc11a1) and Nramp2 (Slc11a2) expressed at the plasma membrane," *Blood*, vol. 102, pp. 1884–1892, Sept. 2003. Publisher: Blood.
- [15] S. Soe-Lin, A. D. Sheftel, B. Wasyluk, and P. Ponka, "Nramp1 equips macrophages for efficient iron recycling," *Experimental hematology*, vol. 36, pp. 929–937, Aug. 2008. Publisher: Exp Hematol.
- [16] I. Yanatori, D. R. Richardson, K. Imada, and F. Kishi, "Iron Export through the Transporter Ferroportin 1 Is Modulated by the Iron Chaperone PCBP2 *," *Journal of Biological Chemistry*, vol. 291, pp. 17303–17318, Aug. 2016. Publisher: Elsevier.
- [17] M. Nairz and G. Weiss, "Molecular and clinical aspects of iron homeostasis: From anemia to hemochromatosis," *Wiener klinische Wochenschrift*, vol. 118, pp. 442–462, Aug. 2006. Publisher: Wien Klin Wochenschr.
- [18] T. Lambe, R. J. Simpson, S. Dawson, T. Bouriez-Jones, T. L. Crockford, M. Lephed, G. O. Latunde-Dada, H. Robinson, K. B. Raja, D. R. Campagna, G. Villarreal, J. C. Ellory, C. C. Goodnow, M. D. Fleming, A. T. McKie, and R. J. Cornall, "Identification of a Steap3 endosomal targeting motif essential for normal iron metabolism," *Blood*, vol. 113, p. 1805, Feb. 2009. Publisher: The American Society of Hematology.
- [19] C. Ji and D. J. Kosman, "Molecular mechanisms of non-transferrin-bound and transferrin-bound iron uptake in primary hippocampal neurons," *Journal of neurochemistry*, vol. 133, pp. 668–683, June 2015. Publisher: J Neurochem.
- [20] L. C. Kühn, "Iron regulatory proteins and their role in controlling iron metabolism," *Metallomics*, vol. 7, pp. 232–243, Feb. 2015. Publisher: The Royal Society of Chemistry.
- [21] J. Wang, G. Chen, J. Lee, and K. Pantopoulos, "Structure of dual function iron regulatory protein 1 complexed with ferritin IRE-RNA," *Science (New York, N.Y.)*, vol. 314, pp. 1903–1908, Dec. 2006. Publisher: Science.
- [22] N. M. Brown, S. A. Anderson, D. W. Steffen, T. B. Carpenter, M. C. Kennedy, W. E. Walden, and R. S. Eisenstein, "Novel role of phosphorylation in Fe-S cluster stability revealed by phosphomimetic mutations at Ser-138 of iron regulatory protein

- 1," *Proceedings of the National Academy of Sciences of the United States of America*, vol. 95, pp. 15235–15240, Dec. 1998. Publisher: Proc Natl Acad Sci U S A.
- [23] K. M. Deck, A. Vasanthakumar, S. A. Anderson, J. B. Goforth, M. C. Kennedy, W. E. Antholine, and R. S. Eisenstein, "Evidence That Phosphorylation of Iron Regulatory Protein 1 at Serine 138 Destabilizes the [4Fe-4S] Cluster in Cytosolic Aconitase by Enhancing 4Fe-3Fe Cycling," *The Journal of Biological Chemistry*, vol. 284, p. 12701, May 2009. Publisher: American Society for Biochemistry and Molecular Biology.
- [24] A. A. Salahudeen, J. W. Thompson, J. C. Ruiz, H. W. Ma, L. N. Kinch, Q. Li, N. V. Grishin, and R. K. Bruick, "An E3 ligase possessing an iron-responsive hemerythrin domain is a regulator of iron homeostasis," *Science (New York, N.Y.)*, vol. 326, pp. 722–726, Oct. 2009. Publisher: Science.
- [25] A. A. Vashisht, K. B. Zumbrennen, X. Huang, D. N. Powers, A. Durazo, D. Sun, N. Bhaskaran, A. Persson, M. Uhlen, O. Sangfeit, C. Spruck, E. A. Leibold, and J. A. Wohlschlegel, "Control of iron homeostasis by an iron-regulated ubiquitin ligase," *Science (New York, N.Y.)*, vol. 326, pp. 718–721, Oct. 2009. Publisher: Science.
- [26] C. P. Anderson, M. Shen, R. S. Eisenstein, and E. A. Leibold, "Mammalian iron metabolism and its control by iron regulatory proteins," *Biochimica et biophysica acta*, vol. 1823, p. 1468, Sept. 2012. Publisher: NIH Public Access.
- [27] M. L. Wallander, E. A. Leibold, and R. S. Eisenstein, "Molecular control of vertebrate iron homeostasis by iron regulatory proteins," *Biochimica et biophysica acta*, vol. 1763, pp. 668–689, July 2006. Publisher: Biochim Biophys Acta.
- [28] E. S. Hanson, M. L. Rawlins, and E. A. Leibold, "Oxygen and Iron Regulation of Iron Regulatory Protein 2 *," *Journal of Biological Chemistry*, vol. 278, pp. 40337–40342, Oct. 2003. Publisher: Elsevier.
- [29] M. C. Ghosh, D.-L. Zhang, and T. A. Rouault, "Iron misregulation and neurodegenerative disease in mouse models that lack iron regulatory proteins," *Neurobiology of disease*, vol. 81, p. 66, 2015. Publisher: NIH Public Access.
- [30] P. V. Uden, N. S. Kenneth, and S. Rocha, "Regulation of hypoxia-inducible factor-1alpha by NF-kappaB," *The Biochemical journal*, vol. 412, pp. 477–484, June 2008. Publisher: Biochem J.
- [31] S. Jenkitkasemwong, C. Y. Wang, R. Coffey, W. Zhang, A. Chan, T. Biel, J. S. Kim, S. Hojyo, T. Fukada, and M. D. Knutson, "SLC39A14 Is Required for the Development of Hepatocellular Iron Overload in Murine Models of Hereditary Hemochromatosis," *Cell metabolism*, vol. 22, pp. 138–150, July 2015. Publisher: Cell Metab.
- [32] J. Neves, T. Haider, M. Gassmann, and M. U. Muckenthaler, "Iron Homeostasis in the Lungs-A Balance between Health and Disease.," *Pharmaceuticals (Basel, Switzerland)*, vol. 12, Jan. 2019. Publisher: Multidisciplinary Digital Publishing Institute (MDPI).
- [33] C. Beaumont, P. Leneuve, I. Devaux, J. Y. Scoazec, M. Berthier, M. N. Loiseau, B. Grandchamp, and D. Bonneau, "Mutation in the iron responsive element of the L ferritin mRNA in a family with dominant hyperferritinaemia and cataract," *Nature genetics*, vol. 11, no. 4, pp. 444–446, 1995. Publisher: Nat Genet.

- [34] S. Luscieti, G. Tolle, J. Aranda, C. B. Campos, F. Risse, Morán, M. U. Muckenthaler, and M. Sánchez, "Novel mutations in the ferritin-L iron-responsive element that only mildly impair IRP binding cause hereditary hyperferritinaemia cataract syndrome," *Orphanet journal of rare diseases*, vol. 8, no. 1, 2013. Publisher: Orphanet J Rare Dis.
- [35] N. Wilkinson and K. Pantopoulos, "The IRP/IRE system in vivo: insights from mouse models," *Frontiers in Pharmacology*, vol. 5, July 2014.
- [36] C. Camaschella, A. Campanella, L. D. Falco, L. Boschetto, R. Merlini, L. Silvestri, S. Levi, and A. Iolascon, "The human counterpart of zebrafish shiraz shows sideroblastic-like microcytic anemia and iron overload," *Blood*, vol. 110, pp. 1353–1358, Aug. 2007. Publisher: Blood.
- [37] J. Kato, K. Fujikawa, M. Kanda, N. Fukuda, K. Sasaki, T. Takayama, M. Kobune, K. Takada, R. Takimoto, H. Hamada, T. Ikeda, and Y. Niitsu, "A mutation, in the iron-responsive element of H ferritin mRNA, causing autosomal dominant iron overload," *American journal of human genetics*, vol. 69, no. 1, pp. 191–197, 2001. Publisher: Am J Hum Genet.
- [38] X. R. Yang, X. Liang, R. M. Pfeiffer, W. Wheeler, D. Maeder, L. Burdette, M. Yeager, S. Chanock, M. A. Tucker, and A. M. Goldstein, "Associations of 9p21 variants with cutaneous malignant melanoma, nevi, and pigmentation phenotypes in melanoma-prone families with and without CDKN2A mutations," *Familial cancer*, vol. 9, pp. 625–633, Dec. 2010. Publisher: Fam Cancer.
- [39] A. R. Kallianpur, P. Jia, R. J. Ellis, Z. Zhao, C. Bloss, W. Wen, C. M. Marra, T. Hulgan, D. M. Simpson, S. Morgello, J. C. McArthur, D. B. Clifford, A. C. Collier, B. B. Gelman, J. A. McCutchan, D. Franklin, D. C. Samuels, D. Rosario, E. Holzinger, D. G. Murdock, S. Letendre, and I. Grant, "Genetic Variation in Iron Metabolism Is Associated with Neuropathic Pain and Pain Severity in HIV-Infected Patients on Antiretroviral Therapy," *PLoS ONE*, vol. 9, p. 103123, Aug. 2014. Publisher: Public Library of Science.
- [40] G. Fehringer, G. Liu, M. Pintilie, J. Sykes, D. Cheng, N. Liu, Z. Chen, L. Seymour, S. D. Der, F. A. Shepherd, M. S. Tsao, and R. J. Hung, "Association of the 15q25 and 5p15 lung cancer susceptibility regions with gene expression in lung tumor tissue," *Cancer Epidemiology Biomarkers and Prevention*, vol. 21, pp. 1097–1104, July 2012. Publisher: American Association for Cancer Research.
- [41] D. L. DeMeo, T. Mariani, S. Bhattacharya, S. Srisuma, C. Lange, A. Litonjua, R. Bueno, S. G. Pillai, D. A. Lomas, D. Sparrow, S. D. Shapiro, G. J. Criner, H. P. Kim, Z. Chen, A. M. K. Choi, J. Reilly, and E. K. Silverman, "Integration of Genomic and Genetic Approaches Implicates IREB2 as a COPD Susceptibility Gene," *American Journal of Human Genetics*, vol. 85, pp. 493–502, Oct. 2009.
- [42] M. Hardin, J. Zielinski, E. S. Wan, C. P. Hersh, P. J. Castaldi, E. Schwinder, I. Hawrylkiewicz, P. Sliwinski, M. H. Cho, and E. K. Silverman, "CHRNA3/5, IREB2, and ADCY2 are associated with severe chronic obstructive pulmonary disease in Poland," *American journal of respiratory cell and molecular biology*, vol. 47, pp. 203–208, Aug. 2012. Publisher: Am J Respir Cell Mol Biol.
- [43] G. F. Korytina, L. Z. Akhmadishina, E. V. Viktorova, O. V. Kochetova, and T. V. Viktorova, "IREB2, CHRNA5, CHRNA3, FAM13A & hedgehog interacting protein genes

- polymorphisms & risk of chronic obstructive pulmonary disease in Tatar population from Russia," *The Indian journal of medical research*, vol. 144, pp. 865–876, Dec. 2016. Publisher: Indian J Med Res.
- [44] Q. Zeng, Q. Chen, D. Zou, R. Guo, D. Xiao, S. Jiang, R. Chen, Y. Wang, and G. Ma, "Different Associations Between the IREB2 Variants and Chronic Obstructive Pulmonary Disease Susceptibility," *Frontiers in Genetics*, vol. 11, p. 1416, Nov. 2020. Publisher: Frontiers Media S.A.
- [45] J. T. Rogers, A. I. Bush, H.-H. Cho, D. H. Smith, A. M. Thomson, A. L. Friedlich, D. K. Lahiri, P. J. Leedman, X. Huang, and C. M. Cahill, "Iron and the translation of the amyloid precursor protein (APP) and ferritin mRNAs: riboregulation against neural oxidative damage in Alzheimer's disease," *Biochemical Society Transactions*, vol. 36, pp. 1282–1287, Dec. 2008. Publisher: Portland Press.
- [46] E. Synowiec, M. Pogorzelska, J. Blasiak, J. Szaflik, and J. P. Szaflik, "Genetic polymorphism of the iron-regulatory protein-1 and -2 genes in age-related macular degeneration," *Molecular biology reports*, vol. 39, pp. 7077–7087, June 2012. Publisher: Mol Biol Rep.
- [47] G. Nicolas, C. Chauvet, L. Viatte, J. L. Danan, X. Bigard, I. Devaux, C. Beaumont, A. Kahn, and S. Vaulont, "The gene encoding the iron regulatory peptide hepcidin is regulated by anemia, hypoxia, and inflammation," *The Journal of Clinical Investigation*, vol. 110, p. 1037, Oct. 2002. Publisher: American Society for Clinical Investigation.
- [48] E. Nemeth, S. Rivera, V. Gabayan, C. Keller, S. Taudorf, B. K. Pedersen, and T. Ganz, "IL-6 mediates hypoferrremia of inflammation by inducing the synthesis of the iron regulatory hormone hepcidin," *Journal of Clinical Investigation*, vol. 113, p. 1271, May 2004. Publisher: American Society for Clinical Investigation.
- [49] A. Pietrangelo, "Ferroportin disease: pathogenesis, diagnosis and treatment," *Haematologica*, vol. 102, p. 1972, Nov. 2017. Publisher: Ferrata Storti Foundation.
- [50] R. E. Fleming, "Hepcidin activation during inflammation: make it STAT," *Gastroenterology*, vol. 132, no. 1, pp. 447–449, 2007. Publisher: Gastroenterology.
- [51] M. P. Soares and G. Weiss, "The Iron age of host-microbe interactions," *EMBO reports*, vol. 16, pp. 1482–1500, Nov. 2015. Publisher: EMBO Rep.
- [52] L. Kautz, G. Jung, V. EV, R. S, N. E, and G. T, "Identification of erythroferrone as an erythroid regulator of iron metabolism," *Nature genetics*, vol. 46, no. 7, pp. 678–684, 2014. Publisher: Nat Genet.
- [53] C. Latour, M. Wlodarczyk, G. Jung, A. Gineste, N. Blanchard, T. Ganz, M.-P. Roth, H. Coppin, and L. Kautz, "Erythroferrone contributes to hepcidin repression in a mouse model of malarial anemia," *Haematologica*, vol. 102, no. 1, pp. 60 – 68, 2017. Publisher: Ferrata Storti Foundation.
- [54] J. Arezes, N. Foy, K. McHugh, A. Sawant, D. Quinkert, V. Terraube, A. Brinth, M. Tam, E. R. LaVallie, S. Taylor, A. E. Armitage, S. R. Pasricha, O. Cunningham, M. Lambert, S. J. Draper, R. Jasuja, and H. Drakesmith, "Erythroferrone inhibits the induction of hepcidin by BMP6," *Blood*, vol. 132, p. 1473, Oct. 2018. Publisher: The American Society of Hematology.

- [55] A. Katsarou and K. Pantopoulos, "Hepcidin Therapeutics," *Pharmaceuticals (Basel, Switzerland)*, vol. 11, Dec. 2018. Publisher: Pharmaceuticals (Basel).
- [56] H. L. Collins, "The role of iron in infections with intracellular bacteria," *Immunology letters*, vol. 85, pp. 193–195, Jan. 2003. Publisher: Immunol Lett.
- [57] A. Panday, M. K. Sahoo, D. Osorio, and S. Batra, "NADPH oxidases: an overview from structure to innate immunity-associated pathologies," *Cellular and Molecular Immunology*, vol. 12, p. 5, Jan. 2015. Publisher: Nature Publishing Group.
- [58] G. Cairo, L. Tacchini, G. Pogliaghi, E. Anzon, A. Tomasi, and A. Bernelli-Zazzera, "Induction of ferritin synthesis by oxidative stress. Transcriptional and post-transcriptional regulation by expansion of the "free" iron pool," *The Journal of biological chemistry*, vol. 270, pp. 700–703, Jan. 1995. Publisher: J Biol Chem.
- [59] P. A. Baeuerle, "IkappaB-NF-kappaB structures: at the interface of inflammation control," *Cell*, vol. 95, pp. 729–731, Dec. 1998. Publisher: Cell.
- [60] Q. Zhang, S. Gupta, D. L. Schipper, G. J. Kowalczyk, A. E. Mancini, J. R. Faeder, and R. E. C. Lee, "NF- κ B Dynamics Discriminate between TNF Doses in Single Cells," *Cell systems*, vol. 5, pp. 638–645.e5, Dec. 2017. Publisher: Cell Syst.
- [61] D. Bandarra, J. Biddlestone, S. Mudie, H. A. J. Müller, and S. Rocha, "HIF-1 restricts NF- κ B-dependent gene expression to control innate immunity signals," *DMM Disease Models and Mechanisms*, vol. 8, pp. 169–181, Feb. 2015. Publisher: Company of Biologists Ltd.
- [62] G. Weiss, G. Werner-Felmayer, E. R. Werner, K. Grünewald, H. Wachter, and M. W. Hentze, "Iron regulates nitric oxide synthase activity by controlling nuclear transcription," *The Journal of experimental medicine*, vol. 180, pp. 969–976, Sept. 1994. Publisher: J Exp Med.
- [63] "WHO | Global tuberculosis report 2018," *WHO*, 2019. Publisher: World Health Organization.
- [64] B. C. d. Jong, M. Antonio, and S. Gagneux, "Mycobacterium africanum—Review of an Important Cause of Human Tuberculosis in West Africa," *PLOS Neglected Tropical Diseases*, vol. 4, p. e744, Sept. 2010. Publisher: Public Library of Science.
- [65] P. J. Brennan, "Structure, function, and biogenesis of the cell wall of Mycobacterium tuberculosis," *Tuberculosis (Edinburgh, Scotland)*, vol. 83, no. 1-3, pp. 91–97, 2003. Publisher: Tuberculosis (Edinb).
- [66] V. Eldholm, J. H.-O. Pettersson, O. B. Brynildsrud, A. Kitchen, E. M. Rasmussen, T. Lillebaek, J. O. Rønning, V. Crudu, A. T. Mengshoel, N. Debech, K. Alfsnes, J. Bohlin, C. S. Pepperell, and F. Balloux, "Armed conflict and population displacement as drivers of the evolution and dispersal of Mycobacterium tuberculosis," *Proceedings of the National Academy of Sciences of the United States of America*, vol. 113, p. 13881, Nov. 2016. Publisher: National Academy of Sciences.
- [67] J. Rehm, A. V. Samokhvalov, M. G. Neuman, R. Room, C. Parry, K. Lönnroth, J. Patra, V. Poznyak, and S. Popova, "The association between alcohol use, alcohol use disorders and tuberculosis (TB). A systematic review," *BMC Public Health 2009 9:1*, vol. 9, pp. 1–12, Dec. 2009. Publisher: BioMed Central.

- [68] S. J. Huang, X. H. Wang, Z. D. Liu, W. L. Cao, Y. Han, A. G. Ma, and S. F. Xu, "Vitamin D deficiency and the risk of tuberculosis: A meta-analysis," *Drug Design, Development and Therapy*, vol. 11, pp. 91–102, 2017. Publisher: Dove Medical Press Ltd.
- [69] I. T. Gangaidzo, V. M. Moyo, E. Mvundura, G. Aggrey, N. L. Murphree, H. Khumalo, T. Saungweme, I. Kasvosve, Z. A. R. Gomo, T. Rouault, J. R. Boelaert, and V. R. Gordeuk, "Association of Pulmonary Tuberculosis with Increased Dietary Iron," tech. rep., 2001. Publication Title: The Journal of Infectious Diseases Volume: 184.
- [70] A. M. Dannenberg and G. A. W. Rook, "Pathogenesis of Pulmonary Tuberculosis: an Interplay of Tissue-Damaging and Macrophage-Activating Immune Responses—Dual Mechanisms That Control Bacillary Multiplication," *Tuberculosis*, pp. 459–483, Apr. 2014. Publisher: John Wiley & Sons, Ltd.
- [71] M. P. Puissegur, C. Botanch, J. L. Duteyrat, G. Delsol, C. Caratero, and F. Altare, "An in vitro dual model of mycobacterial granulomas to investigate the molecular interactions between mycobacteria and human host cells," *Cellular microbiology*, vol. 6, pp. 423–433, May 2004. Publisher: Cell Microbiol.
- [72] F. M. Arnold, M. S. Weber, I. Gonda, M. J. Gallenito, S. Adenau, P. Egloff, I. Zimmermann, C. A. J. Hutter, L. M. Hürlimann, E. E. Peters, J. Piel, G. Meloni, O. Medalia, and M. A. Seeger, "The ABC exporter IrtAB imports and reduces mycobacterial siderophores," *Nature*, vol. 580, p. 413, Apr. 2020. Publisher: Europe PMC Funders.
- [73] P. L. Lin, C. B. Ford, M. T. Coleman, A. J. Myers, R. Gawande, T. Ioerger, J. Sacchettini, S. M. Fortune, and J. L. Flynn, "Sterilization of granulomas is common in active and latent tuberculosis despite within-host variability in bacterial killing," *Nature Medicine* 2013 20:1, vol. 20, pp. 75–79, Dec. 2013. Publisher: Nature Publishing Group.
- [74] S. H. E. Kaufmann, A. Dorhoi, R. S. Hotchkiss, and R. Bartenschlager, "Host-directed therapies for bacterial and viral infections," *Nature Reviews Drug Discovery* 2017 17:1, vol. 17, pp. 35–56, Sept. 2017. Publisher: Nature Publishing Group.
- [75] J. J. D. Voss, K. Rutter, B. G. Schroeder, H. Su, Y. Zhu, and C. E. Barry, "The salicylate-derived mycobactin siderophores of *Mycobacterium tuberculosis* are essential for growth in macrophages," *Proceedings of the National Academy of Sciences of the United States of America*, vol. 97, pp. 1252–1257, Feb. 2000. Publisher: Proc Natl Acad Sci U S A.
- [76] U. E. Schaible, H. L. Collins, F. Priem, and S. H. E. Kaufmann, "Brief Definitive Report Correction of the Iron Overload Defect in-2-Microglobulin Knockout Mice by Lactoferrin Abolishes Their Increased Susceptibility to Tuberculosis," *J. Exp. Med. The*, vol. 196, no. 11, pp. 1507–1513, 2002. Publisher: Rockefeller University Press.
- [77] M. Iturralde, J. K. Vass, R. Oria, and J. H. Brock, "Effect of iron and retinoic acid on the control of transferrin receptor and ferritin in the human promonocytic cell line U937," *Biochimica et biophysica acta*, vol. 1133, pp. 241–246, Feb. 1992. Publisher: Biochim Biophys Acta.
- [78] M. M. Coleman, S. A. Basdeo, A. M. Coleman, C. N. Cheallaigh, C. P. D. Castro, A. M. McLaughlin, P. J. Dunne, J. Harris, and J. Keane, "All-trans Retinoic Acid Augments

- Autophagy during Intracellular Bacterial Infection,” *American journal of respiratory cell and molecular biology*, vol. 59, pp. 548–556, Nov. 2018. Publisher: Am J Respir Cell Mol Biol.
- [79] G. A. Colditz, T. F. Brewer, C. S. Berkey, M. E. Wilson, E. Burdick, H. V. Fineberg, and F. Mosteller, “Efficacy of BCG vaccine in the prevention of tuberculosis: meta-analysis of the published literature,” *JAMA: The Journal of the American Medical Association*, vol. 271, pp. 698–702, Mar. 1994. Publisher: Centre for Reviews and Dissemination (UK).
- [80] M. M. Hossain and M. N. Norazmi, “Pattern recognition receptors and cytokines in Mycobacterium tuberculosis infection—the double-edged sword?,” *BioMed research international*, vol. 2013, 2013. Publisher: Biomed Res Int.
- [81] J. Kleinnijenhuis, M. Oosting, L. A. B. Joosten, M. G. Netea, and R. V. Crevel, “Innate Immune Recognition of Mycobacterium tuberculosis,” *Clinical and Developmental Immunology*, vol. 2011, p. 12, 2011. Publisher: Hindawi Publishing Corporation.
- [82] E. Mortaz, I. M. Adcock, P. Tabarsi, M. R. Masjedi, D. Mansouri, A. A. Velayati, J.-L. Casanova, and P. J. Barnes, “Interaction of Pattern Recognition Receptors with Mycobacterium Tuberculosis,” *Journal of Clinical Immunology 2014 35:1*, vol. 35, pp. 1–10, Oct. 2014. Publisher: Springer.
- [83] B. E. Schneider, D. Korb, K. Hagens, M. Koch, B. Raupach, J. Enders, S. H. E. Kaufmann, H.-W. Mittrücker, and U. E. Schaible, “A role for IL-18 in protective immunity against Mycobacterium tuberculosis,” *European journal of immunology*, vol. 40, p. 396, Feb. 2010. Publisher: Europe PMC Funders.
- [84] Y. A. Z. Persson, R. Blomgran-Julinder, S. Rahman, L. Zheng, and O. Stendahl, “Mycobacterium tuberculosis-induced apoptotic neutrophils trigger a pro-inflammatory response in macrophages through release of heat shock protein 72, acting in synergy with the bacteria,” *Microbes and infection*, vol. 10, pp. 233–240, Mar. 2008. Publisher: Microbes Infect.
- [85] E. D. Weinberg, “Nutritional immunity. Host’s attempt to withhold iron from microbial invaders,” *JAMA*, vol. 231, pp. 39–41, Jan. 1975. Publisher: JAMA.
- [86] R. V. Medapati, S. Suvvari, S. Godi, and P. Gangiseti, “NRAMP1 and VDR gene polymorphisms in susceptibility to pulmonary tuberculosis among Andhra Pradesh population in India: A case-control study,” *BMC Pulmonary Medicine*, vol. 17, June 2017. Publisher: BioMed Central Ltd.
- [87] L. Wu, H. Deng, Y. Zheng, M. Mansjö, X. Zheng, Y. Hu, and B. Xu, “An association study of NRAMP1, VDR, MBL and their interaction with the susceptibility to tuberculosis in a Chinese population,” *International Journal of Infectious Diseases*, vol. 38, pp. 129–135, Sept. 2015. Publisher: Elsevier.
- [88] O. Olakanmi, L. S. Schlesinger, A. Ahmed, and B. E. Britigan, “Intraphagosomal Mycobacterium tuberculosis acquires iron from both extracellular transferrin and intracellular iron pools. Impact of interferon-gamma and hemochromatosis,” *The Journal of biological chemistry*, vol. 277, pp. 49727–49734, Dec. 2002. Publisher: J Biol Chem.

- [89] R. Gozzelino and M. P. Soares, "Coupling heme and iron metabolism via ferritin H chain," *Antioxidants & redox signaling*, vol. 20, pp. 1754–1769, Apr. 2014. Publisher: Antioxid Redox Signal.
- [90] G. A. Snow, "Mycobactins: iron-chelating growth factors from mycobacteria.," *Bacteriological Reviews*, vol. 34, no. 2, p. 99, 1970. Publisher: American Society for Microbiology (ASM).
- [91] R. M. Wells, C. M. Jones, Z. Xi, A. Speer, O. Danilchanka, K. S. Doornbos, P. Sun, F. Wu, C. Tian, and M. Niederweis, "Discovery of a Siderophore Export System Essential for Virulence of *Mycobacterium tuberculosis*," *PLOS Pathogens*, vol. 9, p. e1003120, Jan. 2013. Publisher: Public Library of Science.
- [92] S. Marro, D. Chiabrando, E. Messana, J. Stolte, E. Turco, E. Tolosano, and M. U. Muckenthaler, "Heme controls ferroportin1 (FPN1) transcription involving Bach1, Nrf2 and a MARE/ARE sequence motif at position -7007 of the FPN1 promoter," *Haematologica*, vol. 95, no. 8, pp. 1261–1268, 2010. Publisher: Haematologica.
- [93] K. E. V. Zandt, F. B. Sow, W. C. Florence, B. S. Zwilling, A. R. Satoskar, L. S. Schlesinger, and W. P. Lafuse, "The iron export protein ferroportin 1 is differentially expressed in mouse macrophage populations and is present in the mycobacterial-containing phagosome," *Journal of leukocyte biology*, vol. 84, pp. 689–700, Sept. 2008. Publisher: J Leukoc Biol.
- [94] A. Dumas, D. Corral, A. Colom, F. Levillain, A. Peixoto, D. Hudrisier, Y. Poquet, and O. Neyrolles, "The Host Microbiota Contributes to Early Protection Against Lung Colonization by *Mycobacterium tuberculosis*," *Frontiers in immunology*, vol. 9, Nov. 2018. Publisher: Front Immunol.
- [95] A. Dumas, L. Bernard, Y. Poquet, G. Lugo-Villarino, and O. Neyrolles, "The role of the lung microbiota and the gut–lung axis in respiratory infectious diseases," *Cellular Microbiology*, vol. 20, p. e12966, Dec. 2018. Publisher: John Wiley & Sons, Ltd.
- [96] A. S. Neish, "Microbes in gastrointestinal health and disease," *Gastroenterology*, vol. 136, no. 1, pp. 65–80, 2009. Publisher: Gastroenterology.
- [97] E. A. Grice, H. H. Kong, G. Renaud, A. C. Young, G. G. Bouffard, R. W. Blakesley, T. G. Wolfsberg, M. L. Turner, and J. A. Segre, "A diversity profile of the human skin microbiota," *Genome research*, vol. 18, pp. 1043–1050, July 2008. Publisher: Genome Res.
- [98] W. G. Wade, "The oral microbiome in health and disease," *Pharmacological research*, vol. 69, pp. 137–143, Mar. 2013. Publisher: Pharmacol Res.
- [99] T. Yatsunencko, F. E. Rey, M. J. Manary, I. Trehan, M. G. Dominguez-Bello, M. Contreras, M. Magris, G. Hidalgo, R. N. Baldassano, A. P. Anokhin, A. C. Heath, B. Warner, J. Reeder, J. Kuczynski, J. G. Caporaso, C. A. Lozupone, C. Lauber, J. C. Clemente, D. Knights, R. Knight, and J. I. Gordon, "Human gut microbiome viewed across age and geography," *Nature* 2012 486:7402, vol. 486, pp. 222–227, May 2012. Publisher: Nature Publishing Group.

- [100] J. V. D. Wiggert, H. Borgdorff, R. Verhelst, T. Crucitti, S. Francis, H. Verstraelen, and V. Jaspers, "The Vaginal Microbiota: What Have We Learned after a Decade of Molecular Characterization?," *PLOS ONE*, vol. 9, p. e105998, Aug. 2014. Publisher: Public Library of Science.
- [101] Y. Liu, E. Zhao, L. Zhu, D. Zhang, Z. Wang, and M. Lu, "3'UTR polymorphisms in NRAMP1 are associated with the susceptibility to pulmonary tuberculosis: A MOOSE-compliant meta-analysis," *Medicine (United States)*, vol. 98, p. e15955, June 2019. Publisher: Lippincott Williams and Wilkins.
- [102] S. V. Lynch and O. Pedersen, "The Human Intestinal Microbiome in Health and Disease," *The New England journal of medicine*, vol. 375, pp. 2369–2379, Dec. 2016. Publisher: N Engl J Med.
- [103] K. F. Budden, S. L. Gellatly, D. L. A. Wood, M. A. Cooper, M. Morrison, P. Hugenholtz, and P. M. Hansbro, "Emerging pathogenic links between microbiota and the gut-lung axis," *Nature Reviews Microbiology*, vol. 15, pp. 55–63, Jan. 2017. Publisher: Nature Publishing Group.
- [104] S. Schippa and M. P. Conte, "Dysbiotic Events in Gut Microbiota: Impact on Human Health," *Nutrients*, vol. 6, p. 5786, Dec. 2014. Publisher: Multidisciplinary Digital Publishing Institute (MDPI).
- [105] I. Rowland, G. Gibson, A. Heinken, K. Scott, J. Swann, I. Thiele, and K. Tuohy, "Gut microbiota functions: metabolism of nutrients and other food components," *European Journal of Nutrition*, vol. 57, p. 1, Feb. 2018. Publisher: Springer.
- [106] D. Ríos-Covián, P. Ruas-Madiedo, A. Margolles, M. Gueimonde, C. G. D. I. Reyes-Gavilán, and N. Salazar, "Intestinal Short Chain Fatty Acids and their Link with Diet and Human Health," *Frontiers in microbiology*, vol. 7, Feb. 2016. Publisher: Front Microbiol.
- [107] H. Chung, S. J. Pamp, J. A. Hill, N. K. Surana, S. M. Edelman, E. B. Troy, N. C. Reading, E. J. Villablanca, S. Wang, J. R. Mora, Y. Umesaki, D. Mathis, C. Benoist, D. A. Relman, and D. L. Kasper, "Gut immune maturation depends on colonization with a host-specific microbiota," *Cell*, vol. 149, pp. 1578–1593, June 2012. Publisher: Cell.
- [108] E. Y. Hsiao, S. W. McBride, S. Hsien, G. Sharon, E. R. Hyde, T. McCue, J. A. Codelli, J. Chow, S. E. Reisman, J. F. Petrosino, P. H. Patterson, and S. K. Mazmanian, "Microbiota modulate behavioral and physiological abnormalities associated with neurodevelopmental disorders," *Cell*, vol. 155, pp. 1451–1463, Dec. 2013. Publisher: Cell.
- [109] M. J. Bull and N. T. Plummer, "Part 1: The Human Gut Microbiome in Health and Disease," *Integrative Medicine: A Clinician's Journal*, vol. 13, no. 6, p. 17, 2014. Publisher: InnoVision Media.
- [110] M. B. Zimmermann, C. Chassard, F. Rohner, E. K. N'Goran, C. Nindjin, A. Dostal, J. Utzinger, H. Ghattas, C. Lacroix, and R. F. Hurrell, "The effects of iron fortification on the gut microbiota in African children: a randomized controlled trial in Cote d'Ivoire," *The American journal of clinical nutrition*, vol. 92, pp. 1406–1415, Dec. 2010. Publisher: Am J Clin Nutr.

- [111] T. Jaeggi, G. A. M. Kortman, D. Moretti, C. Chassard, P. Holding, A. Dostal, J. Boekhorst, H. M. Timmerman, D. W. Swinkels, H. Tjalsma, J. Njenga, A. Mwangi, J. Kvalsvig, C. Lacroix, and M. B. Zimmermann, "Iron fortification adversely affects the gut microbiome, increases pathogen abundance and induces intestinal inflammation in Kenyan infants," *Gut*, vol. 64, pp. 731–742, May 2015. Publisher: Gut.
- [112] K. G. Dewey, M. Domellöf, R. J. Cohen, L. L. Rivera, O. Hernell, and B. Lönnerdal, "Iron supplementation affects growth and morbidity of breast-fed infants: results of a randomized trial in Sweden and Honduras," *The Journal of nutrition*, vol. 132, pp. 3249–3255, Nov. 2002. Publisher: J Nutr.
- [113] S. Sazawal, R. E. Black, M. Ramsan, H. M. Chwaya, R. J. Stoltzfus, A. Dutta, U. Dhingra, I. Kabole, S. Deb, M. K. Othman, and F. M. Kabole, "Effects of routine prophylactic supplementation with iron and folic acid on admission to hospital and mortality in preschool children in a high malaria transmission setting: community-based, randomised, placebo-controlled trial," *Lancet (London, England)*, vol. 367, pp. 133–143, Jan. 2006. Publisher: Lancet.
- [114] J. C. Clemente, L. K. Ursell, L. W. Parfrey, and R. Knight, "The Impact of the Gut Microbiota on Human Health: An Integrative View," *Cell*, vol. 148, pp. 1258–1270, Mar. 2012. Publisher: Cell Press.
- [115] M. E. Icaza-Chávez, "Gut microbiota in health and disease," *Revista de Gastroenterología de México (English Edition)*, vol. 78, pp. 240–248, Oct. 2013. Publisher: Elsevier.
- [116] F. Rohlke and N. Stollman, "Fecal microbiota transplantation in relapsing *Clostridium difficile* infection," *Therapeutic Advances in Gastroenterology*, vol. 5, no. 6, p. 403, 2012. Publisher: SAGE Publications.
- [117] J. H. Campbell, C. M. Foster, T. Vishnivetskaya, A. G. Campbell, Z. K. Yang, A. Wymore, A. V. Palumbo, E. J. Chesler, and M. Podar, "Host genetic and environmental effects on mouse intestinal microbiota," *The ISME journal*, vol. 6, pp. 2033–2044, Nov. 2012. Publisher: ISME J.
- [118] A. C. Ericsson and C. L. Franklin, "Manipulating the Gut Microbiota: Methods and Challenges," *ILAR Journal*, vol. 56, p. 205, Aug. 2015. Publisher: Oxford University Press.
- [119] V. K. Ridaura, J. J. Faith, F. E. Rey, J. Cheng, A. E. Duncan, A. L. Kau, N. W. Griffin, V. Lombard, B. Henrissat, J. R. Bain, M. J. Muehlbauer, O. Ilkayeva, C. F. Semenkovich, K. Funai, D. K. Hayashi, B. J. Lyle, M. C. Martini, L. K. Ursell, J. C. Clemente, W. V. Treuren, W. A. Walters, R. Knight, C. B. Newgard, A. C. Heath, and J. I. Gordon, "Gut microbiota from twins discordant for obesity modulate metabolism in mice," *Science (New York, N.Y.)*, vol. 341, no. 6150, 2013. Publisher: Science.
- [120] S. J. Robertson, P. Lemire, H. Maughan, A. Goethel, W. Turpin, L. Bedrani, D. S. Guttman, K. Croitoru, S. E. Girardin, and D. J. Philpott, "Comparison of Co-housing and Littermate Methods for Microbiota Standardization in Mouse Models," *Cell Reports*, vol. 27, pp. 1910–1919.e2, May 2019. Publisher: Elsevier B.V.
- [121] H. Seedorf, N. W. Griffin, V. K. Ridaura, A. Reyes, J. Cheng, F. E. Rey, M. I. Smith, G. M. Simon, R. H. Scheffrahn, D. Woebken, A. M. Spormann, W. V. Treuren, L. K.

- Ursell, M. Pirrung, A. Robbins-Pianka, B. L. Cantarel, V. Lombard, B. Henrissat, R. Knight, and J. I. Gordon, "Bacteria from diverse habitats colonize and compete in the mouse gut," *Cell*, vol. 159, pp. 253–266, Oct. 2014. Publisher: Cell Press.
- [122] K. K. Barfod, M. Roggenbuck, L. H. Hansen, S. Schjørring, S. T. Larsen, S. J. Sørensen, and K. A. Krogh, "The murine lung microbiome in relation to the intestinal and vaginal bacterial communities," *BMC Microbiology*, vol. 13, p. 303, Dec. 2013. Publisher: BioMed Central.
- [123] R. L. Brown, R. P. Sequeira, and T. B. Clarke, "The microbiota protects against respiratory infection via GM-CSF signaling," *Nature Communications*, vol. 8, Dec. 2017. Publisher: Nature Publishing Group.
- [124] T. Ichinohe, I. K. Pang, Y. Kumamoto, D. R. Peaper, J. H. Ho, T. S. Murray, and A. Iwasaki, "Microbiota regulates immune defense against respiratory tract influenza A virus infection," *Proceedings of the National Academy of Sciences of the United States of America*, vol. 108, pp. 5354–5359, Mar. 2011. Publisher: National Academy of Sciences.
- [125] J. L. Pope, Y. Yang, R. C. Newsome, W. Sun, X. Sun, M. Ukhanova, J. Neu, J. P. Issa, V. Mai, and C. Jobin, "Microbial Colonization Coordinates the Pathogenesis of a *Klebsiella pneumoniae* Infant Isolate," *Scientific Reports 2019 9:1*, vol. 9, pp. 1–13, Mar. 2019. Publisher: Nature Publishing Group.
- [126] A. Dumas, L. Bernard, Y. Poquet, G. Lugo-Villarino, and O. Neyrolles, "The role of the lung microbiota and the gut-lung axis in respiratory infectious diseases," *Cellular Microbiology*, vol. 20, p. e12966, Dec. 2018.
- [127] L. Zhang, R. C. Hendrickson, V. Meikle, E. J. Lefkowitz, T. R. Ioerger, and M. Niederweis, "Comprehensive analysis of iron utilization by *Mycobacterium tuberculosis*," *PLOS Pathogens*, vol. 16, p. e1008337, Feb. 2020. Publisher: Public Library of Science.
- [128] R. P. Dickson, B. H. Singer, M. W. Newstead, N. R. Falkowski, J. R. Erb-Downward, T. J. Standiford, and G. B. Huffnagle, "Enrichment of the lung microbiome with gut bacteria in sepsis and the acute respiratory distress syndrome," *Nature Microbiology*, vol. 1, no. 10, p. 16113, 2016. Publisher: Nature Publishing Group.
- [129] Y. Yun, G. Srinivas, S. Kuenzel, M. Linnenbrink, S. Alnahas, K. D. Bruce, U. Steinhoff, J. F. Baines, and U. E. Schaible, "Environmentally Determined Differences in the Murine Lung Microbiota and Their Relation to Alveolar Architecture," *PLOS ONE*, vol. 9, p. e113466, Dec. 2014. Publisher: Public Library of Science.
- [130] R. P. Dickson, J. R. Erb-Downward, C. M. Freeman, N. Walker, B. S. Scales, J. M. Beck, F. J. Martinez, J. L. Curtis, V. N. Lama, and G. B. Huffnagle, "Changes in the lung microbiome following lung transplantation include the emergence of two distinct *Pseudomonas* species with distinct clinical associations," *PLoS ONE*, vol. 9, no. 5, 2014. ISBN: 10.1371/journal.pone.0097214.
- [131] S. J. Salter, M. J. Cox, E. M. Turek, S. T. Calus, W. O. Cookson, M. F. Moffatt, P. Turner, J. Parkhill, N. J. Loman, and A. W. Walker, "Reagent and laboratory contamination can critically impact sequence-based microbiome analyses," *BMC Biology*, vol. 12, no. 87, pp. 1741–7007, 2014.

- [132] A. Remot, D. Descamps, M. L. Noordine, A. Boukadiri, E. Mathieu, V. Robert, S. Riffault, B. Lambrecht, P. Langella, H. Hammad, and M. Thomas, "Bacteria isolated from lung modulate asthma susceptibility in mice," *ISME Journal*, vol. 11, pp. 1061–1074, May 2017. Publisher: Nature Publishing Group.
- [133] L. N. Segal, A. V. Alekseyenko, J. C. Clemente, R. Kulkarni, B. Wu, H. Chen, K. I. Berger, R. M. Goldring, W. N. Rom, M. J. Blaser, and M. D. Weiden, "Enrichment of lung microbiome with supraglottic taxa is associated with increased pulmonary inflammation," *Microbiome*, vol. 1, pp. 1–12, July 2013. Publisher: BioMed Central Ltd.
- [134] E. S. Charlson, K. Bittinger, A. R. Haas, A. S. Fitzgerald, I. Frank, A. Yadav, F. D. Bushman, and R. G. Collman, "Topographical continuity of bacterial populations in the healthy human respiratory tract," *American Journal of Respiratory and Critical Care Medicine*, vol. 184, pp. 957–963, Oct. 2011.
- [135] N. Khan, L. Mendonca, A. Dhariwal, G. Fontes, D. Menzies, J. Xia, M. Divangahi, and I. L. King, "Intestinal dysbiosis compromises alveolar macrophage immunity to *Mycobacterium tuberculosis*," *Mucosal immunology*, vol. 12, pp. 772–783, May 2019. Publisher: Mucosal Immunol.
- [136] M. Nairz, D. Ferring-Appel, D. Casarrubea, T. Sonnweber, L. Viatte, A. Schroll, D. Haschka, F. C. Fang, M. W. Hentze, G. Weiss, and B. Galy, "Iron Regulatory Proteins Mediate Host Resistance to *Salmonella* Infection.," *Cell host & microbe*, vol. 18, pp. 254–61, Aug. 2015. Publisher: NIH Public Access.
- [137] M. C. Ghosh, D. L. Zhang, S. Y. Jeong, G. Kovtunovych, H. Ollivierre-Wilson, A. Noguchi, T. Tu, T. Senecal, G. Robinson, D. R. Crooks, W. H. Tong, K. Ramaswamy, A. Singh, B. B. Graham, R. M. Tuder, Z. X. Yu, M. Eckhaus, J. Lee, D. A. Springer, and T. A. Rouault, "Deletion of iron regulatory protein 1 causes polycythemia and pulmonary hypertension in mice through translational derepression of HIF2," *Cell Metabolism*, vol. 17, no. 2, pp. 271–281, 2013. ISBN: 1550-4131.
- [138] T. LaVaute, S. Smith, S. Cooperman, K. Iwai, W. Land, E. Meyron-Holtz, S. K. Drake, G. Miller, M. Abu-Asab, M. Tsokos, R. Switzer, A. Grinberg, P. Love, N. Tresser, and T. A. Rouault, "Targeted deletion of the gene encoding iron regulatory protein-2 causes misregulation of iron metabolism and neurodegenerative disease in mice," *Nature Genetics*, vol. 27, pp. 209–214, Feb. 2001. Publisher: Nature Publishing Group.
- [139] E. G. Meyron-Holtz, M. C. Ghosh, K. Iwai, T. Lavaute, X. Brazzolotto, U. V. Berger, W. Land, H. Ollivierre-Wilson, A. Grinberg, P. Love, and T. A. Rouault, "Genetic ablations of iron regulatory proteins 1 and 2 reveal why iron regulatory protein 2 dominates iron homeostasis," *The EMBO Journal*, vol. 23, pp. 386–395, 2004. ISBN: 02614189/04.
- [140] F. M. Marim, T. N. Silveira, D. S. Lima, D. S. Zamboni, S. Gordon, N. Morrisette, E. Gold, A. Aderem, P. R. Taylor, L. Martinez-Pomares, M. Stacey, H. H. Lin, G. D. Brown, B. Balint, Z. Ivanovic, M. Petakov, J. Taseski, G. Jovcic, D. Berz, E. M. McCormack, E. S. Winer, G. A. Colvin, P. J. Quesenberry, B. Hiebl, R. Fuhrmann, R. P. Franke, J. S. Danciger, M. Lutz, S. Hama, D. Cruz, A. Castrillo, D. S. Zamboni, M. Rabinovitch, M. D. Englen, Y. E. Valdez, N. M. Lehnert, B. E. Lehnert, K. H. Berger, R. R. Isberg, T. Ren, D. S. Zamboni, C. R. Roy, W. F. Dietrich, R. E. Vance, J. C.

- Feeley, R. J. Gibson, G. W. Gorman, N. C. Langford, J. K. Rasheed, D. S. Zamboni, S. McGrath, M. Rabinovitch, C. R. Roy, D. Kram, C. Thale, H. Kolodziej, A. F. Kiderlen, V. Carregaro, J. G. Valenzuela, T. M. Cunha, W. V. Jr, R. Grespan, J. E. Lovelock, M. W. Bishop, A. D. Donnenberg, E. K. Koch, D. L. Griffin, H. M. Stanczak, J. E. Kiss, M. A. Horwitz, A. B. Molofsky, B. G. Byrne, N. N. Whitfield, C. A. Madigan, E. T. Fuse, D. S. Zamboni, K. S. Kobayashi, T. Kohlsdorf, Y. Ogura, and E. M. Long, "A Method for Generation of Bone Marrow-Derived Macrophages from Cryopreserved Mouse Bone Marrow Cells," *PLoS ONE*, vol. 5, p. e15263, Dec. 2010. Publisher: Public Library of Science.
- [141] C. Schneider, S. P. Nobs, A. K. Heer, M. Kurrer, G. Klinke, N. v. Rooijen, J. Vogel, and M. Kopf, "Alveolar Macrophages Are Essential for Protection from Respiratory Failure and Associated Morbidity following Influenza Virus Infection," *PLOS Pathogens*, vol. 10, no. 4, p. e1004053, 2014. Publisher: Public Library of Science.
- [142] X. Zhang, R. Goncalves, and D. M. Mosser, "The Isolation and Characterization of Murine Macrophages," *Current protocols in immunology / edited by John E. Coligan ... [et al.]*, vol. CHAPTER, no. SUPPL. 83, p. Unit, 2008. Publisher: NIH Public Access.
- [143] P. Griess, "Bemerkungen zu der Abhandlung der HH. Weselsky und Benedikt „Ueber einige Azoverbindungen",," *Berichte der deutschen chemischen Gesellschaft*, vol. 12, pp. 426–428, Jan. 1879. Publisher: John Wiley & Sons, Ltd.
- [144] D. B. Morton and P. H. Griffiths, "Guidelines on the recognition of pain, distress and discomfort in experimental animals and an hypothesis for assessment," *The Veterinary record*, vol. 116, no. 16, pp. 431–436, 1985. Publisher: Vet Rec.
- [145] P. Chomczynski and N. Sacchi, "The single-step method of RNA isolation by acid guanidinium thiocyanate–phenol–chloroform extraction: twenty-something years on," *Nature Protocols 2006 1:2*, vol. 1, pp. 581–585, June 2006. Publisher: Nature Publishing Group.
- [146] Illumina, "16S Metagenomic sequencing library preparation," tech. rep., 2013.
- [147] M. J. Murray, A. B. Murray, M. B. Murray, and C. J. Murray, "The adverse effect of iron repletion on the course of certain infections," *British Medical Journal*, vol. 2, pp. 1113–1115, Oct. 1978.
- [148] J. K. Sia, M. Georgieva, and J. Rengarajan, "Innate Immune Defenses in Human Tuberculosis: An Overview of the Interactions between Mycobacterium tuberculosis and Innate Immune Cells," *Journal of Immunology Research*, vol. 2015, 2015. Publisher: Hindawi Publishing Corporation.
- [149] H. M. Lander, J. S. Ogiste, S. F. A. Pearce, R. Levi, and A. Novogrodsky, "Nitric oxide-stimulated guanine nucleotide exchange on p21ras," *The Journal of biological chemistry*, vol. 270, no. 13, pp. 7017–7020, 1995. Publisher: J Biol Chem.
- [150] M. S. Gomes, G. Dom, J. Pedrosa, J. R. Boelaert, and R. Appelberg, "Effects of iron deprivation on Mycobacterium avium growth," *Tubercle and Lung Disease*, vol. 79, no. 5, pp. 321–328, 1999. Publisher: Churchill Livingstone.

- [151] M. S. Gomes, J. R. Boelaert, and R. Appelberg, "Role of iron in experimental *Mycobacterium avium* infection," *Journal of Clinical Virology*, vol. 20, no. 3, pp. 117–122, 2001.
- [152] N. Wilkinson and K. Pantopoulos, "IRP1 regulates erythropoiesis and systemic iron homeostasis by controlling HIF2 mRNA translation," *Blood*, vol. 122, pp. 1658–1669, Aug. 2013. Publisher: American Society of Hematology.
- [153] H. D. Brightbill, D. H. Libraty, S. R. Krutzik, R. B. Yang, J. T. Belisle, J. R. Bleharski, M. Maitland, M. V. Norgard, S. E. Plevy, S. T. Smale, P. J. Brennan, B. R. Bloom, P. J. Godowski, and R. L. Modlin, "Host defense mechanisms triggered by microbial lipoproteins through toll-like receptors," *Science (New York, N.Y.)*, vol. 285, pp. 732–736, July 1999. Publisher: Science.
- [154] M. Jain, C. J. Petzold, M. W. Schelle, M. D. Leavell, J. D. Mougous, C. R. Bertozzi, J. A. Leary, and J. S. Cox, "Lipidomics reveals control of *Mycobacterium tuberculosis* virulence lipids via metabolic coupling," *Proceedings of the National Academy of Sciences of the United States of America*, vol. 104, no. 12, pp. 5133–5138, 2007.
- [155] M. J. Murray, A. B. Murray, M. B. Murray, and C. J. Murray, "The adverse effect of iron repletion on the course of certain infections," *British Medical Journal*, vol. 2, no. 6145, pp. 1113–1115, 1978. ISBN: 0007-1447.
- [156] B. Galy, D. Ferring, B. Minana, O. Bell, H. G. Janser, M. Muckenthaler, K. Schümann, and M. W. Hentze, "Altered body iron distribution and microcytosis in mice deficient in iron regulatory protein 2 (IRP2)," *Blood*, vol. 106, pp. 2580–2589, Oct. 2005. Publisher: American Society of Hematology.
- [157] S. A. Anderson, C. P. Nizzi, Y. I. Chang, K. M. Deck, P. J. Schmidt, B. Galy, A. Damernsawad, A. T. Broman, C. Kendzioriski, M. W. Hentze, M. D. Fleming, J. Zhang, and R. S. Eisenstein, "The IRP1-HIF-2 axis coordinates iron and oxygen sensing with erythropoiesis and iron absorption," *Cell Metabolism*, vol. 17, pp. 282–290, Feb. 2013. Publisher: Cell Metab.
- [158] S. S. Cooperman, E. G. Meyron-Holtz, H. Olivierre-Wilson, M. C. Ghosh, J. P. McConnell, and T. A. Rouault, "Microcytic anemia, erythropoietic protoporphyria, and neurodegeneration in mice with targeted deletion of iron-regulatory protein 2.," *Blood*, vol. 106, pp. 1084–91, Aug. 2005. Publisher: American Society of Hematology.
- [159] K. Cadwell, K. K. Patel, N. S. Maloney, T. C. Liu, A. C. Y. Ng, C. E. Storer, R. D. Head, R. Xavier, T. S. Stappenbeck, and H. W. Virgin, "Virus-plus-susceptibility gene interaction determines Crohn's disease gene *Atg16L1* phenotypes in intestine," *Cell*, vol. 141, no. 7, pp. 1135–1145, 2010. Publisher: Cell.
- [160] C. Ubeda, L. Lipuma, A. Gobourne, A. Viale, I. Leiner, M. Equinda, R. Khanin, and E. G. Pamer, "Familial transmission rather than defective innate immunity shapes the distinct intestinal microbiota of TLR-deficient mice," *The Journal of Experimental Medicine*, vol. 209, p. 1445, July 2012. Publisher: The Rockefeller University Press.
- [161] E. M. Velazquez, H. Nguyen, K. T. Heasley, C. H. Saechao, L. M. Gil, A. W. L. Rogers, B. M. Miller, M. R. Rolston, C. A. Lopez, Y. Litvak, M. J. Liou, F. Faber, D. N. Bronner, C. R. Tiffany, M. X. Byndloss, A. J. Byndloss, and A. J. Bäumlner, "Endogenous

- Enterobacteriaceae underlie variation in susceptibility to Salmonella infection," *Nature microbiology*, vol. 4, pp. 1057–1064, June 2019. Publisher: Nat Microbiol.
- [162] S. Becattini, M. T. Sorbara, S. G. Kim, E. L. Littmann, Q. Dong, G. Walsh, R. Wright, L. Amoretti, E. Fontana, T. M. Hohl, and E. G. Pamer, "Rapid transcriptional and metabolic adaptation of intestinal microbes to host immune activation," *Cell Host and Microbe*, vol. 29, no. 3, pp. 378–393.e5, 2021. Publisher: Elsevier Inc.
- [163] K. Buhnik-Rosenblau, b. Shirly, M.-B. @bullet, Y. Danin-Poleg, and E. G. Meyron-Holtz, "Genetic modification of iron metabolism in mice affects the gut microbiota,"
- [164] M. G. D. Agüero, S. C. Ganal-Vonarburg, T. Fuhrer, S. Rupp, Y. Uchimura, H. Li, A. Steinert, M. Heikenwalder, S. Hapfelmeier, U. Sauer, K. D. McCoy, and A. J. Macpherson, "The maternal microbiota drives early postnatal innate immune development," *Science*, vol. 351, no. 6279, pp. 1296–1302, 2016.
- [165] J. K. Fraser, F.-K. Lin, and M. V. Berridge, "Expression and modulation of specific, high affinity binding sites for erythropoietin on the human erythroleukemic cell line K562," *Blood*, vol. 71, pp. 104–109, Jan. 1988. Publisher: American Society of Hematology.
- [166] E. B. Rankin, M. P. Biju, Q. Liu, T. L. Unger, J. Rha, R. S. Johnson, M. C. Simon, B. Keith, and V. H. Haase, "Hypoxia-inducible factor-2 (HIF-2) regulates hepatic erythropoietin in vivo," *The Journal of clinical investigation*, vol. 117, pp. 1068–1077, Apr. 2007. Publisher: J Clin Invest.
- [167] A. J. Majmundar, W. J. Wong, and M. C. Simon, "Hypoxia-Inducible Factors and the Response to Hypoxic Stress," *Molecular Cell*, vol. 40, pp. 294–309, Oct. 2010.
- [168] V. H. Haase, "Regulation of erythropoiesis by hypoxia-inducible factors," *Blood reviews*, vol. 27, pp. 41–53, Jan. 2013. Publisher: Blood Rev.
- [169] C. Warnecke, Z. Zaborowska, J. Kurreck, V. A. Erdmann, U. Frei, M. Wiesener, and K.-U. Eckardt, "Differentiating the functional role of hypoxia-inducible factor (HIF)-1 and HIF-2 (EPAS-1) by the use of RNA interference: erythropoietin is a HIF-2 target gene in Hep3B and Kelly cells," *The FASEB Journal*, vol. 18, pp. 1462–1464, Sept. 2004. Publisher: Wiley.
- [170] M. Gruber, C. J. Hu, R. S. Johnson, E. J. Brown, B. Keith, and M. C. Simon, "Acute postnatal ablation of Hif-2alpha results in anemia," *Proceedings of the National Academy of Sciences of the United States of America*, vol. 104, pp. 2301–2306, Feb. 2007. Publisher: Proc Natl Acad Sci U S A.
- [171] M. Sanchez, B. Galy, M. U. Muckenthaler, and M. W. Hentze, "Iron-regulatory proteins limit hypoxia-inducible factor-2 expression in iron deficiency," *Nature Structural & Molecular Biology* 2007 14:5, vol. 14, pp. 420–426, Apr. 2007. Publisher: Nature Publishing Group.
- [172] S. R. Smith, M. C. Ghosh, H. Ollivierre-Wilson, W. H. Tong, and T. A. Rouault, "Complete loss of iron regulatory proteins 1 and 2 prevents viability of murine zygotes beyond the blastocyst stage of embryonic development," *Blood Cells, Molecules, and Diseases*, vol. 36, pp. 283–287, Mar. 2006. Publisher: Blood Cells Mol Dis.

- [173] T. LaVaute, S. Smith, S. Cooperman, K. Iwai, W. Land, E. Meyron-Holtz, S. K. Drake, G. Miller, M. Abu-Asab, M. Tsokos, R. Switzer, A. Grinberg, P. Love, N. Tresser, and T. A. Rouault, "Targeted deletion of the gene encoding iron regulatory protein-2 causes misregulation of iron metabolism and neurodegenerative disease in mice," *Nature Genetics*, vol. 27, pp. 209–214, Feb. 2001.
- [174] B. Galy, S. M. Höltter, T. Klopstock, D. Ferring, L. Becker, S. Kaden, W. Wurst, H. J. Gröne, and M. W. Hentze, "Iron homeostasis in the brain: Complete iron regulatory protein 2 deficiency without symptomatic neurodegeneration in the mouse [4]," *Nature Genetics*, vol. 38, no. 9, pp. 967–969, 2006.
- [175] B. Galy, D. Ferring-Appel, S. Kaden, H. J. Gröne, and M. W. Hentze, "Iron Regulatory Proteins Are Essential for Intestinal Function and Control Key Iron Absorption Molecules in the Duodenum," *Cell Metabolism*, vol. 7, pp. 79–85, Jan. 2008.
- [176] N. Wilkinson and K. Pantopoulos, "IRP1 regulates erythropoiesis and systemic iron homeostasis by controlling HIF2 mRNA translation," *Blood*, vol. 122, pp. 1658–1669, Aug. 2013. Publisher: Blood.
- [177] K. B. Zumbrennen-Bullough, L. Becker, L. Garrett, S. M. Höltter, J. Calzada-Wack, I. Mossbrugger, L. Quintanilla-Fend, I. Racz, B. Rathkolb, T. Klopstock, W. Wurst, A. Zimmer, E. Wolf, H. Fuchs, V. Gailus-Durner, M. H. D. Angelis, S. J. Romney, and E. A. Leibold, "Abnormal brain iron metabolism in Irf2 deficient mice is associated with mild neurological and behavioral impairments," *PLoS ONE*, vol. 9, June 2014. Publisher: Public Library of Science.
- [178] J. Braverman, K. M. Sogi, D. Benjamin, D. K. Nomura, and S. A. Stanley, "HIF-1 Is an Essential Mediator of IFN--Dependent Immunity to Mycobacterium tuberculosis," *Journal of immunology (Baltimore, Md. : 1950)*, vol. 197, pp. 1287–1297, Aug. 2016. Publisher: J Immunol.
- [179] P. M. Elks, S. Brizee, M. v. d. Vaart, S. R. Walmsley, F. J. v. Eeden, S. A. Renshaw, and A. H. Meijer, "Hypoxia Inducible Factor Signaling Modulates Susceptibility to Mycobacterial Infection via a Nitric Oxide Dependent Mechanism," *PLOS Pathogens*, vol. 9, no. 12, p. e1003789, 2013. Publisher: Public Library of Science.
- [180] M. M. Hickey, J. C. Lam, N. A. Bezman, W. K. Rathmell, and M. C. Simon, "von Hippel-Lindau mutation in mice recapitulates Chuvash polycythemia via hypoxia-inducible factor-2alpha signaling and splenic erythropoiesis," *The Journal of clinical investigation*, vol. 117, pp. 3879–3889, Dec. 2007. Publisher: J Clin Invest.
- [181] M. M. Hickey, T. Richardson, T. Wang, M. Mosqueira, E. Arguiri, H. Yu, Q. C. Yu, C. C. Solomides, E. E. Morrissey, T. S. Khurana, M. Christofidou-Solomidou, and M. C. Simon, "The von Hippel-Lindau Chuvash mutation promotes pulmonary hypertension and fibrosis in mice," *The Journal of clinical investigation*, vol. 120, pp. 827–839, Mar. 2010. Publisher: J Clin Invest.
- [182] W. MacNee, "Pathogenesis of chronic obstructive pulmonary disease," *Proceedings of the American Thoracic Society*, vol. 2, no. 4, pp. 258–266, 2005. Publisher: Proc Am Thorac Soc.

- [183] D. L. Zhang, M. C. Ghosh, and T. A. Rouault, "The physiological functions of iron regulatory proteins in iron homeostasis - an update," *Frontiers in Pharmacology*, vol. 5 JUN, no. July, 2014.
- [184] G. Yilmaz, "Normochromic Normocytic Anemia - PubMed," 2021.
- [185] J. Hella, C. I. Cercamondi, F. Mhimbira, M. Sasamalo, N. Stoffel, M. Zwahlen, T. Bodmer, S. Gagneux, K. Reither, M. B. Zimmermann, L. Risch, and L. Fenner, "Anemia in tuberculosis cases and household controls from Tanzania: Contribution of disease, coinfections, and the role of hepcidin," *PLoS ONE*, vol. 13, Apr. 2018. Publisher: Public Library of Science.
- [186] P. N. Rodrigues, S. S. Gomes, J. V. Neves, S. Gomes-Pereira, M. Correia-Neves, C. Nunes-Alves, J. Stolte, M. Sanchez, R. Appelberg, M. U. Muckenthaler, and M. S. Gomes, "Mycobacteria-induced anaemia revisited: a molecular approach reveals the involvement of NRAMP1 and lipocalin-2, but not of hepcidin," *Immunobiology*, vol. 216, pp. 1127–1134, Oct. 2011. Publisher: Immunobiology.
- [187] F. O. Demitto, M. Araújo-Pereira, C. A. Schmaltz, F. M. Sant'Anna, M. B. Arriaga, B. B. Andrade, and V. C. Rolla, "Impact of Persistent Anemia on Systemic Inflammation and Tuberculosis Outcomes in Persons Living With HIV," *Frontiers in immunology*, vol. 11, Sept. 2020. Publisher: Front Immunol.
- [188] Y. Gelaw, Z. Getaneh, and M. Melku, "Anemia as a risk factor for tuberculosis: a systematic review and meta-analysis," *Environmental health and preventive medicine*, vol. 26, Dec. 2021. Publisher: Environ Health Prev Med.
- [189] S. Isanaka, S. Aboud, F. Mugusi, R. J. Bosch, W. C. Willett, D. Spiegelman, C. Duggan, and W. W. Fawzi, "Iron Status Predicts Treatment Failure and Mortality in Tuberculosis Patients: A Prospective Cohort Study from Dar es Salaam, Tanzania," *PLOS ONE*, vol. 7, p. e37350, May 2012. Publisher: Public Library of Science.
- [190] Y. Agrawal, V. Goyal, A. Singh, and S. Lal, "Role of Anaemia and Magnesium Levels at the Initiation of Tuberculosis Therapy with Sputum Conversion among Pulmonary Tuberculosis Patients," *Journal of clinical and diagnostic research : JCDR*, vol. 11, pp. BC01–BC04, June 2017. Publisher: J Clin Diagn Res.
- [191] T. J. Nagu, D. Spiegelman, E. Hertzmark, S. Aboud, J. Makani, M. I. Matee, W. Fawzi, and F. Mugusi, "Anemia at the Initiation of Tuberculosis Therapy Is Associated with Delayed Sputum Conversion among Pulmonary Tuberculosis Patients in Dar-es-Salaam, Tanzania," *PLOS ONE*, vol. 9, p. e91229, Mar. 2014. Publisher: Public Library of Science.
- [192] E. B. d. Mendonça, C. A. S. Schmaltz, F. M. Sant'Anna, A. G. Vizzoni, D. P. Mendes-De-Almeida, R. d. V. C. d. Oliveira, and V. C. Rolla, "Anemia in tuberculosis cases: A biomarker of severity?," *PLoS ONE*, vol. 16, Feb. 2021. Publisher: Public Library of Science.
- [193] L. Gil-Santana, L. A. B. Cruz, M. B. Arriaga, P. F. C. Miranda, K. F. Fukutani, P. S. Silveira-Mattos, E. C. Silva, M. G. Oliveira, E. D. D. Mesquita, A. Rauwerdink, F. Cobelens, M. M. Oliveira, A. Kritski, and B. B. Andrade, "Tuberculosis-associated anemia is linked to a distinct inflammatory profile that persists after initiation of

- antitubercular therapy," *Scientific Reports*, vol. 9, Dec. 2019. Publisher: Nature Publishing Group.
- [194] G. Weiss, T. Ganz, and L. T. Goodnough, "Anemia of inflammation," *Blood*, vol. 133, pp. 40–50, Jan. 2019. Publisher: American Society of Hematology.
- [195] J. A. M. Tufariello, J. R. Chapman, C. A. Kerantzas, K. W. Wong, C. Vilchèze, C. M. Jones, L. E. Cole, E. Tinaztepe, V. Thompson, D. Fenyö, M. Niederweis, B. Ueberheide, J. A. Philips, and W. R. Jacobs, "Separable roles for Mycobacterium tuberculosis ESX-3 effectors in iron acquisition and virulence," *Proceedings of the National Academy of Sciences of the United States of America*, vol. 113, pp. E348–E357, Jan. 2016. Publisher: National Academy of Sciences.
- [196] C. A. Madigan, A. J. Martinot, J. R. Wei, A. Madduri, T. Y. Cheng, D. C. Young, E. Layre, J. P. Murry, E. J. Rubin, and D. B. Moody, "Lipidomic analysis links mycobactin synthase K to iron uptake and virulence in M. tuberculosis," *PLoS pathogens*, vol. 11, pp. 1–21, Mar. 2015. Publisher: PLoS Pathog.
- [197] L. Cronjé, N. Edmondson, K. D. Eisenach, and L. Bornman, "Iron and iron chelating agents modulate Mycobacterium tuberculosis growth and monocyte-macrophage viability and effector functions," *FEMS immunology and medical microbiology*, vol. 45, pp. 103–112, Aug. 2005. Publisher: FEMS Immunol Med Microbiol.
- [198] N. Lounis, C. Truffot-Pernot, J. Grosset, V. R. Gordeuk, and J. R. Boelaert, "Iron and Mycobacterium tuberculosis infection," *Journal of Clinical Virology*, vol. 20, no. 3, pp. 123–126, 2001. ISBN: 1386-6532.
- [199] A. M. Dhople, M. A. Ibanez, and T. C. Poirier, "Role of iron in the pathogenesis of Mycobacterium avium infection in mice," *Microbios*, vol. 87, pp. 77–87, Jan. 1996.
- [200] C. D. Monyé, D. S. Karcher, J. R. Boelaert, and V. R. Gordeuk, "Bone marrow macrophage iron grade and survival of HIV-seropositive patients," *AIDS*, vol. 13, no. 3, pp. 375–380, 1999. Publisher: AIDS.
- [201] A. Lopez, P. Cacoub, I. C. Macdougall, and L. Peyrin-Biroulet, "Iron deficiency anaemia," in *The Lancet*, vol. 387, pp. 907–916, Lancet Publishing Group, Feb. 2016. ISSN: 1474547X Issue: 10021.
- [202] A. Pietrangelo, "Hereditary Hemochromatosis — A New Look at an Old Disease," *New England Journal of Medicine*, vol. 350, pp. 2383–2397, June 2004. Publisher: Massachusetts Medical Society.
- [203] R. Harrington-Kandt, E. Stylianou, L. A. Eddowes, P. J. Lim, L. Stockdale, N. Pinpathomrat, N. Bull, J. Pasricha, M. Ulaszewska, Y. Beglov, S. Vaulont, H. Drakesmith, and H. McShane, "Hepcidin deficiency and iron deficiency do not alter tuberculosis susceptibility in a murine M.tb infection model," *PLOS ONE*, vol. 13, p. e0191038, Jan. 2018.
- [204] U. E. Schaible and S. H. E. Kaufmann, "Malnutrition and infection: complex mechanisms and global impacts.," *PLoS medicine*, vol. 4, p. e115, May 2007. Publisher: Public Library of Science.

- [205] J. N. Feder, Z. Tsuchihashi, A. Irrinki, V. K. Lee, F. A. Mapa, E. Morikang, C. E. Prass, S. M. Starnes, R. K. Wolff, S. Parkkila, W. S. Sly, and R. C. Schatzman, "The Hemochromatosis Founder Mutation in HLA-H Disrupts 2-Microglobulin Interaction and Cell Surface Expression," *Journal of Biological Chemistry*, vol. 272, pp. 14025–14028, May 1997. Publisher: Elsevier.
- [206] J. A. Lebrón, A. P. West, and P. J. Bjorkman, "The hemochromatosis protein HFE competes with transferrin for binding to the transferrin receptor," *Journal of molecular biology*, vol. 294, pp. 239–245, Nov. 1999. Publisher: J Mol Biol.
- [207] J. A. Lebrón and P. J. Bjorkman, "The transferrin receptor binding site on HFE, the class I MHC-related protein mutated in hereditary hemochromatosis," *Journal of Molecular Biology*, vol. 289, pp. 1109–1118, June 1999. Publisher: Academic Press.
- [208] F. A. Dunja, M. W. Hentze, and B. Galy, "Cell-autonomous and systemic context-dependent functions of iron regulatory protein 2 in mammalian iron metabolism," *Blood*, vol. 113, pp. 679–687, Jan. 2009. Publisher: American Society of Hematology.
- [209] D. E. Brown, M. W. McCoy, M. C. Pilonieta, R. N. Nix, and C. S. Detweiler, "Chronic murine typhoid fever is a natural model of secondary hemophagocytic lymphohistiocytosis," *PloS one*, vol. 5, Feb. 2010. Publisher: PLoS One.
- [210] M. W. McCoy, S. M. Moreland, and C. S. Detweiler, "Hemophagocytic macrophages in murine typhoid fever have an anti-inflammatory phenotype," *Infection and Immunity*, vol. 80, pp. 3642–3649, Oct. 2012. Publisher: American Society for Microbiology 1752 N St., N.W., Washington, DC.
- [211] M. Ramos-Casals, P. Brito-Zerón, A. López-Guillermo, M. A. Khamashta, and X. Bosch, "Adult haemophagocytic syndrome," *Lancet (London, England)*, vol. 383, no. 9927, pp. 1503–1516, 2014. Publisher: Lancet.
- [212] D. Girelli, E. Nemeth, and D. W. Swinkels, "Hepcidin in the diagnosis of iron disorders," *Blood*, vol. 127, pp. 2809–2813, June 2016. Publisher: Blood.
- [213] J. Hella, C. I. Cercamondi, F. Mhimbira, M. Sasamalo, N. Stoffel, M. Zwahlen, T. Bodmer, S. Gagneux, K. Reither, M. B. Zimmermann, L. Risch, and L. Fenner, "Anemia in tuberculosis cases and household controls from Tanzania: Contribution of disease, coinfections, and the role of hepcidin," *PloS one*, vol. 13, Apr. 2018. Publisher: PLoS One.
- [214] A. D. Kerkhoff, G. Meintjes, R. Burton, M. Vogt, R. Wood, and S. D. Lawn, "Relationship Between Blood Concentrations of Hepcidin and Anemia Severity, Mycobacterial Burden, and Mortality Among Patients With HIV-Associated Tuberculosis," *The Journal of Infectious Diseases*, vol. 213, pp. 61–70, Jan. 2016. Publisher: Oxford Academic.
- [215] D. K. Kim, J. H. Jeong, J. M. Lee, K. S. Kim, S. H. Park, Y. D. Kim, M. Koh, M. Shin, Y. S. Jung, H. S. Kim, T. H. Lee, B. C. Oh, J. I. Kim, H. T. Park, W. I. Jeong, C. H. Lee, S. B. Park, J. J. Min, S. I. Jung, S. Y. Choi, H. E. Choy, and H. S. Choi, "Inverse agonist of estrogen-related receptor controls *Salmonella typhimurium* infection by modulating host iron homeostasis," *Nature medicine*, vol. 20, no. 4, pp. 419–424, 2014. Publisher: Nat Med.

- [216] J. Arezes, G. Jung, V. Gabayan, E. Valore, P. Ruchala, P. A. Gulig, T. Ganz, E. Nemeth, and Y. Bulut, "Hepcidin-induced hypoferremia is a critical host defense mechanism against the siderophilic bacterium *Vibrio vulnificus*," *Cell host & microbe*, vol. 17, pp. 47–57, Jan. 2015. Publisher: Cell Host Microbe.
- [217] L. Viatte, H. J. Gröne, M. W. Hentze, and B. Galy, "In vivo role(s) of the iron regulatory proteins (IRP) 1 and 2 in aseptic local inflammation," *Journal of molecular medicine (Berlin, Germany)*, vol. 87, pp. 913–921, Sept. 2009. Publisher: J Mol Med (Berl).
- [218] G. Ilyin, B. Courselaud, M. B. Troadec, C. Pigeon, M. Alizadeh, P. Leroyer, P. Brissot, and O. Loréal, "Comparative analysis of mouse hepcidin 1 and 2 genes: evidence for different patterns of expression and co-inducibility during iron overload 1," *FEBS Letters*, vol. 542, pp. 22–26, May 2003. Publisher: John Wiley & Sons, Ltd.
- [219] C. Pigeon, G. Ilyin, B. Courselaud, P. Leroyer, T. B, B. P, and L. O, "A new mouse liver-specific gene, encoding a protein homologous to human antimicrobial peptide hepcidin, is overexpressed during iron overload," *The Journal of biological chemistry*, vol. 276, pp. 7811–7819, Mar. 2001. Publisher: J Biol Chem.
- [220] D.A. Weinstein, C. N. Roy, M. D. Fleming, M. F. Loda, J. I. Wolfsdorf, and N. C. Andrews, "Inappropriate expression of hepcidin is associated with iron refractory anemia: implications for the anemia of chronic disease," *Blood*, vol. 100, pp. 3776–3781, Nov. 2002. Publisher: American Society of Hematology.
- [221] Y. Kanamori, M. Murakami, M. Sugiyama, O. Hashimoto, T. Matsui, and M. Funaba, "Interleukin-1 (IL-1) transcriptionally activates hepcidin by inducing CCAAT enhancer-binding protein (C/EBP) expression in hepatocytes.," *The Journal of Biological Chemistry*, vol. 292, pp. 10275–10287, Apr. 2017. Publisher: American Society for Biochemistry and Molecular Biology Inc.
- [222] A. M. Cooper, J. Magram, J. Ferrante, and I. M. Orme, "Interleukin 12 (IL-12) Is Crucial to the Development of Protective Immunity in Mice Intravenously Infected with *Mycobacterium tuberculosis*," *The Journal of Experimental Medicine*, vol. 186, p. 39, July 1997. Publisher: The Rockefeller University Press.
- [223] R. D. Jong, F. Altare, I. A. Haagen, D. G. Elferink, T. D. Boer, P. J. C. V. B. Vriesman, P. J. Kabel, J. M. T. Draaisma, J. T. V. Dissel, F. P. Kroon, J. L. Casanova, and T. H. M. Ottenhoff, "Severe mycobacterial and *Salmonella* infections in interleukin-12 receptor-deficient patients," *Science (New York, N.Y.)*, vol. 280, pp. 1435–1438, May 1998. Publisher: Science.
- [224] F. Altare, D. Lammas, P. Revy, E. Jouanguy, R. Döffinger, S. Lamhamedi, P. Drysdale, D. Scheel-Toeilner, J. Girdlestone, P. Darbyshire, M. Wadhwa, H. Dockrell, M. Salmon, A. Fischer, A. Durandy, J. L. Casanova, and D. S. Kumararatne, "Inherited interleukin 12 deficiency in a child with bacille Calmette-Guérin and *Salmonella enteritidis* disseminated infection," *The Journal of clinical investigation*, vol. 102, pp. 2035–2040, Dec. 1998. Publisher: J Clin Invest.
- [225] S. E. Dorman and S. M. Holland, "Interferon- and interleukin-12 pathway defects and human disease," *Cytokine and Growth Factor Reviews*, vol. 11, no. 4, pp. 321–333, 2000. Publisher: Elsevier BV.

- [226] J. A. L. Flynn, J. Chan, K. J. Triebold, D. K. Dalton, T. A. Stewart, and B. R. Bloom, "An essential role for interferon gamma in resistance to Mycobacterium tuberculosis infection," *The Journal of experimental medicine*, vol. 178, pp. 2249–2254, Dec. 1993. Publisher: J Exp Med.
- [227] D. B. Lowrie, R. E. Tascon, V. L. D. Bonato, V. M. F. Lima, L. H. Faccoli, E. Stavropoulos, M. J. Colston, R. G. Hewinson, K. Moelling, and C. L. Silva, "Therapy of tuberculosis in mice by DNA vaccination," *Nature*, vol. 400, pp. 269–271, July 1999. Publisher: Nature.
- [228] L. Johnson, J. Gough, Y. Spencer, G. Hewinson, M. Vordermeier, and A. Wangoo, "Immunohistochemical markers augment evaluation of vaccine efficacy and disease severity in bacillus Calmette-Guerin (BCG) vaccinated cattle challenged with Mycobacterium bovis," *Veterinary immunology and immunopathology*, vol. 111, pp. 219–229, June 2006. Publisher: Vet Immunol Immunopathol.
- [229] C. Palma, E. Iona, F. Giannoni, M. Pardini, L. Brunori, G. Orefici, L. Fattorini, and A. Cassone, "The Ag85B protein of Mycobacterium tuberculosis may turn a protective immune response induced by Ag85B-DNA vaccine into a potent but non-protective Th1 immune response in mice," *Cellular microbiology*, vol. 9, pp. 1455–1465, June 2007. Publisher: Cell Microbiol.
- [230] A. M. Green, R. DiFazio, and J. L. Flynn, "IFN- from CD4 T Cells Is Essential for Host Survival and Enhances CD8 T Cell Function during Mycobacterium tuberculosis Infection," *The Journal of Immunology*, vol. 190, pp. 270–277, Jan. 2013. Publisher: American Association of Immunologists.
- [231] S. Sakai, K. D. Kauffman, M. A. Sallin, A. H. Sharpe, H. A. Young, V. V. Ganusov, and D. L. Barber, "CD4 T Cell-Derived IFN- Plays a Minimal Role in Control of Pulmonary Mycobacterium tuberculosis Infection and Must Be Actively Repressed by PD-1 to Prevent Lethal Disease," *PLOS Pathogens*, vol. 12, p. e1005667, May 2016. Publisher: Public Library of Science.
- [232] A. M. Caruso, N. Serbina, E. Klein, K. Triebold, B. R. Bloom, and J. L. Flynn, "Mice Deficient in CD4 T Cells Have Only Transiently Diminished Levels of IFN-, Yet Succumb to Tuberculosis," *The Journal of Immunology*, vol. 162, pp. 5407–5416, May 1999. ISBN: 00221767/99 Publisher: American Association of Immunologists.
- [233] C. A. Scanga, V. P. Mohan, K. Yu, H. Joseph, K. Tanaka, J. Chan, and J. A. L. Flynn, "Depletion of Cd4+ T Cells Causes Reactivation of Murine Persistent Tuberculosis despite Continued Expression of Interferon and Nitric Oxide Synthase 2," *Journal of Experimental Medicine*, vol. 192, pp. 347–358, Aug. 2000. Publisher: The Rockefeller University Press.
- [234] R. Gopal, Y. Lin, N. Obermajer, S. Slight, N. Nuthalapati, M. Ahmed, P. Kalinski, and S. A. Khader, "Interleukin-23 dependent IL-17 drives Th1 responses following Mycobacterium bovis BCG vaccination," *European journal of immunology*, vol. 42, p. 364, Feb. 2012. Publisher: NIH Public Access.
- [235] M. Umemura, A. Yahagi, S. Hamada, M. D. Begum, H. Watanabe, K. Kawakami, T. Suda, K. Sudo, S. Nakae, Y. Iwakura, and G. Matsuzaki, "IL-17-mediated regulation of innate and acquired immune response against pulmonary Mycobacterium bovis bacille

- Calmette-Guerin infection," *Journal of immunology (Baltimore, Md. : 1950)*, vol. 178, pp. 3786–3796, Mar. 2007. Publisher: J Immunol.
- [236] S. Y. Eum, J. H. Kong, M. S. Hong, Y. J. Lee, J. H. Kim, S. H. Hwang, S. N. Cho, L. E. Via, and C. E. Barry, "Neutrophils are the predominant infected phagocytic cells in the airways of patients with active pulmonary TB," *Chest*, vol. 137, pp. 122–128, Jan. 2010. Publisher: Chest.
- [237] T. Dallenga and U. E. Schaible, "Neutrophils in tuberculosis—first line of defence or booster of disease and targets for host-directed therapy?," *Pathogens and disease*, vol. 74, Apr. 2016. Publisher: Pathog Dis.
- [238] V. Yeremeev, I. Linge, T. Kondratieva, and A. Apt, "Neutrophils exacerbate tuberculosis infection in genetically susceptible mice," *Tuberculosis*, vol. 95, pp. 447–451, July 2015. Publisher: Churchill Livingstone.
- [239] S. J. F. Cronin, C. J. Woolf, G. Weiss, and J. M. Penninger, "The Role of Iron Regulation in Immunometabolism and Immune-Related Disease," *Frontiers in molecular biosciences*, vol. 6, Nov. 2019. Publisher: Front Mol Biosci.
- [240] M. Malerba, S. Louis, S. Cuvellier, S. M. Shambat, C. Hua, C. Gomart, A. Fouet, N. Ortonne, J. W. Decousser, A. S. Zinkernagel, J. R. R. Mathieu, and C. Peyssonnaud, "Epidermal hepcidin is required for neutrophil response to bacterial infection," *The Journal of clinical investigation*, vol. 130, pp. 329–334, Jan. 2020. Publisher: J Clin Invest.
- [241] M. Bonadonna, S. Altamura, E. Tybl, G. Palais, M. Qatato, M. Polycarpou-Schwarz, M. Schneider, C. Kalk, W. Rüdiger, A. Ertl, N. Anstee, R. Bogeska, D. Helm, M. D. Milsom, and B. Galy, "Iron regulatory protein (IRP)-mediated iron homeostasis is critical for neutrophil development and differentiation in the bone marrow," *Science advances*, vol. 8, Oct. 2022. Publisher: Sci Adv.
- [242] M. Nairz, S. Dichtl, A. Schroll, D. Haschka, P. Tymoszuk, I. Theurl, and G. Weiss, "Iron and innate antimicrobial immunity—Depriving the pathogen, defending the host," *Journal of Trace Elements in Medicine and Biology*, vol. 48, pp. 118–133, July 2018.
- [243] C. Jagannath, J. K. Actor, and R. L. Hunter, "Induction of Nitric Oxide in Human Monocytes and Monocyte Cell Lines by Mycobacterium tuberculosis," *Nitric Oxide*, vol. 2, pp. 174–186, June 1998. Publisher: Academic Press.
- [244] M. BB, R. VA, M. GW, M. AJ, K. H, F. KA, and S. CM, "Nitric oxide controls the immunopathology of tuberculosis by inhibiting NLRP3 inflammasome-dependent processing of IL-1," *Nature immunology*, vol. 14, pp. 52–60, Jan. 2013. Publisher: Nat Immunol.
- [245] B. B. Mishra, R. R. Lovewell, A. J. Olive, G. Zhang, W. Wang, E. Eugenin, C. M. Smith, J. Y. Phuah, J. E. Long, M. L. Dubuke, S. G. Palace, J. D. Goguen, R. E. Baker, S. Nambi, R. Mishra, M. G. Booty, C. E. Baer, S. A. Shaffer, V. Dartois, B. A. McCormick, X. Chen, and C. M. Sasseti, "Nitric oxide prevents a pathogen-permissive granulocytic inflammation during tuberculosis," *Nature Microbiology* 2017 2:7, vol. 2, pp. 1–11, May 2017. Publisher: Nature Publishing Group.

- [246] W. K. Kim, E. K. Choi, O. J. Sul, Y. K. Park, E. S. Kim, R. Yu, J. H. Suh, and H. S. Choi, "Monocyte Chemoattractant Protein-1 Deficiency Attenuates Oxidative Stress and Protects against Ovariectomy-Induced Chronic Inflammation in Mice," *PLOS ONE*, vol. 8, p. e72108, Aug. 2013. Publisher: Public Library of Science.
- [247] M. Deckert, M. Ticchioni, B. Mari, D. Mary, and A. Bernard, "The glycosylphosphatidylinositol-anchored CD59 protein stimulates both T cell receptor /ZAP-70-dependent and -independent signaling pathways in T cells," *European Journal of Immunology*, vol. 25, no. 7, pp. 1815–1822, 1995.
- [248] A. K. Benson, S. A. Kelly, R. Legge, F. Ma, S. J. Low, J. Kim, M. Zhang, P. L. Oh, D. Nehrenberg, K. Hua, S. D. Kachman, E. N. Moriyama, J. Walter, D. A. Peterson, and D. Pomp, "Individuality in gut microbiota composition is a complex polygenic trait shaped by multiple environmental and host genetic factors," *Proceedings of the National Academy of Sciences of the United States of America*, vol. 107, pp. 18933–18938, Nov. 2010. Publisher: National Academy of Sciences.
- [249] A. Kovacs, N. Ben-Jacob, H. Tayem, E. Halperin, F. A. Iraqi, and U. Gophna, "Genotype Is a Stronger Determinant than Sex of the Mouse Gut Microbiota," *Microbial Ecology*, vol. 61, pp. 423–428, Feb. 2011. Publisher: Springer.
- [250] M. Raman, I. Ahmed, P. M. Gillevet, C. S. Probert, N. M. Ratcliffe, S. Smith, R. Greenwood, M. Sikaroodi, V. Lam, P. Crotty, J. Bailey, R. P. Myers, and K. P. Rioux, "Fecal microbiome and volatile organic compound metabolome in obese humans with non-alcoholic fatty liver disease," *Clinical gastroenterology and hepatology : the official clinical practice journal of the American Gastroenterological Association*, vol. 11, no. 7, pp. 868–875.e3, 2013. Publisher: Clin Gastroenterol Hepatol.
- [251] Y. Zhong, M. Nyman, and F. Fåk, "Modulation of gut microbiota in rats fed high-fat diets by processing whole-grain barley to barley malt," *Molecular nutrition & food research*, vol. 59, pp. 2066–2076, Oct. 2015. Publisher: Mol Nutr Food Res.
- [252] K. Nishitsuji, J. Xiao, R. Nagatomo, H. Umemoto, Y. Morimoto, H. Akatsu, K. Inoue, and K. Tsuneyama, "Analysis of the gut microbiome and plasma short-chain fatty acid profiles in a spontaneous mouse model of metabolic syndrome," *Scientific Reports*, vol. 7, Dec. 2017. Publisher: Nature Publishing Group.
- [253] M. R. Fernando, A. Saxena, J. L. Reyes, and D. M. McKay, "Butyrate enhances antibacterial effects while suppressing other features of alternative activation in IL-4-induced macrophages," *American Journal of Physiology - Gastrointestinal and Liver Physiology*, vol. 310, pp. G822–G831, May 2016. Publisher: American Physiological Society.
- [254] Y. Furusawa, Y. Obata, S. Fukuda, T. A. Endo, G. Nakato, D. Takahashi, Y. Nakanishi, C. Uetake, K. Kato, T. Kato, M. Takahashi, N. N. Fukuda, S. Murakami, E. Miyauchi, S. Hino, K. Atarashi, S. Onawa, Y. Fujimura, T. Lockett, J. M. Clarke, D. L. Topping, M. Tomita, S. Hori, O. Ohara, T. Morita, H. Koseki, J. Kikuchi, K. Honda, K. Hase, and H. Ohno, "Commensal microbe-derived butyrate induces the differentiation of colonic regulatory T cells," *Nature* 2013 504:7480, vol. 504, pp. 446–450, Nov. 2013. Publisher: Nature Publishing Group.

- [255] A. Andoh, T. Bamba, and M. Sasaki, "Physiological and Anti-Inflammatory Roles of Dietary Fiber and Butyrate in Intestinal Functions," *Journal of Parenteral and Enteral Nutrition*, vol. 23, pp. S70–S73, Sept. 1999. Publisher: John Wiley & Sons, Ltd.
- [256] M. García-López, J. P. Meier-Kolthoff, B. J. Tindall, S. Gronow, T. Woyke, N. C. Kyrpides, R. L. Hahnke, and M. Göker, "Analysis of 1,000 Type-Strain Genomes Improves Taxonomic Classification of Bacteroidetes," *Frontiers in microbiology*, vol. 10, Sept. 2019. Publisher: Front Microbiol.
- [257] L. L. Presley, B. Wei, J. Braun, and J. Borneman, "Bacteria Associated with Immunoregulatory Cells in Mice," *Applied and Environmental Microbiology*, vol. 76, p. 936, Feb. 2010. Publisher: American Society for Microbiology (ASM).
- [258] C. Ubeda, Y. Taur, R. R. Jenq, M. J. Equinda, T. Son, M. Samstein, A. Viale, N. D. Socci, M. R. M. V. D. Brink, M. Kamboj, and E. G. Pamer, "Vancomycin-resistant Enterococcus domination of intestinal microbiota is enabled by antibiotic treatment in mice and precedes bloodstream invasion in humans," *The Journal of clinical investigation*, vol. 120, pp. 4332–4341, Dec. 2010. Publisher: J Clin Invest.
- [259] J. Ye, J. W. Lee, L. L. Presley, E. Bent, B. Wei, J. Braun, N. L. Schiller, D. S. Straus, and J. Borneman, "Bacteria and Bacterial rRNA Genes Associated with the Development of Colitis in IL-10^{-/-} Mice," *Inflammatory bowel diseases*, vol. 14, p. 1041, Aug. 2008. Publisher: NIH Public Access.
- [260] D. M. Dinh, G. E. Volpe, C. Duffalo, S. Bhalchandra, A. K. Tai, A. V. Kane, C. A. Wanke, and H. D. Ward, "Intestinal microbiota, microbial translocation, and systemic inflammation in chronic HIV infection," *The Journal of infectious diseases*, vol. 211, pp. 19–27, Jan. 2015. Publisher: J Infect Dis.
- [261] K. M. Wylie, R. M. Truty, T. J. Sharpton, K. A. Mihindukulasuriya, Y. Zhou, H. Gao, E. Sodergren, G. M. Weinstock, and K. S. Pollard, "Novel Bacterial Taxa in the Human Microbiome," *PLoS ONE*, vol. 7, p. 35294, June 2012. Publisher: PLOS.
- [262] R. Marti, Y. Zhang, D. R. Lapen, and E. Topp, "Development and validation of a microbial source tracking marker for the detection of fecal pollution by muskrats," *Journal of microbiological methods*, vol. 87, pp. 82–88, Oct. 2011. Publisher: J Microbiol Methods.
- [263] A. N. Shkoporov, A. G. Clooney, T. D. S. Sutton, F. J. Ryan, K. M. Daly, J. A. Nolan, S. A. McDonnell, E. V. Khokhlova, L. A. Draper, A. Forde, E. Guerin, V. Velayudhan, R. P. Ross, and C. Hill, "The Human Gut Virome Is Highly Diverse, Stable, and Individual Specific," *Cell Host & Microbe*, vol. 26, pp. 527–541.e5, Oct. 2019. Publisher: Cell Press.
- [264] J. Downes, F. E. Dewhirst, A. C. R. Tanner, and W. G. Wade, "Description of *Alloprevotella rava* gen. nov., sp. nov., isolated from the human oral cavity, and reclassification of *Prevotella tanneri* Moore et al. 1994 as *Alloprevotella tanneri* gen. nov., comb. nov.," *International journal of systematic and evolutionary microbiology*, vol. 63, pp. 1214–1218, Apr. 2013. Publisher: Int J Syst Evol Microbiol.
- [265] D. P. Kateete, M. M. Mbabazi, F. Nakazzi, F. A. Katabazi, E. Kigozi, W. Ssengooba, L. Nakiyingi, S. Namiiro, A. Okwera, M. L. Joloba, and A. Muwonge, "Sputum microbiota

- profiles of treatment-naïve TB patients in Uganda before and during first-line therapy,” *Scientific Reports 2021 11:1*, vol. 11, pp. 1–13, Dec. 2021. ISBN: 0123456789 Publisher: Nature Publishing Group.
- [266] J. Wu, W. Liu, L. He, F. Huang, J. Chen, P. Cui, Y. Shen, J. Zhao, W. Wang, Y. Zhang, M. Zhu, W. Zhang, and Y. Zhang, “Sputum Microbiota Associated with New, Recurrent and Treatment Failure Tuberculosis,” *PLOS ONE*, vol. 8, p. e83445, Dec. 2013. Publisher: Public Library of Science.
- [267] O. Kwon, S. Lee, J.-H. Kim, H. Kim, and S.-W. Lee, “Altered Gut Microbiota Composition in Rag1-deficient Mice Contributes to Modulating Homeostasis of Hematopoietic Stem and Progenitor Cells,” *Immune network*, vol. 15, no. 5, p. 252, 2015. Publisher: Immune Netw.
- [268] Q. Ma, Y. Li, J. Wang, P. Li, Y. Duan, H. Dai, Y. An, L. Cheng, T. Wang, C. Wang, T. Wang, and B. Zhao, “Investigation of gut microbiome changes in type 1 diabetic mellitus rats based on high-throughput sequencing,” *Biomedicine & Pharmacotherapy*, vol. 124, p. 109873, Apr. 2020. Publisher: Elsevier Masson.
- [269] Y. Chen and M. J. Blaser, “Inverse associations of *Helicobacter pylori* with asthma and allergy,” *Archives of internal medicine*, vol. 167, pp. 821–827, Apr. 2007. Publisher: Arch Intern Med.
- [270] J. A. Bustamante-Rengifo, A. J. Matta, A. Pazos, and L. E. Bravo, “In vitro effect of amoxicillin and clarithromycin on the 3’ region of *cagA* gene in *Helicobacter pylori* isolates.,” *World Journal of Gastroenterology*, vol. 19, pp. 6044–6054, Sept. 2013. ISBN: 5726670329 Publisher: Baishideng Publishing Group Co.
- [271] S. Perry, B. C. D. Jong, J. V. Solnick, M. D. L. L. Sanchez, S. Yang, P. L. Lin, L. M. Hansen, N. Talat, P. C. Hill, R. Hussain, R. A. Adegbola, J. A. Flynn, D. Canfield, and J. Parsonnet, “Infection with *Helicobacter pylori* Is Associated with Protection against Tuberculosis,” *PLOS ONE*, vol. 5, p. e8804, Jan. 2010. Publisher: Public Library of Science.
- [272] L. Macia, J. Tan, A. T. Vieira, K. Leach, D. Stanley, S. Luong, M. Maruya, C. I. McKenzie, A. Hijikata, C. Wong, L. Binge, A. N. Thorburn, N. Chevalier, C. Ang, E. Marino, R. Robert, S. Offermanns, M. M. Teixeira, R. J. Moore, R. A. Flavell, S. Fagarasan, and C. R. Mackay, “Metabolite-sensing receptors GPR43 and GPR109A facilitate dietary fibre-induced gut homeostasis through regulation of the inflammasome,” *Nature Communications 2015 6:1*, vol. 6, pp. 1–15, Apr. 2015. Publisher: Nature Publishing Group.
- [273] P. V. Chang, L. Hao, S. Offermanns, and R. Medzhitov, “The microbial metabolite butyrate regulates intestinal macrophage function via histone deacetylase inhibition,” *Proceedings of the National Academy of Sciences of the United States of America*, vol. 111, pp. 2247–2252, Feb. 2014. Publisher: Proc Natl Acad Sci U S A.
- [274] H. Lührs, T. Gerke, J. G. Müller, R. Melcher, J. Schaubert, F. Boxberger, W. Scheppach, and T. Menzel, “Butyrate inhibits NF-kappaB activation in lamina propria macrophages of patients with ulcerative colitis,” *Scandinavian journal of gastroenterology*, vol. 37, no. 4, pp. 458–466, 2002. Publisher: Scand J Gastroenterol.

- [275] M. A. R. Vinolo, E. Hatanaka, R. H. Lambertucci, P. Newsholme, and R. Curi, "Effects of short chain fatty acids on effector mechanisms of neutrophils," *Cell biochemistry and function*, vol. 27, no. 1, pp. 48–55, 2009. Publisher: Cell Biochem Funct.
- [276] J. C. Deschemin, M. L. Noordine, A. Remot, A. Willemetz, C. Afif, F. Canonne-Hergaux, P. Langella, Z. Karim, S. Vaulont, M. Thomas, and G. Nicolas, "The microbiota shifts the iron sensing of intestinal cells," *FASEB Journal*, vol. 30, no. 1, 2016.
- [277] Y. M. Shah, T. Matsubara, S. Ito, S. H. Yim, and F. J. Gonzalez, "Intestinal Hypoxia-Inducible Transcription Factors Are Essential for Iron Absorption following Iron Deficiency," *Cell Metabolism*, vol. 9, pp. 152–164, Feb. 2009. Publisher: Cell Press.
- [278] R. C. Edgar and A. Bateman, "Search and clustering orders of magnitude faster than BLAST," *Bioinformatics*, vol. 26, pp. 2460–2461, Oct. 2010. Publisher: Oxford Academic.

Glossary of Symbols and Abbreviations

$\gamma\delta$ T cells	Gamma delta T cells
μg	Microgram
μl	Microliter
μm	Micromolar
$^{\circ}\text{C}$	Degree celsius
-/-	Deficient
4Fe-4S cluster	Iron-sulfur cluster
Aq. dest.	Aqua destilatta (distilled water)
aM \emptyset	Alveolar macrophage
APC	Antigen-presenting cells
approx.	Approximately
BCG	Bacille Calmette-Guérin
BMM \emptyset	Bone-marrow-derived macrophage
BSA	Bovine serum albumin
CCL	C-Chemokine-ligand
CD	Cluster of differentiation
CO ₂	Carbondioxide
DC-SIGN	Dendritic cell-specific intercellular adhesion molecule-3-grabbing non-integrin
DMEM	Dulbecco's modified eagle's medium
DE	Deutschland
DPBS	Dulbecco's phosphate-buffered saline
DMSO	Dimethyl sulfoxide
DNA	Deoxyribonucleic acid
DC	Dendritic cells
EDTA	Ethylenediaminetetraacetic acid
ELISA	Enzyme-linked immunosorbent assay
et al.	et alii, et aliae (and the others)
FCS	Fetal calf serum
Fig	Figure
fl	Femtoliter
Fe	Iron
Fe ²⁺ /Fe ³⁺	Ferrous/Ferric iron
G	Gauge
GF	Germ-free
h	Hour
h.i.	Heat-inactivated
HIF-1 α	Hypoxia-inducible factor-1 alpha
H&E	Hematoxylin and eosin

HGB	Hemoglobin
i.e.	id est (that is)
IFN γ	Interferon gamma
IL	Interleukin
L	Liter
IRE	Iron responsive element
IRP	Iron regulatory protein
KO	Knock-out
M \emptyset	Macrophage
MCH	Mean corpuscular haemoglobin
MCHC	Mean corpuscular hemoglobin concentration
MCV	Mean corpuscular volume
mins	Minute (s)
MDR	Multidrug-resistant tuberculosis
ml	Milliliter
mRNA	Messenger RNA
MPV	Mean platelet volume
MyD88	Myeloid differentiation primary response gene 88
N/A	Not applicable
NF κ B	Nuclear factor kappa light-chain-enhancer of activated B cells
N/A	Not applicable
NK	Natural killer cells
NKT	Natural killer T-cells
NO	Nitric oxide
NOS2	Nitric oxide synthase 2
NLR	Nucleotide-binding oligomerization domain receptors
OD	Optical density
o/n	Overnight
pM \emptyset	Peritoneal macrophages
PAMP	Pathogen-associated molecular pattern
PBS	Phosphate buffered saline
PCoA	Principal coordinate analysis
PERMANOVA	Permutational multivariate analysis of variance
PFA	Paraformaldehyde
p.i.	Post-infection
PMN	Polymorphonuclear neutrophils
PRR	Pattern recognition receptor
RBC	Red blood cells
rcf	Relative centrifugal force
RES	Reticuloendothelial system
RNA	Ribonucleic acid
RNI	Reactive nitrogen intermediates
ROS	Reactive oxygen species
RPMI medium	Roswell Park Memorial Institute medium
rRNA	Ribosomal RNA
RT	Room temperature
s	Second
SD	Standard deviation

s/n	Supernatant
SPF	Specific-pathogen free
spp.	Species
TB	Tuberculosis
TF	Transferrin
TLR	Toll-like Receptor
TNF α	Tumor necrosis factor-alpha
UV	Ultraviolet
v	Version
v/v	Volume per volume
w/	With
w/o	Without
w/v	Weight per volume
WT	Wild type
XDR	Extensively drug-resistant tuberculosis

List of Tables

1.1	Iron cofactors and their essential functions	1
1.2	Human disorders linked to IRE/IRP system defects. Modified from [35].	7
1.3	GWAS involving <i>IRP1</i> and <i>IRP2</i> polymorphisms. Modified from [35] . .	7
2.1	Chemicals and reagents used in this study	21
2.2	Consumables used in this study	23
2.3	Buffers, solutions and media used in this study	24
2.4	Kits used in this study	25
2.5	Antibodies used in this study for Immunohistochemistry	25
2.6	Primers used for Amplicon PCR	26
2.7	qRT-PCR murine primer sequences used in this study	26
2.8	Equipment used in this study	27
2.9	Software used in this study	27
2.10	Bacterial strains used in this study	28
2.11	Mice used in this study	28
3.1	Scoring scheme for experimental animals. Adapted from [144]	33
3.2	Allocation of organs to different experiments following organ harvesting	34
3.3	Paraffin processing of tissues	35
3.4	Tissue processing for cryopreservation	35
3.5	Treatment of tissue sections prior to ZN staining	36
3.6	ZN staining	37
3.7	dsDNAse digestion reaction set-up	39
3.8	cDNA synthesis reaction set-up	39
3.9	Thermal cycling conditions for cDNA synthesis	39
3.10	qRT-PCR reaction set-up	40
3.11	Thermal cycling conditions for qRT-PCR	40
3.12	PCR reaction set-up	41
3.13	Thermal cycling conditions for PCR	41
3.14	Amplicon PCR reaction set-up for one sample	42
3.15	Index PCR reaction set-up for one sample	42
5.1	Distinct phenotype features of mouse models with complete or tissue-specific deletion of <i>Irp1</i> and <i>Irp2</i>. Adapted from [35]	99

List of Figures

- 1.1 **Mechanisms for IRP1 regulation.** IRP1 can be regulated by the assembly or disassembly of the 4Fe-4S cluster resulting in the IRP1 functioning as either a c-aconitase or IRE-binding protein (A). Phosphorylation at S138 can also stimulate iron-sulfur assembly in IRP1 (B). Abbreviations: 4Fe-4S= iron-sulfur cluster, FBXL5= F-box and leucine-rich repeat protein 5, ROS= reactive oxygen species, RNS= reactive nitrogen species, Adapted from [26, 27]. Created with BioRender.com 4
- 1.2 **Mechanisms for IRP2 regulation.** IRP2 is regulated at the level of protein stability in response to cellular iron and oxygen concentrations. In high iron and oxygen conditions, FBXL5 is stabilized, and IRP2 is degraded (A). Under iron or oxygen-deficient conditions, FBXL5 is destabilized, leading to an increase in IRP2 levels (B). Abbreviations: FBXL5= F-box and leucine-rich repeat protein 5, SKPI= S-phase kinase-associated protein 1, CUL1= culin 1, G2-M= Gap 2-mitosis, CDC14A= cell division cycle 14A, CDK1= cyclin-dependent kinase 1. Adapted from [26, 27]. Created with BioRender.com 5
- 1.3 **IRE/IRP regulatory system.** The activity of IRPs is dependent on cellular iron concentrations. Under iron-deficient conditions, IRPs bind to IREs in 5'-UTR of the mRNA and translation of the target protein is repressed. Binding to 3'-UTR of the mRNA stabilizes and protects the transcripts from endonucleolytic cleavage and degradation (A). Under iron-replete conditions, IRP1 functions as a cytosolic aconitase cluster while IRP2 is degraded allowing for the translation of mRNA containing an IRE in the 5'-UTR and the degradation of mRNAs in the 3'-UTR (B). Abbreviations: IRP= iron regulatory protein, IRE= iron responsive element, UTR= untranslated region, TFR1= transferrin receptor 1, DMT1= divalent metal transporter 1, FPN= ferroportin, FtL/FtH= ferritin light and heavy chains, HIF-2 α = hypoxia-inducible factor-2 alpha. Adapted from [32]. Created with BioRender.com 6
- 1.4 **Major molecular mechanisms for hepcidin regulation.** These include BMP6/SMAD (A) and IL-6/JAK/STAT (B) signalling pathways. Hepcidin expression is inhibited by hypoxia to stimulate iron recruitment and erythropoiesis. Other regulators such as erythropoietin (EPO), growth differentiation factor-15 (GDF15) and platelet-driven growth factor-BB (PDGF-BB) and erythroferrone (ERFE) both inhibit hepcidin expression [52, 53] and neutralize BMP6 [54] (C). Abbreviations: EPO= Erythropoietin, GDF15= Growth differentiation factor-15, PDGF-BB= Platelet-driven growth factor-BB, ERFE= Erythroferrone. Numbers and black arrows denote the sequence of events. Red arrows represent inhibitory effects. Adapted from [55]. Created with BioRender.com 9

1.5	Iron metabolism in the macrophage. MØs can acquire iron from various sources including NTBI (A) and TBI uptake (B), and scavenger receptors (C). Excess labile iron generates ROS. ROS stimulates transcription factors' binding activities, which modulates the expression of several iron transport and storage proteins. In turn, the expression of these proteins is regulated posttranscriptionally by the IRPs. Abbreviations: HMOX1= heme oxygenase 1, TBI= transferrin-bound iron, NTBI= non-transferrin-bound iron, LIP= labile iron pool, FRTN= ferritin, FPNI= ferroportin; dRBCs= damaged RBCs, Hgb= hemoglobin. Numbers denote the sequence of events. Arrows represent iron movements (black), stimulatory effects (green), or inhibitory effects (red). Created with BioRender.com	11
1.6	Estimated Global TB incidence rates in 2021 [63]	13
1.7	Granuloma formation during Mtb infection. Mtb infects aMØs. This is followed by an influx of innate immune cells, such as PMNs, DCs, and NK cells, to the site of infection, leading to granuloma formation (A). Granuloma MØs differentiate into giant cells and foamy MØs. Surrounded by B- and T-lymphocytes and a fibrous cuff, the granuloma restricts Mtb dissemination (B). Created with BioRender.com	14
4.1	Experimental set-up for investigating dietary iron supplementation and iron under-supply in mice prior to and during experimental Mtb infection. 3-week-old female C57BL/6J mice were fed an experimental diet containing 46 mg/kg Fe (II) fumarate for 8 weeks for acclimatization. At 11 weeks of age, mice were assigned to 3 feeding groups: iron-control, iron-rich, and iron-low. Mice were sacrificed 8 weeks (d-84 p.i.) and 16 weeks (d-1 p.i.) after the start of the feeding regimen and infection with 100 CFU Mtb H37Rv via the aerosol route on day 0 was performed. The target infection dose was investigated in 8 mice (i.e., n=4 animals per experiment) in the iron-control group on day 1 p.i. Mice were maintained on the respective diets for additional 16 weeks and sacrificed at indicated time points.	46
4.2	Mycobacterial loads in tissue homogenates from mice on iron-control, iron-rich and iron-low diets. SPF female C57BL/6J mice were treated as indicated in Fig. 4.1. CFU assays were performed, and mycobacterial loads in lungs (A-C), spleens (D-F) and livers (G-I) were determined at indicated time points. Each circle represents an individual sample (n=6-8 animals for all panels). Data pooled from 2 independent experiments representing both days 13/16, 26/29, 63/64, and 119/120 p.i. Data were log-transformed and as shown as mean ± SD. Statistical analysis was performed using two-way ANOVA with Tukey's multiple comparisons tests. *p ≤ 0.05, **p ≤ 0.01, *** p≤ 0.001 and **** p ≤ 0.0001 were considered statistically significant. ns represents statistically non-significant differences.	47
4.3	Histopathological analysis of lung tissue sections from mice on iron-control, iron-rich and iron-low diets. SPF female C57BL/6J mice were treated as indicated in Fig. 4.1. Superior lung lobes were collected, PFA fixed, and paraffin-embedded (PFPE). Tissue sections were stained at all time points with H&E stain and examined at indicated magnifications. Representative micrographs of 1 animal out of 8 per group are shown (i.e., from 2 independent experiments). Squares with a black outline and black arrows show inflammatory cellular infiltrates. Scale bars represent 1 mm taken with 4x objective.	48

- 4.4 **Evaluation of indicators of iron status in sera from mice on iron-control, iron-rich and iron-low diets.** SPF female C57BL/6J mice were treated as indicated in Fig. 4.1. Serum was obtained from whole blood collected from the *vena cava caudalis* under terminal anaesthesia to investigate total serum iron (A-C) and serum ferritin (D-F) concentrations at indicated time points. Each circle represents an individual sample (n=4 animals). Data are from 1 experiment and shown as mean \pm SD. Statistical analysis was performed using two-way ANOVA with Tukey's multiple comparison tests. *p \leq 0.05, **p \leq 0.01, *** p \leq 0.001 and **** p \leq 0.0001 were considered statistically significant. ns represents statistically non-significant differences. 49
- 4.5 **Quantification of iron metabolism genes in liver tissue from mice on iron-control, iron-rich and iron-low diets.** SPF female C57BL/6J mice were treated as indicated in Fig 4.1. Livers were collected, total host cellular RNA was extracted, reverse transcribed to complementary DNA, and used for the quantification of *Tfr1* (A-C) *Fpn1* (D-F) *Frtn-L* (G-I) and *Hamp1* (J-L) gene expression by qRT-PCR. All mRNA expression levels were normalized against murine *Hprt* mRNA expression levels. Each circle represents an individual sample (n=4 animals). Data are from 1 experiment and shown as mean \pm SD. Statistical analysis was performed using two-way ANOVA with Tukey's multiple comparison tests. *p \leq 0.05 and **p \leq 0.01 were considered as statistically significant. ns represents non-statistically significant differences. RQ = Relative quantification. 50
- 4.6 **Quantification of mRNA and protein expression levels of inflammatory cytokines in lung tissue and homogenates from mice on iron-control, iron-rich and iron-low diets.** SPF female C57BL/6J mice were treated as indicated in Fig. 4.1. Lungs were collected, total host cellular RNA was extracted, reverse transcribed to complementary DNA, and used for the quantification of *Ifng* (A), *Tnfa* (B) and *Il-6* (C) gene expression by qRT-PCR. All mRNA expression levels were normalized against murine *Hprt* mRNA expression levels. RQ = Relative quantification. In lung homogenates, the protein concentrations of IFN γ (A) and TNF α (B) were investigated. Each circle represents an individual sample (n=4 animals). Data are from 1 experiment and shown as mean \pm SD. Statistical analysis was performed using two-way ANOVA with Tukey's multiple comparison tests. *p \leq 0.05 and **p \leq 0.01 were considered as statistically significant. ns represents non-statistically significant differences. 52
- 4.7 **Histological analysis of iron deposits in lung tissue sections from mice on iron-control, iron-rich and iron-low diets.** SPF female C57BL/6J mice were treated as indicated in Fig 4.1. Superior lung lobes were collected, PFA fixed, and paraffin infiltrated at days -84 and 119 p.i. Tissue sections were stained with Perl's stain and examined under the BX41 light microscope at different magnifications (A). Iron deposits stain bright-deep blue while nuclei and cytoplasm stain pink-red. Representative micrographs of 1 animal out of 8 per group are shown. Black arrows indicate iron deposits stained bright blue. Scale bars represent 100 μ m (400x magnification). Quantitative assessment of iron deposits (B). Data generated from quantification of iron deposits are from 1 experiment, n=4 animals. Statistical analysis was performed using two-way ANOVA with Tukey's multiple comparison tests. *p \leq 0.05 was considered as statistically significant. ns represents non-statistically significant differences. PPB⁺ aM \emptyset = Perl Prussian blue positive alveolar macrophages. 53

- 4.8 **Tissue-resident macrophage numbers in wt, *Irp1*^{-/-} and *Irp2*^{-/-} mice.** 12-16-week-old female wt, *Irp1*^{-/-} and *Irp2*^{-/-} mice were euthanized by CO₂ exposure. Bone marrow cells (A), pMØ (B) and aMØ (C) were collected, and viable cells were counted. Each square represents an individual sample (n=6 animals). Data pooled from 2 independent experiments and shown as mean ± SD. Statistical analysis was performed using Kruskal-Wallis' nonparametric test with Dunn's multiple comparisons test to compare experimental groups. *p ≤ 0.05 and **p ≤ 0.01 were considered statistically significant. 54
- 4.9 **Mycobacterial loads in wt, *Irp1*^{-/-} and *Irp2*^{-/-} macrophages.** Bone marrow cells were isolated from non-infected wt, *Irp1*^{-/-} and *Irp2*^{-/-} mice and allowed to differentiate to mature BMMØs. 10⁵ BMMØs (A-D), pMØ (E-H) and aMØ (I-K) were infected with Mtb H37Rv (MOI of 0.1:1) to determine the mycobacterial burden at indicated time points. Data pooled from 3 independent experiments with 3 technical replicates each and shown as mean ± SD. Statistical analysis was performed using ordinary one-way ANOVA with Tukey's multiple comparison tests, with single pooled variance. *p ≤ 0.05, **p ≤ 0.01, *** p ≤ 0.001 and **** p ≤ 0.0001 were considered statistically significant. 55
- 4.10 **Mycobacterial loads in wt, *Irp1*^{-/-} and *Irp2*^{-/-} macrophages following IFN γ stimulation.** Bone marrow cells were isolated from non-infected wt, *Irp1*^{-/-} and *Irp2*^{-/-} mice and allowed to differentiate to mature BMMØs. 10⁵ BMMØs (A-D), pMØ (E-H) and aMØ (I-K) were stimulated with 500 U/ml IFN γ and infected with Mtb H37Rv (MOI of 0.1:1) to determine the mycobacterial burden at indicated time points. Data pooled from 2 independent experiments with 3 technical replicates each and shown as mean ± SD. Statistical analysis was performed using ordinary one-way ANOVA with Tukey's multiple comparison tests, with single pooled variance. 56
- 4.11 **Determination of phagocytosis rate in wt, *Irp1*^{-/-} and *Irp2*^{-/-} macrophages.** Bone marrow cells were isolated from non-infected wt, *Irp1*^{-/-} and *Irp2*^{-/-} mice and allowed to differentiate to mature BMMØs. 10⁵ BMMØs per well were seeded, and phagocytosis rate was measured in BMMØs which were either untreated with Zymosan particles and unstimulated with IFN γ (A), treated with only Zymosan particles (B), treated with Zymosan particles and stimulated with 500 U/ml IFN γ (C) or treated with Zymosan particles and 10 μ m Cytochalasin D (D). The phagocytosis rate was determined by colourimetric detection at 405 nm. Data are from 1 experiment and shown as mean ± SD. Statistical analysis was performed using Kruskal-Wallis' nonparametric test with Dunn's multiple comparisons test to compare experimental groups. *p ≤ 0.05 and **p ≤ 0.01 were considered statistically significant. ns represents statistically non-significant differences. 57
- 4.12 **Nitric oxide quantification in wt, *Irp1*^{-/-} and *Irp2*^{-/-} non-infected macrophage supernatants.** Bone marrow cells were isolated from non-infected wt, *Irp1*^{-/-} and *Irp2*^{-/-} mice and allowed to differentiate to mature BMMØs. 10⁵ BMMØs per well were seeded, and NO levels were estimated in non-infected and unstimulated BMMØs (A-D), non-infected but stimulated with 500 U/ml IFN γ (E-H). Data pooled from 2 independent experiments with 3 technical replicates each and shown as mean ± SD. Statistical analysis was performed using ordinary one-way ANOVA with Tukey's multiple comparison tests, with single pooled variance. 58

- 4.13 **Nitric oxide quantification in wt, *Irp1*^{-/-} and *Irp2*^{-/-} Mtb infected macrophage supernatants.** Bone marrow cells were isolated from non-infected wt, *Irp1*^{-/-} and *Irp2*^{-/-} mice and allowed to differentiate to mature BMMØs. 10⁵ BMMØs per well were seeded, and NO levels were estimated in BMMØs which were either Mtb infected and unstimulated with IFN γ (A-D) or Mtb infected and stimulated with 500 U/ml IFN γ (E-H). Data pooled from 2 independent experiments with 3 technical replicates each and shown as mean \pm SD. Statistical analysis was performed using ordinary one-way ANOVA with Tukey's multiple comparison tests, with single pooled variance. *p \leq 0.05, **p \leq 0.01 and **** p \leq 0.0001 were considered statistically significant. ns represents statistically non-significant differences. 59
- 4.14 **Mycobacterial loads in wt, *Irp1*^{-/-} and *Irp2*^{-/-} macrophages following FAC or DFO treatment.** Bone marrow cells were isolated from non-infected wt, *Irp1*^{-/-} and *Irp2*^{-/-} mice and allowed to differentiate to mature BMMØs. 10⁵ BMMØs per well were infected with Mtb (MOI of 0.1:1) (A-D) and treated with either FAC (E-H) or DFO (I-L) to determine the mycobacterial burden at indicated time points. Data pooled from 2 independent experiments with 3 technical replicates each and shown as mean \pm SD. Statistical analysis was performed using ordinary two-way ANOVA with Tukey's multiple comparison tests, with single pooled variance. *p \leq 0.05, **p \leq 0.01 and **** p \leq 0.0001 were considered statistically significant. ns represents statistically non-significant differences. 60
- 4.15 **Mycobacterial loads in tissue homogenates from wt, *Irp1*^{-/-} and *Irp2*^{-/-} mice.** 8-20-week-old female wt, *Irp1*^{-/-} and *Irp2*^{-/-} mice were infected with 100 CFU Mtb via the aerosol route. CFU assays were performed, and the mycobacterial loads in lungs (A), spleens (B), and livers (C) were determined at indicated time points. Each square represents an individual sample. Data pooled from 2 independent experiments (n=8 animals for panels A and B, n= 5 animals for panel C), log-transformed and as shown as mean \pm SD. Statistical analysis was performed using two-way ANOVA with Tukey's multiple comparisons tests. *p \leq 0.05, **p \leq 0.01, *** p \leq 0.001 and **** p \leq 0.0001 were considered statistically significant. 61
- 4.16 **Mean body weights of wt, *Irp1*^{-/-} and *Irp2*^{-/-} mice.** 8-20-week-old female wt, *Irp1*^{-/-} and *Irp2*^{-/-} mice were monitored for fluctuations in weight prior to and during infection with 100 CFU Mtb via the aerosol route. Data pooled from 2 independent experiments (n=7-8 animals) and shown as mean \pm SD. Statistical analysis was performed using two-way ANOVA with Tukey's multiple comparisons tests. *p \leq 0.05, **p \leq 0.01 and *** p \leq 0.001 were considered statistically significant. 62
- 4.17 **Relative organ weight and viable immune cell count in lungs from wt, *Irp1*^{-/-} and *Irp2*^{-/-} mice.** 8-20-week-old wt, *Irp1*^{-/-} and *Irp2*^{-/-} mice were infected with 100 CFU Mtb via the aerosol route. Lungs were collected, and lung weights (A), lung-to-body-weight-ratio (B) and the number of immune cells (C) were recorded. Each square represents an individual sample (n=7-8 animals for panels A and B, 5 animals for panel C). Data pooled from 2 independent experiments and shown as mean \pm SD. Statistical analysis was performed using two-way ANOVA with Tukey's multiple comparisons tests. *p \leq 0.05 and **p \leq 0.01 were considered statistically significant. ns represents statistically non-significant differences. 62

- 4.18 **Relative organ weight and viable immune cell count in spleens from wt, *Irp1*^{-/-} and *Irp2*^{-/-} mice.** 8–20-week-old wt, *Irp1*^{-/-} and *Irp2*^{-/-} mice were infected with 100 CFU Mtb via the aerosol route. Spleens were collected, and respective weights (A), spleen-to-body-weight-ratio (B) and number of viable immune cells (C) were recorded. Each square represents an individual sample (n=7-8 animals for panels A and B, 5 animals for panel C). Data pooled from 2 independent experiments and shown as mean ± SD. Statistical analysis was performed using two-way ANOVA with Tukey's multiple comparisons tests. *p ≤ 0.05 and **p ≤ 0.01 were considered statistically significant. ns represents statistically non-significant differences. Macroscopic assessment of mice spleens was performed (D). Representative photograph of 1 animal spleen per mouse strain out of 8 per group are shown, i.e., from 2 independent experiments. 63
- 4.19 **Cytokines and chemokine quantification in lung homogenates from wt, *Irp1*^{-/-} and *Irp2*^{-/-} mice.** 8-20- week-old female wt, *Irp1*^{-/-} and *Irp2*^{-/-} mice were infected with 100 CFU of Mtb via the aerosol route and sacrificed at indicated time points. Lungs were collected and homogenized for the investigation of IFN γ (A) TNF α (B) IL-1 β (C) IL-6 (D) IL-10 (E) KC/GRO (F) MCP-1 (G) MIP-2 (H) production. Each square represents an individual sample (n=5 animals). Data pooled from 2 independent experiments and shown as mean ± SD. Statistical analysis was performed using two-way ANOVA with Tukey's multiple comparisons tests. *p ≤ 0.05, **p ≤ 0.01, *** p ≤ 0.001 and **** p ≤ 0.0001 were considered statistically significant. ns represents statistically non-significant differences. 65
- 4.20 **Cytokines and chemokine quantification in spleen homogenates from wt, *Irp1*^{-/-} and *Irp2*^{-/-} mice.** 8-20- week-old female wt, *Irp1*^{-/-} and *Irp2*^{-/-} mice were infected with 100 CFU of Mtb via the aerosol route and sacrificed at indicated time points. Spleens were collected, and homogenates were used for the investigation of IFN γ (A), TNF α (B), IL-1 β (C), IL-6 (D), IL-10 (E), IL-17A (F), KC/GRO (G) MCP-1 (H) MIP-2 (I) production. Each square represents an individual sample (n=5 animals). Data pooled from 2 independent experiments and shown as mean ± SD. Statistical analysis was performed using two-way ANOVA with Tukey's multiple comparisons tests. *p ≤ 0.05, **p ≤ 0.01, *** p ≤ 0.001 and **** p ≤ 0.0001 were considered statistically significant. ns represents statistically non-significant differences. 66
- 4.21 **Immunohistological staining for NOS2-positive macrophages in lung tissue sections from wt, *Irp1*^{-/-} and *Irp2*^{-/-} mice.** 8-20- week-old female wt, *Irp1*^{-/-} and *Irp2*^{-/-} were infected with 100 CFU of Mtb H37Rv via the aerosol route. Superior lung lobes were collected, PFA fixed, and paraffin-embedded. NOS2 in lung tissue sections was detected by anti-NOS2 antibody followed by treatments with biotinylated goat anti-rabbit secondary antibody, avidin-biotin complex, and DAB peroxidase substrate. Sections were counterstained with Gill's Hematoxylin and examined under the BX41 light microscope. Gill's Hematoxylin stains the nuclei purple while anti-NOS2 antibody stains the NOS2 within M ϕ s copper brown. Representative micrographs of 1 animal out of 4 per group are shown. Scale bars represent 500 μ m and 100 μ m. Abbreviation: IHC= immunohistochemistry. 67

4.22 **Determination of RNI in lungs from wt, *Irp1*^{-/-} and *Irp2*^{-/-} mice.** 8-20-week-old female wt, *Irp1*^{-/-} and *Irp2*^{-/-} mice were infected with 100 CFU of Mtb H37Rv via the aerosol route and sacrificed at indicated time points. Lungs were collected, and total host cellular RNA was extracted. Complementary DNA was synthesized and used to quantify *Nos2* gene expression via qRT-PCR (A). All mRNA expression levels were normalized against murine *Hprt* mRNA expression levels. In lung homogenates, the protein concentrations of nitric oxide was also measured (B). Data are from 1 experiment (n=4 animals) and shown as mean ± SD. Statistical analysis was performed using two-way ANOVA with Tukey's multiple comparison tests. *p ≤ 0.05, *** p ≤ 0.001 and **** p ≤ 0.0001 were considered statistically significant. ns represents non-statistically significant differences. Abbreviations: RQ = Relative quantification, Nos2= Nitric oxide synthase 2.

68

4.23 **Histopathological analysis of lung tissue sections from wt, *Irp1*^{-/-} and *Irp2*^{-/-} mice.** 8-20-week-old female wt, *Irp1*^{-/-} and *Irp2*^{-/-} mice were infected with 100 CFU of Mtb via the aerosol route. Superior lung lobes were collected, PFA fixed, and paraffin-embedded. Tissue sections were stained at days 28 (A) and 63 p.i. (B) with H&E stain and examined at indicated magnifications. Representative micrographs of 1 animal out of 8 per group are shown, i.e., from 2 independent experiments. Black squares and arrows show inflammatory cellular infiltrates. Scale bars represent Scale bars represent 500 μm, 200 μm and 50 μm (40x, 10x and 40x magnification, respectively). Quantitative assessment of cellular infiltrates and lesions of lung tissue (C). Data generated from quantification is from 1 experiment (n=4 animals). Statistical analysis was performed using two-way ANOVA with Tukey's multiple comparisons tests. **p ≤ 0.01 and *** p ≤ 0.001 were considered statistically significant, and ns represents statistically non-significant differences

69

4.24 **Histopathological analyses of liver tissue sections from wt, *Irp1*^{-/-} and *Irp2*^{-/-} mice.** 8-20-week-old female wt, *Irp1*^{-/-} and *Irp2*^{-/-} mice were infected with 100 CFU of Mtb H37Rv via the aerosol route. Left liver lobes were collected, PFA fixed, and paraffin infiltrated at 63 days p.i., stained with H&E stain, and examined under the BX41 light microscope (A). Hematoxylin stains the nuclei blue-purple while eosin stains the cytoplasm and extracellular matrix pink. Representative micrographs of 1 animal out of 8 per group (i.e., from 2 independent experiments) are shown. Scale bars represent 500 μm, 200 μm and 50 μm (40x, 10x and 40x magnification, respectively). Black squares and arrows indicate inflammatory cellular infiltrates. Quantitative assessment of cellular infiltrates and lesions of lung tissue (B). Data generated from quantification is from 1 experiment, n=4 animals. Statistical analysis was performed using two-way ANOVA with Tukey's multiple comparisons test tests. **p ≤ 0.01 and *** p ≤ 0.001 were considered statistically significant, and ns represents statistically non-significant differences.

70

4.25 **Histopathological determination of neutral lipids in lung tissue sections from wt, *Irp1*^{-/-} and *Irp2*^{-/-} mice.** 8-20-week-old female wt, *Irp1*^{-/-} and *Irp2*^{-/-} mice were infected with 100 CFU of Mtb via the aerosol route. Superior lung lobes were collected, PFA fixed, and paraffin-embedded. Tissue sections were stained with ORO stain to visualize lipid droplets and examined at indicated magnifications. ORO stains neutral lipids red containing lipid droplets and hematoxylin stains the nuclei blue-purple. Representative micrographs of 1 animal out of 3 per group are shown, i.e., from 1 experiment. Scale bars represent 500 μm and 100 μm.

71

- 4.26 **Quantification of iron metabolism genes in lung tissue from wt, *Irp1*^{-/-} and *Irp2*^{-/-} mice.** 8-20-week-old non-infected and Mtb infected female wt, *Irp1*^{-/-} and *Irp2*^{-/-} mice were sacrificed at indicated time points. Lungs were collected, and total host cellular RNA was extracted. Complementary DNA was synthesized and used for the quantification of *Tfr1* (A) *Dmt1* (B) *Frt-L* (C) *Hamp1* (D) *Fpn1* (E) and *Lcn2* (F) gene expression via qRT-PCR. All mRNA expression levels were normalized against murine *Hprt* mRNA expression levels. Data are from 1 experiment (n=4 animals) and shown as mean ± SD. Statistical analysis was performed using two-way ANOVA with Tukey's multiple comparison tests. ns represents statistically non-significant differences. Abbreviations: RQ= Relative quantification, *Tfr1*= transferrin receptor 1, *Dmt1*= divalent metal transporter, *Frt-L*= ferritin-light chain, *Hamp1*= hepcidin, *Fpn1* = ferroportin, *Lcn2* =lipocalin 2. 72
- 4.27 **Quantification of iron metabolism genes in liver tissue from wt, *Irp1*^{-/-} and *Irp2*^{-/-} mice.** 8-20-week-old non-infected and Mtb infected female wt, *Irp1*^{-/-} and *Irp2*^{-/-} mice were sacrificed at indicated time points. Livers were collected, and total host cellular RNA was extracted. Complementary DNA was synthesized and used for the quantification of *Tfr1* (A) *Dmt1* (B) *Frt-L* (C) *Il-6* (D) *Hamp1* (E) *Fpn1* (F) gene expression via qRT-PCR. All mRNA expression levels were normalized against murine *Hprt* mRNA expression levels. Data are from 1 experiment (n=4 animals) and shown as mean ± SD. Statistical analysis was performed using two-way ANOVA with Tukey's multiple comparison tests. ns represents statistically non-significant differences. Abbreviations: RQ= Relative quantification, *Tfr1*= transferrin receptor 1, *Dmt1*= divalent metal transporter, *Frt-L*= ferritin-light chain, *Il-6*= Interleukin-6, *Hamp1*= hepcidin, *Fpn1* = ferroportin. 73
- 4.28 **Histological analysis of iron deposits in lung tissue sections from wt, *Irp1*^{-/-} and *Irp2*^{-/-} mice.** 8-20-week-old female wt, *Irp1*^{-/-} and *Irp2*^{-/-} mice were infected with 100 CFU of Mtb via the aerosol route. Superior lung lobes were collected, PFA fixed, and paraffin-embedded. Tissue sections were stained with Perl's stain and examined at indicated magnifications (A). Iron deposits stain bright-deep blue while nuclei and cytoplasm stain pink-red. Representative micrographs of 1 animal out of 8 per group are shown. Scale bars represent 100 μm. Quantitative assessment of iron deposits (B). Data generated from quantification is from 1 experiment (n=4 animals). Statistical analysis was performed using two-way ANOVA with Tukey's multiple comparison tests. *p ≤ 0.05, **p ≤ 0.01 and ***p ≤ 0.0001 were considered statistically significant. ns represents statistically non-significant differences 74
- 4.29 **Histological analysis of iron deposits in liver tissue sections from wt, *Irp1*^{-/-} and *Irp2*^{-/-} mice.** 8-20-week-old female wt, *Irp1*^{-/-} and *Irp2*^{-/-} mice were infected with 100 CFU of Mtb via the aerosol route. Left liver lobes were collected, PFA fixed, and paraffin-embedded. Tissue sections were stained with Perl's stain and examined at indicated magnifications (A). Iron deposits stain bright-deep blue while nuclei and cytoplasm stain pink-red. Representative micrographs of 1 animal out of 8 per group are shown. Scale bars represent 100 μm. Quantitative assessment of iron deposits (B). Data generated from quantification is from 1 experiment (n=4 animals). Statistical analysis was performed using two-way ANOVA with Tukey's multiple comparison tests. *p ≤ 0.05 was considered statistically significant 75

4.30	Histological analysis of iron in spleen tissue sections from wt, <i>Irp1</i>^{-/-} and <i>Irp2</i>^{-/-} mice. 8-20-week-old non-infected female wt, <i>Irp1</i> ^{-/-} and <i>Irp2</i> ^{-/-} mice were sacrificed, spleens were collected, PFA fixed, and paraffin-embedded. Tissue sections were stained with Perl's stain and examined at indicated magnifications. Iron deposits stain bright-deep blue while nuclei and cytoplasm stain pink-red. Representative micrographs of 1 animal out of 4 per group are shown. Scale bars represent 200 μ m and 100 μ m.	76
4.31	Experimental design. 20-week-old female wt, <i>Irp1</i> ^{-/-} and <i>Irp2</i> ^{-/-} mice were infected with 100 CFU of Mtb H37Rv via aerosol route and sacrificed at indicated time points.	77
4.32	Measurement of blood cell count and RBC indices in whole blood from wt, <i>Irp1</i>^{-/-} and <i>Irp2</i>^{-/-} mice. 20-week-old non-infected and Mtb infected female wt, <i>Irp1</i> ^{-/-} and <i>Irp2</i> ^{-/-} mice were sacrificed. Blood was obtained from the <i>vena cava caudalis</i> under terminal anaesthesia for investigation of RBC (A), HGB (B), HCT (C), MCV (D), MCH (E), MCHC (F) and RDWc (G) at indicated timepoints. Each square represents an individual sample (n=5 animals). Data pooled from 2 independent experiments and shown as mean \pm SD. Statistical analysis was performed using two-way ANOVA with Tukey's multiple comparison tests. *p \leq 0.05, **p \leq 0.01 and **** p \leq 0.0001 were considered statistically significant. ns represents statistically non-significant differences.	78
4.33	Genotyping by PCR from liver tissues from mice presumed to be wt, <i>Irp1</i>^{-/-} and <i>Irp2</i>^{-/-} mice. Non-infected and Mtb infected female mice presumed to be wt, <i>Irp1</i> ^{-/-} and <i>Irp2</i> ^{-/-} mice were sacrificed at indicated time points. Livers were collected, and total host cellular DNA was extracted, amplified by PCR and separated by size for visualization by agarose gel electrophoresis. Photographs of 2% agarose gels showing DNA bands from wt (A and D), <i>Irp1</i> ^{-/-} (B and E) and " <i>Irp2</i> ^{-/-} " (C and F) mice. Std= standard, i.e., 100 bp Marker, wt control= wild type control, ho.= homozygous, het.= heterozygous.	79
4.34	Measurement of blood cell count and RBC indices in whole blood from wt, <i>Irp1</i>^{-/-} and <i>Irp2</i>^{+/-} mice. 20-week-old female wt, <i>Irp1</i> ^{-/-} and <i>Irp2</i> ^{+/-} mice were infected with 100 CFU of Mtb via aerosol route. Blood was obtained from the <i>vena cava caudalis</i> under terminal anaesthesia for investigation of RBC (A), HGB (B), HCT (C), MCV (D), MCH (E), MCHC (F) and RDWc (G) at indicated timepoints. Each square represents an individual sample (n=5 animals). Data pooled from 2 independent experiments and shown as mean \pm SD. Statistical analysis was performed using two-way ANOVA with Tukey's multiple comparison tests. *p \leq 0.05, **p \leq 0.01 and **** p \leq 0.0001 were considered statistically significant. ns represents statistically non-significant differences.	80
4.35	Evaluation of indicators of iron status in sera from wt, <i>Irp1</i>^{-/-} and <i>Irp2</i>^{-/-} mice 20-week-old female wt, <i>Irp1</i> ^{-/-} and <i>Irp2</i> ^{-/-} mice were infected with 100 CFU of Mtb via the aerosol route. Serum was obtained from whole blood collected from the <i>vena cava caudalis</i> under terminal anaesthesia for investigation of serum iron (A), total iron-binding capacity (B), transferrin saturation (C), and serum ferritin (D) at indicated timepoints. Each square represents an individual sample (n=3-5 animals). Data are from 1 experiment and shown as mean \pm SD. Statistical analysis was performed using two-way ANOVA with Tukey's multiple comparison tests. *p \leq 0.05, **p \leq 0.01 and *** p \leq 0.001 were considered as statistically significant. ns represents statistically non-significant differences.	81

- 4.36 **Cohousing experimental approach to investigate the influence of microbiota composition on host phenotypic variation during Mtb infection.** Pregnant GF mice in the 2nd gestational week were cohoused in a 1:1 ratio per cage with wt, IRP1 homozygous (ho or *Irp1*^{-/-}) and IRP2 heterozygous (het or *Irp2*^{+/-}) mice (referred to as donors) from SPF housing conditions. After the birth of pups, all mice were cohoused for 4 weeks before weaning. Afterwards, female pups (referred to as acceptors) from ex-GF mice were cohoused in a 3:2 ratio per cage with the same donor mouse genotypes before weaning. At 6 weeks of age, only acceptors were infected with 100 CFU of Mtb via aerosol route and further cohoused with non-infected donors. Before infection (i.e. at day -1 (dm1)) and at days 13 and 28 p.i., acceptor animals were sacrificed. Non-infected donor animals were sacrificed at day 32 p.i. (i.e., at the end of the study). Experimental set-up illustrates one experiment, n=8 animals per donor genotype and 3-4 per acceptor genotype. 82
- 4.37 **Visualization of differences in the caecal microbial community structure of donor and acceptor mice.** 6-week-old female acceptors were cohoused with non-infected donors in a genotype-specific manner and infected with 100 CFU of Mtb via the aerosol route. All mice were sacrificed at indicated time points, and their caecal content was collected for 16S rRNA sequencing. Distinct clustering of samples was observed between the donors (A) and acceptors (B). Data from 1 experiment are shown, n=8 animals per donor genotype and 3-4 per acceptor genotype. 83
- 4.38 **Within-group and between-group dissimilarities in the caecal microbial community structure of donor mice.** Non-infected wt-, IRP1- and IRP2-donor mice were sacrificed at the end of the experiment and caecal contents were collected for 16S rRNA sequencing. Differences in microbiota compositions were observed between IRP1- (A) and IRP2- (B) compared to wt donor mice were observed. Data from 1 experiment are shown, n=8 animals per donor genotype and 3-4 per acceptor genotype. Significance was tested using the adonis function from the vegan package in R; ** and *** indicate $p \leq 0.01$ and $p \leq 0.001$, respectively. 84
- 4.39 **Within-group and between-group dissimilarities in the caecal microbial community structure of donor vs acceptor mice.** 6-week-old female acceptors were cohoused with non-infected female donors in a genotype-specific manner prior to and following Mtb H37Rv infection via the aerosol route. All mice were sacrificed at specific time points, and caecal content was collected for 16S rRNA sequencing. Comparable microbiota compositions between and within wt-acceptors and -donors (A), dissimilar microbiota compositions between but not within IRP1-acceptors and -donors (B), and comparable microbiota compositions between and within IRP2-acceptors and -donors (C) were observed. Data from 1 experiment are shown, n=8 animals per donor genotype and 3-4 per acceptor genotype. Significance was tested using the adonis function from the vegan package in R; ** and *** indicate $p \leq 0.01$ and $p \leq 0.001$, respectively. Abbreviations: Acc= acceptor, Don= donor. 85

4.40	Within-group and between-group dissimilarities in the caecal microbial community structure of acceptor mice. 6-week-old female acceptors were cohoused with non-infected donors in a genotype-specific manner. Acceptors were infected with 100 CFU of Mtb via aerosol route, sacrificed at specific time points, and caecal content was collected for 16S rRNA sequencing. Data from 1 experiment are shown, n=3-4 animals. Significance was tested using the adonis function from the vegan package in R; ** and *** indicate $p \leq 0.01$ and $p \leq 0.001$, respectively. Abbreviations: Acc= acceptor, Don= donor.	86
4.41	Differentially abundant families in caeca from IRP1- vs wt-donor mice. IRP1-donors from SPF animal husbandry were cohoused in a 1:1 ratio per cage with pregnant GF mice and handled as indicated in Fig. 4.36. All non-infected IRP1 donor- and wt-donor mice were sacrificed and caecal contents were collected for 16S rRNA sequencing. Only families with a p-value ≤ 0.2 are shown. Data from 1 experiment are shown, n=3-4 animals. Abbreviations: f= family, o= order, c= class, o= order, uncl= unclassified. Significance was tested using the exact Wilcoxon test.	87
4.42	Differentially abundant families in caeca from IRP2- vs wt-donor mice. IRP2-donors from SPF animal husbandry were cohoused in a 1:1 ratio per cage with pregnant GF mice and handled as indicated in Fig. 4.36. All non-infected IRP2 donor- and wt-donor mice were sacrificed and caecal contents were collected for 16S rRNA sequencing. Only families with a p-value ≤ 0.2 are shown. Data from 1 experiment are shown, n=3-4 animals. Abbreviations: f= family, o= order, c= class, o= order, uncl= unclassified. Significance was tested using the exact Wilcoxon test.	88
4.43	Differentially abundant genera in caeca from IRP1- vs wt-donor mice. IRP1-donors from SPF animal husbandry were cohoused in a 1:1 ratio per cage with pregnant GF mice as indicated in Fig. 4.36. All non-infected IRP1- and wt-donor mice were sacrificed and caecal contents were collected for 16S rRNA sequencing. Only families with a p-value ≤ 0.2 are shown. Data from 1 experiment are shown, n=3-4 animals. Abbreviations: c= class, o= order, f= family, g= genus, uncl = unclassified. Significance was tested using the Wilcoxon Signed-Ranks Tests; $p \leq 0.2$	89
4.44	Differentially abundant genera in caeca from IRP2- vs wt-donor mice. IRP2-donors from SPF animal husbandry were cohoused in a 1:1 ratio per cage with pregnant GF mice as indicated in Fig. 4.36. All non-infected IRP2-donor and wt-donor mice were sacrificed and caecal contents were collected for 16S rRNA sequencing. Only families with a p-value ≤ 0.2 are shown. Data from 1 experiment are shown, n=3-4 animals. Abbreviations: c= class, o= order, f= family, g= genus, uncl= unclassified. Significance was tested using the Wilcoxon Signed-Ranks Tests; $p \leq 0.2$	90

- 4.45 **Mycobacterial loads in tissue homogenates from wt-, IRP1- and IRP2-acceptor mice.** 6-week-old wt-, IRP1-, and IRP2-acceptor mice handled as indicated in Fig. 4.36 were infected with 100 CFU of Mtb via the aerosol route. Mice were sacrificed, lungs (A and B), spleens (C), and livers (D) were collected, and CFU assays were performed at indicated time points. Data from 1 experiment are shown. Each square represents an individual sample (n=3-4 animals) with horizontal lines indicating the median. Statistical analyses were performed using Kruskal-Wallis with Dunn's posttest to compare experimental groups *p = 0.0272 was considered statistically significant. ns represents statistically non-significant differences 91
- 4.46 **Histopathological analysis of lung tissue sections from wt-, IRP1- and IRP2-acceptor mice.** 6- week-old female wt-, IRP1- and IRP2-acceptor mice handled as indicated in Fig. 4.36 were infected with 100 CFU Mtb H37Rv via the aerosol route and sacrificed at day 13 p.i. Superior lung lobes were collected, PFA fixed, paraffin infiltrated, stained with H&E stain, and examined under the BX41 light microscope (A). The affected lung area was measured using the cellSens software. Representative micrographs of 1 animal out of 3 per group are shown (i.e., from 1 experiment). Black squares indicate inflammatory cellular infiltrates. Scale bars represent 200 μm (4 x magnification, upper panel), 20 μm (40 x magnification, lower panel). Quantitative assessment of cellular infiltrates and lesions of lung tissue of wt-, IRP1-, and IRP2-acceptor mice at days 13 and 28 p.i (B). Statistical analysis was performed using Kruskal-Wallis' non-parametric test with Dunn's post-test to compare experimental groups; ns represents not-statistically significant differences. 92
- 4.47 **Measurement of blood cell count and RBC indices in whole blood from wt-, IRP1- and IRP2-acceptor mice.** 6- week-old female wt-, IRP1- and IRP2-acceptor mice were handled as indicated in Fig. 4.36 and infected with approx. 100 CFU Mtb H37Rv via aerosol route. Blood was obtained from the inferior vena cava under terminal anaesthesia for the investigation of RBC (A), HGB(B), HCT (C), MCV (D), MCH (E), MCHC and (F) RDWc (G) indicated timepoints. Each square represents an individual sample (n=3-4 animals). Data from 1 experiment are shown. Statistical analysis was performed using two-way ANOVA with Tukey's multiple comparison tests. *p \leq 0.05 were considered statistically significant; ns represents non-statistically significant differences. 93
- 4.48 **Measurement of immune cells in whole blood from wt-, IRP1- and IRP2-acceptor mice.** 6- week-old female wt-, IRP1- and IRP2-acceptor mice handled as indicated in Fig. 4.36 were infected with 100 CFU Mtb H37Rv via aerosol route. Whole blood was obtained from the inferior *vena cava caudalis* under terminal anaesthesia for the investigation of blood immune cells WBC (A), Lymphocytes (B), Monocytes (C) Neutrophils (D) at indicated timepoints. Each square represents an individual sample (n=3-4 animals) with horizontal lines indicating the median. Data from 1 experiment are shown. Statistical analysis was performed using two-way ANOVA with Tukey's multiple comparison tests. *p \leq 0.05 were considered statistically significant; ns represents non-statistically significant differences. 94

4.49 **Quantification of cytokine concentrations in sera from wt-, IRP1- and IRP2-acceptor mice.** 6- week-old female wt-, IRP1- and IRP2-acceptor mice handled as indicated in Fig. 4.36 were infected with approx. 100 CFU Mtb H37Rv via aerosol route and sacrificed at indicated time points. Serum was obtained from whole blood collected from the *vena cava caudalis* under terminal anaesthesia and used to investigate IFN γ (A) and TNF α (B) production. Each square represents an individual sample (n=3-4 animals) with horizontal lines indicating the median. Data from 1 experiment are shown. Statistical analysis was performed using two-way ANOVA with Tukey's multiple comparison tests. *p \leq 0.05 and **p \leq 0.01 were considered statistically significant; ns represents non-statistically significant differences.

95

5.1 **Hypothetical scheme of dietary iron supplementation and IRP2-mediated function during experimental TB:** In mice deficient for IRP2 and mice on an iron-rich diet, non-infected and resting M ϕ s showed higher iron accumulation (A). In activated M ϕ s (B), **I. Increased iron concentration acts as a micronutrient source, promotes higher Mtb loads and spread:** Higher expression of scavenger receptors e.g., CD91, CD163, or increased phagocytosis of RBCs potentially enhances increased the iron accumulation phenotype. During Mtb infection (1), Mtb is phagocytosed and resides in iron-rich phagosomes (2). Mtb relies on iron for growth and uses its iron-chelating molecules called mycobactins to take iron from the host (3). Excess labile iron (4) generates ROS which aggravates pulmonary pathology (5). **II. Iron also hampers immunity:** This occurs through ROS (6) which stimulates binding activity of transcription factors such as NF κ B and Nrf2 (7) to induce the higher expression of cytokines such as IL-1 β , IL-6, and TNF α (8). Th1 cells (9) produce IL-1 β , TNF α , and IFN γ (10) which can induce expression of nitric oxide (11) by M ϕ s, which can contribute to controlling Mtb but can also aggravate pulmonary pathology (5). Higher nitric oxide also impairs neutrophil recruitment (12). Production of proinflammatory cytokines and chemokines produced hinders erythropoiesis (13) which induces anemia (14). **III. Iron leads to neutrophil-driven disease exacerbation:** IL-17A (15) induces neutrophil recruitment (16). Neutrophils produce ROS which exacerbates TB disease (17) and leads to aggravated pulmonary pathology (5) **IV. IRP2 deficiency alters body iron distribution:** This is achieved by higher IL-6 concentrations (18) which induce *Hamp1* mRNA transcripts (19) which results in (a) iron sequestration within macrophages leading to iron overload which rather provides a survival advantage for Mtb and exacerbates pathology, (b) hypoferremia (c) potentially anemia of inflammation (20). Created with BioRender.com . . .

117

Appendix

Curation and clustering of sequencing data using bioinformatics techniques

Generation of OTU table with USEARCH

For the bioinformatics analysis, USEARCH, a sequence analysis tool was used [278].

#1. Export path definition

```
export usearch64=/bin/usearch64
```

#2. Preparation of files

```
sudo find ./ -type f -exec cp '{}' ./ \;  
sudo gunzip *.gz
```

#3. Merge files

```
sudo $usearch64 -fastq_mergepairs *_R1_001.fastq -fastqout  
merged.fq -relabel @
```

2020-run

```
sudo $usearch64 -fastq_mergepairs *_R1_001.fastq -fastqout  
merged_trunctail30_minovlen40.fq -fastq_trunctail 30 -  
fastq_minovlen 40 -relabel @ -report  
mergereport_trunctail30_minovlen40.txt
```

#4. Primer check

```
sudo $usearch64 -search_oligodb merged_trunctail30_minovlen40.  
fq -db ~/tools/ primers.fa -strand both \-userout  
primer_hits.txt -userfields query+qlo+qhi +qstrand
```

#5. Quality check

```
sudo $usearch64 -fastq_eestats2 merged_trunctail30_minovlen40.  
fq -output qual_trunctail30_minovlen40.txt  
$usearch64 -fastq_eestats2 Cell13_S50_L001_R1_001.fastq -output  
qualCel1.txt
```

#6. Removal of indices, overhangs and primers

```
sudo $usearch64 -fastx_truncate merged_trunctail30_minovlen40.  
fq -stripleft 17 -stripriht 20 \-fastqout  
stripped_trunctail30_minovlen40.fq
```

#7. Quality filtering

```
sudo $usearch64 -fastq_filter stripped.fq -fastq_maxee 1.0 \-
  fastaout filteredstripped.fa -relabel Filt
sudo $usearch64 -fastq_filter stripped_trunctail30_minovlen40.
  fq -fastq_minlen 330 -fastq_maxee 1.0 \-fastaout filtered.fa
  -relabel Filt
```

#8. Filtering for unique sequences

```
sudo $usearch64 -fastx_uniques filtered.fa -sizeout -relabel
  Uniq -fastaout uniques.fa
```

#9. Sorting by length

```
sudo $usearch64 -sortbylength uniques.fa -fastaout seqs_sorted.
  fasta
```

#10. OTU clustering

```
sudo $usearch64 -cluster_otus uniques.fa -otus otust.fa -
  relabel Otu
```

#11. Generation of OTU table

```
sudo $usearch64 -otutab merged_trunctail30_minovlen40.fq -otus
  otust.fa -sample_delim . -otutabout otutab.csv
```

#11. Taxonomic assignment of OTU representative sequences

```
sudo $usearch64 -sintax otust.fa -db ~/tools/rdp_16s_v16s_sp.
  fa -strand both \-tabbedout sintaxOTUST.csv -sintax_cutoff
  0.8
```

Publications and Presentations

Publications:

Nils-Jørgen K. Dal, Gabriela Schäfer, Andrew M. Thompson, Sascha Schmitt, Natalja Redinger, Noelia Alonso-Rodriguez, Kerstin Johann, **Jessica Ojong**, Jens Wohlmann, Andreas Best, Kaloian Koynov, Rudolf Zentel, Ulrich E. Schaible, Gareth Griffiths, Matthias Barz, Federico Fenaroli. " π - π interactions stabilize PeptoMicelle-based formulations of Pretomanid derivatives leading to promising therapy against tuberculosis in zebrafish and mouse models". *Journal of Controlled Release*, Volume 354, 2023, Pages 851-868, ISSN 0168-3659, <https://doi.org/10.1016/j.jconrel.2023.01.037>. **Published**

Matthias Hauptmann, Barbara Kalsdorf, **Jessica Ojong**, Christoph Lange, Ulrich E. Schaible. "Differential microbiota alterations in tuberculosis patients treated for susceptible versus multi drug resistant infections". **In Prep**

Jessica Ojong, Matthias Hauptmann, Esther Meyron-Holtz, Ulrich E. Schaible. "Alterations in Iron Metabolism and the Differential Roles of Iron Regulatory Proteins 1 and 2 on Antimicrobial Host Defenses to *Mycobacterium tuberculosis*". **In Prep**

Presentations (oral presentation: OP/ poster presentation: PP) at conferences

Jessica E. Ojong, Esther Meyron-Holtz, Matthias Hauptmann, Ulrich E. Schaible „Iron-driven host-microbiota coadaptation: A factor in *Mycobacterium tuberculosis infection*?", 8th DGFI Autumn School "Current Concepts in Immunology", Merseburg, Germany, 09.-14.10.2016, **PP**

Jessica E. Ojong, Esther Meyron-Holtz, Matthias Hauptmann, Ulrich E. Schaible „Iron-driven host-microbiota coadaptation: A factor in *Mycobacterium tuberculosis infection*?", Symposium on Pathogen Evolution, Kiel, Germany, 28.11.2016, **OP**

Jessica E. Ojong, Esther Meyron-Holtz, Matthias Hauptmann, Ulrich E. Schaible „Iron-driven host-microbiota coadaptation: A factor in *Mycobacterium tuberculosis infection*?", Infektion und Immunabwehr, Burg Rothenfels Germany, 08.-10.03.2017, **OP**

Jessica E. Ojong, Esther Meyron-Holtz, Matthias Hauptmann, Ulrich E. Schaible „Iron-driven host-microbiota coadaptation: A factor in *Mycobacterium tuberculosis infection*?", 8th BBRS Retreat, Ammersbek, Germany, 07.-08.06.2017, **OP**

Jessica E. Ojong, Esther Meyron-Holtz, Matthias Hauptmann, Ulrich E. Schaible „Iron-driven host-microbiota coadaptation: A factor in *Mycobacterium tuberculosis infection*?", Symposium on Pathogen Evolution, Kiel, Germany, 20.-21.07.2017, **OP**

Jessica E. Ojong, Esther Meyron-Holtz, Matthias Hauptmann, Ulrich E. Schaible „Iron-driven host-microbiota coadaptation: A factor in *Mycobacterium tuberculosis* infection?", Symposium on Pathogen Evolution, Kiel, Germany, 20.-21.07.2017, **OP**

Jessica E. Ojong, Esther Meyron-Holtz, Matthias Hauptmann, Ulrich E. Schaible „Iron-driven host-microbiota coadaptation: An influencing factor in *Mycobacterium tuberculosis* infection?", 3rd Annual ISEMPH conference 2017, Groningen, Netherlands, 18.-21.08.2017, **OP**

Jessica E. Ojong, Thomas A. Kohl, Stefan Niemann, Ulrich E. Schaible, Matthias Hauptmann „Iron-driven host-microbiota coadaptation: An influencing factor in *Mycobacterium tuberculosis* infection?", ISEMPH 4th Annual meeting, Utah, USA, 01.-04.08.2018, **OP**

Jessica E. Ojong, Thomas A. Kohl, Stefan Niemann, Ulrich E. Schaible, Matthias Hauptmann „Iron-driven host-microbiota coadaptation: An influencing factor in *Mycobacterium tuberculosis* infection?", Joint Congress on Evolutionary Biology, Montpellier, France, 18.-22.08.2018, **PP**

Jessica E. Ojong, Esther Meyron-Holtz, Matthias Hauptmann, Ulrich E. Schaible „Iron-driven host-microbiota coadaptation: A factor in *Mycobacterium tuberculosis* infection?", 9th BBRS Retreat, Ammersbek, Germany, 23.-24.08.2018, **OP**

Jessica E. Ojong, Esther Meyron-Holtz, Matthias Hauptmann, Ulrich E. Schaible „Iron-driven host-microbiota coadaptation: A factor in *Mycobacterium tuberculosis* infection?", EvoLUNG Retreat, Kattendorf, Germany, 06.-07.09.2018, **PP + OP**

Jessica E. Ojong, Esther Meyron-Holtz, Matthias Hauptmann, Ulrich E. Schaible „Iron-driven host-microbiota coadaptation: An influencing factor in *Mycobacterium tuberculosis* infection?", 2019 Keystone Symposia Conference, Alberta, Canada, 17.-21.01.2019, **PP**

Jessica E. Ojong, Esther Meyron-Holtz, Matthias Hauptmann, Ulrich E. Schaible „Iron-driven host-microbiota coadaptation: An influencing factor in *Mycobacterium tuberculosis* infection?", Congress of the Bioiron Society, Heidelberg, Germany, 05.-10.05.2019, **PP**

Jessica E. Ojong, Esther Meyron-Holtz, Matthias Hauptmann, Ulrich E. Schaible „Iron-driven host-microbiota coadaptation: An influencing factor in *Mycobacterium tuberculosis* infection?", 12th Seeon Conference, Seeon, Germany, 27.-30.06.2019, **PP**

Jessica E. Ojong, Esther Meyron-Holtz, Matthias Hauptmann, Ulrich E. Schaible „Iron-driven host-microbiota coadaptation: A influencing factor in *Mycobacterium tuberculosis* infection?", Autumn School for PhD students on the role of the microbiome in complex and metabolic and inflammatory disease, Ebberup, Denmark, 29.09-02.10.2019, **PP**

Acknowledgements

I would like to express my sincere appreciation to my supervisor, **Prof. Dr Ulrich E. Schaible**, for providing me with the opportunity to work in his research group (RG) during my PhD. His expertise, valuable advice, ongoing support, and unwavering faith in my abilities have been instrumental in my success, particularly during the writing of this dissertation. I am also grateful for his open-door policy at work and his encouragement of a team-oriented approach within the research group. Working under his guidance and supervision has been an absolute pleasure.

I would like to extend my gratitude to my practical supervisor, **Dr Matthias Hauptmann** for inspiring my interest in microbiome research and for generously sharing his time and expertise in bioinformatic analyses with me. I have learned a great deal from him and have grown as a scientist under his watch.

I also want to thank my co-supervisor, **Prof. Dr Susanne Krauss-Etschmann**, for her valuable advice and recommendations during my thesis committee meetings, and **Prof. Dr Esther Meyron-Holtz** for providing the *Irp1*^{-/-} and *Irp2*^{-/-} mice used in my study, as well as for the enlightening scientific discussions and suggestions.

I am deeply grateful to **Nina Grohmann** for her technical assistance with *in vivo* experiments and library preparations for 16S rRNA sequencing, and to **Dagmar Meyer** for her training in histological techniques and staining. I would also like to thank **Jacqueline Eich** and **Kristine Hagens** for their technical assistance during the initial phase of my PhD. I would like to thank **Dr Natalja Redinger** for her help with the initial aerosol infections of some of the mice used in my study. I am particularly grateful for her cheerful and optimistic character, which made sharing an office space with her enjoyable.

I would like to express my appreciation to everyone in the CellMiBi RG, including **Dr Uwe Mamat**, **Dr Tobias Dallenga**, **Dr Christian Alexander**, **Claire Sophie Taylor**, **Pit Engling**, **Celina Prosch**, **Christoph Leschzyk**, **Olaitan Tijani**, **Flor del Milagro Vasquez Sotomayor**, **Benthe Beu**, **Folake Aina**, **Dorte Grella**, **Manuel Hein** for their support and thought-provoking questions during lab meetings. I am thankful for the great working environment and fun times, especially during our team-building events. Working with this group of individuals has been a truly remarkable experience, and I could not have asked for a better research group.

Lastly, I would like to thank the Leibniz Science Campus **Evolutionary Medicine of the Lung (EvoLUNG)** for the funding opportunity to pursue my PhD, as well as for awarding me numerous stipends to attend conferences to present my research. I am grateful to **Prof. Dr Stefan Niemann** and **Prof. Dr Hinrich Schulenberg**, spokespersons of EvoLUNG and **Dr Christiane Gerlach**, program coordinator of Evolung, for their support.

I would like to express my gratitude to the **BAB 26, Afro-Borstelians** and **Ausländerbande** for the enjoyable moments. Specifically, I am thankful to **Guhrun Lehwruk** for her support, interest, and dedication to helping international scientists in Borstel.

I extend my heartfelt appreciation to my friends, **Lindsay, Eleanor, Harriet, Joy, Ghislaine, Leslie, Claire, Henri, Fri, Kiky, Velma, Ireti, Sandra, Coretta, Sumanta and Sowmya** for their support.

I am grateful to my mother and siblings, particularly **Lucy, Merilyne** and **Manyo** for their constant love and encouragement. To **Heiko**, my dog, thank you for bringing immense joy into my life.

Lastly, I owe a debt of gratitude to my best friend and life partner **AA** for his unwavering love, encouragement, and support. I could not have accomplished this without him.

Curriculum vitae



Personal details:

Jessica Ebot-Otang Akoh-Arrey
(born Ojong)
Parkallee 1-40, 23845, Borstel
Tel: +49 4537 188 5820
Email: jojong@fz-borstel.de

Academic qualifications:

09/2016 – present PhD candidate, Research Center Borstel-Leibniz Lung Center (RCB), Germany
04/2014 – 08/2016 MSc. Biology (Major in Molecular Biosciences), Ulm University
06/2007– 10/2010 B.Ed. Biology, Buea University, Cameroon
09/2005 – 06/2007 Advanced level General Certificate of Education
09/1999 – 06/2005 Ordinary level General Certificate of Education

Professional Experience:

10/2020 – present Postdoctoral Research Fellow, RCB, Germany
09/2016 – 10/2020 Doctorate, Priority Area „Infections“, Cellular Microbiology, RCB, Germany. Supervisor: Prof. Dr Ulrich E. Schaible
02/2016 – 08/2016 Master thesis, Institute of Microbiology and Biotechnology, Ulm University, Germany. Supervisor: apl. Prof. Dr Christian Riedel
01/2016 – 02/2016 Internship towards MSc thesis, Institute of Comparative Molecular Endocrinology, Ulm University, Germany. Supervisor: Prof. Dr Jan Tuckermann
07/2015 – 08/2015 Internship towards MSc thesis, Institute of Molecular Virology, Ulm University, Germany. Supervisor: Prof. Dr Jan Munch

Stipends and prizes:

08/2018 EvoLUNG travel stipend (2500 EUR)
06/2019 EvoLUNG travel stipend (670 EUR)
10/2019 Best poster presentation (Autumn school for PhD students on the role of the microbiome, Ebberup, Denmark)

Languages:

English – Fluent
French - Fluent
German – Intermediate/ Advanced (B2/C1)

